UCLouvain

UNIVERSITÉ CATHOLIQUE DE LOUVAIN

PH.D. THESIS

Generation of Synthetic Atmospheric Events for the Evaluation of Millimeter Wave Earth-Space Propagation Impairments

By:
MOJTABA RAZAVIAN

Thesis submitted in partial fulfillment of the requirements for the degree of
Docteur en sciences de l'ingénieur et technologie

Composition of the jury

Prof. Danielle Vanhoenacker-Janvier - *Supervisor*	UCLouvain, BE
Prof. Claude Oestges - *Supervisor*	UCLouvain, BE
Prof. Christophe Craeye - *President*	UCLouvain, BE
Prof. David Bol - *Secretary*	UCLouvain, BE
Prof. Philippe De Doncker	ULB, BE
Dr. Laurent Féral	U. Toulouse III, FR

Louvain-la-Neuve
2025

Acknowledgments

First and foremost, I would like to express my deepest gratitude to my supervisor, Prof. Danielle Vanhoenacker-Janvier, for welcoming me into her research group and for her continuous support throughout this PhD journey. Her patience, invaluable guidance, and encouragement have been a source of inspiration, and I will always remain grateful for the trust she placed in me from the very beginning.

I would also like to acknowledge my co-supervisor, Prof. Claude Oestges, for his involvement as co-supervisor of this thesis and for his valuable comments and ideas during the course of this work.

I wish to sincerely thank the members of my jury for dedicating their time and expertise to evaluate this work. Special thanks go to Prof. Christophe Craeye (UCLouvain), who kindly accepted to serve as President of the jury, to Dr. Laurent Féral (Université Toulouse III – Paul Sabatier, France) for sharing his expertise as an external specialist in propagation and NWP applications, to Prof. Philippe De Doncker (ULB) for generously accepting to be part of the jury and for his valuable remarks, and to Prof. David Bol (UCLouvain) for serving as Secretary of the jury and for his thoughtful contributions to this evaluation.

I am very grateful to my colleagues at UCLouvain, who made this journey much more enjoyable. In particular, I wish to thank Laurent Quibus for his generous help and collaboration, and my colleagues Farzad Jabbarigargari and Masood Arash for the many stimulating discussions—both academic and non-academic—that brought balance to my PhD life. I would also like to warmly thank my colleagues and office mates Florian Quatresooz, François De Saint Moulin, and Guillaume Thiran, whose support and companionship made the daily work environment both pleasant and motivating.

My sincere thanks also go to the administrative staff, Brigitte Dupont and François Hubin, for their constant assistance and efficiency in handling countless practical matters with kindness and patience.

Finally, I owe my deepest gratitude to my family, who, despite being far away in another country, have always supported me with their unconditional love and encouragement. Their constant presence, even from a distance, gave me the strength to overcome challenges and complete this journey. I am equally grateful to my partner, Tarlan, whose patience, understanding, and unwavering support have been invaluable throughout this PhD. This thesis is dedicated to them.

Abstract

This thesis investigates the modeling and validation of rain attenuation in satellite communication systems, with a particular focus on high-frequency bands and the integration of numerical weather prediction (NWP) data. The increasing demand for higher data rates and wider coverage in future satellite systems—especially at frequencies above 20 GHz—necessitates a better understanding of atmospheric impairments, particularly those due to precipitation. This work provides a comprehensive framework to model, simulate, and validate rain-induced attenuation for both geostationary (GEO) and low Earth orbit (LEO) satellite links, using data collected at the Alphasat ground station in Louvain-la-Neuve, Belgium.

The study begins by characterizing the individual contributions of gaseous, cloud, and rain attenuation based on NWP data from the Weather Research and Forecasting (WRF) model. A detailed investigation of model lead time and run time is conducted to optimize the accuracy of the simulated weather fields. The azimuth-elevation attenuation maps are constructed and analyzed for each attenuation component, highlighting the spatial dependencies and limitations of commonly used scaling laws. The gaseous component shows limited variability, making it suitable for cosecant-based approximations. In contrast, cloud and rain components exhibit strong spatial and temporal dynamics, justifying the need for full 3D atmospheric data.

To model rain attenuation, three approaches are employed: (1) a volumetric rainwater content model using Mie scattering, (2) a direct rain rate-based model from WRF outputs, and (3) a hybrid model combining MultiEXCELL synthetic rain fields with optical flow techniques for temporal refinement. The models are evaluated both in terms of time series accuracy and long-term statistics, using beacon measurement data and ITU-R recommendations as references. Notably, the MultiEXCELL-based method exhibits superior performance in replicating measured attenuation distributions, especially in the critical 0.1% to 1% excess probability range.

The thesis also includes a thorough validation of the WRF-derived attenuation against ITU-R models and experimental data. Error metrics such as mean error, standard deviation, and root-mean-square (r.m.s.) deviation are calculated for each attenuation component across multiple frequencies (19.701 GHz and 39.402 GHz) and for multiple years (2018–2019). While WRF performs well in estimating gaseous attenuation, cloud attenuation is often underestimated, and rain attenuation requires careful treatment of high-intensity events.

Year-to-year variability, particularly for extreme rain events, is also analyzed.

A dedicated section presents the methodology used to extract rain and cloud attenuation from the Alphasat ground station. Manual flagging of atmospheric events, followed by automated attenuation extraction using a reference level derived from clear-sky periods, enables accurate comparison with modeled results.

Finally, the validated attenuation models are applied to LEO satellite trajectories (e.g., Starlink passes) to assess the impact of atmospheric effects on non-geostationary systems. The findings show that, while individual passes may avoid rain entirely, the statistical treatment must account for rain-induced outages properly—especially when designing systems based on GEO-derived statistics.

In conclusion, this thesis demonstrates that the integration of NWP data into rain attenuation modeling, when carefully tuned and validated, can serve as a powerful tool for future satellite communication system design. The MultiEXCELL-based approach, in particular, offers a promising pathway toward achieving realistic, high-resolution attenuation simulations with statistical consistency. The framework developed here contributes both methodologically and practically to the field of propagation modeling, offering insights for both scientific research and engineering deployment.

Contents

Acknowledgments iii

Abstract v

Contents vii

List of Figures xi

List of Tables xvii

List of publications xix

List of Acronyms xxi

1 Introduction 1
- 1.1 Earth-space propagation impairments . . . 2
- 1.2 FMTs for Tropospheric Degradations in Satellite Communication 3
  - 1.2.1 Fade Mitigation Techniques (FMTs) . . . 4
  - 1.2.2 FMTs for GEO Satellites . . . 4
  - 1.2.3 FMTs for Non-GEO Satellites (LEO/MEO) . . . 5
- 1.3 Numerical Weather Predictions (NWPs) . . . 5
- 1.4 State of the Art: NWP in Radio Wave Propagation Impairments . 6
  - 1.4.1 NWP for Time Series Generation . . . 7
  - 1.4.2 NWP for Cumulative Statistics . . . 7
  - 1.4.3 Applications for GEO Links . . . 7
  - 1.4.4 Applications for LEO Links . . . 7
  - 1.4.5 Short-Term Forecasting and Real-Time Applications . . 8
  - 1.4.6 Regional and Climate-Specific Studies . . . 8
- 1.5 Problem Statement . . . 8
  - 1.5.1 Limitations of ITU-R Models for LEO Links . . . 9
- 1.6 Thesis Outline . . . 10

2 Numerical Weather Prediction 13
- 2.1 Overview of Numerical Weather Predictions . . . 14
  - 2.1.1 Advanced Research WRF (ARW) . . . 15
- 2.2 Simulation grids, coordinates and nesting . . . 16
  - 2.2.1 Vertical grid . . . 16

2.2.2 Horizontal grid . . . 18
2.2.3 Nesting . . . 20
2.3 Time Discretization in WRF . . . 22
2.3.1 Time Step (`time_step`) . . . 22
2.3.2 History Interval (`history_interval`) . . . 22
2.3.3 Constraints and Best Practices . . . 23
2.4 Initial Conditions . . . 23
2.4.1 Initialization for Real-Data Conditions . . . 24
2.4.2 GRIB Data and UNGRIB Software . . . 25
2.4.3 Static Data and GEOGRID Software . . . 26
2.5 Description of the Output . . . 27
2.5.1 Geopotential Height . . . 27
2.5.2 Pressure . . . 29
2.5.3 Temperature . . . 29
2.5.4 Gas Mixtures Properties . . . 30
2.5.5 Humidity . . . 31
2.5.6 Rain rate . . . 32
2.5.7 Cloud . . . 33
2.5.8 Wind . . . 33
2.6 Conclusion . . . 34

3 Electromagnetic Scattering by Atmospheric Particles 35
3.1 Atmospheric refractive index . . . 36
3.2 Atmospheric Specific Attenuation . . . 37
3.3 Water Droplet Refractive Index . . . 37
3.3.1 Liebe Model of Liquid Water Permittivity . . . 38
3.3.2 Ray Model of Liquid Water Permittivity . . . 40
3.4 Cloud Attenuation . . . 41
3.5 Gaseous Attenuation . . . 41
3.5.1 Exact Solution . . . 42
3.5.2 Approximate Solution . . . 46
3.6 Rain Attenuation . . . 47
3.6.1 Specific Rain Attenuation Using Mie Scattering . . . 48
3.6.2 Specific Rain Attenuation Using Rayleigh Scattering . . . 51
3.6.3 Rain Drop-Size Distribution . . . 52
3.6.4 Specific Rain Attenuation from the Rain Rate . . . 54
3.7 Conclusion . . . 57

4 Post-Processing of the NWP's Data 59
4.1 Geographical Coordinate Systems . . . 60
4.1.1 Geodetic vs Geocentric Coordinates . . . 60
4.1.2 Geocentric vs ENU Coordinates . . . 63
4.1.3 ENU vs AER Coordinates . . . 65
4.1.4 Earth Global Inertial Coordinates . . . 66
4.2 Map Projection . . . 68
4.2.1 Cylindrical Projection . . . 68
4.2.2 Lambert Conformal Conic Projection . . . 70
4.2.3 Polar Azimuthal (Tangent Plane) . . . 70

4.3 Satellite Position . . . 71
4.4 Atmospheric Attenuation Time Series . . . 72
4.4.1 Link Attenuation Time Series from Azimuth-Elevation Maps . . . 72
4.4.2 Complementary Cumulative Distribution Function . . . 73
4.4.3 Fade Dynamics on Earth-Space Paths . . . 74
4.4.3.1 Fade Duration of Time Series . . . 74
4.4.3.2 Fade Slope of Time Series . . . 78
4.5 Error Analysis . . . 80
4.5.1 Rainfall Rate Prediction Analysis . . . 80
4.5.2 Attenuation Prediction Analysis . . . 81
4.5.3 Fade Duration Prediction Analysis . . . 81
4.5.4 Fade Slope Prediction Analysis . . . 82
4.6 Conclusion . . . 83

5 Rain Cell Spatial Resolution Developing 85
5.1 MultiEXCELL Model . . . 86
5.1.1 Rain Cell Probability of Occurrence . . . 89
5.2 Implementation of MultiEXCELL on WRF Data . . . 89
5.2.1 Cells Detection . . . 90
5.2.1.1 Fix Parameters in Cells Detection . . . 90
5.2.1.2 Search and Track the Rain Cells . . . 91
5.2.2 Solving Cell's Characteristics Equations . . . 93
5.2.2.1 Suitable Non-Linear Equations in Solver Engine 96
5.2.2.2 Restriction on Variable ρ_0 . . . 96
5.2.2.3 Center of Rain Cell . . . 97
5.2.3 New Rain Cells Execution . . . 99
5.2.3.1 Rain Cells Termination Limit . . . 100
5.2.3.2 Rain Cells Intersection Area . . . 100
5.3 Conclusion . . . 100

6 Improving Rain Cell Temporal Resolution 103
6.1 Rain Cell Displacement and Wind Field Complexity . . . 104
6.2 Optical Flow . . . 106
6.2.1 Preliminary Theory . . . 106
6.2.2 Methods of Determination . . . 107
6.2.3 Lucas-Kanade Method . . . 109
6.2.4 TV-L1 . . . 112
6.2.5 Performance Comparison of LK and TV-L1 Algorithms 114
6.3 Rain Motion . . . 120
6.3.1 Rain Rate to Brightness Image . . . 121
6.3.2 Rain Rate Registration . . . 122
6.3.3 Rain Intensity Correction in Optical Flow . . . 126
6.4 Attenuation Time Series . . . 130
6.5 Conclusion . . . 131

7 Model Validation **133**
7.1 WRF Initialization . . . 133
7.1.1 Lead Time and Run Time . . . 135
7.2 Estimation of Excess Attenuation from Alphasat Measurements 140
7.3 Summary of Attenuation Time Series Generation and Resolution Considerations . . . 142
7.3.1 Overview of Attenuation Time Series Generation . . . 143
7.3.2 Resolution Choices and Limitations . . . 144
7.3.3 Verification and Validation Strategy . . . 145
7.3.4 Limitations of MultiEXCELL . . . 146
7.3.5 Lead Time and Run Time Considerations . . . 147
7.3.6 Model Limitations and Physical Assumptions . . . 147
7.4 Results . . . 147
7.4.1 Propagation Azimuth-Elevation Maps . . . 148
7.4.2 Time Series of Attenuation . . . 151
7.4.3 Attenuation Probability for GEO Satellite Components 155
7.4.3.1 Gaseous attenuation for GEO Satellite . . . 155
7.4.3.2 Cloud attenuation for GEO Satellite . . . 160
7.4.3.3 Rain attenuation for GEO Satellite . . . 161
7.4.3.4 Excess Attenuation for GEO Satellite vs Measurememnt . . . 165
7.4.4 Excess Attenuation Probability for LEO Satellite . . . 169
7.5 Conclusion . . . 178

8 Conclusion and Future Work **181**

Appendix I **185**

Appendix II **187**

Appendix III **191**

Appendix IV **193**

Bibliography **195**

List of Figures

2.1 WRF system components 15
2.2 ARW η coordinate 17
2.3 $B(\eta)$ profiles for sigma (σ) coordinate and for hybrid coordinate for $\eta_c = 0., 0.1, 0.2, 0.3, 0.4,$ and 0.5 displayed (a) as a function of η, and (b) as a function of height for a standard atmosphere in a domain with a 30 km upper boundary. 19
2.4 Horizontal and vertical grids of the ARW 19
2.5 Various nest configurations for multi level grids. (a) Telescoping nests. (b) Nests at the same level with respect to a parent grid. (c) Overlapping grids: not allowed with feedback activated. (d) Inner-most grid has more than one parent grid: not allowed . . 21
2.6 Schematic showing data flow and program components in WPS, and how WPS feeds initial data to ARW. 24

3.1 Refractive index of water at 298 K for frequency range 1-1000 GHz with either the Liebe, Ray or the ITU-R P.840 models . . 39
3.2 Cloud specific attenuation at frequency 39.402 GHz. 42
3.3 Specific attenuation due to atmospheric gases at T=288 K, P=1013.15 hPa, and $\rho_{vap} = 7.5\, g/m^3$ for `exact` and `approximation` solutions. 43
3.4 Evolution of some Mie scattering parameters as a function of the radius of the water drop at 298 K and 40 GHz 50
3.5 Specific rain attenuation power law terms κ^H, κ^V, α^H, and α^V in the frequency range from 1 to 1000 GHz 57

4.1 Geodetic coordinate $R(\phi, \lambda, h)$ vs ECEF coordinate. ϕ and λ are the latitude and longitude angles respectively. The a and b are the semi-major and semi-minor axis of the Earth. 61
4.2 The ECEF vs ENU coordinate configuration and translating steps (b)-(d) between the two systems 64
4.3 ENU vs AER coordinates. 66
4.4 Projection of the Earth onto the three major surfaces. 69
4.5 Example of Two Line Elements (TLE) for METOP-A satellite 71
4.6 Features characterizing the dynamics of fade events 75
4.7 Fade duration description by two method (a) the probability of occurrence of fades duration $P(d > D \mid a > A)$, and (b)the cumulative exceedance probability $F(d > D \mid a > A)$ 77

5.1 Typical rain cell 87
5.2 WRF and synthetic cell combination 88
5.3 (a) and (b) show the original rain rate with the central location at Louvain-la-Neuve. The R_{rms} in (a) is 2.6 and in (b) is 77.9 . 91
5.4 (a) Original and (b-d) synthetic rain cells showing the effects of restriction parameters R_{th} and ρ_{th} on the final synthetic rain cells. The central location is at Louvain-la-Neuve and the time is 2019-06-05 03:25:00 92
5.5 original rain rate : before and after discarding low rain rates. The central location is at Louvain-la-Neuve and the time is 2019-06-05 08:40:00 93
5.6 Search and track rain cells by finding the maximum(s) and adapting the rain rate pixels close to the nearest maximum rain rate. 94
5.7 Rain cell characteristics versus R_M [mm/hr] with fixed value of $\rho_0 = 1.5$ km. (a) shows the solid values of each descriptors and (b) represents the gradient or changes of each descriptors over R_M parameter. 96
5.8 Rain cells' probability of occurrence relative to Spino d'Adda and to Miami- Luini et. al. 2011 97
5.9 Manually modify the $\rho_0 = 12\,km$ parameter for 9^{th} rain event to $\rho_0 = 10/2 = 5\,km$. The Figures (b-d) do not contains all the rain cells and the focus was on 9^{th} rain cell to clearly show the effect of ρ_0. The ground station is at Louvain-la-Neuve at time slot of 2019-06-05 05:05:00. 98
5.10 Rain cell center: 'x' marks the peak location of rain rates, and '•' are the rain mass's locations. The ground station is at Louvain-la-Neuve at the time slot of 2019-07-27 03:00:00. 99
5.11 Rain rate Termination effect on the final rain cell's execution. The ground station is at Louvain-la-Neuve at time slot of 2019-06-05 08:40:00. 101
5.12 Redistribution of the overlapping rain rates around the structure 102
5.13 The $R_{rms} > 5mm/hr$ in the original domain, then the minimum $(R_M) = 5$ mm/hr 102

6.1 Simulated precipitation intensity and wind vectors at the 700 hPa level using WRF output. Wind field includes horizontal (u, v). The ground station is at Louvain-la-Neuve 105
6.2 Image registration using Lucas-Kanade algorithm 110
6.3 Propose of three types of transformation for performance investigation of optical flow algorithms. (a) shows the initial image frame, (b) depicts a simple horizontal movement of the cup, (c) contains the movement of the cup and elimination of the spoon, and (d) includes complex movements of the cup and spoon. . . 115

6.4 Performance investigation of the two optical flow algorithms, Lucas-Kanade and TV-L1 for the transformation case from I_0 to I_1 at Figure 6.3. (a,c) the transformation result and optical flow magnitude and vector field by Lucas-Kanade, and (b,d) the transformation result and Optical flow magnitude and vector field by TV-L1. (e-f) shows the error function L_1 norm $= \sum_{\mathbf{k}\in S(\mathbf{k})} \left| I_1(\mathbf{k}) - \tilde{I}_0(\mathbf{k}+\mathbf{u}(\mathbf{k})) \right|$. The window size in LK is about 20 pixels, and the regularization term in TV-L1 is $\lambda = 20$. . . . 117

6.5 Performance investigation of the two optical flow algorithms, Lucas-Kanade and TV-L1 for the transformation case from I_0 to I_2 at Figure 6.3. (a,c) the transformation result and optical flow magnitude and vector field by Lucas-Kanade, and (b,d) the transformation result and Optical flow magnitude and vector field by TV-L1. (e-f) shows the error function L_1 norm $= \sum_{\mathbf{k}\in S(\mathbf{k})} \left| I_2(\mathbf{k}) - \tilde{I}_0(\mathbf{k}+\mathbf{u}(\mathbf{k})) \right|$. The window size in LK is about 20 pixels, and the regularization term in TV-L1 is $\lambda = 20$. . . . 118

6.6 Performance investigation of the two optical flow algorithms, Lucas-Kanade and TV-L1 for the transformation case from I_0 to I_3 at Figure 6.3. (a,c) the transformation result and optical flow magnitude and vector field by Lucas-Kanade, and (b,d) the transformation result and Optical flow magnitude and vector field by TV-L1. (e-f) shows the error function L_1 norm $= \sum_{\mathbf{k}\in S(\mathbf{k})} \left| I_3(\mathbf{k}) - \tilde{I}_0(\mathbf{k}+\mathbf{u}(\mathbf{k})) \right|$. The window size in LK is about 20 pixels, and the regularization term in TV-L1 is $\lambda = 20$. . . . 119

6.7 Comparison of the normalized rain rate versus normalized reflectivity. (a) Normalized rain rate in two time sample which is moved horizontally, and the intensity is increased over time, (b) Normalized reflectivity, which highly cover the change of intensity over time. The blue curve is a cross-section of rain rate distribution at time t and the orange curve is the cross-section of the same rain event after a period of dt time which is displaced horizontally and the intensity of rain rate is increased too. . . . 122

6.8 Transformation of rain rate to normalized reflectivity to be fed in optical flow models. The ground station is at Louvain-la-Neuve on 2019-06-05. 123

6.9 Normalized reflectivity registration and warping using optical flow algorithms (TV-L1). (a) shows the flow field vector, (b) the registration of $\tilde{I}_0(\mathbf{k}+\mathbf{u}(\mathbf{k}))$ using the flow fields vectors $\mathbf{u}(\mathbf{k})$, (c) representing the registered image $\tilde{I}_0(\mathbf{k}+\mathbf{u}(\mathbf{k}))$ as the red channel and target image $I_1(\mathbf{k})$ as the green and blue channel of an RGB image, (d) the error values L_1 norm between the registered image and target image. The rain event's happened at 2019-06-05 03:30:00 at Louvain-la-Neuve. 125

6.10 Rain motion using optical flow method in 5-min at the dates 2019-06-05 03:30:00 and 2019-06-05 03:35:00 with temporal resolution of 1-min. The figures are normalized reflectivity which the equivalence rain rate will be known using the inverse procedure at eq. 6.22-6.23 127
6.11 Rain motion using optical flow method in 5-min at the dates 2019-06-05 06:00:00 and 2019-06-05 06:05:00 with temporal resolution of 1-min. The ground station is at Louvain-la-Neuve. . 128
6.12 Rain rate intensity correction after registration in optical flow. The event is on the date 2019-06-05 at Louvain-la-Neuve ground station. 129
6.13 (a) The time series attenuation of cloud and rain for two models of MultiEXCELL and original WRF rain rates which, the rain rates have been processed through optical flow algorithm. (b) Contribution of rain and cloud which the temporal resolution of cloud attenuation has been increased by interpolation. The ground station is at Louvain-la-Neuve and the frequency is 39.402 GHz. 130
6.14 (a) shows the CCDF (2018-09-01 to 2019-08-30 at Louvain-la-Neuve) of the total attenuation time series with 5-min resolution and (b) displays the CCDF of the total attenuation with increased time resolution to 1-min by optical flow model 131
6.15 The effect of rain intensity correction in registering images at the resulting time series of attenuation. The ground station is at Louvain-la-Neuve and the frequency is 39.402 GHz. 131

7.1 WPS domain configuration with three subdomains d01, d02, and d03 centered at Louvain-la-Neuve, Belgium 134
7.2 Lead and Run time configuration in NWP 136
7.3 Received signal and noise level of Alphasat station at Louvain-la-Neuve at frequency 39.402 GHz. 136
7.4 Studying the effect of lead time and run time in rain rate simulation of NWP. Lead time for the left and right columns are 06 and 12 hours. The fix time of the event is 2019-10-01 10:40:00 centered at Louvain-la-Neuve. 137
7.5 Studying the effect of **lead time 6 hours** and different run time of NWP in rain attenuation time series. The experiment data is of Alphasat station at 2019-10-01, centered in Louvain-la-Neuve. 138
7.6 Studying the effect of **lead time 12 hours** and different run time of NWP in rain attenuation time series. The experiment data is of Alphasat station at 2019-10-01, centered in Louvain-la-Neuve. 139
7.7 Raw received signal power at 39.402 GHz from the Alphasat ground station. Rain and cloud events are manually flagged based on visible drops in signal level. 141

7.8 Low-pass filtered reference signal (blue) overlaid on the raw signal (gray). Clear-sky intervals were used to estimate the stable baseline level. 141
7.9 Computed rain and cloud attenuation as the difference between the raw signal and reference level. This attenuation time series represents the atmospheric impact on the downlink. 142
7.10 Processing chains for rain rate, rainwater content, and cloud/gas. 144
7.11 Resolution cascade from ERA5 forcing and static geog data to nested WRF domains and post-processing (Optical Flow for temporal refinement; MultiEXCELL for spatial downscaling) yielding *1-min* / *100-m* products. 146
7.12 Example of WRF-derived attenuation maps at 39.402 GHz for Louvain-la-Neuve on the 2018-09-23 at 10:55:00 UTC 150
7.13 Difference of the (a)gaseous and (b)cloud attenuation vs their cosecant law at 39.402 GHz for Louvain-la-Neuve on the 2018-09-23 at 10:55:00 UTC 151
7.14 Example of WRF-derived attenuation time series at 39.402 GHz for Louvain-la-Neuve, at 30° in elevation and 154.6° in azimuth, on the 2018-09-23 153
7.15 Example of WRF-derived attenuation time series at 39.402 GHz for Louvain-la-Neuve, for a couple of Starlink satellites on the 2018-09-23 154
7.16 Oxygen attenuation CCDFs with WRF and ITU-R P.676-11, at 19.701 and 39.402 GHz and 30° in elevation, for Louvain-la-Neuve in 2018-2019 155
7.17 Water vapour attenuation CCDFs with WRF and ITU-R P.676-11, at 19.701 and 39.402 GHz and 30° in elevation, for Louvain-la-Neuve in 2018-2019 156
7.18 Gaseous (Oxygen+Water Vapour) attenuation CCDFs with WRF and ITU-R P.676-11 , at 19.701 and 39.402 GHz and 30° in elevation, for Louvain-la-Neuve in 2018-2019 157
7.19 Cloud attenuation CCDFs with WRF and ITU-R P.840, at 19.701 and 39.402 GHz and 30° in elevation, for Louvain-la-Neuve in 2018-2019 160
7.20 Rain attenuation CCDFs with WRF and ITU-R P.618, at 19.701 and 39.402 GHz and 30° in elevation, for Louvain-la-Neuve in 2018-2019 163
7.21 Rain and cloud attenuation time series at 39.402 GHz and 30° in elevation, for Louvain-la-Neuve ground station. 166
7.22 Rain and cloud attenuation time series at 39.402 GHz and 30° in elevation, for Louvain-la-Neuve ground station. 167
7.23 Excess attenuation (rain + cloud) CCDFs with WRF, MultiEXCELL rain rate, Mie and ITU-R P.618 and Experimental, at 19.701 GHz and 30° in elevation, for Louvain-la-Neuve in 2018, 2019 170

7.24 Excess attenuation (rain + cloud) CCDFs with WRF, MultiEXCELL rain rate, Mie, ITU-R P.618 and Experimental, at 39.402 GHz and 30° in elevation, for Louvain-la-Neuve in 2018, 2019 . 171
7.25 Statistics of Elevation and Azimuth for Starlink satellites at Louvain-la-Neuve in 2018-2019 173
7.26 Total attenuation (rain+cloud+gaseous) CCDFs with WRF, MultiEXCELL, Mie rain attenuation style and the ITU-R conditional probability attenuation ITU-R P.618, at 19.701 GHz for Starlink Satellites, for Louvain-la-Neuve in 2018, and 2019 separately 174
7.27 Total attenuation (rain+cloud+gaseous) CCDFs with WRF, MultiEXCELL, Mie rain attenuation style and the ITU-R conditional probability attenuation ITU-R P.618, at 19.701 GHz for Starlink Satellites, for Louvain-la-Neuve in 2018-2019 combination. 175
7.28 Total attenuation (rain+cloud+gaseous) CCDFs with WRF, MultiEXCELL, Mie rain attenuation style and the ITU-R conditional probability attenuation ITU-R P.618, at 39.402 GHz for Starlink Satellites, for Louvain-la-Neuve in 2018, and 2019 separately 176
7.29 Total attenuation (rain+cloud+gaseous) CCDFs with WRF, MultiEXCELL, Mie rain attenuation style and the ITU-R conditional probability attenuation ITU-R P.618, at 39.402 GHz for Starlink Satellites, for Louvain-la-Neuve in 2018-2019 combination. 177

List of Tables

2.1 WRF output variables useful to model propagation impairments 28
2.2 Basic constant parameters in thermodynamics 29

3.1 Spectroscopic data for oxygen attenuation 44
3.2 Spectroscopic data for water-vapour attenuation. The colored rows which are marked with asterisk too, are used in approximation solution at section 3.5.2 45
3.3 Rain classification based on characteristic parameters 47
3.4 Coefficients to compute the power law term κ^H 55
3.5 Coefficients to compute the power law term κ^V 55
3.6 Coefficients to compute the power law term α^H 55
3.7 Coefficients to compute the power law term α^V 56

4.1 Earth's ellipsoid dimensions as WGS-84 63

5.1 Details of first rain cell in Figure 5.6a 95

6.1 The dense Lucas-Kanade update 112

7.1 Ground station parameters at Louvain-la-Neuve 140
7.2 Cloud attenuation vs it's cosecant law for three elevation angles. The data is for Louvain-la-Neuve on the 2018-09-23 at 10:55:00 UTC at 39.402 GHz. 149
7.3 Gaseous attenuation vs it's cosecant law for three elevation angles. The data is for Louvain-la-Neuve on the 2018-09-23 at 10:55:00 UTC at 39.402 GHz. 151
7.4 Error analysis of Figure 7.16 for oxygen attenuation. μ, σ, and ρ are mean, standard deviation and r.m.s of relative error. ITU-R P. 676 is considered as the reference value in error analysis. Data for comparison of prediction methods are tabulated at fixed probability levels, 0.1%, 1%, 10%, and 100% of the year. . . . 158
7.5 Error analysis of Figure 7.17 for water vapour attenuation. μ, σ, and ρ are mean, standard deviation and r.m.s of relative error. ITU-R P. 676 is considered as the reference value in error analysis. Data for comparison of prediction methods are tabulated at fixed probability levels, 0.1%, 1%, 10%, and 100% of the year. 158

7.6 Error analysis of Figure 7.18 for gaseous attenuation. μ, σ, and ρ are mean, standard deviation and r.m.s of relative error. ITU-R P. 676 is considered as the reference value in error analysis. Data for comparison of prediction methods are tabulated at fixed probability levels, 0.1%, 1%, 10%, and 100% of the year. . . . 158
7.7 Error analysis of Figure 7.19 for cloud attenuation. μ, σ, and ρ are mean, standard deviation and r.m.s of relative error. ITU-R P. 840 is considered as the reference value in error analysis. Data for comparison of prediction methods are tabulated at fixed probability levels, 0.1%, 1% and 10% of the year. 161
7.8 Error analysis of Figure 7.20 for rain attenuation. μ, σ, and ρ are mean, standard deviation and r.m.s of relative error. ITU-R P. 618 is considered as the reference value in error analysis. Data for comparison of prediction methods are tabulated at fixed probability levels : Part 1 =[0.1, 0.2, 0.3, 0.5, 1]% and Part 2=[0.01, 0.02, 0.03, 0.05, 0.1]% 164
7.9 Error analysis of Figure 7.23 and 7.24 for total attenuation. μ, σ, and ρ are mean, standard deviation and r.m.s of relative error. EXP curve (Experimental curve) is considered as the reference value in error analysis. Data for comparison of prediction methods are tabulated at fixed probability levels : Part 1 =[0.1, 0.2, 0.3, 0.5, 1]% and Part 2=[0.01, 0.02, 0.03, 0.05, 0.1]% 172

List of publications

Articles in scientific journals

- Razavian, M., Oestges, C., & Vanhoenacker-Janvier, D. (2023). "Synthetic rain models and optical flow algorithms for improving the resolution of rain attenuation time series simulated from Numerical Weather Prediction", Radio Science, 58, e2022RS007553. https://doi.org/10.1029/2022RS007553

Articles in conferences' proceedings

- M. Razavian, C. Oestges, D. Vanhoenacker-Janvier,"Combined use of MultiEXCELL and Numerical Weather Prediction to improve the prediction of rain attenuation at Q band", EuCAP 2021.
- M. Razavian, L. Quibus, D. Vanhoenacker-Janvier,"Using Numerical Weather Predictions to Compare the LEO Attenuation Statistics Computed from Fixed-Elevation Statistics and from LEO Time Series", 25th Ka and Broadband Communications Conference, 2019, Sorrento, Italy.

Abstract in workshop's proceedings

- M. Razavian, L. Quibus, Danielle Vanhoenacker-Janvier. "Roadmap to model LEO links attenuation by integrating Numerical Weather Pre- dictions, ST-MultiEXCELL, and traffic radar data," 28th URSI Benelux Forum, Brussels, BE, 3 Dec. 2019.

List of acronyms

ACM	Advanced Coding Modulation
ACTS	Advanced Communication Technology Satellite
AER	Azimuth-Elevation-Range
APSK	Amplitude and Phase-Shift Keying
ARW	Advanced Research WRF
ATS	Application Technology Satellite
CCDF	Complementary Cumulative Distribution Function
CFL	Courant–Friedrichs–Lewy condition
DVB	Digital Video Broadcasting
ECEF	Earth Centered Earth Fixed
ECMWF	European Centre for Medium Range Weather Forecasts
EGM	Earth Gravitational Model
ENU	East-North-Up
EODDL	Earth Orbit Data Download
ETS	Engineering Test Satellite
ERA5	ECMWF 5th re-analysis
ERA-15	ECMWF 15 years re-analysis
ERA-40	ECMWF 40 years re-analysis
ERA-Interim	ECMWF interim re-analysis
ESA	European Space Agency
FMT	Fade Mitigation Technique
GEO	Geosynchronous Equatorial Orbit or Geostationary Orbit
GFS	Global Forecast System
GLONASS	Russian Global Navigation Satellite System
GNSS	Global Navigation Satellite System
GPS	Global Positioning System
GSO	Geosynchronous Orbit
IFS	Integrated Forecast System
ITU	International Telecommunication Union
ITU-R	ITU Radiocommunication sector
IWV	Integrated Water Vapour
LCC	Lambert Conformal Conic
LEO	Low Earth Orbit
LLA	Latitude Longitude Altitude

MAE	Mean Absolute Error
ME	Mean Error
MEO	Medium Earth Orbit
METOP	Meteorological Operational Satellite
MM5	5th generation Mesoscale Model
MWR	Microwave Radiometer
NCAR	National Center for Atmospheric Research
NCC	Network Control Center
NCEP	National Centers for Environmental Prediction
NMM	Non-hydrostatic Mesoscale Model
NOAA	National Oceanic and Atmospheric Administration
NWP	Numerical Weather Prediction
ONERA	Office National d'Etudes et de Recherches Aérospatiales
OTS	Orbital Test Satellite
PBL	Planetary Boundary Layer
PDE	Partial Differential Equation
PEF	Pseudo Earth Fixed
PRM	Parametric Radiopropagation Model
PSK	Phase-Shift Keying
QoS	Quality of Service
RAOBS	Radio-soundings observations
RCST	Return Channel Satellite Terminals
RMIB	Royal Meteorological Institute of Belgium
RMSE	Root Mean Square Error
RRTM	Rapid Radiative Transfer Model
SG	Study Group
SGP4	Simplified General Perturbations 4
SNR	Signal-to-Noise Ratio
TDP	Technology Demonstration Payload
TEME	True Equator Mean Equinox
TLEs	Two Line Elements
WGS	World Geodetic System
WPS	WRF Pre-processing System
WRF	Weather Research and Forecasting

Chapter 1

Introduction

In today's world, technology is advancing faster than ever, especially in how we share and communicate information. The demand for faster and more efficient data transmission is constantly growing. Satellite communication plays a crucial role in connecting people and devices across the globe. Since the Earth's atmosphere is often the only available medium for transmitting signals, satellites help bridge the gap by enabling seamless communication between the ground and space.

The foundation of these Earth-space links rests upon the propagation of electromagnetic waves, following a near line-of-sight trajectory. This mode of communication is not without its challenges, as inherent power loss occurs when these waves traverse vast distances, and latency becomes a pertinent concern. However, the Earth-space configuration offers unique advantages, especially in terms of expansive coverage and as a complement to terrestrial networks, such as optical fibers.

Satellites play a vital role in monitoring the Earth and providing essential services. Equipped with advanced instruments, they collect valuable data that need to be sent to ground stations for processing. This process is at the heart of satellite communication, allowing us to gather, transfer, and use data for a wide range of important applications.

As the demand for satellite communications continues to grow, the radio frequencies traditionally used for these systems—such as the C band (4/6 GHz) and Ku band (12/14 GHz) [1]—are becoming increasingly crowded. To accommodate more applications and avoid interference, the industry is shifting towards higher frequencies, above 20 GHz. This move offers more bandwidth, higher antenna gain and directivity [2]. However, it also brings new technical challenges in designing communication systems that operate in these higher-frequency bands.

One major challenge is how radio waves travel through the atmosphere. At frequencies above 20 GHz, signals weaken significantly due to higher attenuation, meaning they lose power more quickly. Environmental factors, particularly rain, further intensify this issue, making it harder to maintain a strong Signal-to-Noise Ratio (SNR) needed for clear and accurate communication.

As satellite communication continues to evolve, ensuring both high data

speeds and reliable service quality (QoS) has become more important than ever. To achieve this, there is a growing focus on developing methods to predict and understand how signals behave when traveling between Earth and space. By modeling these challenges in advance, engineers can create proactive solutions to minimize signal disruptions and maintain strong, efficient communication systems.

Predictive modeling plays a key role in this process, helping researchers anticipate potential issues, analyze their effects, and develop strategies to reduce their impact. This forward-thinking approach ensures that modern telecommunication networks remain stable and efficient, even in the face of environmental challenges. Ultimately, investing in predictive modeling is essential for driving innovation and shaping the future of satellite communication.

This thesis explores the use of Numerical Weather Predictions (NWPs) to model signal propagation challenges in Earth-space radio links at frequencies of 20 GHz and above. To demonstrate the value of NWPs in this context, the rest of this introduction provides an overview of the main propagation impairments affecting Earth-space links (see Section 1.1) and discusses previous efforts to study them. The techniques to ensure link reliability under impairemets are summarized in Section 1.2. A brief introduction to the concept of NWPs follows (see Section 1.3). Then, a review of how NWPs have been used in propagation modeling helps position this research within the current state-of-the-art (see Section 1.4). Finally, the introduction concludes with an outline of the document (see Section 1.6).

1.1 Earth-space propagation impairments

The primary effect of the atmosphere on Earth-to-space communication links is the attenuation of the received power. Several factors contribute to this phenomenon [3, 4]:

- Attenuation due to gases, primarily caused by oxygen and water vapor.
- Attenuation due to clouds, mainly from liquid water droplets.
- Attenuation due to hydrometeors, primarily from raindrops.
- Amplitude scintillation, which refers to rapid fluctuations in received power, either positive or negative, caused by the turbulent motion of the air along the signal path.

In addition to these, there are other impairments that affect different aspects of the signal. These include changes in the angle of arrival (due to refraction and multipath effects), phase variations (such as phase scintillation [5,6]), coherence issues (like dispersion and antenna gain degradation), and polarization shifts (caused by rain droplets or ice crystals [7]). Changes in the signal-to-noise ratio due to thermal noise also play a role. Additionally, weather conditions at ground antennas, such as the wet antenna effect [8] or vibrations caused by wind, can further impact performance.

While the origins of these impairments are generally well understood, having a more precise understanding of atmospheric conditions over time would be ideal for better modeling and predicting their effects.

As the demand for telecommunication systems grows across various sectors—including military, commercial, and emergency services—the focus is shifting toward higher frequency bands, particularly Ka and Q-bands. This move is driven by the need to support a growing number of communication systems while benefiting from wider bandwidths, higher data rates, and smaller components. These advancements are particularly important for secure communications, where there is a strong need for improved anti-jamming performance.

The focus of the telecommunication industry has increasingly shifted to low Earth orbit (LEO) satellite systems, which operate at altitudes between 500 and 1500 km [9]. LEO satellites are seen as game-changers, offering low propagation delay, which enables real-time communication. They also provide much higher throughput compared to traditional geostationary (GEO) satellite links. Because LEO satellites are closer to the Earth's surface, they not only ensure fast and efficient data transmission, but they also relax the strict power requirements seen in higher orbit satellites, making them more versatile and capable of supporting higher data rates and increased mobility.

The increasing need for faster and larger-scale data transmission, combined with the growing congestion of the available spectrum, has driven the development of smaller and more affordable microsatellites. These microsatellites are particularly useful for applications like remote sensing and Earth Observation (EO), and they play a key role in the rise of Ka and V bands (40-75 GHz) in Low Earth Orbit (LEO) satellites [10, 11]. This shift reflects the changing demands of modern telecommunications, highlighting how these frequency bands are becoming essential for overcoming today's challenges efficiently.

Looking ahead, the integration of satellite and terrestrial links at millimeter waves has gained significant attention, especially with the upcoming 5G-6G era. This intersection represents a more comprehensive approach to telecommunications, where the combined strengths of satellite and terrestrial technologies have the potential to reshape connectivity standards and create a seamlessly integrated, high-performance telecommunications ecosystem.

1.2 Fade Mitigation Techniques for Tropospheric Degradations in Satellite Communication

Tropospheric conditions, particularly rain, clouds, and water vapor, significantly impact the performance of satellite communication systems, especially in frequencies above 10 GHz (e.g., Ku, Ka, and Q/V bands). These impairments lead to signal attenuation, commonly referred to as "fade," which can severely degrade link quality, throughput, and system availability. The effect is especially critical for high-frequency and high-throughput satellite (HTS) systems.

To counteract these degradations, a variety of *Fade Mitigation Techniques*

(FMTs) have been developed and employed, depending on the satellite orbit (GEO or non-GEO), frequency band, and application requirements.

1.2.1 Fade Mitigation Techniques (FMTs)

The main categories of fade mitigation techniques include [12–16]:

- **Adaptive Modulation and Coding (AMC):** The system dynamically adjusts the modulation order and coding rate based on real-time channel conditions. During deep fades, lower-order modulations (e.g., QPSK) and stronger error correction codes are used to maintain link integrity. ACMs (AMCs)[1] are a key feature of *Digital Video Broadcasting (DVB)* standards [17–20].
- **Uplink Power Control (UPC):** The gateway increases the transmit power in response to attenuation caused by rain or clouds, compensating for signal loss on the uplink path [21–23].
- **Site Diversity:** Multiple ground stations are deployed geographically apart, so that when one site experiences severe fading (e.g., due to a localized rain cell), another site with better conditions can take over the link [24–28].
- **Time Diversity:** Data is transmitted multiple times across different time slots to exploit time-varying channel conditions. It is especially useful in bursty or delay-tolerant applications [26, 29].
- **Frequency Diversity:** Multiple carrier frequencies are used, with data switching to less affected frequencies during fade events. However, this technique requires spectrum availability and additional coordination [30–34].
- **Polarization Diversity:** By transmitting signals on orthogonal polarizations, the system can switch or combine them based on which polarization experiences less attenuation.
- **Link Layer Protocols and ARQ:** At higher layers, protocols like Automatic Repeat reQuest (ARQ) and Hybrid ARQ can detect and retransmit lost or corrupted packets to improve overall reliability [35].

1.2.2 FMTs for GEO Satellites

Geostationary Earth Orbit (GEO) satellites, due to their high altitude (approximately 35,786 km), experience long propagation delays and limited real-time feedback. Therefore, certain techniques are more suitable:

[1] There is a subtle but important difference between Advanced Coding and Modulation (ACMs) and Adaptive Modulation and Coding (AMC) — though in practice, the terms are often used interchangeably or confused, especially in satellite communication literature. See Appendix IV 8

- *Uplink power control* and *AMC* are typically performed at the gateway, with link adaptation based on predicted or slowly varying channel estimates.
- *Site diversity* is highly effective for GEO systems, especially when combined with centralized control at the gateway.
- Real-time techniques like fast feedback for AMC are less effective due to the long round-trip delay.

1.2.3 FMTs for Non-GEO Satellites (LEO/MEO)

Low Earth Orbit (LEO) and Medium Earth Orbit (MEO) systems benefit from shorter propagation delays and more dynamic link geometries. As a result, additional techniques become viable [36–39]:

- *Fast link adaptation (AMC)* is feasible due to shorter round-trip time, allowing real-time responsiveness to channel changes.
- *Beam hopping* and *adaptive footprint shaping* are employed to reallocate power and coverage based on user demand and fade conditions.
- *Routing diversity* and *inter-satellite links* allow rerouting data through less-attenuated paths (satellite diversity).

While GEO satellites rely more on predictive and centralized methods, non-GEO constellations can exploit their agility and low latency to implement more responsive adaptation strategies. An optimal combination of these techniques, tailored to the system architecture and application requirements, is essential for maintaining robust performance in the presence of tropospheric fading.

1.3 Numerical Weather Predictions (NWPs)

Numerical Weather Predictions (NWPs) stand as sophisticated simulations of the Earth's atmosphere, encompassing both global models that simulate the entire atmosphere and regional models that focus on specific geographic domains. The underpinning physics of NWPs revolves around a set of partial differential equations (PDEs) that meticulously capture the complex interplay of motion and thermodynamic state parameters—pressure, temperature, and humidity—within the humid air.

Horizontally, the resolution of these simulations spans a spectrum, ranging from tens of kilometers for extensive domains to occasionally dipping below one kilometer for more localized regions. Vertically, the atmospheric layers are delineated into pressure-based levels, typically numbering in the tens and, in some instances, exceeding a hundred. The spacing between these levels is finer near the Earth's surface, with intervals measured in tens of meters, gradually expanding to more than one kilometer at higher altitudes.

The numerical integration stability of the PDEs dictates a minimum time step size, denoted as `time_step` , which can range from a few minutes to seconds. The `history_interval` parameter in WRF controls the frequency of

output writing in minutes and does not influence the numerical stability of the model. Unlike the `time_step` parameter, which is constrained by the CFL[2] condition to ensure simulation stability, `history_interval` simply determines how often model state variables are written to disk. Therefore, reducing the `history_interval` (e.g., to 1–2 minutes) is safe and can be useful for high-resolution temporal analysis, such as convective systems or turbulence studies. However, frequent output writing increases I/O overhead and disk usage, which can significantly slow down the simulation and consume large amounts of storage. For most applications, a `history_interval` of 5–60 minutes is considered a practical balance between detail and performance.

Initiating the NWP process requires meticulous attention to initial boundary conditions for the PDEs. The atmospheric state, along with surface conditions, is reconstructed based on observations collected during the data acquisition phase. These initial conditions serve as the foundation for the NWP model, guiding its simulation and enabling the projection of atmospheric behavior over time.

Despite the impressive capabilities of NWPs, it is crucial to acknowledge the inherent challenges tied to their computational demands, temporal resolutions, and data storage limitations. Continuous advancements in technology and methodologies are pivotal in addressing these challenges, ensuring that NWPs remain reliable tools for predicting and understanding atmospheric phenomena across varying spatial and temporal scales.

The output of an NWP implementation typically includes the following (or equivalent):

- pressure p [Pa], temperature T [K], moisture mixture ratio q [kg / kg],
- Liquid water mixture ratio q [kg / kg],
- Mixture ratio of rain q [kg / kg] and / or the amount of ground rain R [mm per hour],
- Wind speed east, north and vertical (u, v and w) [m / s].

These values are easily entered into the models of some Earth-Space or terrestrial propagation impairments.

1.4 State of the Art: NWP in Radio Wave Propagation Impairments

The use of Numerical Weather Prediction (NWP) for modeling Earth–space propagation impairments has evolved significantly in the last two decades. We will group the literature by application domains, highlighting their objectives, limitations, and relevance to this thesis.

[2]The CFL (Courant–Friedrichs–Lewy) condition is a numerical stability constraint that limits the maximum allowable time step based on the model's grid resolution and the speed of wave propagation. $time_step \leq dx/max_velocity$ or $time_step \approx 6 \times dx(in\,km)$

1.4.1 NWP for Time Series Generation

Several works have used NWP to produce attenuation time series suitable for satellite communication studies. Watson and Hodges (2005) [40] proposed a real-time forecasting system combining NWP and radar data to generate high-resolution rain/cloud attenuation predictions above 20 GHz. Jeannin et al. (2014) [41] extended this idea to LEO satellites by coupling WRF outputs with a channel simulator to produce time-series of rain attenuation and scintillation, validated against ITALSAT campaign data. More recently, Biscarini et al. (2024) [42] introduced the Multisite Time-Series Synthesizer (MTS), producing high-resolution (1 s) synthetic time series for Q/V-band links, validated with Alphasat beacon data. These studies confirm the feasibility of generating propagation time series directly from NWP, but their accuracy strongly depends on microphysics parameterizations and rain-rate representation.

1.4.2 NWP for Cumulative Statistics

Other efforts target cumulative distribution functions (CCDFs) rather than instantaneous series. Quibus et al. (2023) [43] and Quibus et al. (2021) [44] showed that microphysics schemes in WRF (e.g., Lin, WSM6, NSSL) strongly affect long-term attenuation statistics at 20–40 GHz. These statistical approaches are well suited for link budgeting but do not capture the fast variability needed for fade mitigation techniques.

1.4.3 Applications for GEO Links

Many studies validate NWP-based models against geostationary (GEO) beacon data. Marziani et al. (2019) [45] used GFS and IFS outputs to predict excess attenuation and scintillation in Rome, showing good agreement with Alphasat beacon data. Nebuloni et al. (2024) [46] developed a propagation model chain (PRM[3]) using NWP inputs to compute path attenuation across multiple frequencies (19.7–50.9 GHz), again validated against Alphasat. These works demonstrate the robustness of NWP-based methods for GEO, but rain attenuation tends to be overestimated during intense events, and cloud attenuation is often simplified.

1.4.4 Applications for LEO Links

The use of NWP for LEO links remains less mature. Outeiral et al. (2013) [47] simulated a 30 GHz LEO pass using WRF at 2 km resolution, producing attenuation maps during the satellite overpass. Such studies highlight the potential for dynamic attenuation prediction but remain limited by spatial/temporal resolution and lack of validation data.

[3]Parametric Radiopropagation Model

1.4.5 Short-Term Forecasting and Real-Time Applications

Grythe et al. (2018) [48] used AROME-MetCoOp for near-real-time Ka-band rain attenuation forecasts in Scandinavia, achieving 65–77% hit rates. Kourogiorgas et al. (2018) [49] combined ECMWF ensemble forecasts with machine learning for multi-hour predictions. Tjelta et al. (2023) [50] proposed an operational system integrating NWP, radar, and ground station data for smart gateway management. These works show that NWP forecasts can improve short-term system operation but still suffer from uncertainties in rainfall timing and intensity, especially beyond 6-hour lead times.

1.4.6 Regional and Climate-Specific Studies

NWP has also been tailored for specific climatic regimes. Mire et al. (2020) [51] applied WRF-EMM in French Guiana (tropical climate), highlighting sensitivity to drop size distribution (DSD) assumptions. Wardah et al. (2014) [52] combined WRF with radar and Kalman filtering to improve rainfall input in Malaysia (flood-prone region). Alsaker and Rytir (2020) [53] studied gaseous attenuation at very low elevation angles in the Arctic using AROME-Arctic. These applications confirm the adaptability of NWP but also emphasize regional challenges (e.g., convective rain in tropics, ice/snow at high latitudes).

1.5 Problem Statement

Low Earth Orbit (LEO) satellite communication systems are increasingly expected to support real-time, high-throughput multimedia services under all weather conditions. Meeting these demands requires a detailed understanding of the radio propagation challenges in LEO frequency bands, particularly the severe signal attenuation caused by atmospheric phenomena such as rain, clouds, and water vapor.

Unlike GEO systems, LEO satellites operate in a fast-moving and dynamically changing environment, where the Earth-space link is highly sensitive to short-term atmospheric variations. These variations introduce rapid fluctuations in received signal power, making the mitigation of tropospheric fading a crucial factor in ensuring service continuity and link reliability.

To address these challenges, a range of advanced techniques have been developed, including adaptive modulation and coding (AMC), uplink power control, robust error correction, and smart antennas with dynamic beam shaping. These mechanisms collectively improve the resilience of satellite communication links to atmospheric interference. Nevertheless, their effectiveness is inherently dependent on the accuracy and resolution of the atmospheric data used to support them.

Numerical Weather Prediction (NWP) models, such as those provided by the Weather Research and Forecasting (WRF) model and the European Centre for Medium-Range Weather Forecasts (ECMWF), offer valuable insights into atmospheric processes. However, their utility for propagation modeling in LEO contexts is constrained by resolution and latency limitations. For in-

stance, ERA5 data typically has a temporal resolution of one hour and a spatial resolution of about 0.25 degrees (roughly 30 km), which may not be sufficient to resolve the rapid atmospheric changes that affect LEO links. While finer resolutions are possible, they come at the cost of significant computational demands and increased data volume.

This trade-off between resolution and practicality presents a major bottleneck for LEO system designers. Because LEO satellites experience very short visibility periods—often less than 10% of a full orbital pass—the need for high temporal and spatial accuracy in atmospheric modeling becomes even more critical. Models designed for GEO systems, which rely on long-term averaged statistics, fall short when applied to the more dynamic and transient environment of LEO systems.

1.5.1 Limitations of ITU-R Models for LEO Links

The ITU-R recommendations (e.g., P.618 [3] for rain and total attenuation, P.676 [54] for gaseous absorption, P.840 [55] for cloud attenuation, P.838 [56] for rain attenuation) provide the reference framework for Earth–space propagation modeling. These models have been widely adopted and are well suited for geostationary (GEO) systems, but their direct application to low Earth orbit (LEO) links involves several important limitations:

- **Stationarity assumption:** ITU-R models are designed for quasi-stationary propagation paths. In contrast, LEO satellites traverse the sky quickly, with continuously changing elevation and azimuth angles, producing fast-varying attenuation that cannot be fully captured by static ITU-R formulations.

- **Time-series generation:** ITU-R recommendations primarily provide long-term statistics (e.g., annual or monthly exceedance probabilities). A dedicated method for generating attenuation time series does exist in Recommendation ITU-R P.1853 [57], but it is limited to GEO satellites and does not cover the fast dynamics of LEO links.

- **LEO CCDF estimation:** For LEO systems, ITU-R proposes method to estimate the cumulative distribution of attenuation by combining statistics at fixed elevation angles with the probability density function of satellite elevation during passes [3]. While this is useful for availability studies, it does not reproduce the temporal evolution of fades within a single pass.

- **Spatial homogeneity:** Rain and cloud attenuation in ITU-R are treated statistically and horizontally homogeneous, which neglects the localized variability of convective cells or frontal systems. For LEO satellites, this simplification can underestimate fade dynamics during a pass.

- **Event-to-event variability:** ITU-R methods do not allow direct simulation of individual weather events (e.g., convective storms, frontal passages). This is a limitation for LEO, where intermittent fades during one pass can be critical.

In summary, ITU-R models remain the reference for link design and availability assessment, but they are not sufficient to capture the **short-term dynamics and event-based variability** required for LEO systems.

The approach proposed in this thesis, based on Numerical Weather Prediction (NWP) and downscaling methods (MultiEXCELL [58], optical flow [59, 60]), addresses these gaps by generating time series with enhanced spatial and temporal resolution. This enables more realistic evaluation of fade dynamics, outage clustering, and mitigation strategies in next-generation LEO communication systems.

1.6 Thesis Outline

This thesis is divided into two main parts. Part One (Chapters 2-6) focuses on classical models for calculating earth-space attenuation, providing an in-depth discussion of numerical weather prediction (NWP) data and electromagnetic wave propagation through the atmosphere. Part Two (Chapter 7) presents the evaluation of the proposed models using experimental data.

Part One: Classical Attenuation Models

1. **Chapter 2 - Numerical Weather Prediction Models:** This chapter introduces NWP models, their output data, and the thermodynamic relationships governing rain events. The role of NWP data in modeling precipitation-related attenuation is also discussed.

2. **Chapter 3 - Electromagnetic Wave Attenuation:** Covers the fundamental principles of electromagnetic wave propagation through the atmosphere, with a specific focus on the electromagnetic properties of water particles and how they contribute to signal attenuation. This discussion is limited to models and algorithms that utilize NWP data.

3. **Chapter 4 - Post Processing NWP's Data** This chapter presents the methodologies used to transform 4D meteorological data from Numerical Weather Prediction (NWP) models into the initial input required for propagation impairment analysis.

4. **Chapter 5 - Synthetic Rainfall Modeling for Attenuation Estimation:** This chapter presents the core methodology of the thesis, describing the generation of artificial rainfall models and their integration with numerical weather prediction techniques for improved attenuation estimation.

5. **Chapter 6 - Synthetic Rainfall Temporal Resulotion Imporovement :** This chapter focuses on using the optical flow algorithm to detect the movement direction of rain cells between two consecutive time steps. This information is then used to shift the rain cells accordingly, enhancing the dynamic modeling of rain attenuation and enabling a temporal resolution of less than 5 minutes.

Part Two: Model Evaluation and Future Work

6. **Chapter 7 - Experimental Validation of the Proposed Model:** The proposed attenuation models, combining synthetic rainfall (from Chapter 5) with NWP data (from Chapter 2), are evaluated using experimental measurements from two ground stations: Spino d'Adda, Italy, and Louvain-la-Neuve, Belgium.

7. **Chapter 8 - Conclusion and Future Work:** Summarizes key findings of the thesis and outlines directions for future research, including potential refinements to the attenuation models and additional validation using larger datasets.

Chapter 2

Numerical Weather Prediction

This chapter introduces the use of Numerical Weather Prediction (NWP) models in the context of satellite communication link modeling. It begins by establishing a foundational understanding of key concepts, including the fundamental parameters and boundary conditions required to configure the Weather Research and Forecasting (WRF) model.

WRF was selected for this work due to its open-source nature, wide adoption in both research and operational forecasting, and proven reliability in atmospheric modeling. Its extensive validation by the scientific community and support for high-resolution simulations make it an ideal choice for studies that require detailed meteorological inputs. Furthermore, WRF has been used in previous research involving radio wave propagation and attenuation modeling, which strengthens its suitability for this study.

The discussion then focuses on how meteorological parameters are extracted from WRF outputs and how these values are used to characterize atmospheric conditions. Particular attention is given to the derivation of secondary parameters, especially those involving thermodynamic conversions. These conversions are essential for accurately representing the physical processes that govern atmospheric behavior.

As the chapter progresses, these parameters—both primary and derived—form the basis for modeling the impact of atmospheric phenomena on earth-space wave propagation. By incorporating NWP-derived data into the modeling framework, we improve the reliability of simulation results and gain deeper insights into the interaction between weather conditions and satellite communication performance.

Ultimately, this chapter provides a practical and conceptual framework for integrating NWP data into satellite link modeling. It sets the stage for the more advanced analyses in subsequent chapters by clarifying how meteorological inputs influence signal propagation through the atmosphere.

2.1 Overview of Numerical Weather Predictions

Numerical Weather Prediction (NWP) data forms the foundation of modern weather modeling. By using advanced computer algorithms, these models process past and real-time atmospheric observations to generate forecasts for a wide range of meteorological variables—including precipitation, temperature, and atmospheric dynamics spanning from the surface to the upper atmosphere. These simulations are typically run on high-performance computing systems due to their complexity and computational demands.

Among the most widely used and robust NWP tools is the Weather Research and Forecasting (WRF) system, a state-of-the-art mesoscale forecasting platform designed for both research and operational applications. WRF supports simulations at various spatial and temporal scales, from a few meters to thousands of kilometers, making it suitable for a wide array of atmospheric studies.

One of WRF's strengths lies in its flexible and modular architecture. As shown in Figure 2.1, the WRF Software Framework (WSF) serves as the core infrastructure, enabling the integration of multiple physics packages and dynamic solvers through a standardized interface. This framework includes powerful tools for initialization, such as WRF-Var for data assimilation, and supports specialized extensions that significantly broaden the scope of WRF's applications:

- **WRF-Chem**: Integrates atmospheric chemistry processes with meteorology, enabling the simulation of air quality, aerosol transport, chemical dispersion, and interactions between pollutants and weather systems.

- **WRF-Hydro**: Extends WRF for hydrological modeling, allowing detailed simulations of surface and subsurface water flow, including river routing, runoff generation, and flood forecasting.

- **WRF-Fire**: Designed for wildfire modeling and prediction, this module couples atmospheric dynamics with fire spread models to simulate the behavior of wildland fires and their interactions with the atmosphere.

At the heart of WRF are two dynamic solvers: the Advanced Research WRF (ARW) solver—also known as the Eulerian mass or "em" solver—developed primarily by the National Center for Atmospheric Research (NCAR) [61], and the Non-hydrostatic Mesoscale Model (NMM) solver, developed at the National Centers for Environmental Prediction (NCEP) [62]. Although the WRF system supports a dual-solver architecture—including the Advanced Research WRF (ARW) and the Non-hydrostatic Mesoscale Model (NMM) solvers—this work specifically utilizes the ARW core. ARW was selected due to its extensive documentation, strong community support, and widespread use in atmospheric research, particularly in high-resolution applications. While the NMM solver provides additional modeling options, the ARW core was deemed more suitable for the objectives of this thesis.

In summary, the WRF system represents a powerful and versatile tool in the field of numerical weather prediction. Its adaptability, wide range of applications, and strong community support make it an ideal choice for atmospheric research and forecasting. In this thesis, WRF serves as a key component in generating the meteorological inputs required for accurate modeling of atmospheric effects on satellite communication links.

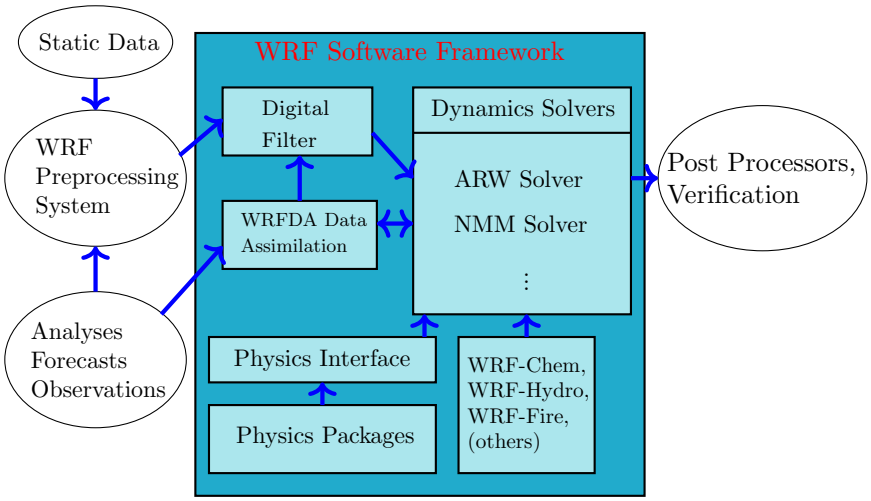


Figure 2.1: WRF system components

2.1.1 Advanced Research WRF (ARW)

The Advanced Research WRF (ARW) configuration within the Weather Research and Forecasting (WRF) system is a highly flexible and widely adopted framework for atmospheric modeling [63]. As one of the primary cores of the WRF system, ARW includes a powerful dynamic solver, a broad selection of physics parameterizations, customizable numerical options, initialization procedures, and an integrated data assimilation package known as WRFDA.

At the heart of ARW is an efficient and scalable dynamic solver that drives the simulation process. Designed for portability and modularity, ARW runs on a wide range of computing environments, from personal workstations to high-performance supercomputers. This flexibility makes it suitable for both research-focused studies and real-time operational forecasting.

A key strength of ARW lies in its extensive range of physics and numerical options. These include schemes for microphysics, planetary boundary layer processes, radiation, surface interactions, and more—many of which have been developed or refined through contributions from the global research community. This breadth allows users to tailor simulations for specific scientific goals, including real-time weather prediction, climate case studies, process-level investigations, and model development.

The inclusion of WRFDA in the ARW configuration further amplifies its capabilities. WRFDA, designed to accommodate various data assimilation ap-

proaches, proves instrumental in capturing a wide array of observation types. This versatility positions ARW as a tool capable of supporting atmospheric simulations across scales, ranging from Large-Eddy Simulations (LES) to global perspectives.

The versatility of ARW finds expression in its diverse applications, showcasing its adaptability to an array of atmospheric studies. These applications include real-time NWP, investigations into climate events, development of data assimilation methodologies, parametric physics refinement, regional climate simulations, air quality modeling, atmospheric-ocean coupling studies, and idealized atmosphere investigations.

In essence, ARW emerges not merely as a computational tool but as a comprehensive framework that empowers researchers and meteorologists to delve into the intricacies of atmospheric phenomena across scales. As we explore its multifaceted applications, ARW stands as a testament to the collaborative efforts of the scientific community, providing a versatile and powerful platform for advancing our understanding of the atmosphere and its dynamic processes.

2.2 Simulation grids, coordinates and nesting

Within the WRF system, the computational grids are structured as rectilinear, meaning they follow a regular, grid-like pattern. This configuration provides a systematic and organized framework for representing atmospheric variables in the model. Each variable associated with a WRF grid cell—identified by the indices (i, j, k)—can be located at one of several distinct positions within the cell, depending on its physical meaning and role in the simulation.

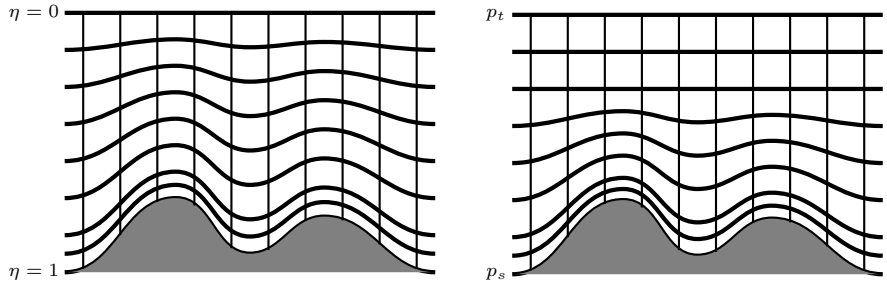
Understanding where each variable is positioned in the grid is essential for accurate data interpretation and analysis. This information can be obtained by consulting the WRF Registry or by examining the metadata of the NetCDF files used for input and output. These resources help determine the exact spatial placement of each variable within the model's grid structure.

2.2.1 Vertical grid

The ARW core of the WRF model uses a terrain-following hydrostatic-pressure vertical coordinate, denoted by η, also referred to as the vertical mass coordinate. This coordinate system is designed to follow the shape of the terrain while maintaining a smooth representation of the atmosphere in the vertical dimension. The η coordinate is defined as:

$$\eta = \frac{p_d - p_t}{p_s - p_t} \tag{2.1}$$

In this equation, p_d represents the hydrostatic pressure of dry air at a given model level, p_s is the hydrostatic pressure at the surface, and p_t is the pressure at the top of the model domain. This formulation is based on the traditional sigma coordinate system, which is widely used in many hydrostatic atmospheric models.



(a) Traditional sigma coordinate (b) Hybrid sigma coordinate

Figure 2.2: ARW η coordinate

The η coordinate varies smoothly from 1 at the surface to 0 at the top of the atmosphere, providing a normalized vertical reference that simplifies the representation of vertical profiles (see Figure 2.2a). This coordinate system is essential for accurately resolving the vertical distribution of atmospheric variables, allowing for a consistent and terrain-aware description of pressure and other meteorological fields throughout the model domain.

In the latest version of the ARW core, the treatment of vertical coordinates has been significantly improved to reduce the distortion caused by steep terrain. This enhancement is illustrated in Figure 2.2b, where the vertical levels rise more smoothly above the surface, especially in complex terrain. To achieve this, ARW now employs a hybrid sigma-pressure vertical coordinate, which provides a more accurate and flexible representation of the vertical structure of the atmosphere.

The hybrid coordinate is defined by the following expression:

$$p_d = B(\eta)(p_s - p_t) + [\eta - B(\eta)](p_0 - p_t) + p_t \tag{2.2}$$

In this equation:

- p_d is the dry hydrostatic pressure at a given model level,
- p_s is the surface pressure,
- p_t is the pressure at the top of the model domain, and
- p_0 is a reference sea-level pressure.

The function $B(\eta)$ governs the transition between a purely terrain-following sigma coordinate and a pure pressure coordinate. When $B(\eta) = \eta$, the formulation reduces to the traditional sigma coordinate described earlier in Equation 2.1. On the other hand, if $B(\eta) = 0$, the coordinate becomes a pure pressure level, independent of surface topography.

To ensure a smooth and gradual transition from sigma-like behavior near the surface to pressure-based coordinates at higher altitudes, $B(\eta)$ is defined using a third-order polynomial:

$$B(\eta) = c_0 + c_1\eta + c_2\eta^2 + c_3\eta^3 \tag{2.3}$$

This polynomial is subject to boundary conditions that enforce continuity and smoothness in the vertical coordinate system:

$$B(1) = 1, \qquad B_\eta(1) = 1, \qquad B(\eta_c) = 0, \qquad B_\eta(\eta_c) = 0 \tag{2.4}$$

Here, η_c is the critical level at which the coordinate fully transitions into a pure pressure coordinate. The polynomial coefficients c_0, c_1, c_2, and c_3 are computed based on this transition point:

$$\begin{aligned} c_0 &= \frac{2\eta_c^2}{(1-\eta_c)^3} & c_1 &= \frac{-\eta_c(4+\eta_c+\eta_c^2)}{(1-\eta_c)^3} \\ c_2 &= \frac{2(1+\eta_c+\eta_c^2)}{(1-\eta_c)^3} & c_3 &= \frac{-(1+\eta_c)}{(1-\eta_c)^3} \end{aligned} \tag{2.5}$$

This hybrid approach effectively balances the need for terrain-following near the surface with the advantages of pressure-based coordinates at higher altitudes. As a result, it reduces vertical grid distortion over complex topography and improves numerical stability and accuracy in atmospheric simulations.

Figure 2.3 displays the $B(\eta)$ profiles for the traditional sigma coordinate and for the hybrid coordinate for several values of the parameter η_c. These profiles, as a function of η (Figure 2.3a), represent the polynomial shape defined in eq. 2.3. However, drawing $B(\eta)$ as a function of height (Figure 2.3b) provides a better physical sense of the transition to the pressure coordinates with increasing altitude. For example, with a model domain having a depth of 30 km, for $\eta_c = 0.2$ the vertical coordinate becomes a pure pressure coordinate at an altitude of about 12 km.

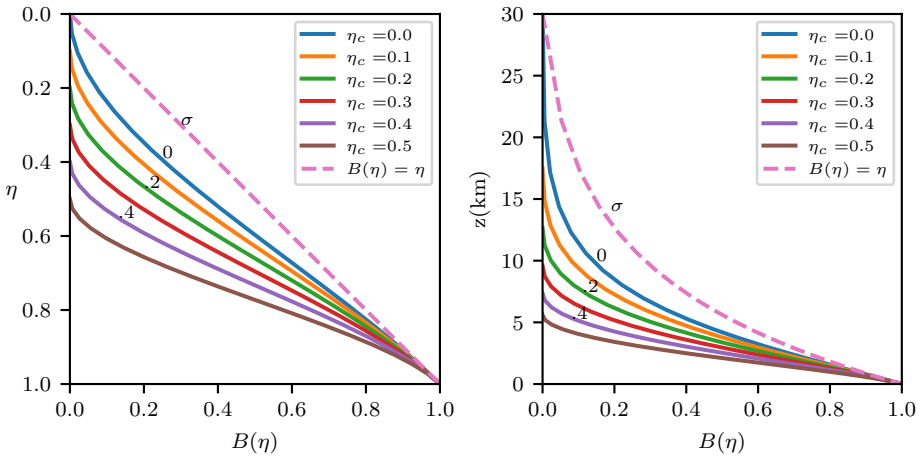
2.2.2 Horizontal grid

The spatial discretization in the ARW solver uses a C grid staggering for the variables as shown in Figure 2.4. Normal velocities (u, v, w) are staggered one-half grid length from the thermodynamic variables (θ) . The variable indices, (i, j, k) indicate variable locations with $(x, y, \eta) = (i\Delta x, j\Delta y, k\Delta\eta)$. We will denote the points where θ is located as being mass points, and like-wise we will denote locations where u, v, and w are defined as u points, v points, and w points, respectively.

Because of this staggering, the number of grid points for staggered variables is one greater along the staggered dimension compared to the mass grid. This ensures that variables are defined at both faces of the domain boundaries, which is necessary for accurate numerical calculations.

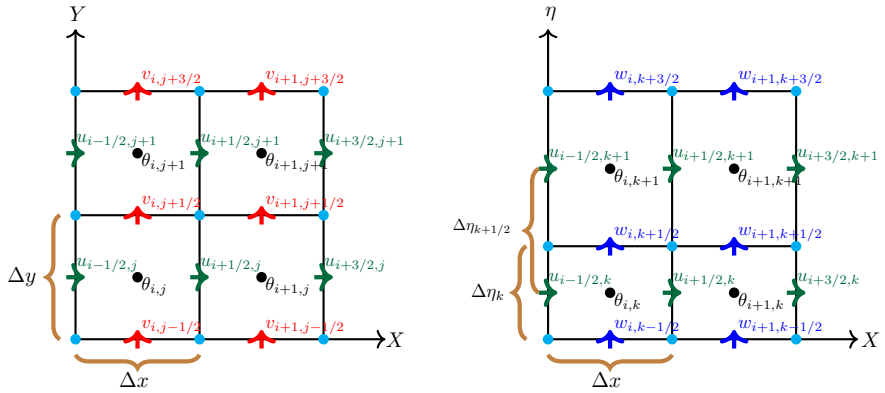
The different grids used in ARW are described as follows:

- The Mass Grid - non-staggered: Mass-related quantities such as pressure, temperature, humidity, etc. are computed at the center of a grid cell where θ is located as being mass points in Figure 2.4).



(a) (b)

Figure 2.3: $B(\eta)$ profiles for sigma (σ) coordinate and for hybrid coordinate for $\eta_c = 0., 0.1, 0.2, 0.3, 0.4,$ and 0.5 displayed (a) as a function of η, and (b) as a function of height for a standard atmosphere in a domain with a $30\,km$ upper boundary.



(a) Horizontal grid (b) Vertical grid

Figure 2.4: Horizontal and vertical grids of the ARW

- The U Grid - staggered in X: The u-component of the horizontal wind is computed at the center of the left and right sides of a grid cell, at points indicated by u in Figure 2.4

- The V Grid - staggered in Y: The v-component of the horizontal wind is computed at the center of the top and bottom sides of a grid cell, at points shown by the v in Figure 2.4.

- The W Grid - staggered in η: The vertical components of the variables defined at w points in Figure 2.4 like the geopotential height ϕ.

- The Staggered Grid: The points defining the corners of the mass grid cells are indicated by the cyan dots in the Fig. 2.4. Collectively, these points are referred to as the "staggered grid". The WRF staggered grid has one additional point than the dimensions of the mass grid in each direction.

The horizontal grid spacing Δx and Δy are typically constant throughout the domain in ARW, although the physical distance between grid points may vary slightly due to the map projection used. In contrast, the vertical grid spacing $\Delta\eta$ is not fixed. Instead, the user defines the η levels during model initialization, with the constraints that $\eta = 1$ at the surface, $\eta = 0$ at the top of the model domain, and η decreases monotonically from bottom to top. This flexible vertical layering allows for higher resolution near the surface where atmospheric gradients are strongest.

2.2.3 Nesting

ARW has a versatile feature that enables users to concentrate on specific simulation areas through nested options. This capability, known as horizontal nesting, proves invaluable in enhancing the resolution of a designated target area through the introduction of additional grids into the simulation. In this arrangement, the subdomain with increased horizontal resolution is entirely embedded within the parent domain, typically denoted as the coarse domain (CG). Conversely, the subdomain itself is commonly acknowledged as the child domain or fine domain (FG).

The implementation of horizontal nesting in ARW involves several strategies aimed at refining a coarse-grid simulation. This dynamic feature accommodates diverse user requirements and simulation scenarios. Users can strategically leverage nested grids to focus on specific regions of interest, providing a localized and detailed perspective within the broader atmospheric context. Various types of nesting are available:

- 1-way nesting with consecutive runs. The output of a run on a coarse grid domain can be post-processed to start a run on a nested fine grid domain.

- 1-way nesting with concurrent runs. In a single run the information from a coarse grid domain is fed to nested fine grid domains at each time step.

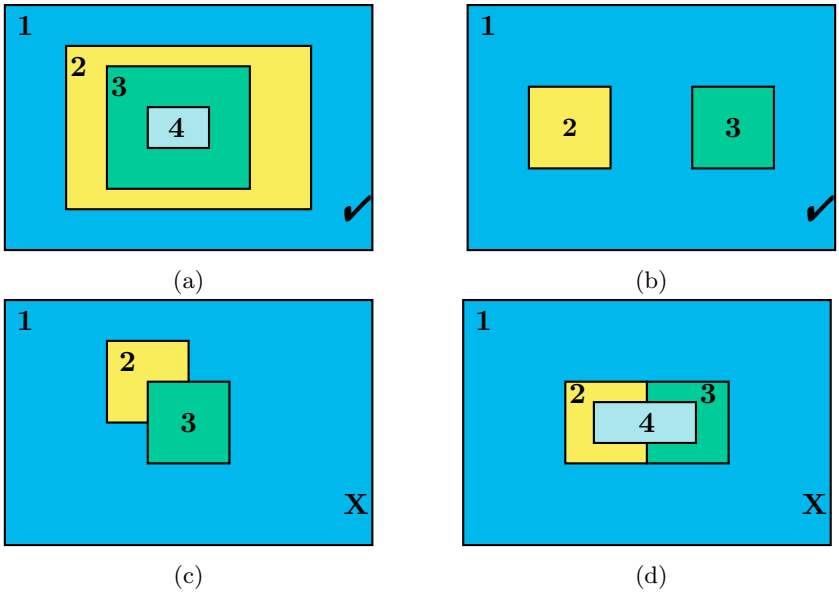


Figure 2.5: Various nest configurations for multi level grids. (a) Telescoping nests. (b) Nests at the same level with respect to a parent grid. (c) Overlapping grids: not allowed with feedback activated. (d) Inner-most grid has more than one parent grid: not allowed

- 2-way nesting with concurrent runs. In a single run the information from a coarse grid domain is fed to nested fine grid domains at each time step, and then fed back to the coarse grid domain.

A comprehensive simulation within ARW entails the presence of a primary coarse outer grid, referred to as the *parent* grid, which may incorporate multiple inner fine nested grids designated as *child* grids. The term *child* domain might also signify a *parent* domain, particularly in scenarios involving multi-level nesting. It is important to note that ARW strictly prohibits the occurrence of overlapping grids, where a coarse grid point resides within more than one child grid. This prohibition ensures a clear and unambiguous spatial hierarchy within the simulation.

Furthermore, ARW adheres to the principle that each grid can have no more than a single parent, emphasizing a straightforward and non-ambiguous grid relationship. The organization of parent and child grids within the simulation is crucial for maintaining computational integrity and ensuring accurate representations of atmospheric phenomena. To illustrate these principles, Figure 2.5 provides visual examples, demonstrating permissible and impermissible nesting configurations. These examples serve as a visual guide to help users understand and implement effective nesting strategies within the ARW framework, ensuring a robust and coherent simulation setup.

2.3 Time Discretization in WRF

Time discretization is a fundamental aspect of the numerical integration process in the Weather Research and Forecasting (WRF) model. It determines how the model progresses through time during a simulation and directly impacts both computational cost and numerical stability. In WRF, this is controlled primarily through two parameters: `time_step` and `history_interval` [63, 64].

2.3.1 Time Step (`time_step`)

The `time_step` parameter in WRF defines the basic time increment (in seconds) used during numerical integration. It determines how often the model's physical and dynamical equations are updated. Choosing an appropriate value for `time_step` is crucial: if it is too large, the simulation may become numerically unstable; if too small, the model becomes computationally expensive.

A general empirical guideline suggests setting the `time_step` based on horizontal grid spacing:

$$\texttt{time_step} \approx 6 \times \Delta x \quad \text{(in km)} \tag{2.6}$$

For example, a 3 km domain would typically use a `time_step` of about 18 seconds. However, this must be validated based on the model configuration, vertical resolution, and physical schemes in use.

The model internally adjusts or applies sub-stepping for some physics and numerical schemes. Additionally, compliance with the Courant–Friedrichs–Lewy (CFL) condition is essential to avoid instability, particularly in domains with steep topography or high wind speeds.

2.3.2 History Interval (`history_interval`)

While `time_step` governs how frequently the model updates internally, the `history_interval` setting controls how often WRF writes output to disk. This parameter is specified in minutes and is independent of the internal time step:

- Smaller `history_interval` (e.g., 15 minutes) values produce more frequent output files, which improves temporal resolution for post-processing and diagnostics.

- Larger `history_interval` (e.g., 60 or 180 minutes) values reduce disk usage and I/O overhead, which can be substantial in long or high-resolution simulations.

Although reducing the `history_interval` improves data granularity, it does not affect the accuracy of the simulation itself. However, very small intervals can lead to excessive I/O operations and slow down the simulation runtime.

2.3.3 Constraints and Best Practices

Several constraints and best practices should be considered when choosing `time_step` and `history_interval`:

- **Numerical Stability:** The chosen `time_step` must satisfy the CFL condition:
$$\text{CFL} = \frac{U \cdot \Delta t}{\Delta x} < 1$$
where U is the maximum wind speed, Δt is the time step, and Δx is the grid spacing.

- **Model Performance:** Output frequency should balance the need for detailed temporal resolution against the overhead of data writing. Excessively frequent output can slow down simulations and create large storage requirements.

- **Physics Compatibility:** Some physical parameterization schemes (e.g., cumulus or microphysics) may have internal time scales that affect or interact with the global `time_step`. It is important to review their documentation for compatibility.

- **Nesting Considerations:** In nested domains, child domains often use smaller time steps than the parent domain (commonly in a 1:3 or 1:5 ratio). This ensures synchronization across domains while maintaining numerical stability in finer-resolution grids.

In summary, time discretization in WRF is a critical aspect that must be carefully tuned for both stability and efficiency. Properly configuring `time_step` and `history_interval` ensures that the model runs smoothly, remains computationally efficient, and produces outputs at a useful temporal resolution for analysis.

2.4 Initial Conditions

ARW offers the flexibility to execute simulations with either user-defined initial conditions for ideal scenarios or through the utilization of interpolation data derived from external analyses or real-time prediction datasets. For ideal simulations, both 2D and 3D test cases are readily available, catering to diverse modeling requirements.

In the realm of real-data simulations, ARW accommodates several sample cases, leveraging preprocessing capabilities from an external package known as the WRF Preprocessing System (WPS). WPS plays a pivotal role in the conversion of large-scale GRIB-formatted data into an intermediate format suitable for ingestion by ARW's real-data processor. This preprocessing step is essential for seamlessly integrating real-world observational or prediction data into the ARW simulation environment.

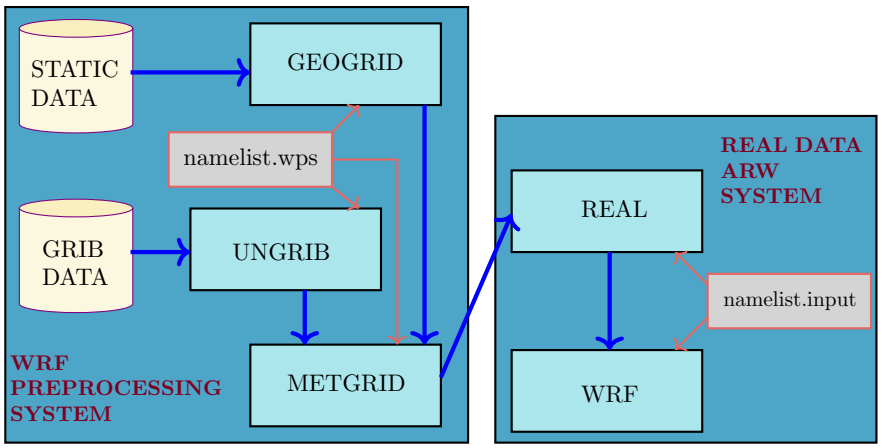


Figure 2.6: Schematic showing data flow and program components in WPS, and how WPS feeds initial data to ARW.

2.4.1 Initialization for Real-Data Conditions

Initial conditions for real data simulations undergo preprocessing using a dedicated package known as the WRF Preprocessing System (WPS), illustrated in Figure 2.6. Comprising a suite of applications, WPS plays a pivotal role in transforming terrestrial and meteorological data, typically available in GRIB file format, into a format compatible with the Advanced Research Weather (ARW) preprocessor for real data items. The data flow into and out of WPS is visualized in Figure 2.6. `GEOGRID`, defines the model domain and creates static files of terrestrial data. `UNGRIB`, decodes GRIB-formatted real data files. `METGRID`, interpolates meteorological data to the model domain and prepare them to be ingested to the ARW.

The initial step in WPS involves defining a physical grid, encompassing key parameters such as projection type, earth location, grid dimensions, nest locations, and grid distances. Simultaneously, static fields within the specified domain undergo interpolation. Irrespective of the domain configuration, external analyses or predictions are processed by the WPS GRIB decoder. This decoder identifies the requisite fields and reformats the GRIB data into an internal binary format.

With the domain specifications in place, WPS undertakes horizontal interpolation of meteorological data within the projected domains. The output from WPS, which serves as input for the ARW preprocessor program in real data cases, presents a comprehensive three-dimensional snapshot of the atmosphere at selected time slots, appropriately aligned with the model grid's horizontal staggering. This preprocessing step is integral to ensuring that real-world observational or predictive data seamlessly integrates into the ARW simulation environment, providing accurate and representative initial conditions for simulations based on real atmospheric data.

ARW real data processor input from WPS including surface and 3D fields

of temperature (K), relative humidity (%), geopotential height (m), pressure (Pa), and horizontal wind speed components (m/s, previously rotated to the model projection). The two-dimensional static ground fields include albedo, Coriolis parameters, terrain elevation, vegetation/land-use type, land/water mask, map scale factors, map rotation angle, soil texture category, vegetation greenness fraction, average annual temperature, and latitude/longitude. After WPS processing, time-dependent 2D fields from the external model include surface pressure and sea-level pressure (Pa), soil temperature layers (K), and soil moisture (kg/kg, either total moisture, or binned into total and liquid content), snow depth (m), skin temperature (K), sea surface temperature (K), and sea ice flag.

2.4.2 GRIB Data and UNGRIB Software

In the operational workflow of WRF-ARW (as depicted in Figure 2.6), the inclusion of `GRIB` data is imperative to furnish the model grid domain with dynamic atmospheric data, encompassing both surface and volume (pressure level) variables. These `GRIB` data are commonly sourced from other regional or global models, such as NCEP's NAM, GFS (Global Forecast System), or ECMWF (European Centre for Medium-Range Weather Forecasts) models, ensuring a comprehensive representation of atmospheric conditions.

It is noteworthy that `GRIB` files, which serve as the carriers of these data, typically contain a multitude of fields that extend beyond the specific requirements for initializing WRF. In the frame of WRF-ARW, the essential data types that must be included in the GRIB files are important for initializing and accurately representing the atmospheric state within the model. The careful selection and inclusion of these specific data types from the broader array of fields in `GRIB` files ensure that WRF starts with the requisite information, fostering precision and reliability in the simulation results. The data types that must be included in the `GRIB` files are

- 3D Data (e.g. data on pressure levels)
  - Temperature
  - U and V components of Wind
  - Geopotential Height
  - Relative Humidity (the code can calculate RH if Specific Humidity is available -this is controlled in the `Vtables, see below-`)
- 2D Data
  - Surface Pressure
  - Mean Sea Level Pressure
  - Skin Temperature/SST
  - 2-meter Temperature
  - 2-meter Relative or Specific Humidity
  - Snow depth

- Sea-ice coverage
- Land-sea mask
- 10-meter U and V components of wind
- Soil data (temperature and moisture) and soil height

The UNGRIB program, a crucial component in the WRF-ARW workflow (refer to Figure 2.6), utilizes diverse codes to discern variables and levels within the GRIB file. To accomplish this, UNGRIB relies on tables known as Vtables, where V stands for "Variable Tables." These tables play a pivotal role in guiding the extraction process, determining which fields from the GRIB file need to be extracted and subsequently written in the intermediate format.

Vtables are specifically crafted for different grid configurations and datasets, offering a tailored approach to variable identification. They are available for various models and formats, including GFS (Global Forecast System), ECMWF, and other datasets.

These Vtables, bundled with the UNGRIB software, ensure a seamless and accurate translation of data from the GRIB files to the intermediate format. The comprehensive coverage of Vtables allows UNGRIB to efficiently handle a diverse range of atmospheric datasets, enhancing the adaptability and versatility of the WRF-ARW modeling system.

2.4.3 Static Data and GEOGRID Software

The primary function of GEOGRID is to delineate simulation domains and facilitate the interpolation of diverse terrestrial datasets onto model grids. The definition of simulation domains is a user-driven process, specified in the "GEOGRID" namelist record within the WPS namelist file, commonly named "namelist.wps."

GEOGRID not only computes latitude, longitude, and map scale factors at any point on the grid but also undertakes the default interpolation of various critical parameters to the model grids. These parameters encompass soil categories, land use categories, terrain height, annual mean deep soil temperature, monthly vegetation fraction, monthly albedo, maximum snow albedo, and slope category. By default, GEOGRID interpolates these essential variables based on user-defined simulation domains.

To facilitate this interpolation process, global datasets for each of the mentioned fields are made available through the Geographical Static Data Downloads page [65]. These datasets, being time-invariant, necessitate a one-time download. The Geographical Static Data Downloads page provides both low and high terrestrial resolution options for these static datasets, enabling users to choose the level of detail based on their modeling requirements. This streamlined approach enhances the accessibility and efficiency of incorporating critical terrestrial information into the WRF-ARW simulation framework.

2.5 Description of the Output

The typical output of a NWP model, useful for Earth-space propagation modeling, are given in Table 2.1. These parameters are the direct output of WRF, however other NWP models have similar outcomes.

In thermodynamic view of data conversion some typical constants are needed which will be used regularly in the following sections. These constants and their common units are expressed in Table 2.2.

2.5.1 Geopotential Height

Geopotential height is a fundamental concept in atmospheric science, representing the height of a given pressure surface above mean sea level. Unlike geometric height, which is a direct physical measure, geopotential height accounts for the variation in gravity with latitude and elevation[1]. It is especially useful in meteorology for analyzing pressure levels and for comparing atmospheric data across different altitudes.

At a geometric height z, the geopotential $\Phi(z)$ is defined as the work required to raise a unit mass from sea level to that height against gravity:

$$\Phi(z) = \int_0^z g(\phi, z)\, dz \qquad [\mathrm{m^2\, s^{-2}}] \tag{2.7}$$

Here, $g(\phi, z)$ is the gravitational acceleration, which depends on the latitude ϕ and geometric height z. This integral represents the gravitational potential energy per unit mass at height z.

To convert this potential into a more interpretable measure, we define the **geopotential height** Z_g by normalizing $\Phi(z)$ using the standard gravitational acceleration at sea level $g_0 = 9.81$ m/s^2:

$$Z_g = \frac{\Phi(z)}{g_0} \qquad [\mathrm{m}] \tag{2.8}$$

In the WRF model, geopotential is separated into two components: the base-state geopotential `PHB` (representing $\Phi(0)$) and the perturbation geopotential `PH` (representing $\Phi(z) - \Phi(0)$). Thus, the geopotential height is computed as:

$$Z_g = \frac{\mathrm{PH} + \mathrm{PHB}}{g_0} \tag{2.9}$$

Since these geopotential values are defined on a staggered vertical grid, it is often necessary to compute the geopotential height on mass levels (unstaggered) by averaging adjacent staggered levels:

$$Z_g = \frac{Z_g(t, k+1, j, i) + Z_g(t, k, j, i)}{2} \tag{2.10}$$

[1] In atmospheric or geophysical texts Elevation usually refers to geometric height above a reference surface (typically mean sea level). So, strictly speaking: Elevation = z (geometric height) Not the same as geopotential height h

Table 2.1: WRF output variables useful to model propagation impairments [63, 64]

Variable	Unit	Description	Symbol
RAINC	mm	Convective accumulated precipitation	$\int_0^t R_{rain,c}dt$
RAINNC	mm	Microphysics accumulated precipitation	$\int_0^t R_{rain,nc}dt$
RAINSH	mm	Shallow accumulated precipitation	$\int_0^t R_{rain,sh}dt$
PH	m^2/s^2	Perturbation geopotential	$-\Phi(h)$
PHB	m^2/s^2	base-state geopotential	$\Phi(0)$
HGT	m	Terrain Height	
P	pa	perturbation pressure	p'
PB	pa	base state pressure	
PSFC	pa	surface pressure	
T	$^\circ K$	perturbation potential temperature	$\theta - T_0$
U	m/s	U-wind component	u_g
V	m/s	V-wind component	v_g
W	m/s	W-wind component	w
QCLOUD	kg/kg	Cloud water mixing ratio	w_{cloud}
QRAIN	kg/kg	Rain water mixing ratio	w_{rain}
QVAPOR	kg/kg	Water vapor mixing ratio	w_{vapor}
QSNOW	kg/kg	Snow mixing ratio	w_{snow}
QICE	kg/kg	Ice mixing ratio	w_{ice}
QGRAUP	kg/kg	Graupel mixing ratio	w_{graup}
COSALPHA		Local cosine of map rotation	$\cos\alpha$
SINALPHA		Local sine of map rotation	$\sin\alpha$
XLAT	$^\circ E$	Latitude	ϕ
XLON	$^\circ N$	Longitude	λ

Table 2.2: Basic constant parameters in thermodynamics

Constant	**Unit**	**Description**
$M_{dry} = 28.9647$	$gr\,mol^{-1}$	Dry air molar mass
$M_{wv} = 18.015$	$gr\,mol^{-1}$	Water vapor molar mass
$R = 8.31432$	$J\,mol^{-1}\,K^{-1}$	Ideal gas constant
$R_{dry} = R/M_{dry} = 287.058$	$J\,kg^{-1}\,K^{-1}$	Specific gas constant for dry air
$R_{wv} = R/M_{wv} = 461.52$	$J\,kg^{-1}\,K^{-1}$	Specific gas constant for water vapor
$c_p = 29.07$		specific heat capacity of dry air at a constant pressure
$\kappa = R/c_p = 0.286$		

This transformation ensures consistency when aligning geopotential height with other variables defined at mass points.

2.5.2 Pressure

Calculation of total pressure using WRF output variables can be done as:

$$P_{tot} = P + PB \tag{2.11}$$

which P is the perturbation pressure and PB is the base state pressure. These variable are called pressure at eta or mass grid (see Section 2.2).

2.5.3 Temperature

The potential temperature of a parcel of fluid at pressure P is the temperature that the parcel would attain if adiabatically brought to a standard reference pressure P_0, usually $1000\,hPa\,(1000\,mb)$. The potential temperature is denoted θ and, for a gas well-approximated as ideal, is given by

$$\theta = T\left(\frac{P_0}{P}\right)^{R/c_p} \tag{2.12}$$

where T is the current absolute temperature (in K) of the parcel, R is the gas constant of air, and c_p is the specific heat capacity at a constant pressure. For clear air we have the constant ratio

$$\frac{R}{c_p} = \frac{8.314}{29.07} = 0.286 \tag{2.13}$$

In WRF output variables the perturbation potential temperature $(\theta - T_0)$ is provided for $T_0 = 300K$ and is denoted by T (different from absolute tem-

perature). Absolute temperature is derived by:

$$Absolute_Temp = (T + 300) \times \left(\frac{P_{tot}}{P00}\right)^{R/c_p} \tag{2.14}$$

with P_{tot} being the total pressure calculated as indicated in 2.5.2 and $P00$ being the base state pressure at ground levelprovided in WRF output variables.

2.5.4 Gas Mixtures Properties

A full understanding of the various terms for humidity and moisture requires some basic knowledge about the properties of gas mixtures. In a gas mixture such as air, the total pressure (same as atmospheric or barometric pressure) of the gas is the sum of all the individual partial pressures of its gas components. The atmospheric pressure, usually around 1000 hPa, is the total of the partial gas pressure of nitrogen (∼775 hPa), oxygen (∼205 hPa), water vapor (∼10 hPa), argon (∼10 hPa) carbon dioxide (∼0.4 hPa) and a number of other gases with lower partial pressures.

Specific humidity (q) is the density of water vapor (mass per unit volume) divided by the density of all air, including the water vapor:

$$q = \frac{m_{water\,vapour}}{m_{all\,air}} = \frac{\rho_{water\,vapour}}{\rho_{all\,air}} = \frac{\rho_v}{\rho} \tag{2.15}$$

Specific humidity is used to calculate virtual temperature. This parameter is unitless, but often put $g\,kg^{-1}$ or $kg\,kg^{-1}$ as the unit of this parameter.

Water vapor mixing ratio (w) is the density of water vapor divided by the density of dry air without the water vapor (or weight of water in the volume occupied by one kilogram of dry gas). Mixing ratio like specific humidity is a unitless parameter but usually followed by $g\,kg^{-1}$. This quantity is mainly used for calculating water content when the mass flow of air is known.

$$w = \frac{m_{water\,vapour}}{m_{dry\,air}} = \frac{\rho_{water\,vapour}}{\rho_{dry\,air}} = \frac{\rho_v}{\rho_d} \tag{2.16}$$

Since $\rho_d = \rho – \rho_v$, we can rearrange the equations to get the relationship between w (water vapor mixing ratio) and q (specific humidity):

$$\begin{aligned} w &= \tfrac{q}{1-q} \\ q &= \tfrac{w}{1+w} \end{aligned} \tag{2.17}$$

The water vapor mixing ratio, w, typically at maximum value is about $40gkg^{-1}$ or $0.04kgkg^{-1}$. For this amount of water vapor, $q = 0.040/(1 + 0.040) = 0.038$ or $38gkg^{-1}$. Thus, water vapor mixing ratio and specific humidity are the same to within a few percent. But specific humidity is less than the water vapor mixing ratio if the humidity is more than zero.

In the WRF netCDF output files, the water vapor mixing ratio (w) is provided and is denoted by QVAPOR $[kg/kg]$.

The air temperature dictates the maximum partial water vapor pressure in air, in other words, the water vapor saturation pressure. The ability of

water to be in gaseous form is strongly dependent on its temperature. The higher the temperature, the higher the partial pressure of the water vapor. The partial water vapor pressure in the immediate presence of liquid water equals the saturation pressure at that specific temperature.

Using ideal gas law:

$$PV = nRT \qquad n = m/M \qquad \rho = m/V \tag{2.18}$$

Where $P\,[pa]$ is the pressure of the gas, $V\,[m^3]$ is the volume taken up by the gas, $T\,[K]$ is the temperature of the gas, $R = 8.31\,[\frac{J}{K.mol}]$ is the gas constant, and n is the number of moles of the gas. The amount (n) (in moles) is equal to total mass of the gas [kg] divided by the molar mass (M [kg/mol]) .

the water vapour pressure can be derived from water vapour mixing ration (w).

$$p_v = \rho_v R_v T \qquad p_d = \rho_d R_d T \qquad \epsilon = R_d/R_v = M_v/M_d = 0.622 \tag{2.19}$$

$$w = \frac{\rho_v}{\rho_d} = \frac{p_v}{p_d}\epsilon = \frac{\epsilon p_v}{p - p_v} \tag{2.20}$$

In WRF output netCDF files the variables p(total pressure in Section 2.5.2) and w are provided which by using Eq. 2.20 and 2.19, the water vapour density (M) is calculated. If this variable is integrated over altitude the variable IWVC is achieved which in calculation of water vapour attenuation is used.

2.5.5 Humidity

When the term humidity is used, it usually means water vapor in a gas, typically air. Moisture, on the other hand, is used for liquids and solid materials. The term moisture also applies to extremely dry gases, when water vapor is considered an impurity. The 'relative' in relative humidity expresses the relation between the amount of water vapor present and the maximum amount that is physically possible at that temperature. Relative humidity is expressed by

- partial vapor and air pressure,
- density of the vapor and air,
- the actual mass of the vapor and air,
- the mixing water vapour,

Relative humidity is usually expressed in per cent and abbreviated by RH.

$$RH = 100\% \times \left(\frac{p_v}{p_{vs}}\right) = 100\% \times \left(\frac{m_v}{m_{vs}}\right) = 100\% \times \left(\frac{w}{w_s}\right) \tag{2.21}$$

where p_v is partial water vapor pressure (or water vapor density [kg/m3]), p_{vs} is the water vapor's saturation pressure or water vapor density at saturation at actual dry bulb temperature [kg/m3] which can be approximated mathematically [66], m_v is mass of water vapor in the given air volume [kg] and m_{vs}

is the mass of water vapor required to saturate at this volume [kg]. w_s is the saturation mixing ratio (the mixing ratio at which RH = 100%).

As mentioned above, the ability of air to hold water vapor is strongly dependent on temperature. This, of course, means that relative humidity is also strongly temperature dependent. Let's imagine that the outside temperature on a crisp winter day is $-14°C$, and the relative humidity is 60%. As this air enters a building, it is heated to $+21°C$, but the amount of water remains constant - no water is removed or added to the air in normal ventilation systems. Because of this heating, the saturation pressure of the water vapor rises (i.e. the maximum possible amount of water vapor in the air), but the partial pressure of the water vapor is unchanged. In this case, the relative humidity will drop to 5%, which is usually considered too dry for comfort.

2.5.6 Rain rate

Total amount of rainfall in the domain is calculated by adding all types of direct output of rain events in WRF. Typically three different rain evens are simulated by WRF. The `RAINC`, `RAINSH`, and `RAINNC` fields contain the total accumulated precipitation from the convective (CU), shallow convective (SHCU), and microphysics (MP) schemes respectively. Think *rain cumulus*, *rain shallow*, and *rain non-convective*.

$$R_{acc}(t) = \texttt{RAINC}(t) + \texttt{RAINSH}(t) + \texttt{RAINNC}(t) \tag{2.22}$$

Ordinarily these variables are dependent to the physics packages chosen in WRF system configuration. The type of physics can be set by users in `namelist.input` file in the field of `cu_physics`. Typical schemes for this field variable are:

- No cumulus
- Kain-Fritsch
- Betts-Miller-Janjic
- Grell-Devenyi ensemble
- Simplied Arakawa-Schubert (NMM only)
- Grell 3D ensemble

Only two of above schemes are suitable for ARW solvers which are (a) `no cumulus` and (b) `Grell 3D ensemble`. The outcome precipitation in `no cumulus` scheme will be saved in `RAINNC` and the other rain types, `RAINC` and `RAINSH` will be set to zero. While in the `Grell 3D ensemble` scheme very small amounts of shallow precipitation will be stored in the variables `RAINC` and `RAINSH`.

To calculate the rainfall rate (in mm/h) from these quantities, it is sufficient to subtract the accumulated rainfall in two consecutive time slots according to Eq. 2.23 and divide it by the unit of time.

$$R_{rate}(t_{i+1}) = \frac{R_{acc}(t_{i+1}) - R_{acc}(t_i)}{t_{i+1} - t_i} \tag{2.23}$$

Another way to represent the rainfall rate is by adding a field parameter in the `namelist.input` file. This field parameter is called `prec_acc_dt` which is one of the options in field of physics packages. This parameter calculates the rainfall in millimeters in the specified time period and empties the rain bucket after each period. The advantage of this method is that the user is not obliged to have the accumulated rain in two successive time slots to measure the rain rate. It is enough to divide the amount of accumulated precipitation in each period over the duration of a period to calculate the desired rainfall rate.

In addition to rain rate, other parameters of rain events are demanded to model satellite propagation impairments. In models of rain drop size distribution (chapter 3.6.3), one of the important parameters is the mass of rain in unit volume or simply rain density. Knowing the rain water mixing ratio (w_{rain}) and total pressure (P_{tot}), the rain density is simply defined as

$$w_{rain} = \frac{\rho_{rain}}{\rho_d} \tag{2.24}$$

$$M_{rain} = \rho_{rain} = \frac{w_{rain}\, P_{tot}}{R_d\, T} \tag{2.25}$$

The w_{rain}, R_d, P_{tot}, and T are defined in Tables 2.1-2.2 and Sections 2.5.2-2.5.3 respectively.

2.5.7 Cloud

To extract cloud properties, two important parameters of volumetric mass and relative humidity are needed. The calculation of the volumetric mass of the cloud is done according to the process of calculating the volumetric mass of water vapor in the previous section, with the difference that the initial parameter "QVAPOR" is replaced by "QCLOUD". The summary of these relationships is as follows:

$$w = \frac{\rho_{cloud}}{\rho_d} \tag{2.26}$$

$$M_{rain} = LWC = \rho_{cloud} = \frac{w\, P_{tot}}{R_d\, T} \tag{2.27}$$

It is noteworthy that there are different methods for calculating the effects of clouds in Earth-space wave propagation. Two of the prominent methods are the use of ITU-R P.840 [55] and the other are Salonen and Mattioli methods [67], in the latter two cases the relative humidity parameter will be required.

2.5.8 Wind

The components of the wind speed vector in the three directions U, V, W are shown in Fig. 2.4. These are in the geometrically horizontal (U, V) and vertical (W) directions. On flat ground, W on the first level $k = 1$ is zero. However, when the ground has nonzero slope, the vertical velocity components W are generally not zero, because the vector normal to the ground is not vertical.

These variables are all staggered type and to access the non staggered one average over two consecutive values; we have

$$\begin{array}{lcl} U_\theta(i,j,k) & = & 0.5 \times (U(i,j,k) + U(i+1,j,k)) \\ V_\theta(i,j,k) & = & 0.5 \times (V(i,j,k) + V(i,j+1,k)) \\ W_\theta(i,j,k) & = & 0.5 \times (W(i,j,k) + W(i,j,k+1)) \end{array} \tag{2.28}$$

It necessary to rotate winds to earth-relative using the correct formulas:

$$\begin{array}{ll} U_e = & U_\theta \times \text{COSALPHA} - V_\theta \times \text{SINALPHA} \\ V_e = & V_\theta \times \text{COSALPHA} + U_\theta \times \text{SINALPHA} \end{array} \tag{2.29}$$

Which $COSALPHA$ and $SINALPHA$ are local cosine and local sine of map location respectively that are provided in WRF output netCDF files.

2.6 Conclusion

This chapter presented a comprehensive overview of Numerical Weather Prediction (NWP) and its integration into satellite communication modeling, with a focus on the Weather Research and Forecasting (WRF) system. By highlighting WRF's flexibility, open-source nature, and proven performance in both research and operational contexts, we established its suitability for atmospheric modeling in propagation studies.

Key aspects such as model initialization, grid structure, vertical and horizontal coordinate systems, and variable staggering were discussed in detail, providing the foundation for interpreting WRF output data. The importance of preprocessing tools such as WPS, and components like GEOGRID and UNGRIB, was underscored in the context of domain setup and real-data assimilation.

Additionally, we explored the derivation of essential meteorological parameters—temperature, pressure, humidity, rain rate, and wind fields—using WRF output. These parameters are fundamental for modeling atmospheric impairments in satellite communication links.

Through this exploration, we have established a robust framework for leveraging WRF as a key input source for modeling and analyzing Earth-space propagation effects. This framework will be instrumental in subsequent chapters that address attenuation modeling, rain dynamics, and other atmospheric phenomena impacting satellite communication systems.

Chapter 3

Electromagnetic Scattering by Atmospheric Particles

Electromagnetic plane waves propagating through the Earth's atmosphere interact with various constituents such as precipitation, clouds, and gases. These interactions result in scattering and absorption caused by atmospheric gases and particles including water droplets, ice crystals, snow, hail, etc. Among the key parameters influencing these effects, the *refractive index* plays a central role in characterizing how electromagnetic waves are attenuated as they travel through the atmosphere.

The refractive index of a medium is a complex-valued quantity, typically written as:

$$n = n' - jn''$$

where:

- n' is the *real part*, which determines the phase velocity of the wave and governs refraction and scattering,
- n'' is the *imaginary part*, which quantifies the absorptive loss and contributes directly to attenuation due to thermal dissipation.

In essence, the *real part* of the refractive index influences how waves bend or scatter as they pass through different media, while the *imaginary part* represents the amount of wave energy absorbed and transformed into heat. A larger imaginary component corresponds to stronger absorption, and thus more significant signal attenuation.

Among atmospheric constituents, liquid water has a particularly high dielectric constant and a substantial imaginary component in its refractive index, especially at microwave frequencies. This makes water a more efficient medium for both scattering and absorption compared to ice or atmospheric gases. As a result, the presence of water droplets in rain or clouds leads to a greater degree of signal attenuation.

To understand how different atmospheric constituents affect electromagnetic wave propagation, Section 3.1 explores the refractive index properties of

atmospheric gases and clear-sky conditions. This provides foundational insight into wave behavior in the absence of hydrometeors.

Then, in Section 3.3, the discussion focuses on models that describe the refractive index of water droplets, which are essential for predicting signal degradation in rainy and cloudy conditions. These models help quantifying the impact of water on wave propagation, particularly in the microwave spectrum.

A comprehensive understanding of the refractive index across various atmospheric components is not only crucial for theoretical analysis but also for practical applications. One key application is in meteorological radar systems, where accurate modeling of rain-induced scattering is vital for reliable weather prediction and satellite communication system performance.

3.1 Atmospheric refractive index

The characteristics of both the phase and amplitude responses of a plane radio wave propagating a distance L at frequency f can be derived from the expression:

$$E(L) = E_0\, e^{-j\frac{2\pi f}{c_0}L.n} \tag{3.1}$$

Here, E_0 represents the initial amplitude, c_0 is the speed of light in a vacuum, and $j = \sqrt{-1}$. The refractive index n is a key factor that is contingent on the frequency (f) and atmospheric conditions.

Given that air typically has a refractive index close to 1, introducing the concept of refractivity N [ppm] becomes valuable [66]. This refractivity provides a succinct representation of the refractive index, taking into account variations in atmospheric conditions.

$$n = 1 + N \times 10^{-6} \tag{3.2}$$

and then

$$N(f) = N_0 + N'(f) - j\, N''(f) \tag{3.3}$$

with terms corresponding to the equivalent refractive index components.

The non-dispersive term N_0 for moist air in [66] is presented as

$$N_0 = 77.6\frac{P}{T} - 5.6\frac{e}{T} + 3.75 \times 10^5 \frac{e}{T^2} \tag{3.4}$$

where P, e, and T are total pressure [hPa], water vapour pressure [hPa], and temperature [K] respectively. The total pressure is

$$P = P_d + e \tag{3.5}$$

The parameter P_d in the equation corresponds to dry air pressure. In sea-level pressure conditions, P typically hovers around $\approx$ 1024 [hPa], with an average range for water vapor pressure (e) of approximately $\approx$ 7 [hPa]. These values, however, are not constants; rather, they exhibit variability based on location and elevation.

Generally, N_0 greatly exceeds $N'(f)$, indicating that the real part of air refractivity is approximately frequency-independent under good approximation. In other words, the influence of air properties on the refractivity is relatively stable across different frequencies.

Conversely, the imaginary part of the dispersive term, denoted as $N''(f)$, stems from absorption and/or scattering by diverse atmospheric constituents. It is this particular aspect that becomes a primary focus in the study of electromagnetic propagation, as it introduces frequency-dependent characteristics and constitutes a significant factor in understanding and mitigating impairments in signal transmission through the atmosphere.

3.2 Atmospheric Specific Attenuation

Refractivity is easily converted into path-specific propagation rates. The imaginary part of eq. 3.3 leads to power attenuation

$$\begin{aligned} A(f) &= -20\log_{10}\left(\frac{\mathbf{E}}{\mathbf{E_0}}\right) \\ &= -20\log_{10}\left(\exp\left[-\frac{2\pi f}{c}n''(f)L\right]\right) \\ &= \frac{20}{\ln 10}\frac{2\pi}{c_0}fn''(f)L \\ &= \frac{20}{\ln 10}\frac{2\pi}{c_0}f\times 10^9 N''(f)\times 10^{-6}L\times 10^3 \\ &\approx 0.182\, f\, N''(f)\, L \end{aligned} \tag{3.6}$$

where L is expressed in $[km]$. The specific attenuation γ is defined as

$$\gamma(f) = 0.182\, f\, N''(f) \quad [\text{dB/km}] \tag{3.7}$$

The real part of refractivity is converted to the phase dispersion by

$$\beta = 1.2008\, f\, N'(f) \tag{3.8}$$

or group delay

$$\tau = 3.336\, N'(f) \tag{3.9}$$

where frequency f is in gigahertz (GHz) throughout.

3.3 Water Droplet Refractive Index

To accurately model the interaction between a plane wave and a water droplet, it is crucial to possess knowledge about the refractive index inside the droplet, denoted as n, which corresponds to the refractive index of liquid water. Alternatively, this information can be expressed in terms of relative permittivity, ϵ_r, using the relationship $n = \sqrt{\epsilon_r \mu_r}$, where the relative permeability μ_r is unity for water.

In the realm of electromagnetic modeling of water droplets, two widely-used models for ϵ_r are detailed in Sections 3.3.1 and 3.3.2. The first model, advocated by [55] and discussed in Section 3.3.1, is particularly effective for modeling cloud particle attenuation. On the other hand, the second model, known as the Ray model, outlined in Section 3.3.2, finds its primary application in simulating rain droplet attenuation.

The representation of permittivity for any material, including water, follows the general expression:

$$\epsilon_r(f,T) = \epsilon_r'(f,T) - j\epsilon_r''(f,T) \tag{3.10}$$

This equation captures both the real (ϵ_r') and imaginary (ϵ_r'') parts of the permittivity, where the imaginary part accounts for absorption and scattering effects.

Figure 3.1 illustrates the refractive index $n = \sqrt{\epsilon_r}$ outcomes of three models—Liebe, ITU-R P.840 (modified Liebe model), and Ray models—at a temperature $T = 298, [K]$ across the frequency range of 1-1000 GHz. Notably, the differences among these models are subtle, particularly below 200 GHz, showcasing the frequency-dependent characteristics of water's refractive index as a crucial consideration in electromagnetic modeling.These models are used to predict and address attenuation effects in various atmospheric conditions.

3.3.1 Liebe Model of Liquid Water Permittivity

This comprehensive model serves as a broadband representation for complex refractivity, designed to forecast the propagation effects of loss and delay in the neutral atmosphere, especially applicable at frequencies up to 1000 GHz [68]. The utilization of this model is particularly prominent in this dissertation, specifically for predicting cloud attenuation propagation.

In various atmospheric conditions such as haze, fog, or clouds, suspended water droplets emerge as highly effective absorbers of millimeter-wave radiation. The characteristic size range of these droplets, with radii below 50 μm, permits the application of the Rayleigh approximation within Mie scattering theory. This approximation proves instrumental in formulating refractivity contributions denoted as $N''(f)$.

$$N''(f) = \frac{9}{2} M \frac{1}{\epsilon''(1+\eta^2)} \tag{3.11}$$

and

$$N'(f) = \frac{9}{2} M \left[\frac{1}{\epsilon_0 + 2} - \frac{\eta}{\epsilon''(1+\eta^2)}\right] \tag{3.12}$$

and

$$\eta = (2+\epsilon')/\epsilon'' \tag{3.13}$$

where ϵ_0 is the static (f = 0) and ϵ', ϵ'' are the real and imaginary parts of the permittivity for liquid water. M is the liquid water density in the cloud or fog (g/m^3).

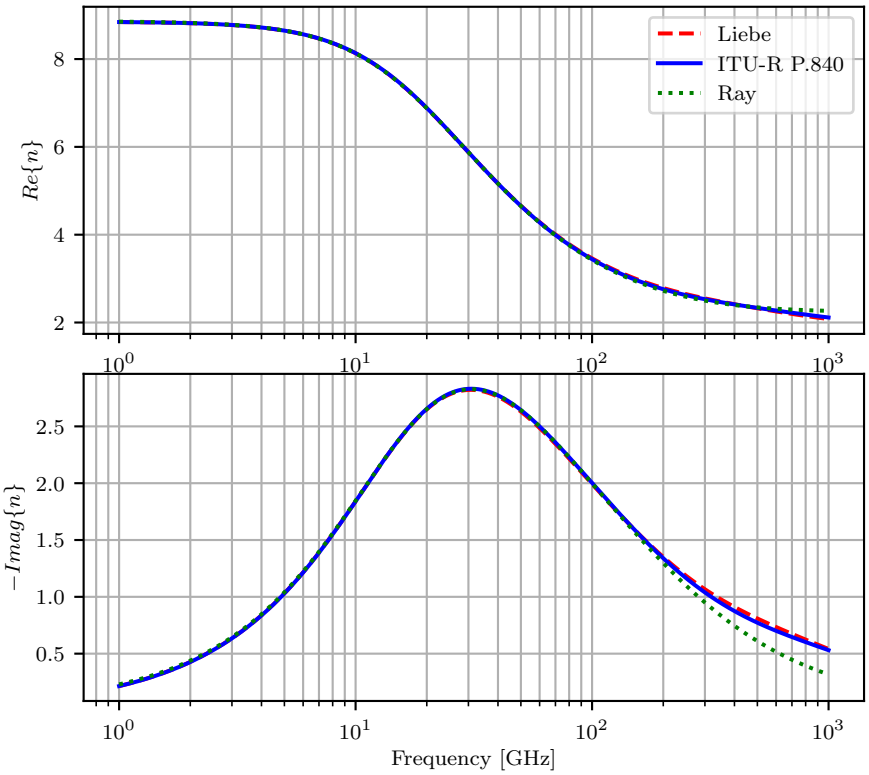


Figure 3.1: Refractive index of water at 298 K for frequency range 1-1000 GHz with either the Liebe [68], Ray [69] or the ITU-R P.840 [55] models

Dielectric permittivity $\epsilon(f)$ of water is determined with the double-Debye model [70]:

$$\epsilon''(f) = \frac{(\epsilon_0 - \epsilon_1)f}{f_p\left[1 + \left(\frac{f}{f_p}\right)^2\right]} + \frac{(\epsilon_1 - \epsilon_2)f}{f_s\left[1 + \left(\frac{f}{f_s}\right)^2\right]} \tag{3.14}$$

and

$$\epsilon'(f) = \frac{\epsilon_0 - \epsilon_1}{1 + \left(\frac{f}{f_p}\right)^2} + \frac{\epsilon_1 - \epsilon_2}{1 + \left(\frac{f}{f_s}\right)^2} + \epsilon_2 \tag{3.15}$$

with the permittivity terms ϵ_0, ϵ_1, and ϵ_2 given by

$$\epsilon_0 = 77.66 + 103.3(\theta_T - 1) \tag{3.16}$$

$$\epsilon_1 = 0.0671\epsilon_0 \tag{3.17}$$

$$\epsilon_2 = 3.52 \tag{3.18}$$

with the relaxation frequencies $f_p[GHz]$ and $f_s[GHz]$ given by

$$f_p = 20.20 - 146(\theta_T - 1) + 316(\theta_T - 1)^2 \quad \text{[GHz]} \tag{3.19}$$

$$f_s = 39.8 f_p \quad \text{[GHz]} \tag{3.20}$$

Here, the parameters include the frequency f measured in gigahertz (GHz), and the function $\theta_T = 300/T$ associated with the temperature T measured in kelvin (K). Equations 3.17-3.20 represent modified and updated forms found in [55], which differ from the original references presented in [68].

3.3.2 Ray Model of Liquid Water Permittivity

The Ray model, as introduced by [69], relies on an extension of the Debye theory through the incorporation of the Cole-Cole model. This model incorporates a frequency-independent conductivity term, denoted as $\sigma = 12.5664 \times 10^8$ [S], and is expressed in the following form:

$$\epsilon_r(f,t) = \epsilon'(f,t) - j\epsilon''(f,t) \tag{3.21}$$

which

$$\epsilon'_r(f,t) = \epsilon_\infty + \frac{(\epsilon_s - \epsilon_\infty)\left[1 + (\lambda_s/\lambda)^{1-\alpha}\sin(\alpha\pi/2)\right]}{1 + 2(\lambda_s/\lambda)^{1-\alpha}\sin(\alpha\pi/2) + (\lambda_s/\lambda)^{2(1-\alpha)}} \tag{3.22}$$

$$\epsilon''_r(f,t) = \frac{(\epsilon_s - \epsilon_\infty)(\lambda_s/\lambda)^{1-\alpha}\cos(\alpha\pi/2)}{1 + 2(\lambda_s/\lambda)^{1-\alpha}\sin(\alpha\pi/2) + (\lambda_s/\lambda)^{2(1-\alpha)}} + \frac{\sigma\lambda}{18.8496 \times 10^{10}} \tag{3.23}$$

where ϵ_∞ is the high frequency dielectric constant, and ϵ_s is the static constant given by

$$\begin{aligned}\epsilon_s = 78.54\,[\,1 - 4.579 \times 10^{-3}(t-25) + 1.19 \times 10^{-5}(t-25)^2 \\ - 2.8 \times 10^{-8}(t-25)^3\,]\end{aligned} \tag{3.24}$$

$$\epsilon_\infty = 5.2717 + 0.0216474\,t - 0.00131198\,t^2 \tag{3.25}$$

with the exponent α given by

$$\alpha = 0.0609265 - \frac{16.8129}{t + 273} \tag{3.26}$$

and the relaxation wavelength λ_s given by

$$\lambda_s = 0.00033836 \exp\left[2513.98/(t + 273)\right] \tag{3.27}$$

The parameters in this context include the wavelength denoted as λ measured in centimeters (cm), and the temperature t expressed in degrees Celsius ($°C$).

3.4 Cloud Attenuation

For clouds or fog comprising predominantly small droplets, typically less than 0.01 cm in size, the Rayleigh approximation holds true for frequencies up to 200 GHz. The specific attenuation within such a cloud or fog can be expressed as a combination of equations 3.7 and 3.11 [55, 71]:

$$\gamma_c = \frac{0.819\,f}{\epsilon''(1 + \eta^2)} M \tag{3.28}$$

Here, η and ϵ'' are derived from equations 3.13 and 3.14, respectively.

Two pivotal parameters governing cloud-specific attenuation are the temperature (T in Kelvin $[K]$) and liquid water content (M in grams per cubic meter $[g/m^3]$) in the medium. These parameters are readily available from Numerical Weather Prediction (NWP) models, as indicated in Table 2.1. Figure 3.2 provides a visual representation of the combined effects of temperature and liquid water content on cloud-specific attenuation. These relationships are crucial for accurately predicting and mitigating attenuation effects in cloud or fog conditions.

3.5 Gaseous Attenuation

The attenuation of electromagnetic waves caused by atmospheric gases—primarily oxygen and water vapor—is a significant factor in radio wave propagation, particularly at frequencies up to 1000 GHz. Accurate estimation of this *specific attenuation* can be performed under varying atmospheric conditions, including temperature, humidity, and pressure.

The total attenuation is calculated by summing the individual resonance absorption lines of oxygen and water vapor. Additional effects are also included to improve accuracy:

- The **non-resonant Debye absorption** spectrum of oxygen, significant below 10 GHz,
- **Pressure-induced attenuation by nitrogen**, particularly relevant above 100 GHz,

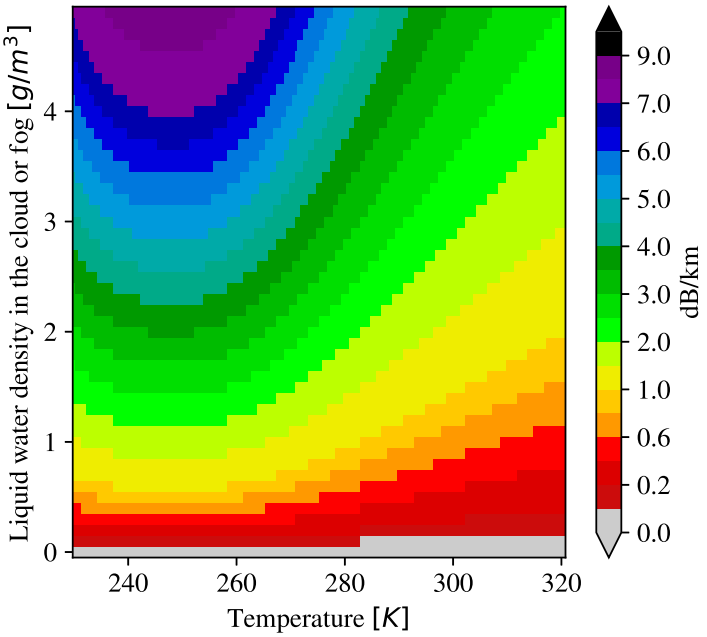


Figure 3.2: Cloud specific attenuation at frequency 39.402 GHz.

- A **wet continuum component**, which accounts for experimentally observed excess absorption by water vapor not explained by resonance lines alone [54].

To compute gaseous attenuation, two methods are available: the `Exact` solution and the `Approximation` solution. These are described in detail in Sections 3.5.1 and 3.5.2, respectively.

Figure 3.3 compares the specific attenuation of oxygen and water vapor over the 1–1000 GHz frequency range for both methods. The results show that:

- For frequencies below 400 GHz, the difference between the two methods is minimal,
- In the case of oxygen attenuation, both methods remain nearly identical even up to 1000 GHz,
- The computational performance (runtime) is effectively the same for both methods.

Given the negligible differences in output and performance, the `Exact` solution is recommended for all use cases to ensure maximum precision without any computational cost penalty.

3.5.1 Exact Solution

The computation of specific gaseous attenuation begins with Equation 3.7, which allows for the separation of refractivity contributions from dry air and

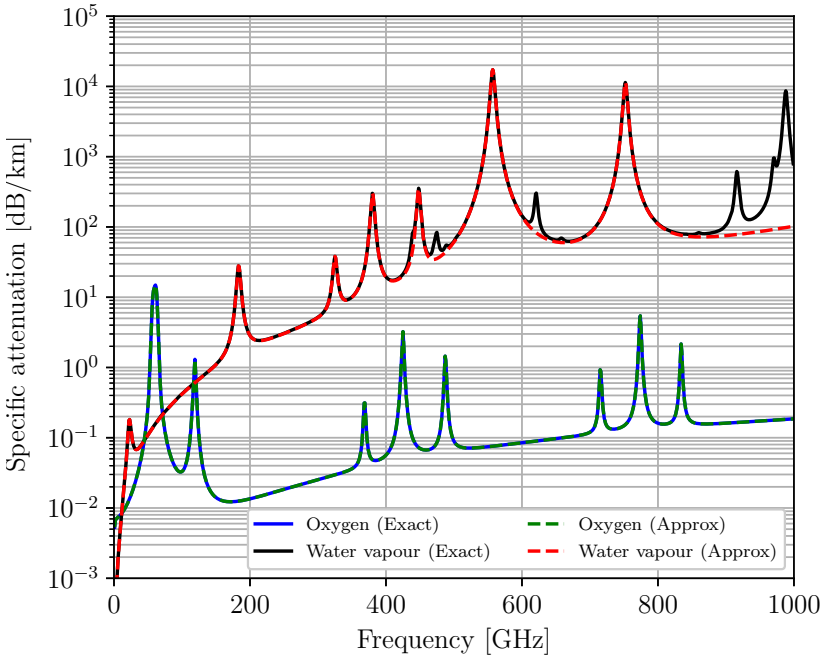


Figure 3.3: Specific attenuation due to atmospheric gases at T=288 K, P=1013.15 hPa, and $\rho_{vap} = 7.5\, g/m^3$ for `exact` and `approximation` solutions.

water vapor:

$$\gamma_{gas} = \gamma_o + \gamma_w = 0.182\, f\, \left(N''_{oxygen}(f) + N''_{water\,Vapour}(f)\right) \tag{3.29}$$

Here, γ_o and γ_w represent specific attenuation ([dB/km]) attributed to dry air (including oxygen, pressure-induced nitrogen, and non-resonant Debye attenuation) and water vapor, respectively. The variable f denotes the frequency (GHz).

The imaginary parts of the frequency-dependent complex refractivity for both oxygen and water vapor are expressed according to [54].

$$N''_{oxygen}(f) = \sum_{i(oxygen)} S_i F_i + N''_D(f) \tag{3.30}$$

$$N''_{Water\,Vapour}(f) = \sum_{i(Water\,Vapour)} S_i F_i \tag{3.31}$$

S_i represents the strength of the i^{th} oxygen or water vapor line, while F_i denotes the line shape factor for either oxygen or water vapor. The summations encompass all lines specified in Tables 3.1 and 3.2.

The line strength is given by:

$$S_i = \begin{cases} a_1 \times 10^{-7}\, p\, \theta^3 \quad \exp\left[a_2(1-\theta)\right] & \text{for oxygen} \\ b_1 \times 10^{-1}\, e\, \theta^{3.5} \exp\left[b_2(1-\theta)\right] & \text{for water vapour} \end{cases} \tag{3.32}$$

Table 3.1: Spectroscopic data for oxygen attenuation

f_0	a_1	a_2	a_3	a_4	a_5	a_6
50.474214	0.975	9.651	6.690	0.0	2.566	6.850
50.987745	2.529	8.653	7.170	0.0	2.246	6.800
51.503360	6.193	7.709	7.640	0.0	1.947	6.729
52.021429	14.320	6.819	8.110	0.0	1.667	6.640
52.542418	31.240	5.983	8.580	0.0	1.388	6.526
53.066934	64.290	5.201	9.060	0.0	1.349	6.206
53.595775	124.600	4.474	9.550	0.0	2.227	5.085
54.130025	227.300	3.800	9.960	0.0	3.170	3.750
54.671180	389.700	3.182	10.370	0.0	3.558	2.654
55.221384	627.100	2.618	10.890	0.0	2.560	2.952
55.783815	945.300	2.109	11.340	0.0	–1.172	6.135
56.264774	543.400	0.014	17.030	0.0	3.525	–0.978
56.363399	1331.800	1.654	11.890	0.0	–2.378	6.547
56.968211	1746.600	1.255	12.230	0.0	–3.545	6.451
57.612486	2120.100	0.910	12.620	0.0	–5.416	6.056
58.323877	2363.700	0.621	12.950	0.0	–1.932	0.436
58.446588	1442.100	0.083	14.910	0.0	6.768	–1.273
59.164204	2379.900	0.387	13.530	0.0	–6.561	2.309
59.590983	2090.700	0.207	14.080	0.0	6.957	–0.776
60.306056	2103.400	0.207	14.150	0.0	–6.395	0.699
60.434778	2438.000	0.386	13.390	0.0	6.342	–2.825
61.150562	2479.500	0.621	12.920	0.0	1.014	–0.584
61.800158	2275.900	0.910	12.630	0.0	5.014	–6.619
62.411220	1915.400	1.255	12.170	0.0	3.029	–6.759
62.486253	1503.000	0.083	15.130	0.0	–4.499	0.844
62.997984	1490.200	1.654	11.740	0.0	1.856	–6.675
63.568526	1078.000	2.108	11.340	0.0	0.658	–6.139
64.127775	728.700	2.617	10.880	0.0	–3.036	–2.895
64.678910	461.300	3.181	10.380	0.0	–3.968	–2.590
65.224078	274.000	3.800	9.960	0.0	–3.528	–3.680
65.764779	153.000	4.473	9.550	0.0	–2.548	–5.002
66.302096	80.400	5.200	9.060	0.0	–1.660	–6.091
66.836834	39.800	5.982	8.580	0.0	–1.680	–6.393
67.369601	18.560	6.818	8.110	0.0	–1.956	–6.475
67.900868	8.172	7.708	7.640	0.0	–2.216	–6.545
68.431006	3.397	8.652	7.170	0.0	–2.492	–6.600
68.960312	1.334	9.650	6.690	0.0	–2.773	–6.650
118.750334	940.300	0.010	16.640	0.0	–0.439	0.079
368.498246	67.400	0.048	16.400	0.0	0.000	0.000
424.763020	637.700	0.044	16.400	0.0	0.000	0.000
487.249273	237.400	0.049	16.000	0.0	0.000	0.000
715.392902	98.100	0.145	16.000	0.0	0.000	0.000
773.839490	572.300	0.141	16.200	0.0	0.000	0.000
834.145546	183.100	0.145	14.700	0.0	0.000	0.000

Table 3.2: Spectroscopic data for water-vapour attenuation. The colored rows which are marked with asterisk too, are used in approximation solution at section 3.5.2

f_0	b_1	b_2	b_3	b_4	b_5	b_6
*22.235080	0.1079	2.144	26.38	0.76	5.087	1.00
67.803960	0.0011	8.732	28.58	0.69	4.930	0.82
119.995940	0.0007	8.353	29.48	0.70	4.780	0.79
*183.310087	2.273	0.668	29.06	0.77	5.022	0.85
*321.225630	0.0470	6.179	24.04	0.67	4.398	0.54
*325.152888	1.514	1.541	28.23	0.64	4.893	0.74
336.227764	0.0010	9.825	26.93	0.69	4.740	0.61
*380.197353	11.67	1.048	28.11	0.54	5.063	0.89
390.134508	0.0045	7.347	21.52	0.63	4.810	0.55
437.346667	0.0632	5.048	18.45	0.60	4.230	0.48
439.150807	0.9098	3.595	20.07	0.63	4.483	0.52
443.018343	0.1920	5.048	15.55	0.60	5.083	0.50
*448.001085	10.41	1.405	25.64	0.66	5.028	0.67
470.888999	0.3254	3.597	21.34	0.66	4.506	0.65
474.689092	1.260	2.379	23.20	0.65	4.804	0.64
488.490108	0.2529	2.852	25.86	0.69	5.201	0.72
503.568532	0.0372	6.731	16.12	0.61	3.980	0.43
504.482692	0.0124	6.731	16.12	0.61	4.010	0.45
547.676440	0.9785	0.158	26.00	0.70	4.500	1.00
552.020960	0.1840	0.158	26.00	0.70	4.500	1.00
*556.935985	497.0	0.159	30.86	0.69	4.552	1.00
620.700807	5.015	2.391	24.38	0.71	4.856	0.68
645.766085	0.0067	8.633	18.00	0.60	4.000	0.50
658.005280	0.2732	7.816	32.10	0.69	4.140	1.00
*752.033113	243.4	0.396	30.86	0.68	4.352	0.84
841.051732	0.0134	8.177	15.90	0.33	5.760	0.45
859.965698	0.1325	8.055	30.60	0.68	4.090	0.84
899.303175	0.0547	7.914	29.85	0.68	4.530	0.90
902.611085	0.0386	8.429	28.65	0.70	5.100	0.95
906.205957	0.1836	5.110	24.08	0.70	4.700	0.53
916.171582	8.400	1.441	26.73	0.70	5.150	0.78
923.112692	0.0079	10.293	29.00	0.70	5.000	0.80
970.315022	9.009	1.919	25.50	0.64	4.940	0.67
987.926764	134.6	0.257	29.85	0.68	4.550	0.90
*1 780.000000	17506.	0.952	196.3	2.00	24.15	5.00

where p is the dry air pressure [hPa], e is the water vapour partial pressure [hPa], $\theta = 300/T$ and T is the temperature in [K]. The water-vapour partial pressure, e, at an altitude may be obtained from the water-vapour density, ρ

and the temperature, T, at that altitude using the expression:

$$e = \frac{\rho T}{216.7} \tag{3.33}$$

The line-shape factor is given by:

$$F_i = \frac{f}{f_i}\left[\frac{\Delta f - \delta\,(f_i - f)}{(f_i - f)^2 + \Delta f^2} + \frac{\Delta f - \delta\,(f_i + f)}{(f_i + f)^2 + \Delta f^2}\right] \tag{3.34}$$

where f_i is the oxygen or water vapour line frequency and Δf is the width of the line:

$$\Delta f = \begin{cases} a_3 \times 10^{-4}\,\left(p\,\theta^{(0.8-a_4)} + 1.1e^{\theta}\right) & \text{for oxygen} \\ b_3 \times 10^{-4}\,\left(p\,\theta^{b_4} + b_5\,e\,\theta^{b_6}\right) & \text{for water vapour} \end{cases} \tag{3.35}$$

The line width Δf is adjusted to accommodate both Zeeman splitting in oxygen lines and Doppler broadening in water vapor lines:

$$\Delta f = \begin{cases} \sqrt{\Delta f^2 + 2.25 \times 10^{-6}} & \text{for oxygen} \\ 0.535\Delta f + \sqrt{0.217\Delta f^2 + \frac{2.1316\times 10^{-12} f_i^2}{\theta}} & \text{for water vapour} \end{cases} \tag{3.36}$$

δ serves as a correction factor that arises from interference effects in oxygen lines:

$$\delta = \begin{cases} (a_5 + a_6\theta) \times 10^{-4}\,(p + e)\,\theta^{0.8} & \text{for oxygen} \\ 0 & \text{for water vapour} \end{cases} \tag{3.37}$$

The dry air continuum originates from the non-resonant Debye spectrum of oxygen below 10 GHz and pressure-induced nitrogen attenuation above 100 GHz.

$$N_D''(f) = f\,p\,\theta^2\left[\frac{6.14 \times 10^{-5}}{d\,[1+(\,\frac{f}{d}\,)^2]} + \frac{1.4 \times 10^{-12}\,p\,\theta^{1.5}}{1 + 1.9 \times 10^{-5} f^{1.5}}\right] \tag{3.38}$$

where d is the width parameter for the Debye spectrum:

$$d = 5.6 \times 10^{-4}\,(p + e)\;\theta^{0.8} \tag{3.39}$$

3.5.2 Approximate Solution

The specific attenuation resulting from dry air and water vapor, spanning from sea level to an altitude of 10 km, can be estimated through simplified algorithms. These algorithms rely on the specific attenuation values obtained from the line-by-line calculation for oxygen and water vapor, along with the effective heights for oxygen and water vapor. These approximations demonstrate good agreement with the detailed line-by-line calculation. However, for altitudes surpassing 10 km or scenarios demanding heightened accuracy, the line-by-line calculation is recommended.

It's worth noting that the approximation solution provided by Equation 3.36 is no longer utilized for both oxygen and water vapor specific attenuation. Additionally, the summation for water vapor is performed over a subset of 9 water vapor lines from Table 3.2, denoted with an asterisk.

3.6 Rain Attenuation

Rain, as a meteorological phenomenon, originates from convective clouds forming in saturated air masses. Its vertical structure, particularly with respect to the 0°C isotherm, typically consists of two distinct layers extending up to 6 km above the ground. The lower layer contains liquid rain droplets, while the upper layer is dominated by frozen particles. Occasionally, this upper region includes supercooled water droplets, especially in the presence of strong updrafts that prevent immediate freezing.

To characterize the influence of rain on electromagnetic wave propagation, the point rainfall rate, denoted as R, is a widely used parameter. This rate provides insight into the dynamic behavior of rain and is associated with the following quantities:

- The percentage of time, P_R, that a given rainfall rate occurs over an average year,
- The effective proportion of the path length affected by rain, represented by L_R/L,
- The concentration of suspended liquid water, expressed as $W_R = m_R \cdot R$, in grams per cubic meter (g/m^3), where m_R is a proportionality factor.

Typical rainfall characteristics in mid-latitude regions can be classified based on these parameters. Table 3.3 provides an example of this classification for a horizontal propagation path of $L = 10$ km [68].

Table 3.3: Rain classification based on characteristic parameters (horizontal path, $L = 10$ km) [68]

	Drizzle	Steady	Heavy	Downpour	Cloudburst
R	1	5	20	100	200 mm/h
P_R	2	0.5	0.07	0.001	0.0001 %/year
L_R/L	1	1	0.7	0.35	0.2
m_R	0.1	0.07	0.05	0.04	0.04

This classification system highlights the differences between rain types. For instance, steady, widespread rain typically consists of smaller droplets (diameter ≤ 1 mm) that remain airborne for longer durations. In contrast, intense rain showers are usually more localized and are characterized by larger droplets (diameter ≤ 5 mm), which fall more rapidly and occur less frequently. The factor m_R provides insight into the raindrop size distribution, which is directly tied to the nature of the rain event.

To model rain attenuation, two primary approaches are commonly found in the literature:

1. **Mie Scattering-Based Model** — discussed in Section 3.6.1, this model is rooted in Mie theory and uses parameters such as the liquid water content and temperature to compute attenuation.

2. **Rain Rate Power-Law Model** — introduced in Section 3.6.4, this approach relates the rain rate R to the specific attenuation through an empirical power-law relationship.

These models offer complementary perspectives on the interaction between rainfall and electromagnetic waves. Understanding their underlying principles is essential for accurately predicting signal degradation in wireless communication systems, especially at microwave and millimeter-wave frequencies.

3.6.1 Specific Rain Attenuation Using Mie Scattering

Mie theory offers a comprehensive framework for analyzing how electromagnetic waves scatter when they encounter homogeneous spherical particles. This theory, rooted in frequency-domain macroscopic electromagnetics, is fundamental in modern physics for understanding wave-particle interactions in the atmosphere.

Mie scattering—sometimes referred to as scattering by non-molecular airborne particles—typically occurs in the lower atmosphere, around 4.5 km above the Earth's surface. At this altitude, the atmosphere contains a large number of spherical particles, such as rain droplets or cloud droplets, whose sizes are often comparable to the wavelength of the incident electromagnetic waves.

To apply Mie theory effectively, several input parameters are required, most notably the complex dielectric constants of both the scattering particles and their surrounding medium. These parameters determine how much of the incident wave is scattered or absorbed.

This theory is especially useful for characterizing atmospheric attenuation due to particles whose dimensions fall within the range of the operating electromagnetic wavelength—conditions common in rain, fog, and cloud environments. Understanding these interactions is critical for accurately modeling signal degradation in satellite and terrestrial communication systems, remote sensing applications, and meteorological radar systems.

Within the Mie framework, the **specific attenuation**, denoted by γ_{ext} and measured in $dB\,\text{km}^{-1}$, quantifies the loss of signal strength per unit distance due to scattering and absorption. It is defined as [47, 72–74]:

$$\gamma_{ext}(z) = \left(\frac{20}{\ln 10} \times 10^3\right) \frac{1}{2} \int_0^\infty \sigma_{ext}(D) N(D) dD \tag{3.40}$$

Here, $N(D)$ represents the raindrop size distribution as defined in Eq. 3.63 in section 3.6.3, and σ_{ext} represents the equivalent extinction cross-section of these raindrops. According to [73], σ_{ext} is expressed as:

$$\sigma_{ext} = \frac{\lambda^2}{2\pi} \sum_{\nu=1}^{\infty} (2\nu + 1)\, \Re\{a_\nu + b_\nu\} \tag{3.41}$$

where λ is wavelength, a_ν and b_ν are the Mie scattering coefficients of order ν, and $\Re$ denotes the real part of the complex coefficients. The extinction

efficiency quantifies the total attenuation due to absorption and scattering of the incident electromagnetic wave by spherical water droplets.

$$a_\nu = \frac{\psi'_\nu(y)\psi_\nu(x) - m\psi_\nu(y)\psi'_\nu(x)}{\psi'_\nu(y)\zeta_\nu(x) - m\psi_\nu(y)\zeta'_\nu(x)} \tag{3.42}$$

$$b_\nu = \frac{m\psi'_\nu(y)\psi_\nu(x) - \psi_\nu(y)\psi'_\nu(x)}{m\psi'_\nu(y)\zeta_\nu(x) - \psi_\nu(y)\zeta'_\nu(x)} \tag{3.43}$$

where $n = \sqrt{\epsilon_r \mu_r}$ is the refractive index of liquid water and the variable $x = kr_d$, $y = nkr_d = nx$ are defined in function of the wavenumber k and the drop radius r_d, and where the Ricatti-Bessel functions ψ_ν, ζ_ν are

$$\psi_\nu(z) = zj_\nu(z) \tag{3.44}$$

$$\chi_\nu(z) = -zy_\nu(z) \tag{3.45}$$

$$\zeta_\nu(z) = zh_\nu^{(2)}(z) = \psi_\nu(z) + j\chi_\nu(z) \tag{3.46}$$

in function of the better known spherical Bessel functions j_ν and y_ν of the first and second kind, and of the spherical Hankel function $h^{(2)}$ of the second kind. The spherical Bessel functions j_n and y_n are related to the ordinary Bessel functions J_n and Y_n :

$$j_n(z) = \sqrt{\frac{\pi}{2z}} J_{n+\frac{1}{2}}(z) \tag{3.47}$$

$$y_n(z) = \sqrt{\frac{\pi}{2z}} Y_{n+\frac{1}{2}}(z) \tag{3.48}$$

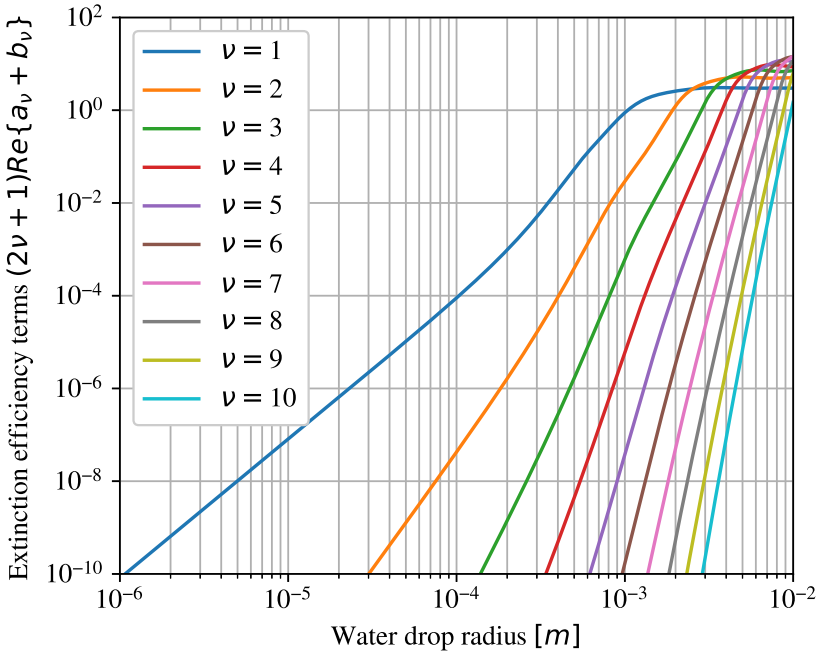
For numerical reasons, it is still necessary to select a value D_{max} to bound the integral in Equation 3.40, and to limit the number of terms used for the sum in Equation 3.41. The strategy is the one found within [41]. The number of terms ν_{max} follows the heuristic of Jeannin et al.

$$\nu_{max} = \text{round}\left(2 + x_m ax + 4x_m ax^{1/3}\right) \tag{3.49}$$

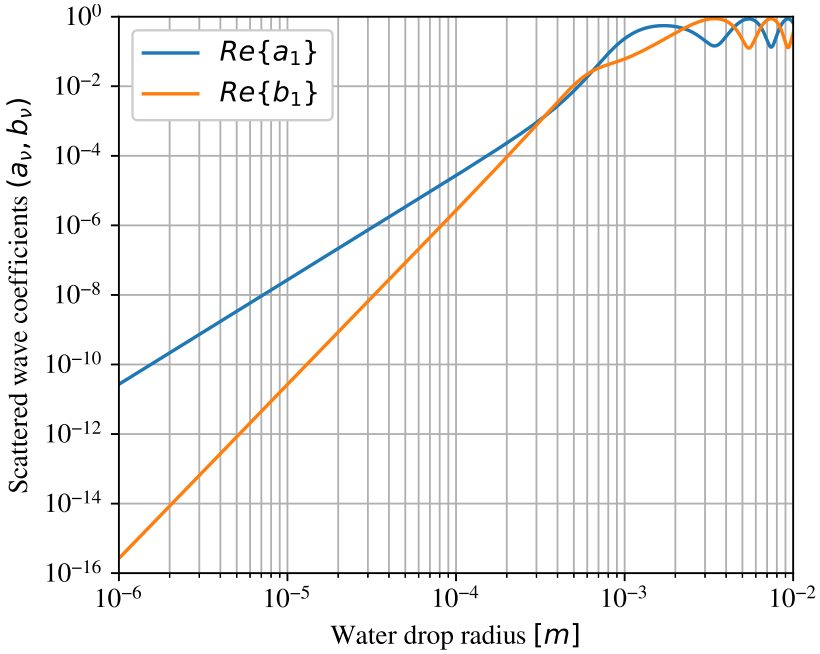
with $x_{max} = kD_{max}/2$.

Figure 3.4a illustrates the contributions of the terms in function of ν at $f = 40\,GHz$ and $T = 298\,K$, and based on them 3.41 is expected to converge quite well for ≈ 5 terms, though $\nu_{max} = 8$ is this case. Hence 3.49 is rather safe. Notably representing in Figure 3.4b, as the droplet radius increases, the extinction efficiency shows oscillatory behavior due to resonant scattering effects, which are characteristic of Mie theory. This behavior is particularly relevant for predicting rain-induced attenuation in high-frequency communication links, as variations in raindrop size distribution directly impact signal degradation. These coefficients, a_1 and b_1 , describe the amplitude of the scattered wave components in perpendicular and parallel polarization states, respectively.

As shown in the plot, both $\Re\{a_1\}$ and $\Re\{b_1\}$ exhibit strong dependency on the droplet size. For small radii, the coefficients follow Rayleigh-like behavior, where scattering is proportional to the sixth power of the radius. As the droplet radius increases, higher-order resonance effects emerge, leading to oscillatory



(a) Extinction efficiency terms



(b) Scattered wave coefficients a_1 and b_1

Figure 3.4: Evolution of some Mie scattering parameters as a function of the radius of the water drop at 298 K and 40 GHz

variations in the real part of the coefficients. These fluctuations play a crucial role in understanding differential attenuation in polarized wave propagation and the impact of droplet distributions on signal coherence.

Performing Mie scattering computations for each individual dataset can be computationally intensive. Instead, the approach proposed in [41] is adopted. The strategy involves pre-computing results for arrays in (T, M_{rain}), such as a grid with $230 \leq T \leq 320$ $[K]$ and a resolution of 0.5 K, and $0 \leq M_{\text{rain}} \leq 15$ $[g/m^3]$ with a resolution of 0.01 $[g/m^3]$. Subsequently, γ_{rain} is estimated at any (T, M_{rain}) using bilinear interpolation. This approach significantly reduces computation time by providing pre-computed values for a wide range of environmental conditions.

3.6.2 Specific Rain Attenuation Using Rayleigh Scattering

As outlined in Section 3.6.1, the process of calculating rain-specific attenuation using full Mie scattering theory is computationally expensive. To reduce complexity, the Rayleigh scattering approximation is often employed.

Rayleigh theory assumes that the particle size is much smaller than the wavelength. This approximation is valid when the particle radius is at least an order of magnitude smaller than the wavelength of the incident wave. In practice, this condition applies to cloud droplets, which typically have radii of the order of 10 μm, but not to raindrops, which are much larger (radii of hundreds of μm up to a few mm).

Therefore, Rayleigh scattering is only an effective approximation for cloud events. For realistic rain events at microwave frequencies, the drop sizes exceed the Rayleigh validity range, and full Mie scattering theory is required to accurately compute specific attenuation.

Examining Figure 3.4a, it becomes evident that for raindrop radii below 10 μm, the weight term of $\nu = 1$ dominates over other terms. Furthermore, Figure 3.4b illustrates that for the $\nu = 1$ term, the a_1 coefficient is dominant over the b_1 coefficient. Consequently, a highly accurate approximation reduces the extinction cross-section in Equation 3.40 to the following equation:

$$\sigma_{ext} \approx \frac{3\lambda^2}{2\pi}\text{Re}\{a_1\} = \frac{6}{x^2}\text{Re}\{a_1\} \times \pi r_d^2 \tag{3.50}$$

and this expression can be simplified further by working more on a_1.

In order to simplify 3.42, it is useful to study the Ricatti-Bessel functions by using the Rayleigh formulas for the spherical Bessel functions

$$j_\nu(z) = \left(-\frac{d}{dz}\right)^\nu \left[\frac{\sin(z)}{z}\right] \tag{3.51}$$

$$y_\nu(z) = -\left(-\frac{d}{dz}\right)^\nu \left[\frac{\cos(z)}{z}\right] \tag{3.52}$$

Then, if $z \to 0$, it can be found that

$$\psi_1(z) \approx \frac{1}{3}z^2 \qquad \psi_1'(z) \approx \frac{2}{3}z \tag{3.53}$$

$$\chi_1(z) \approx \frac{1}{z} \qquad \chi_1'(z) \approx \frac{-1}{z^2} \tag{3.54}$$

Certainly, the variable x in Equation 3.42 is considerably small at microwave frequencies, given that $r_d \ll \lambda$ (e.g., $\lambda = 7.5$ mm at 40 GHz). Similarly, this holds true for the variable y since for liquid water, $|m| \leq 10$ (refer to Figure 3.1).

For easier manipulations, the Equation 3.42 is rewritten as

$$a_\nu = \frac{1}{1 + j\frac{\psi_\nu'(y)\chi_\nu(x) - m\psi_\nu(y)\chi_\nu'(x)}{\psi_\nu'(y)\psi_\nu(x) - m\psi_\nu(y)\psi_\nu'(x)}} \tag{3.55}$$

replacing equations 3.53-3.54 in 3.55, we will have

$$\begin{aligned} a_1 &\approx \frac{1}{1 - j\frac{\frac{2}{3}mx\frac{1}{x} - m\frac{1}{3}(mx)^2(-\frac{1}{x^2})}{\frac{2}{3}mx\frac{1}{3}x^2 - m\frac{1}{3}(mx)^2\frac{2}{3}x}} \\ &= \frac{1}{1 + j\frac{3}{2x^3}\frac{m^2+2}{m^2-1}} \approx j\frac{2x^3}{3}\frac{m^2-1}{m^2+2} \end{aligned} \tag{3.56}$$

where the assumption that $x \ll 1$ is is re-used in the last step. Finally, a_1 is expanded to obtain its real part

$$\begin{aligned} a_1 =& j\frac{2x^3}{3}\frac{\epsilon_r - 1}{\epsilon_r + 2} = j\frac{2x^3}{3}\frac{(\epsilon_r' - 1) - j\epsilon_r''}{(\epsilon_r' + 2) - j\epsilon_r''} = \frac{2x^3}{3}\frac{\epsilon_r'' + j(\epsilon_r' - 1)}{(\epsilon_r' + 2) - j\epsilon_r''} \\ =& \frac{2x^3}{3}\frac{\epsilon_r''\left((\epsilon_r' + 2) - (\epsilon_r' - 1)\right) + j(\epsilon_r''^2 + (\epsilon_r' - 1)(\epsilon_r' + 2))}{(\epsilon_r' + 2)^2 + \epsilon_r''^2} \\ =& \frac{2x^3}{3}\frac{3\epsilon_r'' + j(\epsilon_r''^2 + (\epsilon_r' - 1)(\epsilon_r' + 2))}{(\epsilon_r' + 2)^2 + \epsilon_r''^2} \end{aligned} \tag{3.57}$$

and after some re-arrangements in 3.50

$$\sigma_{ext} \approx 24\pi^2\frac{r_d^3}{\lambda}\frac{\epsilon_r''}{(\epsilon_r' + 2)^2 + \epsilon_r''^2} = 24\pi^2\frac{r_d^3}{\lambda}\frac{1}{\epsilon_r''\left(\left(\frac{\epsilon_r' + 2}{\epsilon_r''}\right)^2 + 1\right)} \tag{3.58}$$

Presently, as the extinction cross-section relies solely on the drop dimension represented by r_d^3, the integration in 3.40 is directly proportional to the third moment of the drop size distribution, specifically the mass of drops per unit volume as denoted in 3.61. Consequently, if this mass is known, there is no requirement to possess intricate details regarding the distribution.

3.6.3 Rain Drop-Size Distribution

The raindrop-size distribution $[m^{-3}m^{-1}]$ characterizes the distribution of raindrops based on their diameter (D) within a unit volume. Typically, the drop size distribution is expressed as a truncated gamma function, covering diameters from zero to the maximum size attainable for rain droplets [72] :

$$N(D) = N_{R,0}D^\mu e^{-\Lambda D} \tag{3.59}$$

where μ is a fixed value and $(N_{R,0}, \Lambda)$ vary with atmospheric conditions.

The mass of rainwater $M, [kg/m^3]$ per unit volume can be computed as a function of Λ using Eq. 3.59. The total mass of raindrops within a unit volume is the summation over all drops with varying sizes:

$$M = \frac{\sum_i m_i}{V} = \frac{\sum_D N(D) m_D}{1m^3} \tag{3.60}$$

where m_i represents the mass of the i^{th} droplet, and m_D is the mass of a droplet with a diameter of D. Replacing the summation with an integral and using $m_D = \rho_w \times V_w(D)$, where ρ_w is the density of water and $V_w(D) = \frac{4}{3}\pi(D/2)^3$ is the volume of a droplet with diameter D, Equation 3.60 transforms into:

$$M = \rho_w \frac{\pi}{6} \int_0^\infty N(D) D^3 dD \tag{3.61}$$

By substituting Eq. 3.59 into Eq. 3.61, the parameter Λ can be determined, as follows:

$$\Lambda = \left(\frac{\pi}{6} \frac{\rho_w}{M} N_{R,0} \Gamma(\mu + 4) \right)^{\frac{1}{\mu+4}} \tag{3.62}$$

One of the pioneering studies on raindrop size distribution was conducted by Marshall and Palmer at McGill University in Montréal in 1948 [75]. For stratiform rain, they adopted the value $\mu = 0$ and proposed an exponential drop size distribution, as follows:

$$N(D) = N_{R,0} e^{-\Lambda D} \tag{3.63}$$

Here, $N_{R,0} = 0.08, \mathrm{cm}^{-3}\mathrm{cm}^{-1}$ is considered suitable for rainfall of any intensity. The variable M provides comprehensive information about the rain (or cloud) and is extracted from WRF output netCDF files, as detailed in section 2.5.4.

The calculation of rainfall rates can be expressed through the drop size distribution using the following equation:

$$R_{rain} = 3600 \rho_w \frac{\pi}{6} \int_0^\infty N(D) D^3 \nu(D) dD \tag{3.64}$$

where $\nu(D)\,[m/s]$ denotes the fall velocity of a raindrop with diameter D, defined by [76] as:

$$\nu^2 = \frac{4\,g\,D}{3} \frac{\rho_w - \rho}{\rho\,c} \tag{3.65}$$

Here, $g\ [m/s^2]$ represents the acceleration due to gravity, ρ_w is the density of the raindrop, ρ is the density of the surrounding fluid (air), and c is the drag coefficient. The drag coefficient, a dimensionless quantity quantifying the drag or resistance of an object in a fluid environment (such as air or water), generally depends on the body shape.

In this work, the Marshall–Palmer (MP) distribution was selected to describe the raindrop size distribution (DSD) in the Mie scattering computations. This distribution has historically been adopted in propagation studies due to its simplicity and widespread use in ITU-R recommendations.

However, it is acknowledged that the MP distribution represents an average mid-latitude rain and is not necessarily optimal for all rainfall conditions. In particular:

- For heavy convective rain, the MP model tends to underestimate the occurrence of large drops.
- For light or stratiform rain, the MP distribution may overestimate the number of medium-sized drops. Modified gamma distributions or double-moment microphysics schemes (e.g., Thompson or Morrison schemes within WRF) are generally more representative in such cases.

The impact of choosing a different DSD model is non-negligible for Mie attenuation calculations, particularly at higher frequencies (e.g., Q/V-band). Since specific attenuation is a function of both drop size and frequency-dependent scattering cross-section, distributions with more large drops (as in convective events) will increase the attenuation tail in the CCDF, whereas narrower distributions (light rain) may reduce it.

Several studies confirm this sensitivity. For example, in [44] it is demonstrated that the choice of microphysics/DSD scheme in WRF significantly affects rain attenuation predictions at 20 GHz and 39.4 GHz. In their results, the NSSL two-moment scheme provided better agreement with beacon measurements compared to MP-based models, especially for high-frequency bands.

In summary, the Marshall–Palmer model was chosen here primarily for consistency with ITU-R recommendations and computational tractability. Nevertheless, alternative distributions could yield more accurate attenuation estimates for specific rainfall regimes. This remains an important avenue for future work, particularly in improving the representation of heavy convective rainfall.

3.6.4 Specific Rain Attenuation from the Rain Rate

For modeling the impact of rainfall rate on a propagation link, the starting point is often Equation 3.7. A crucial component in this equation is $N''(f)$ for the rain. The proposed model for $N''(f)$ in the literature is a power-law relation, as stated in [56, 68]:

$$N''_R(f) = c\, R^{\alpha} \tag{3.66}$$

Here, both coefficients c and α are frequency-dependent. The combination of Equations 3.7 and 3.66 is summarized in [56]:

$$\gamma_R = \kappa\, R^{\alpha} \tag{3.67}$$

The coefficients κ and α are not theoretically determined and are typically estimated through data fitting based on experimental measurements. This model incorporates the non-sphericity of raindrops and introduces a dependence on the polarization direction. Considering the polarizations $P \in H, , V$, where H denotes horizontal and V vertical, the power-law terms are:

$$\log_{10} \kappa^P = \sum_{j=1}^{4} a_{j,\kappa}^P \exp\left(- \left(\frac{\log_{10} f - b_{j,\kappa}^P}{c_{j,\kappa}^P} \right)^2 \right) + m_\kappa^P \log_{10} f + c_\kappa^P \tag{3.68}$$

$$\alpha^P = \sum_{j=1}^{5} a_{j,\alpha}^P \exp\left(-\left(\frac{\log_{10} f - b_{j,\alpha}^P}{c_{j,\alpha}^P}\right)^2\right) + m_\alpha^P \log_{10} f + c_\alpha^P \tag{3.69}$$

for which all the necessary coefficients are given in Tables 3.4-3.7 for κ^H, κ^V, α^H, and α^V respectively.

Table 3.4: Coefficients to compute the power law term κ^H

j	$a_{j,\kappa}^H$	$b_{j,\kappa}^H$	$c_{j,\kappa}^H$	m_κ^H	c_κ^H
1	–5.33980	–0.10008	1.13098	–0.18961	0.71147
2	–0.35351	1.26970	0.45400		
3	–0.23789	0.86036	0.15354		
4	–0.94158	0.64552	0.16817		

Table 3.5: Coefficients to compute the power law term κ^V

j	$a_{j,\kappa}^H$	$b_{j,\kappa}^H$	$c_{j,\kappa}^H$	m_κ^H	c_κ^H
1	–3.80595	0.56934	0.81061	–0.16398	0.63297
2	–3.44965	–0.22911	0.51059		
3	–0.39902	0.73042	0.11899		
4	0.50167	1.07319	0.27195		

Table 3.6: Coefficients to compute the power law term α^H

j	$a_{j,\alpha}^H$	$b_{j,\alpha}^H$	$c_{j,\alpha}^H$	m_α^H	c_α^H
1	–0.14318	1.82442	–0.55187	0.67849	–1.95537
2	0.29591	0.77564	0.19822		
3	0.32177	0.63773	0.13164		
4	–5.37610	–0.96230	1.47828		
5	16.1721	–3.29980	3.43990		

For both linear and circular polarizations, as well as for all path geometries, the coefficients in equation 3.67 can be determined from the values provided by equations 3.68 and 3.69 using the following equations:

$$\kappa = \left[\kappa^H + \kappa^V + \left(\kappa^H - \kappa^V\right)\cos^2\theta\cos 2\tau\right]/2 \tag{3.70}$$

$$\alpha = \left[\kappa^H\alpha^H + \kappa^V\alpha^V + \left(\kappa^H\alpha^H - \kappa^V\alpha^V\right)\cos^2\theta\cos 2\tau\right]/2\kappa \tag{3.71}$$

In the equation above, θ represents the path elevation angle, and τ is the polarization tilt angle relative to the horizontal. In the context of LEO links,

Table 3.7: Coefficients to compute the power law term α^V

j	$a^H_{j,\alpha}$	$b^H_{j,\alpha}$	$c^H_{j,\alpha}$	m^H_α	c^H_α
1	–0.07771	2.33840	–0.76284	–0.053739	0.83433
2	0.56727	0.95545	0.54039		
3	–0.20238	1.14520	0.26809		
4	–48.2991	0.791669	0.116226		
5	48.5833	0.791459	0.116479		

a common choice is $\tau = 45°$ for circular polarization, providing a preferred configuration. For linear polarization, if the specific value of τ is unknown, $\tau = 45°$ is often used as a suitable compromise. Notably, this angle selection is beneficial for quick reference and practical implementation.

Figure 3.5 illustrates the frequency dependence of the specific attenuation coefficients κ^H, κ^V, α^H, and α^V.

- κ^H and κ^V (Attenuation Coefficients): These parameters quantify the proportionality factor of rain attenuation, directly affecting signal absorption by raindrops. As frequency increases, both κ^H and κ^V exhibit a rising trend due to increased scattering and absorption effects, particularly beyond 10 GHz where resonance phenomena become significant.

- α^H and α^V (Exponent Factors): In the frequency range of < 30 GHz, a noticeable difference exists between α^H and α^V. This difference is attributed to polarization-dependent scattering effects, which cause variations in how attenuation scales with rainfall intensity. However, at frequencies above 30 GHz, this deviation between horizontal and vertical polarization reduces, indicating that the frequency dependence of attenuation becomes more uniform for both polarizations. This behavior suggests that at higher frequencies, the impact of raindrop shape and orientation on polarization-dependent attenuation diminishes, leading to more similar values of α for both polarizations.

The observed differences between horizontal and vertical polarizations in both κ and α highlight the anisotropic nature of rain attenuation, which is crucial for dual-polarization radar applications and communication link design. Polarization effects must be accounted for in dual-polarized satellite and terrestrial links, particularly in the 1–30 GHz range, where differences between α^H and α^V are more pronounced.

To comprehensively evaluate rain attenuation across all directions along azimuth, elevation, and slant paths, it is essential to define rain rate in a 3D domain. Since surface measurements most commonly provide rain rate data, a pragmatic approach is to assume that the ground-level value of R_{rain} remains constant in altitude up to a specific level. A rough approximation considers the rain height to be the 0°C isotherm, although this assumption is not strictly accurate since liquid raindrops can persist above the freezing height. If no additional correction for rain height is applied, as outlined in

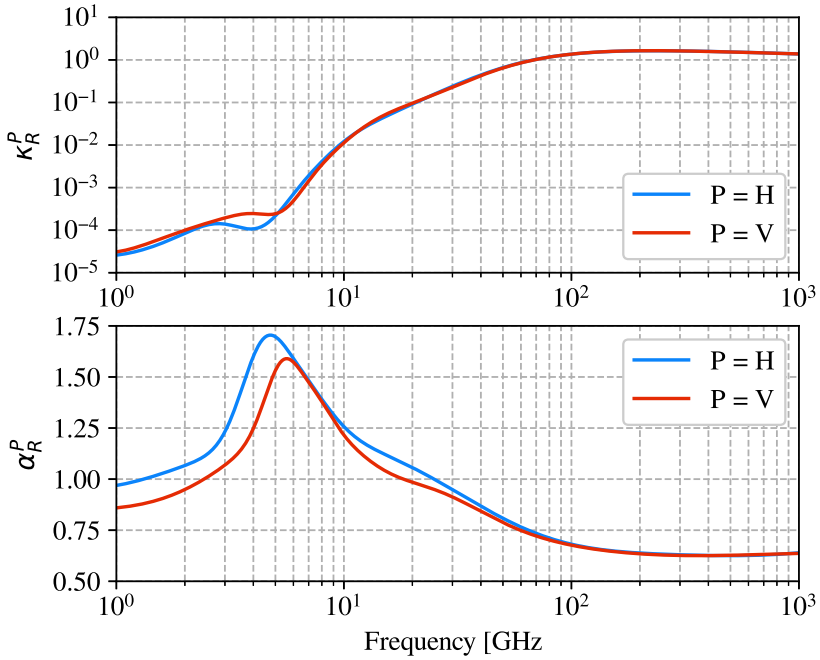


Figure 3.5: Specific rain attenuation power law terms κ^H, κ^V, α^H, and α^V in the frequency range from 1 to 1000 GHz

methods such as [77], there is a likelihood that slant path rain attenuation may be underestimated with this approach.

3.7 Conclusion

This chapter provides a comprehensive analysis of electromagnetic wave propagation through the atmosphere, focusing on attenuation caused by various atmospheric constituents such as gases, clouds, and precipitation. Central to this study is the complex refractive index, whose real and imaginary components respectively govern wave refraction and absorption. Understanding this dual nature is essential to accurately model and predict signal degradation.

The chapter begins by establishing the role of atmospheric gases and the refractive index in clear-sky conditions. We showed how frequency-dependent absorption by water vapor and oxygen, especially through resonance line contributions and continuum effects, leads to specific attenuation patterns that can be precisely modeled using exact or approximate methods. Given the minimal performance trade-off, the exact solution is recommended for high-fidelity applications.

Cloud and fog attenuation were explored using models based on liquid water content and temperature, with particular emphasis on the Liebe model for permittivity. This model, combined with Rayleigh scattering principles, effectively characterizes the interaction of electromagnetic waves with suspended

water droplets in the millimeter-wave spectrum.

The discussion then progress to rain attenuation, distinguishing between the effects of large and small raindrops using Mie and Rayleigh scattering theories. The Mie-based approach offered high accuracy by accounting for droplet size distribution and resonance behavior, while the Rayleigh approximation provided computational efficiency for scenarios with small droplets. Furthermore, an empirical power-law model relating rain rate to specific attenuation is introduced, including polarization-dependent parameters that highlight the anisotropic nature of rain scattering.

In summary, this chapter offers a layered understanding of how different atmospheric conditions affect electromagnetic propagation. These insights are particularly valuable for designing and optimizing satellite communication systems, weather radars, and remote sensing applications, where atmospheric attenuation must be anticipated and mitigated for reliable performance.

Chapter 4

Post-Processing of the NWP's Data

This chapter provides a comprehensive overview of the methodology employed to transform 4-D meteorological data derived from Numerical Weather Prediction (NWP) models into calculation of propagation impairments. The process of converting raw meteorological data into tropospheric attenuation for satellite communication systems involves multiple distinct steps, each crucial to the accuracy of the simulation.

The initial step involves the conversion of the geographical coordinates utilized in the Weather Research and Forecasting (WRF) model to azimuth and elevation coordinates, which are standard in describing satellite communication link parameters. Section 4.1 expounds on this transformation, presenting various common coordinate systems to ensure a comprehensive understanding.

Following this coordinate transformation, the data are utilized in propagation models that aim to assess the attenuation caused by various tropospheric constituents. Detailed explanations of these propagation models can be found in Chapter 3.

The resulting attenuation output is then subjected to interpolation within azimuth and elevation bins, facilitating the evaluation of the time series of attenuation for a satellite link. Section 4.3 elaborates on the methodology used to define the direction of the satellite over time, for various types of orbit.

Subsequently, the complementary cumulative distribution of attenuation is derived from the time series of attenuation, offering a comprehensive statistical perspective. Section 4.4 elucidates common statistical definitions that play a pivotal role in models related to propagation impairments.

In summary, this chapter provides an in-depth exploration of the intricate steps involved in transforming NWP-derived 4-D meteorological data into a simulation of propagation impairments in satellite communication systems. The combination of coordinate transformations, propagation models, and statistical analyses contributes to a thorough understanding of the atmospheric conditions affecting satellite communication links.

4.1 Geographical Coordinate Systems

The first step in mapping real-world meteorological data onto a two-dimensional surface began with the need to identify every location on Earth uniquely. Early maps, which often focused on small local or regional areas, used basic grid methods. These relied on measuring distances and directions between known points and projecting them onto a flat surface—effectively assuming that the Earth was flat.

As scientific understanding progressed and it became widely accepted that the Earth is roughly spherical, this flat-Earth approach proved insufficient. This realization led to the development of a more advanced coordinate system—based on latitude, longitude, and altitude—that could accurately describe any location on the planet. Together, these three coordinates form a comprehensive framework for representing positions on the Earth's surface.

While this geographic coordinate system works well for static, Earth-based applications, it does not effectively describe the position of moving or elevated objects, such as aircraft or satellites, relative to fixed locations on Earth. To overcome this limitation, more specialized Earth-centered coordinate systems were developed. These systems allow for more accurate tracking and description of the positions of objects in motion or located above the surface, both in the atmosphere and in space.

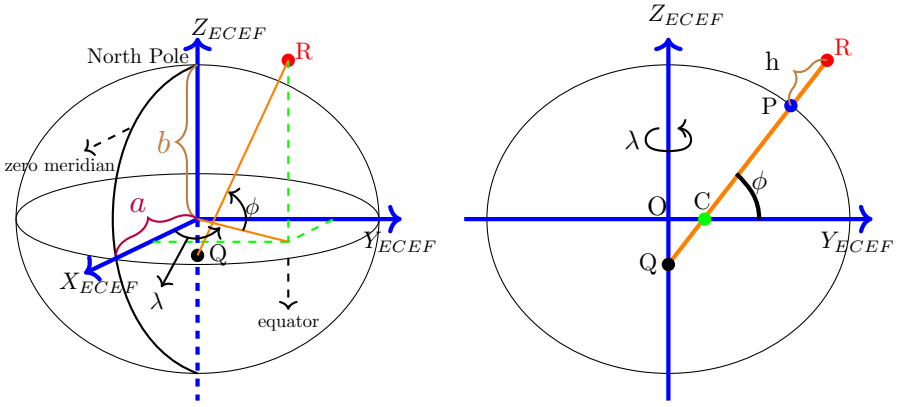
This section explores the foundational coordinate systems used in geospatial and satellite applications, along with the mathematical transformations between them. By understanding these systems, we gain the ability to accurately model and interpret the spatial relationships between terrestrial and spaceborne objects—an essential capability for applications such as satellite communications, weather modeling, and aerospace navigation.

4.1.1 Geodetic vs Geocentric Coordinates

The geodetic coordinate system, encompassing latitude, longitude, and altitude, represents a curvilinear orthogonal coordinate system specifically designed to define the locations of objects on or above the Earth's surface within an ellipsoidal framework (see Figure 4.1). Latitude (ϕ) and longitude (λ) play an essential role in this system.

Longitude, denoted by λ, measures the rotational angle between the prime meridian (also known as the zero meridian) and the target point. This parameter is expressed in degrees within the ranges of $-180°$ to $180°$ or $0°$ to $360°$. Latitude (ϕ) measures the proximity of a point along a meridian to either the poles or the equator, represented by an angle from $-90°$ to $90°$, where $0°$ corresponds to the equator.

Notably, geodetic coordinates can be directly converted to Earth-centered, Earth-fixed (ECEF) coordinates. The ECEF system, also recognized as the geocentric coordinate system, is a Cartesian spatial reference system. It signifies locations through X, Y, and Z measurements from the Earth's center of mass (O in Figure 4.1). This system is extensively utilized in satellite navigation systems to precisely measure the projected locations of satellites on the



(a) 3D view (b) Ellipsoid cut view

Figure 4.1: Geodetic coordinate $R(\phi, \lambda, h)$ vs ECEF coordinate. ϕ and λ are the latitude and longitude angles respectively. The a and b are the semi-major and semi-minor axis of the Earth.

Earth's surface.

Understanding these coordinate systems is fundamental for various applications, from cartography to satellite navigation. In the subsequent sections, classical coordinate systems and detailed coordinate transformations will be explored, shedding light on their relevance and significance in diverse scenarios. The versatility of geodetic and ECEF coordinates makes them indispensable tools for accurately representing and navigating locations on Earth and in satellite systems.

Transformation of the geodetic coordinates into geocentric Cartesian coordinates is as follows:

$$\begin{aligned} X_{ECEF} &= (N(\phi) + h)\cos\phi\cos\lambda \\ Y_{ECEF} &= (N(\phi) + h)\cos\phi\sin\lambda \\ Z_{ECEF} &= (\frac{b^2}{a^2}N + h)\sin\phi \end{aligned} \tag{4.1}$$

In the given expression, a and b correspond to the semi-major and semi-minor axes of the Earth, as illustrated in Figure 4.1. The semi-major axis, denoted by a, represents the Earth's longest radius, while the semi-minor axis, represented by b, is the Earth's shortest radius.

The term $N(\phi)$, referred to as the prime vertical radius of curvature, is a crucial parameter in geodetic coordinates and is inherently dependent on latitude. This parameter is defined as the length of the line segment $\overline{PQ}$ in Figure 4.1b and can be quantified by the expression:

$$N(\phi) = \frac{a^2}{\sqrt{a^2\cos^2\phi + b^2\sin^2\phi}} = \frac{a}{\sqrt{1 - e^2\sin^2\phi}} \tag{4.2}$$

where e is the eccentricity of the ellipsoid and is defined as follows:

$$e = \sqrt{1 - \frac{b^2}{a^2}} \tag{4.3}$$

The process of converting coordinates from Earth-Centered, Earth-Fixed (ECEF) to geodetic coordinates is not a straightforward task. While the calculation of longitude (λ) retains simplicity through the expression:

$$\lambda = \arctan 2(Y_{ECEF}, X_{ECEF}) \tag{4.4}$$

The conversion of latitude and altitude is more intricate, involving a nonlinear system. This complexity arises due to a circular relationship entailing the prime vertical radius of curvature, denoted as $N(\phi)$. The circular interdependence of these variables adds a layer of complexity to the conversion process, requiring specialized algorithms to accurately determine the geodetic latitude and altitude from their corresponding ECEF coordinates.

$$h = \frac{p}{\cos\phi} - N(\phi) \tag{4.5}$$

$$\phi = \arctan\left(\frac{Z/p}{1 - \frac{e^2 N}{N+h}}\right) \tag{4.6}$$

with

$$\begin{aligned} p &= \sqrt{X_{ECEF}^2 + Y_{ECEF}^2} \\ Z &= \left(\frac{b^2}{a^2} N + h\right) \cos\phi \end{aligned} \tag{4.7}$$

To solve this nonlinear equation system, an iterative method is employed, typically initiated with an initial value for the geodetic altitude (h). A prudent starting point is often $h = 0$, and convergence is typically achieved after around 5 iterations, ensuring a sufficiently accurate result. For a detailed exploration of this iterative process, interested readers can refer to [78, 79].

For those seeking a non-iterative alternative, [80] presents a transformation method for converting Earth-Centered, Earth-Fixed (ECEF) Cartesian coordinates to geodetic coordinates with satisfactory accuracy, offering an efficient solution for specific applications.

The precision of these conversions hinges on the accurate knowledge of the Earth's ellipsoidal shape. Various authors have presented ellipsoidal models based on diverse measurements. One of the most widely adopted models is the WGS-84 ellipsoid, particularly prevalent in Global Positioning System (GPS) applications. Key dimensions of the Earth under the WGS-84 ellipsoid are detailed in Table 4.1, providing essential information for precise coordinate transformations in different systems. Understanding and utilizing the correct ellipsoidal shape is foundational for accurate geodetic computations across diverse applications.

Table 4.1: Earth's ellipsoid dimensions as WGS-84

Constant	Value	Unit	Description
a	6378137.0	m	WGS-84 Earth semimajor axis
b	6356752.3142	m	WGS-84 Earth semiminor axis
e	8.1819191×10^{-2}		Eccentricity

4.1.2 Geocentric vs ENU Coordinates

Local Tangent Plane coordinates (LTP), also referred to as East-North-Up (ENU) coordinates, represent a spatial Cartesian reference system established on the tangent plane defined by the local vertical direction and the Earth's axis of rotation (refer to Figure 4.2a). This system provides a convenient and intuitive framework for expressing positions relative to a local reference point.

The ENU system is characterized by a right-handed coordinate system, exhibiting a clear analogy with the familiar Cartesian coordinates. The transformation between two Cartesian coordinate systems is achieved through matrix multiplication. The initial step involves shifting the center of the Earth to the origin of the tangent plane by subtracting the Earth's radius (r_0) from the Earth-Centered, Earth-Fixed (ECEF) coordinates. Let r' denote the resulting translated coordinate.

$$\begin{aligned} \mathbf{r'} &= \mathbf{r} - \mathbf{r_0} \\ \begin{bmatrix} x' \\ y' \\ z' \end{bmatrix} &= \begin{bmatrix} x \\ y \\ z \end{bmatrix} - \begin{bmatrix} x_0 \\ y_0 \\ z_0 \end{bmatrix} \end{aligned} \tag{4.8}$$

Here, $\mathbf{r}$ represents a vector in ECEF coordinates, while $\mathbf{r_0}$ denotes the initial reference location (refer to Figure 4.2b). It is crucial to note that the axes of $\mathbf{r'}$ are aligned parallel to those of ECEF $\mathbf{r}$.

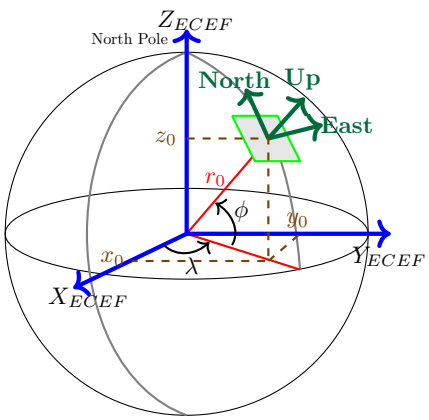
In the subsequent transformation, $\mathbf{r'}$ undergoes a rotation along the z-axis, specifically by the longitude angle λ. This rotation results in the alignment of Y_{ECEF} with the East-axis (refer to Figure 4.2c).

$$\mathbf{r''} = \begin{bmatrix} e \\ x'' \\ z'' \end{bmatrix} = \mathbf{R_1}[\lambda] \times \mathbf{r'} = \begin{bmatrix} -\sin\lambda & \cos\lambda & 0 \\ \cos\lambda & \sin\lambda & 0 \\ 0 & 0 & 1 \end{bmatrix} \times \begin{bmatrix} x' \\ y' \\ z' \end{bmatrix} \tag{4.9}$$

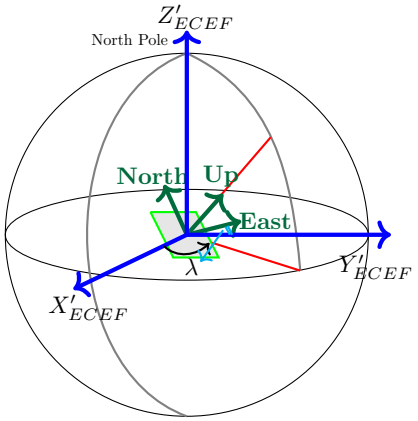
To finalize the conversion to East-North-Up (ENU) coordinates, a rotation is necessary to orient the x''-axis about the East-axis by the latitude angle ϕ. Fortunately, the latitude angle ϕ is precisely defined as the angle between the equator and the local normal vector.

This last rotation step can be succinctly expressed as:

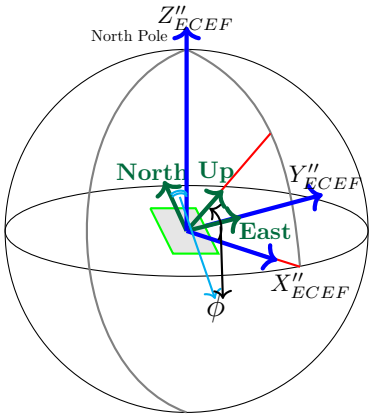
$$\mathbf{r_t} = \begin{bmatrix} e \\ n \\ u \end{bmatrix} = \mathbf{R_2}[\phi] \times \mathbf{r''} = \begin{bmatrix} 1 & 0 & 0 \\ 0 & -\sin\phi & \cos\phi \\ 0 & \cos\phi & \sin\phi \end{bmatrix} \times \begin{bmatrix} e \\ x'' \\ z'' \end{bmatrix} \tag{4.10}$$



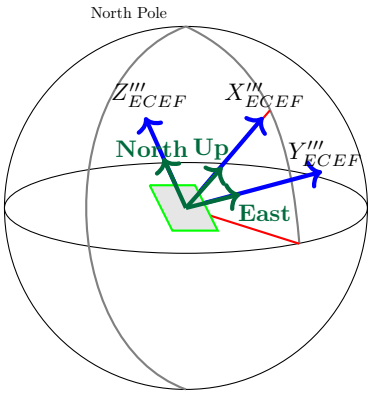
(a) Default orientation of ECEF and ENU coordinates



(b) Transforming the ECEF coordinates along the r_0 path



(c) Rotating the ECEF coordinates around the $z-axis$



(d) Rotating the ECEF coordinates around the East-axis

Figure 4.2: The ECEF vs ENU coordinate configuration and translating steps (b)-(d) between the two systems

where $\mathbf{r_t}$ represents the coordinates in the ENU systems. Combining the entire transformation out gives:

$$\begin{bmatrix} e \\ n \\ u \end{bmatrix} = \mathbf{R_t}[\lambda, \phi] \times \begin{bmatrix} x - x_0 \\ y - y_0 \\ z - z_0 \end{bmatrix} \tag{4.11}$$

where the $\mathbf{R_t}[\lambda, \phi]$ is the product of the two transformation $\mathbf{R_1}[\lambda]$ and $\mathbf{R_2}[\phi]$ as follow

$$\begin{aligned} \mathbf{R_t}[\lambda, \phi] &= \mathbf{R_1}[\lambda] \times \mathbf{R_2}[\phi] \\ &= \begin{bmatrix} -\sin\lambda & \cos\lambda & 0 \\ -\cos\lambda\sin\phi & -\sin\lambda\sin\phi & \cos\phi \\ \cos\lambda\cos\phi & \sin\lambda\cos\phi & \sin\phi \end{bmatrix} \end{aligned} \tag{4.12}$$

For the reverse transformation from ENU to ECEF coordinates, the process involves inverting the matrix $\mathbf{R_t}[\lambda, \phi]$ and subsequently adding the reference location r_0 to the result. This step reinstates the original ECEF coordinates from the ENU representation.

$$\begin{bmatrix} x \\ y \\ z \end{bmatrix} = \mathbf{R_t}[\lambda, \phi]^{-1} \times \begin{bmatrix} e \\ n \\ u \end{bmatrix} + \begin{bmatrix} x_0 \\ y_0 \\ z_0 \end{bmatrix} \tag{4.13}$$

where

$$\mathbf{R_t}[\lambda, \phi]^{-1} = \begin{bmatrix} -\sin\lambda & -\cos\lambda\sin\phi & \cos\lambda\cos\phi \\ \cos\lambda & -\sin\lambda\sin\phi & \sin\lambda\cos\phi \\ 0 & \cos\phi & \sin\phi \end{bmatrix} \tag{4.14}$$

4.1.3 ENU vs AER Coordinates

Azimuth, Elevation, and Slant Range coordinates (AER) constitute a spherical coordinate system widely employed in navigation and satellite tracking systems. This coordinate system holds a direct connection with East-North-Up (ENU) coordinates, allowing for straightforward conversions between spherical and Cartesian representations.

In the AER system, the elevation angle (El) defines the angle between the horizontal tangent plane (East-North Plane) and the slant range extending from the satellite to the object in space. On the other hand, the azimuth angle (Az) specifies the direction in a clockwise rotation, commencing from the North-axis in ENU coordinates and extending to the horizontal projection of the slant range on the East-North plane. The orientation of ENU and AER coordinates is illustrated in Figure 4.3.

The transformation from AER to ENU coordinates is expressed as follows:

$$\begin{aligned} E &= R\cos(EL)\sin(Az) \\ N &= R\cos(El)\cos(Az) \\ U &= R\sin(EL) \end{aligned} \tag{4.15}$$

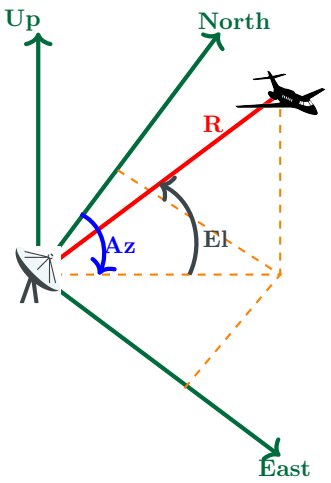


Figure 4.3: ENU vs AER coordinates.

Conversely, the reverse transformation from ENU to AER coordinates is articulated as:

$$\begin{aligned} Az &= \arctan 2(E, N)\%2\pi \\ El &= \arctan 2(U, \sqrt{E^2 + N^2}) \\ R &= \sqrt{E^2 + N^2 + U^2} \end{aligned} \tag{4.16}$$

Here, the % symbol denotes the Modulus operator, representing the remainder of the division of the left operand by the right. These transformations facilitate the seamless conversion between AER and ENU coordinates, essential for applications requiring precise spatial orientation and tracking.

4.1.4 Earth Global Inertial Coordinates

In the previous sections, we focused on fixed, time-independent coordinate systems. However, when tracking a satellite orbiting the Earth, it becomes more practical to describe its motion relative to a coordinate system that is fixed in space rather than tied to the rotating Earth. This requires converting from an Earth-fixed (non-inertial) frame to an inertial frame of reference to accurately model the satellite's motion from an Earth-based perspective.

Earth itself exhibits two main types of motion: its daily rotation around its axis and the slow, periodic wobble of its rotational axis (polar motion). These motions must be considered when transforming coordinates from a rotating Earth-centered frame to a fixed celestial frame.

The transformation from the Earth-Centered, Earth-Fixed (ECEF) coordinate system to an inertial coordinate system involves two main steps:

- **ECEF to PEF (Pseudo Earth-Fixed)**: The first step accounts for polar motion, which causes the rotation axis of the Earth to shift slightly

over time. This correction transforms ECEF coordinates into the PEF frame.

- **PEF to TEME (True Equator, Mean Equinox)**: The second step removes Earth's rotation, converting the coordinates into the TEME frame—an inertial reference frame commonly used for satellite tracking.

These transformations allow us to shift from a ground-based perspective to a space-based one, enabling more accurate prediction and analysis of satellite positions. The first transformation, from ECEF to PEF, is accomplished using the following matrix:

$$\begin{bmatrix} x \\ y \\ z \end{bmatrix}_{PEF} = \begin{bmatrix} \cos x_p & 0 & -\sin x_p \\ \sin x_p \sin y_p & \cos y_p & \cos x_p \sin y_p \\ \sin x_p \cos y_p & -\sin y_p & \cos x_p \cos y_p \end{bmatrix} \begin{bmatrix} x \\ y \\ z \end{bmatrix}_{ECEF} \tag{4.17}$$

In practice, due to the challenges in obtaining accurate polar motion data, a simplification is often made where $x_p = 0$ and $y_p = 0$, effectively rendering PEF equivalent to ECEF.

$$\begin{bmatrix} x \\ y \\ z \end{bmatrix}_{PEF} \approx \begin{bmatrix} 1 & 0 & -x_p \\ 0 & 1 & y_p \\ x_p & -y_p & 1 \end{bmatrix} \begin{bmatrix} x \\ y \\ z \end{bmatrix}_{ECEF} \tag{4.18}$$

In practical applications, it is often difficult to obtain precise values for the polar motion parameters x_p and y_p. As a result, these are frequently assumed to be zero—i.e., $x_p = 0$ and $y_p = 0$—which simplifies the transformation process. Under this assumption, the Pseudo Earth-Fixed (PEF) frame can be considered equivalent to the Earth-Centered, Earth-Fixed (ECEF) frame.

To complete the transformation from PEF to the True Equator, Mean Equinox (TEME) inertial frame [81], we must compute the Greenwich Mean Sidereal Time (GMST), which represents the rotation of the Earth relative to the fixed stars. GMST is expressed as:

$$\begin{aligned} \text{GMST} = -6.2 \times 10^{-6}\, t_{UT1}^3 + 0.09104\, t_{UT1}^2 + (3.15576 \times 10^9 + \\ 8640184.812866)\, t_{UT1} + 67310.54841 \end{aligned} \tag{4.19}$$

where t_{UT1} is the Universal Time or, more specifically UT1, is counted from 0 hours at midnight, with unit of duration the *mean solar day*, defined to be as uniform as possible despite variations in the rotation of the Earth. The relation between the UT1 and Julian day is

$$t_{UT1} = (jd_{UT1} - 2451545.0)/36525.0 \tag{4.20}$$

with jd_{UT1} as the Julian day which is a count of days elapsed since Greenwich mean noon on 1 January 4713 B.C., Julian proleptic calendar. The GMST in 4.19 serves the angle for the Earth rotation and then

$$\begin{bmatrix} x \\ y \\ z \end{bmatrix}_{TEME} = \begin{bmatrix} \cos(GMST) & \sin(GMST) & 0 \\ -\sin(GMST) & \cos(GMST) & 0 \\ 0 & 0 & 1 \end{bmatrix} \begin{bmatrix} x \\ y \\ z \end{bmatrix}_{PEF} \tag{4.21}$$

This comprehensive transformation enables the accurate representation of satellite motion with respect to a cosmos-centered reference, essential for precise tracking and navigation applications.

4.2 Map Projection

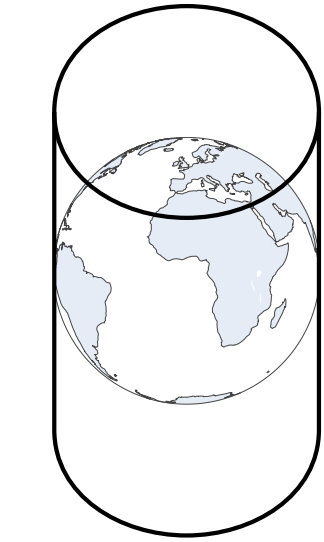
Map projection is a systematic representation of all or part of the surface of a three-dimensional object, typically the Earth, onto a two-dimensional plane. This process involves creating a visual display that includes lines representing meridians and parallels, as stipulated by some map projection definitions, although the choice may vary based on the map's intended purpose. Due to the inherent challenge of representing a curved surface on a flat plane without distortion, cartographers face the critical task of selecting a feature to be accurately depicted, often at the expense of others or through a compromise of multiple characteristics. It's important to note that there is no universally superior or "best" map projection, as the choice depends on the specific needs of the map.

Commonly, map projections involve geometrically projecting the Earth's surface onto developable surfaces. Three primary types of surfaces are employed in these projections: the cylinder, the cone, and the plane. Each surface introduces specific distortions, and cartographers must carefully select a projection method that aligns with their mapping objectives.

For a comprehensive understanding of available projection models, detailed descriptions, and comparisons, refer to [82]. Additionally, various Python software packages provide powerful tools for expressing map projections and facilitating transformations between them. Notable among these packages are Basemap [83], Plotly [84], GeoPandas [85], and Contextily [86]. These toolboxes offer versatile functionalities for map plotting and projection, making them valuable resources for scientists, cartographers, and researchers engaged in spatial data visualization and analysis.

4.2.1 Cylindrical Projection

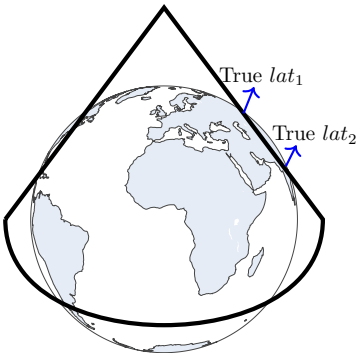
Imagine wrapping a cylinder around the Earth (as illustrated in Figure 4.4a), ensuring that its surface makes contact with the Equator along its entire circumference. In this scenario, the meridians of longitude can be projected onto the cylinder as equidistant straight lines that are perpendicular to the Equator. Simultaneously, the parallels of latitude are depicted as lines parallel to the Equator, encircling the cylinder and strategically spaced based on certain mathematical characteristics. The visual outcome of this mapping approach is captured in Figure 4.4b, showcasing a cylindrical projection model commonly known as the Mercator projection.



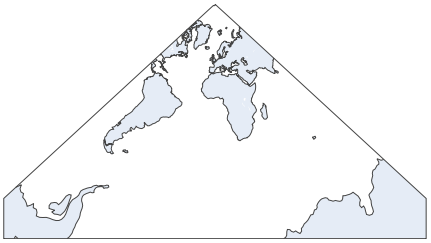
(a) Regular cylindrical projection



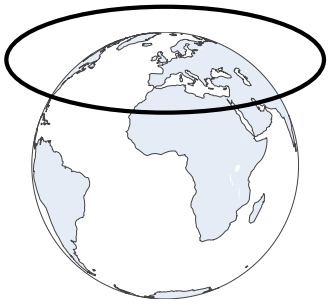
(b) Projected map by cylindrical plane



(c) Regular conic conformal



(d) Projected map by conic conformal



(e) Polar azimuthal (Plane)



(f) Projected map by polar azimuthal

Figure 4.4: Projection of the Earth onto the three major surfaces.

While the Mercator projection is widely used and has its merits, it introduces distortions, one of which is the exaggeration of locations at higher latitudes. For instance, in Figure 4.4b, Greenland appears as large as the entire African continent, a clear distortion from reality. This distortion arises because the Mercator projection preserves angles, making it suitable for navigation but resulting in significant size discrepancies, particularly towards the poles. It is essential for cartographers and users of maps to be aware of such distortions when interpreting and utilizing maps generated using the Mercator projection. Understanding the strengths and limitations of different projection models is crucial for selecting the most appropriate one for a given application or analysis.

4.2.2 Lambert Conformal Conic Projection

Visualize placing a cone over the Earth, aligning its apex with the polar axis and ensuring the cone's surface touches the globe along a specific parallel of latitude. This configuration gives rise to a conic (or conical) projection. In this scenario, the meridians are projected onto the cone as equidistant straight lines radiating from the apex, while the parallels are depicted as lines encircling the cone in planes perpendicular to the Earth's axis and strategically spaced to maintain desired characteristics (refer to Figure 4.4c).

Within the conic projection model, two crucial parameters are accessible: $True\ lat_1$ and $True\ lat_2$. Properly choosing these parameters enables the adjustment of the perpendicular plane over the desired location. This model finds extensive use in this thesis, particularly as it involves perpendicular planes over the center of ground stations. Opting for $True\ lat_1 = True\ lat_2$ ensures that the ground station resides at the center of the perpendicular plane. Figure 4.4d illustrates an example of a map projection using the conformal conic model.

This conic projection model provides advantages such as maintaining accurate shapes and angles, making it suitable for mapping mid-latitude regions with minimal distortion. However, like any projection method, it involves trade-offs, and users should know the specific characteristics and distortions introduced by the chosen model to interpret maps accurately. Understanding the flexibility and constraints of conic projections enhances their effectiveness in various applications, especially in scenarios involving ground station placements and mapping localized regions.

4.2.3 Polar Azimuthal (Tangent Plane)

The polar azimuthal projections are grounded on a plane tangent to one of the Earth's poles. In this scenario, the meridians are projected as straight lines radiating from a central point, and what sets them apart is that they are spaced at their true angles, in contrast to the smaller angles seen in conic projections. The parallels of latitude in this projection model form complete circles, with their center coinciding with the pole (refer to Figure 4.4e). An illustrative example of a map resulting from this model is depicted in Figure 4.4f.

Within azimuthal projections, there is a variety of approaches. In projections like the Stereographic (specifically designed for a sphere), the parallels are geometrically projected from a common point of perspective. In contrast, others like the Azimuthal Equidistant employ a nonperspective approach for depicting parallels.

Polar azimuthal projections offer unique advantages, especially for mapping polar regions with reduced distortion. They are particularly useful for navigational purposes at high latitudes. However, users should be aware of the specific characteristics and potential distortions associated with polar azimuthal projections. As with any map projection, understanding the inherent trade-offs is crucial for selecting the most suitable model for a given application, ensuring accurate interpretation and analysis of spatial information.

4.3 Satellite Position

To generate time series depicting propagation impairments based on azimuth-elevation maps, it is imperative to possess accurate information regarding the satellite's position over time. This entails having a comprehensive time series that describes the propagation slant path through the satellite's azimuth and elevation variations. In the case of a Geostationary Earth Orbit (GEO), where the satellite remains fixed relative to an observer on Earth's surface, the azimuth and elevation are constant over time. For a more general Geosynchronous Earth Orbit (GSO), the azimuth and elevation exhibit variations, tracing an eight-shaped figure in the sky. Nevertheless, for GSO satellites with low inclination to the equatorial plane, these variations are minimal, allowing them to be disregarded, and their orbitography can be simplified to a fixed link.

The characteristics of nearly GEO satellites' orbitography depend primarily on the longitude difference between the ground station and the satellite, as well as the latitude of the ground station. Generally, all else being equal, a ground station at a higher latitude will observe the satellite at a lower elevation.

In contrast, for non-GSO satellites like those in Medium Earth Orbit (MEO) or Low Earth Orbit (LEO), a detailed understanding of the orbitography is crucial to accurately model the slant paths. Obtaining orbital parameters at a specific epoch under the Two Line Elements (TLE) format is one approach. A TLE provides a time-varying set of orbital elements, offering essential information for tracking satellites. An example of a TLE format for the METOP-A satellite is illustrated in Figure 4.5.

This information serves as the foundation for computing azimuth and elevation values over time, allowing for the precise modeling of slant paths, essential for assessing and mitigating propagation impairments in satellite communication systems.

```
METOP-A
1 29499U 06044A 22045.80572937 .00000887 00000+0 12638-3 0 9996
2 29499 98.4687 86.4309 0199448 32.7068 85.6508 14.66935214792694
```

Figure 4.5: Example of Two Line Elements (TLE) for METOP-A satellite

A comprehensive description of each field in Two-Line Element (TLE) sets can be found in [81]. For practical purposes, obtaining TLE data for various satellites is conveniently facilitated by websites such as www.CelesTrak.com [87]. It's important to note that the focus of this dissertation does not involve extracting orbital characteristics from TLE files. Numerous Python packages are available to perform this task with the required accuracy for our purposes. Trustworthy implementations such as the SGP4 and Skyfield Python packages [88, 89] are recommended for reliable satellite position computations.

The SGP4 package outputs the satellite's position and velocity in True Equator Mean Equinox (TEME) coordinates. To integrate this information into propagation models, a conversion to Earth-Centered, Earth-Fixed (ECEF) coordinates is necessary, as outlined in the procedure detailed in Section 4.1.4. On the other hand, the Skyfield Python library provides the output in various coordinate systems, including Geodetic, ECEF, and Azimuth, Elevation, and Range (AER). Given the flexibility and reliability of the Skyfield library, it has been chosen as the reference software for satellite position processing in this thesis.

The result of employing the Skyfield library is a time series $(\psi(t), \theta(t))$, representing the azimuth and elevation of an Earth-space link over time. This data forms a crucial component for analyzing and mitigating propagation impairments in satellite communication systems, contributing to a more accurate understanding of the dynamic satellite-ground station relationships.

4.4 Atmospheric Attenuation Time Series

The post-processed Numerical Weather Prediction (WRF) data yield 2D azimuth and elevation maps representing propagation impairments at a specific radio frequency for a given ground station. However, to obtain the attenuation for a fixed link between the ground station and the satellite, an interpolation procedure is essential to access the attenuation time series. Section 4.4.1 delves into the details of creating this time series of attenuation.

Subsequently, Section 4.4.2 provides procedures to calculate first-order statistics of time series of attenuation. Moving beyond, Sections 4.4.3.1 and 4.4.3.2 proposes a methodology for extracting second-order statistical information from time series of attenuation. These sections collectively contribute to a comprehensive understanding of the statistical characteristics of propagation impairments, allowing for analysis of communication link performance under varying atmospheric conditions.

4.4.1 Link Attenuation Time Series from Azimuth-Elevation Maps

For Geostationary Earth Orbit (GSO) satellites, the azimuth (ψ) and elevation (θ) remain approximately constant over time, indicated by $\psi(t) \approx \bar{\psi}(t)$ and $\theta(t) \approx \bar{\theta}(t)$. This simplification enables the construction of a time series $A(t)$ with a resolution of T_{NWP}. Specifically, $A(t_i)$ is determined through bilinear interpolation of each $A_i(\psi, \theta)$ at the fixed values $(\bar{\psi}(t), \bar{\theta}(t))$.

However, for non-GSO satellites, the time during which the satellite is visible from a given ground station may be short, comparable to T_{NWP}. During this period, the azimuth and elevation may undergo significant changes every few seconds. To utilize the maps $A_i(\psi, \theta)$ in this dynamic scenario, an initial assumption is made that these maps represent a frozen state of the atmosphere. Subsequently, the time series $A_i(t)$ is derived by bilinear interpolation of $A_i(\psi, \theta)$ at the varying values $(\psi(t), \theta(t))$.

To construct a time series $A(t)$ representative of Earth-space links over any time period, not just when the frozen atmosphere assumption holds, a piecewise approach is proposed. For a given time interval $[t_i, t_{i+1}]$, the time series $A_i(t)$ and $A_{i+1}(t)$ are linearly combined using the formula:

$$A(t) = (1 - w_i(t))A_i(t) + w_i(t)\, A_{i+1}(t) \tag{4.22}$$

Here, the linear weight in time, $w_i(t)$, changes from 0 to 1 and is defined as:

$$w_i(t) = \frac{(t - t_i)}{T_{NWP}} \tag{4.23}$$

This implies that $A(t)$ depends on the two nearest frozen atmospheres available, allowing for a more accurate representation of the dynamic atmospheric conditions over time.

4.4.2 Complementary Cumulative Distribution Function

Obtaining time series data of propagation impairments from Numerical Weather Prediction (NWP) data provides an opportunity to conduct various statistical analyses on the simulated data and compare them with measurements and reference models.

The Complementary Cumulative Distribution Function (CCDF) of the propagation impairment A is graphically represented as $(P(A \geq A^\star), A^\star)$, where each exceeded level $A^\star$ of the impairment corresponds to the probability of exceedance $P(A \geq A^\star)$.

There are at least two different approaches to computing the CCDF from a time series $A(t)$:

1. Sorting $A(t)$ in decreasing order and associating, for each t, a probability of exceedance corresponding to the natural frequency of occurrence in the sorted time series.

2. Binning $A(t)$ into consecutive intervals and obtaining the exceedance probability for each bin by performing a cumulative sum of the histogram count.

ITU-R Study Group 3 (SG3) provides guidelines for processing propagation data into statistics [90]. It is crucial to note that, concerning measurements, the CCDFs must be normalized with respect to the full observation period and not just the period with valid data. When comparing NWP-derived CCDFs with experimental CCDFs or CCDFs from ITU-R models, this consideration is paramount.

The procedure for computing the CCDF of, for instance, a Low Earth Orbit (LEO) satellite is not fundamentally different from that presented for fixed links. However, since the satellite is not visible 100% of the time, the normalization of the CCDF should include only the samples during the visibility periods. This ensures a more accurate representation of the impairment statistics for the given satellite.

Note that a procedure exists in [3] to approach the CCDF of a non-GSO links from the knowledge of the CCDFs at several fixed elevation angles. This procedure is summarized by

$$\begin{aligned} P(A \geq A^*) &= \int_{\theta_{min}}^{\theta_{max}} P(A \geq A^* \mid \theta)\, P(\theta)\, d\theta \\ &\approx \sum_i P(A \geq A^* | \tilde{\theta}_i)\, P(\theta_{i+1} \geq \theta \geq \theta_i) \end{aligned} \tag{4.24}$$

where the fixed elevation CCDFs $P(A \geq A^* \mid \tilde{\theta}_i)$ are assumed to be known for the elevation angles $\tilde{\theta}_i \in [\theta_i, \theta_{i+1}]$, and where the histogram $P(\theta_{i+1} \geq \theta \geq \theta_i)$ is also known from the orbitography. With NWP data processed as azimuth-elevation maps, it is possible to compare this approach with the CCDFs computed directly from time series with varying azimuths and elevations.

4.4.3 Fade Dynamics on Earth-Space Paths

The assessment of parameters associated with the risk of failure in satellite communication links is intricately linked to the statistics of two key quantities: fade slope and fade duration of the received signal during atmospheric attenuation. To ensure a predetermined quality and reliability of services, prior knowledge of the probability of occurrence in fade slope and fade duration of the received signal from satellites is essential. Section 4.4.3.1 will delve into the statistics of fade duration, while section 4.4.3.2 will provide insights into obtaining the statistics of fade slopes.

Fade slope, fade duration, and inter-fade duration are crucial concepts depicted in Figure 4.6, illustrating the dynamic nature of signal attenuation in satellite communication. Understanding these parameters is fundamental in predicting and managing the potential disruptions in the received signal, thereby contributing to the overall robustness and performance of satellite communication systems.

4.4.3.1 Fade Duration of Time Series

Understanding the fade duration in system design offers several advantages:

- system outage and unavailability : Providing information about the duration and unavailability of the system during propagation impairments is crucial. This insight helps in designing systems that can efficiently handle and recover from disruptions caused by fading events.
- sharing of the system resource : Having a statistical view of resource allocation during attenuation events is vital. It allows for optimized resource

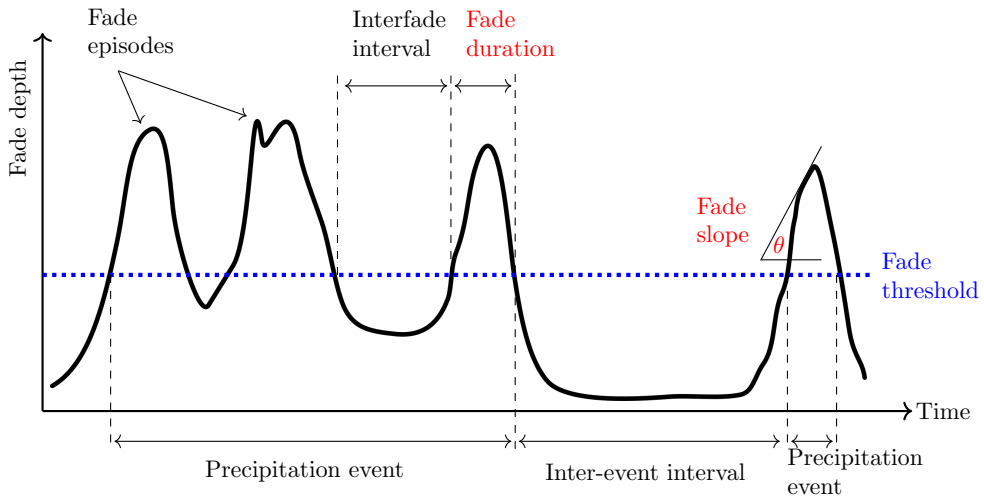


Figure 4.6: Features characterizing the dynamics of fade events

management, ensuring that system resources are allocated judiciously to other users during periods of signal degradation.

- Fade Mitigation Techniques : Knowledge of fade duration is essential for implementing effective Fade Mitigation Techniques (FMT). These techniques enable the system to maintain connectivity and performance, adapting to varying atmospheric conditions and ensuring a more reliable communication link.

- system coding and modulation : Fade duration plays a pivotal role in the selection of forward error correction codes and modulation schemes. Understanding the statistical characteristics of fade duration allows for the implementation of coding and modulation strategies that are tailored to the specific challenges posed by different atmospheric events.

Fade duration, being a statistical process, can be effectively characterized using two different distribution functions. This statistical approach enables a more comprehensive understanding of the variability and dynamics associated with fade duration, facilitating informed decisions in system design and optimization.

1. $P(d > D \mid a > A)$: the probability of occurrence of fades of duration d longer than $D\,(s)$, when the attenuation a is greater than $A\,(dB)$.

$$P(d > D \mid a > A) = \frac{N_{d>D}}{N} \tag{4.25}$$

where $N_{d>D}$ is the number of fades of duration longer than D and N is the total number of fades observed (See Figure 4.7a)

2. $F(d > D \mid a > A)$: the cumulative exceedance probability of fade time due to fades of duration d longer than $D\,(s)$ where the attenuation a is larger than A.

$$F(d > D \mid a > A) = \frac{N_{s_{d>D}}}{N_{a>A}} \tag{4.26}$$

where $N_{s_{d>D}}$ is the total number of seconds when the fade of duration d is longer than D, and N_A is a total exceedance time of the threshold A (see Figure 4.7b).

The above procedure is for simulation or measurement results processing. To predict the fade duration estimation, the model represented in [91] will be used. Based on this model, the long fade duration has a log-normal distribution and short fade durations has a power-law function distribution. The model is valid for fade duration longer than 1 s.

The step-by-step calculation of the fade duration is as follows:

1. Mean duration D_0:

$$D_0 = 80\phi^{-0.4}\, f^{1.4}\, A^{-0.39} \tag{4.27}$$

which ϕ, f and A are elevation angle [°], frequency [GHz], and excess attenuation [dB] respectively.

2. Standard deviation:

$$\sigma = 1.85\, f^{-0.05}\, A^{-0.027} \tag{4.28}$$

3. exponent γ of the power-law distribution:

$$\gamma = 0.055\, f^{0.65}\, A^{-0.003} \tag{4.29}$$

4. boundary between short and long fade durations:

$$D_t = D_0\, e^{p_1\sigma^2 + p_2\sigma - 0.39} \tag{4.30}$$

where

$$p_1 = 0.885\gamma - 0.814 \tag{4.31}$$

$$p_2 = -1.05\gamma^2 + 2.23\gamma - 1.61 \tag{4.32}$$

5. mean duration D_2 of the log-normal distribution

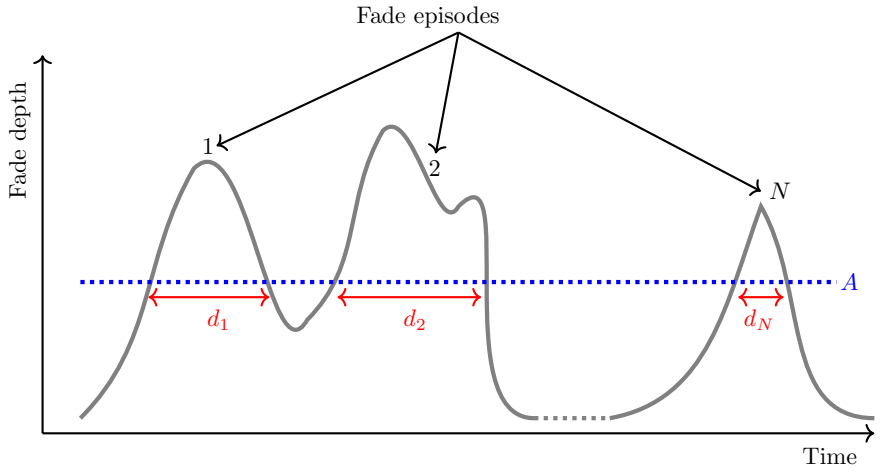
$$D_2 = D_0\, e^{-\sigma^2} \tag{4.33}$$

6. fraction of time k due to fades of duration less than D_t:

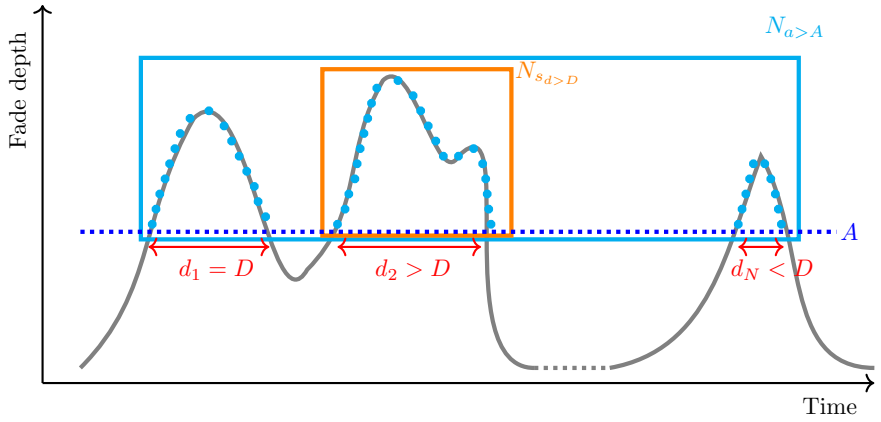
$$k = \left[1 + \frac{\sqrt{D_0 D_2}\,(1-\gamma)\, Q\left(\frac{\ln(D_t) - \ln(D_0)}{\sigma}\right)}{D_t\,\gamma\, Q\left(\frac{\ln(D_t) - \ln(D_2)}{\sigma}\right)}\right]^{-1} \tag{4.34}$$

where Q is the standard cumulative distribution function for a normally distributed variable:

$$Q(z) = \frac{1}{\sqrt{2\pi}} \int_z^{\infty} e^{-\frac{1}{2}x^2}\, dx \tag{4.35}$$



(a)



(b)

Figure 4.7: Fade duration description by two method (a) the probability of occurrence of fades duration $P(d > D \mid a > A)$, and (b)the cumulative exceedance probability $F(d > D \mid a > A)$

7. probability of occurrence of fade events of duration d longer than D given that attenuation a is greater than A

$$P(d > D \mid a > A) = D^{-\gamma} \qquad \text{for} \quad 1 \leq D \leq D_t \tag{4.36}$$

$$P(d > D \mid a > A) = D_t^{-\gamma} \frac{Q\left(\frac{\ln(D) - \ln(D_2)}{\sigma}\right)}{Q\left(\frac{\ln(D_t) - \ln(D_2)}{\sigma}\right)} \qquad \text{for} \quad D > D_t \tag{4.37}$$

8. cumulative probability of exceedance:

$$F(d > D \mid a > A) = \left[1 - k\left(\frac{D}{D_t}\right)^{1-\gamma}\right] \qquad \text{for} \quad 1 \leq D \leq D_t \tag{4.38}$$

$$F(d > D \mid a > A) = (1 - k) \frac{Q\left(\frac{\ln(D) - \ln(D_0)}{\sigma}\right)}{Q\left(\frac{\ln(D_t) - \ln(D_0)}{\sigma}\right)} \qquad \text{for} \quad D > D_t \tag{4.39}$$

4.4.3.2 Fade Slope of Time Series

Understanding the fading slope of satellite communication systems is crucial as it provides the basis for implementing Fade Mitigation Techniques (FMTs). Determining the fade slope of the received signal serves multiple purposes, such as facilitating the design of a control loop capable of tracking signal changes and enabling more accurate short-term prediction of propagation conditions. This becomes particularly significant in filtering out scintillation and rapid changes in rain attenuation.

The probability distribution of fade slope is contingent on various atmospheric factors, including atmospheric events, rain shape, drop size distribution during rain events, horizontal wind speed, and path length. The fade slope holds a direct correlation with the elevation angle of the received signal. The elevation angle, in turn, determines the length of the communication link path. This parameter assumes heightened importance in Low Earth Orbit (LEO) satellite communication, given the variant elevation angles these satellites experience over time.

In conducting fade slope analysis, certain considerations must be taken into account based on excess attenuation time series. Initially, the attenuation time series is down-sampled to 1 Hz, thereby excluding fade events lasting less than 1 second. Subsequently, a low-pass filter is applied to the time series of attenuation to eliminate high fluctuations attributed to tropospheric scintillation. The 3-dB cut-off frequency for the low-pass filter varies from event to event, typically ranging from 0.001 to 1 Hz. Experimental results suggest that a value of 0.02 Hz effectively filters out rapid variations in rain and scintillation attenuation. However, it is essential to note that this low-pass filter also disregards attenuation variations occurring within time periods shorter than 50 seconds (1/0.02 Hz) [91, 92].

The type of filter utilized is not critical in this context. One may opt for a 5^{th}-10^{th} order Butterworth filter or a 30-second moving average filter [93, 94].

These considerations collectively contribute to a comprehensive understanding of fade slope dynamics in satellite communication systems, enhancing the efficiency of Fade Mitigation Techniques.

The fade slope $\zeta(t)$ is defined as the fraction of the difference between attenuation levels $A(t)$ at time $t + \Delta t/2$ and $t - \Delta t/2$ over the time interval Δt. Mathematically, it is expressed as follows:

$$\zeta(t) = \frac{A\left(t + \frac{1}{2}\Delta t\right) - A\left(t - \frac{1}{2}\Delta t\right)}{\Delta t} \qquad [dB/s] \tag{4.40}$$

The values of the slope obtained from Equation 4.40 can be either positive or negative. A positive value indicates an increase in attenuation during the time interval Δt, while a negative value signifies a decrease in attenuation during the same interval. Commonly, the time interval Δt falls within the range of 2-200 seconds, and the impact of this interval on fade slope measurements is discussed in Section 7.

In the statistical analysis of fade slope, attention is particularly directed towards attenuation levels ranging from 1 dB to 20 dB. It involves examining the conditional probability density function (PDF) and conditional complementary cumulative distribution function (CCDF) of fade slopes. This analysis is conducted with fade slope bins set at 0.005 dB/s and attenuation bins at 1 dB. Such a meticulous approach is applicable to both measured and simulated data of time series of attenuation.

To predict the conditional probability distribution function of fade slope for a given attenuation value A, the following equation is employed [91, 92, 95]:

$$p(\zeta \mid A) = \frac{2}{\pi\sigma_\zeta \left(1 + \left(\frac{\zeta}{\sigma_\zeta}\right)^2\right)^2} \tag{4.41}$$

with

$$\sigma_\zeta = s\, F(f_B, \Delta t)\, A \tag{4.42}$$

$$F(f_B, \Delta t) = \sqrt{\frac{2\pi^2}{\left(\frac{1}{f_B^b} + (2\Delta t)^b\right)^{\frac{1}{b}}}} \tag{4.43}$$

In the provided model, the parameter b is assigned a value of 2.3, and s represents a climate and elevation-dependent parameter. For regions such as Europe and the United States of America, characterized by elevation angles ranging from 10° to 50°, an overarching average value of $s = 0.01$ is commonly applied. Notably, this parameter plays a pivotal role in shaping the characteristics of the model in different environmental conditions. The 3 dB cut-off frequency of the low pass filter, denoted as f_B, further refines the model's performance.

The applicability of this model spans frequencies within the 10 to 30 GHz range and attenuation levels from 0 to 20 dB. This range aligns with the operational parameters commonly encountered in satellite communication systems.

Should the need arise, the conditional complementary cumulative distribution function $P(\zeta \mid A)$, expressing the likelihood that the fade slope ζ exceeds

a given attenuation level A, can be determined using the following equation:

$$P(\zeta \mid A) = \frac{1}{2} - \frac{\left(\frac{\zeta}{\sigma_\zeta}\right)}{\pi\left(1+\left(\frac{\zeta}{\sigma_\zeta}\right)^2\right)} - \frac{arctan\left(\frac{\zeta}{\sigma_\zeta}\right)}{\pi} \tag{4.44}$$

The conditional complementary cumulative distribution function that the absolute value of the fade slope ζ is exceeded for a given attenuation value, A is calculated by

$$\begin{aligned} P(\mid \zeta \mid \mid A) &= \int_{-\infty}^{-\zeta} p(x \mid A)dx + \int_{\zeta}^{\infty} p(x \mid A)dx \\ &= 1 - \frac{2\left(\frac{|\zeta|}{\sigma_\zeta}\right)}{\pi\left(1+\left(\frac{|\zeta|}{\sigma_\zeta}\right)^2\right)} - \frac{2\,arctan\left(\frac{|\zeta|}{\sigma_\zeta}\right)}{\pi} \end{aligned} \tag{4.45}$$

This calculation provides valuable insights into the probability distribution of fade slopes relative to specific attenuation thresholds, offering a quantitative understanding of signal behavior in varying environmental conditions.

4.5 Error Analysis

The final stage in the introduction of new models and algorithms involves rigorous testing and error analysis. This step entails evaluating the performance of each new model against measurement data or established models from previous iterations. The comprehensive testing and error analysis process is detailed in the work referenced as [96], and the key findings are summarized in the subsequent sections.

The evaluation extends across various datasets and propagation prediction methods, providing a thorough examination of the models' capabilities under diverse conditions. The comparative analysis of prediction methods emphasizes the identification of the most effective method, which is determined by its ability to yield the smallest values for statistical parameters. This critical comparison aids in selecting and refining models and algorithms that exhibit superior accuracy and reliability in predicting propagation behavior.

4.5.1 Rainfall Rate Prediction Analysis

Rainfall rate predictions necessitate testing at specific, fixed locations. The validation of time series data is deemed unsuitable for testing propagation impairment models. Instead, a more effective approach involves testing the statistics of each variable within the models. Optimal validation choices include fixed probability levels for rain rate, such as 0.001%, 0.01%, and 0.1%.

To evaluate the performance of the models, the relative error of predicted rainfall rate is calculated for each percentage of time using the formula:

$$V_i = \frac{R_{p,i} - R_{m,i}}{R_{m,i}} \tag{4.46}$$

Here, $R_{p,i}$ denotes the predicted rainfall rate, and $R_{m,i}$ represents the measured rainfall rate for the i^{th} percentage of time. Subsequently, statistical measures including the mean (μ_V), standard deviation (σ_V), and root mean square value (ρ_V) for the variable V are computed over each percentage of time.

$$\rho_V = \sqrt{\mu_V^2 + \sigma_V^2} \tag{4.47}$$

This comprehensive analysis allows for a nuanced assessment of the predictive accuracy and reliability of the rainfall rate models at specified probability levels.

4.5.2 Attenuation Prediction Analysis

The attenuation analysis is fundamentally tested across multiple transmission paths at fixed probability levels, such as 0.001%, 0.01%, and 0.1% of the year.

$$S_i = \frac{A_{p,i}}{A_{m,i}} \tag{4.48}$$

The ratio S_i, calculated for the i^{th} radio link, is defined as the quotient of the predicted attenuation $A_{p,i}$ to the measured attenuation $A_{m,i}$. To facilitate analysis, the natural logarithm of these ratios is employed as a test variable.

To mitigate the impact of contributions from attenuation sources other than rain and address inaccuracies in measurements, particularly affecting lower attenuation values, a modification is necessary. For attenuations below 10 dB, the logarithm is scaled by a factor influenced by the measured attenuation. This scale factor takes the form of a power function, resulting in the modified test variable:

$$\begin{aligned} V_i &= \ln(S_i)\left(\frac{A_{m,i}}{10}\right)^{0.2} && \text{for} \quad A_{m,i} < 10\,dB \\ &= \ln(S_i) && \text{for} \quad A_{m,i} \geq 10\,dB \end{aligned} \tag{4.49}$$

Following this modification, the mean (μ_V), standard deviation (σ_V), and root mean square value (ρ_V) for the variable V are then computed over each percentage of time. This comprehensive analysis provides valuable insights into the performance and reliability of attenuation models under varying probability levels.

$$\rho_V = \sqrt{\mu_V^2 + \sigma_V^2} \tag{4.50}$$

4.5.3 Fade Duration Prediction Analysis

To facilitate the comparison of fade duration prediction methods, data is organized for both fixed individual fade durations (e.g., D=6 s, 180 s, or 3,600 s) and fixed attenuation thresholds (e.g., A=3 dB, 10 dB, or 25 dB). Section 4.4.3.1 outlines two distinct ways to represent fade duration statistics, resulting in two test values for error analysis [96].

The comparison involves calculating the ratio of predicted to measured fractions of time for each radio link, with the natural logarithm of this ratio serving

as the test variable. This variable, denoted as $\varepsilon_{P,i}(D, A)$ for fade duration prediction, is defined as follows:

$$\varepsilon_{P,i}(D, A) = \ln\left(\frac{P_p(D \mid A)}{P_m(D \mid A)}\right) \tag{4.51}$$

Here, $P_p(D \mid A)$ and $P_m(D \mid A)$ represent the predicted and measured probabilities, respectively, for each attenuation threshold A and fade duration D. The mean and standard deviation of this test variable are subsequently computed, providing essential statistics for comparing prediction methods.

For testing the cumulative probability of exceedance F, a similar test variable, $\varepsilon_{N,i}(D, A)$, is utilized:

$$\varepsilon_{N,i}(D, A) = \ln\left(\frac{1 - F_p(D \mid A)}{1 - F_m(D \mid A)}\right) \tag{4.52}$$

In this case, $F_p(D \mid A)$ and $F_m(D \mid A)$ represent the predicted and measured fractions of time, respectively, for each attenuation threshold A and fade duration D. These test variables allow for a robust evaluation of the prediction methods, considering both individual fade durations and cumulative exceedance probabilities.

4.5.4 Fade Slope Prediction Analysis

In this testing method, the predicted distribution of fade slope aligns with the cumulative distribution of a fade slope to be exceeded at a specified attenuation threshold. The comparison of fade slope prediction methods involves tabulating data for both a fixed time percentage P (ranging from 0.001% to 50%) and a fixed attenuation threshold A (e.g., 3 dB, 10 dB, or 25 dB). The assessment is conducted through the calculation of the ratio of predicted to measured fade slopes for each radio link, and the logarithm of this ratio serves as the test variable. Subsequently, the mean and standard deviation of this test variable are computed, providing crucial statistics for the comparison of prediction methods.

The test variable $\varepsilon_i(\zeta, A)$ for the i^{th} radio link is expressed as:

$$\varepsilon_i(\zeta, A) = 2\,\frac{P_p(\zeta \mid A) - P_m(\zeta \mid A)}{P_p(\zeta \mid A) + P_m(\zeta \mid A)} \tag{4.53}$$

Here, $P_p(\zeta \mid A)$ and $P_m(\zeta \mid A)$ represent the predicted and measured exceedance probabilities, respectively. Subsequently, the mean, standard deviation, and root mean square (r.m.s.) values of the error ε_i are calculated. In the comparison of prediction methods, the most effective approach is determined by its ability to produce the smallest values for these statistical parameters. This comprehensive analysis allows for a robust evaluation of the accuracy and reliability of fade slope prediction methods across various conditions.

4.6 Conclusion

This chapter presented a detailed methodology for transforming meteorological data produced by Numerical Weather Prediction (NWP) models into time-dependent simulations of propagation impairments relevant to satellite communication systems. By leveraging outputs from the Weather Research and Forecasting (WRF) model, the study outlined how spatial and temporal data can be systematically processed—from raw 4D atmospheric parameters to refined metrics such as attenuation time series and statistical characterizations.

The transformation process began with converting geographical data into coordinate systems compatible with satellite link analysis, progressing through geodetic, ECEF, ENU, and AER coordinate systems. This was followed by the application of satellite orbit models and projection methods that establish the spatial relationship between ground stations and satellites across different orbits. These steps culminated in the generation of attenuation maps and, ultimately, time series of atmospheric impairments.

Statistical processing techniques, including the calculation of CCDFs, fade durations, and fade slopes, provided deeper insight into the nature of atmospheric attenuation. These metrics are essential for designing and evaluating robust satellite communication systems. Furthermore, the use of prediction models and error analysis validated the accuracy and applicability of the methodology, with comparisons made against ITU standards and real-world measurements.

In essence, this chapter provides a comprehensive workflow to bridge meteorological forecasting with practical engineering applications in satellite communications. The tools, models, and transformations described here serve as a foundation for both simulation-based studies and performance evaluation of Earth-space communication links.

Chapter 5

Rain Cell Spatial Resolution Developing

Propagation of radio waves at frequencies above 10 GHz is highly sensitive to atmospheric conditions, particularly the presence of rain and clouds. Rain attenuation has been widely studied, and several models have been developed to estimate its long-term impact using annual statistics [3, 97, 98]. However, these models are typically built upon statistical observations made at fixed elevation angles, which limits their ability to accurately reflect complex, three-dimensional rain events—especially in the presence of asymmetry in spatial rainfall distribution.

One key limitation of conventional models is their lack of azimuthal resolution. They treat rain as a spatially uniform phenomenon and therefore fall short in accurately representing irregular or localized rain structures. To address this, modern tools like meteorological radars and Numerical Weather Prediction (NWP) systems offer more detailed, spatially-resolved data that are vital for constructing realistic physical models of rainfall.

However, the spatial resolution of NWP outputs (e.g. 1-2 km) is inherently limited and cannot resolve small-scale (e.g.100 m) rain cell structures relevant to high-frequency propagation analysis. Attempting to push NWP data to finer resolutions often leads to impractically long runtimes, reduced accuracy, and numerical instability. This is especially problematic for studies involving Low Earth Orbit (LEO) satellite links, where fine-scale atmospheric variations can have a significant impact on signal attenuation and fading characteristics. Consequently, to effectively model the smaller-scale dynamics of rain fields, synthetic and theoretical approaches are required.

A well-known solution to this problem is the EXCELL model [99], which represents rain fields using analytical exponential profiles derived from radar-based observations of single-peaked rain cells. This model offers a compact and computationally efficient method for reproducing realistic rain patterns at scales that NWP models cannot resolve.

To further extend spatial modeling capabilities, the MultiEXCELL model was introduced by [58]. It enhances EXCELL by simulating the natural ag-

gregation of multiple rain cells. Key parameters such as inter-cell distances, the number of cells per cluster, and rain rate thresholds are used to construct synthetic but realistic large-scale rain field configurations.

In this dissertation, we propose a hybrid approach that combines the strengths of NWP and MultiEXCELL. Rather than relying on radar data, we use NWP-derived rain rates as the initial input to the MultiEXCELL model. This enables a time-resolved, physically consistent, and scalable representation of atmospheric rain fields—significantly improving the accuracy of radio propagation impairment analysis, particularly for LEO satellite communication systems.

5.1 MultiEXCELL Model

A rain cell is defined as a spatially connected region where the rainfall intensity exceeds a certain threshold—typically around 5 mm/h. This model aims to accurately reproduce the cumulative distribution of point rain rates, denoted as $P(R)$. A theoretical expression for the radial profile of the rain rate within a single rain cell is given by:

$$R(\rho) = R_M \exp\left[-\left(\rho/\rho_0\right)^{2/k}\right] \tag{5.1}$$

In this equation:

- $R(\rho)$ [mm/h] is the rain rate at distance ρ from the center of the rain cell,
- R_M [mm/h] is the peak rain rate at the center of the cell,
- ρ [km] is the radial distance from the center,
- ρ_0 [km] is the equivalent radius at which the rain rate drops to $R_M/e^{2/k}$.

This equation describes a family of rain cell profiles, where the shape is controlled by the parameter k:

- $k = 1$ results in a **Gaussian** profile,
- $k = 2$ corresponds to an **exponential** profile,
- $k = 3$ gives a **hyper-exponential** profile.

According to [99], the exponential profile ($k = 2$) shows the best agreement with empirical radar observations. The influence of the k parameter will also be statistically evaluated later in this work.

Full model definition requires identifying parameter R_M and ρ_0 accurately. They can be measured by forcing appropriate descriptions to be the same in the radar cell (or WRF cell) and the model cell. Not all options are possible, of the many options, the one choosen should best meet the basic requirements of $P(R)$.

The goal can be achieved by fitting two main quantities of each rain cell which are (a) the rain cell area A_{th}, and (b) the average rain rate $\bar{R}$ [58]. These basic quantities of a rain cell are represented as

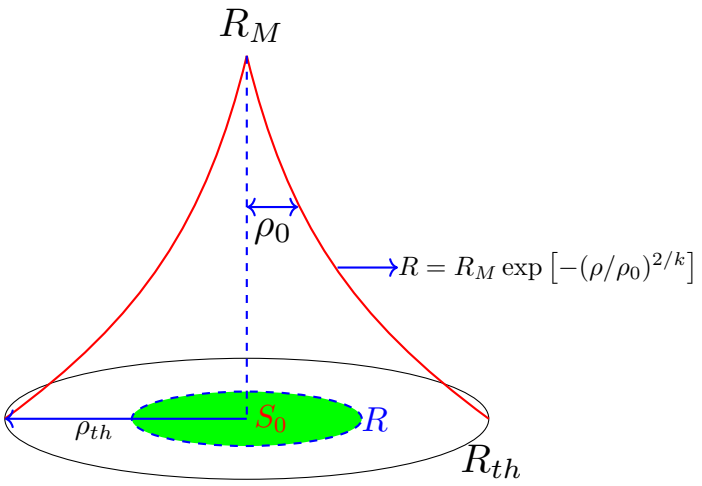


Figure 5.1: Typical rain cell

$$A_{th} = \pi\rho_{th}^2 = \pi\rho_0^2 \ln^k(R_M/R_{th}) \tag{5.2}$$

$$\bar{R}_{th} = \frac{1}{A_{th}} \int_0^{\rho_{th}} R(\rho) 2\pi\rho \, d\rho = \frac{k\, R_M}{\ln^k(R_M/R_{th})} \gamma(k, \ln(R_M/R_{th})) \tag{5.3}$$

where R_{th} is the minimum acceptance of rain rate to define a rain cell (e.g. 1-5 mm/h), ρ_{th} is the maximum radius of the rain cell equivalent to R_{th} (see Figure 5.1). $\gamma(s, x)$ is the lower incomplete gamma function:

$$\gamma(s, x) = \int_0^x t^{s-1} e^{-t} dt = x^s\, \Gamma(s)\, e^{-x} \sum_{k=0}^{\infty} \frac{x^k}{\Gamma(s+k+1)} \tag{5.4}$$

The left side of equations 5.2-5.3 is numerically computed using NWP (or radar) data, whereas the expressions on the right side are computed for synthetic cells with properties defined by eq. 5.1. Solving these equations yields the two key parameters, R_M and ρ_0, under the assumption of a fixed value for k.

During the numerical calculation, various possibilities for the parameters R_M and ρ_0 may arise. The most suitable profile can be selected by comparing other complementary descriptors of NWP (or radar) data and synthetic rain cells. Typically, peak rainfall rate ($\bar{R}max$), root mean square of the rain rate ($Rrms$), and cell dynamics (R_{dyn}) are other relevant descriptors. The descriptor $\bar{R}_{max}$ can be expressed as:

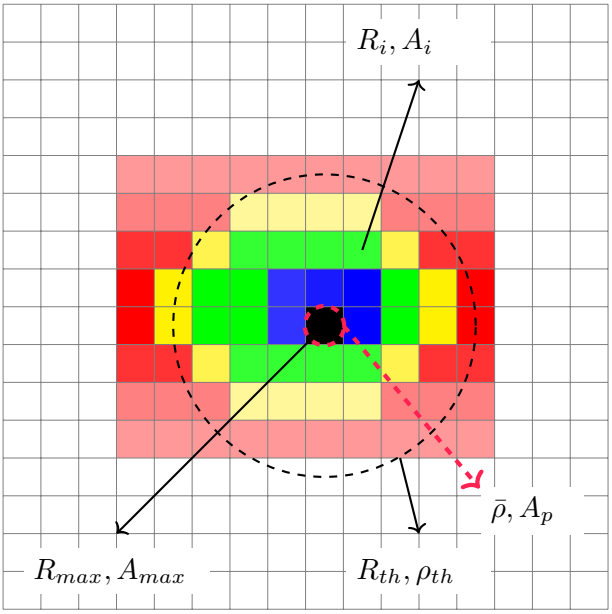


Figure 5.2: WRF and synthetic cell combination

$$\bar{R}_{max} = \frac{1}{A_p}\int_0^{\bar{\rho}} R(\rho) 2\pi\rho d\rho = \frac{k\,\pi\,R_M\,\rho_0^2}{A_p}\,\gamma(k,\bar{x}) \tag{5.5}$$

$$\bar{x} = \left(\frac{\bar{\rho}}{\rho_0}\right)^{2/k} \tag{5.6}$$

$$\bar{\rho} = \sqrt{A_p/\pi} \tag{5.7}$$

Where $\bar{\rho}$ and A_p represent the equivalent radius and the area of a single pixel (smallest grid size in the NWP or radar data) where the maximum rain rate occurs, typically at the center of each cell (see Figure 5.2). The second set of descriptors for rain cells includes R_{rms}, defined by:

$$R_{rms} = \sqrt{\frac{1}{A_{th}}\int_0^{\rho_{th}} R^2(\rho) 2\pi\rho d\rho} = \sqrt{\frac{k\,R_M^2}{2^k \ln^k(R_M/R_{th})}\,\gamma(k, 2\ln(R_M/R_{th}))} \tag{5.8}$$

where ρ_{th} and R_{th} have been previously explained and can also be seen in Figure 5.2. The last but not least descriptor is R_{dyn}, which is evaluated by:

$$R_{dyn} = \frac{\bar{R}_{th}}{R_M} = \frac{k}{\ln^k(R_M/R_{th})}\,\gamma(k, \ln(R_M/R_{th})) \tag{5.9}$$

Similarly to equations 5.2-5.3, the left side of equations 5.5, 5.8, and 5.9 are computed using WRF (or radar data), while the right side is determined from

synthetic rain cells. All three complementary descriptors are however not needed to calcuate the parameters of the rain cells. This will be discussed in section 5.2.2.1

5.1.1 Rain Cell Probability of Occurrence

The comprehensive definition of the cell model involves modeling the joint density function of R_M and ρ_0 for rain cells described by 5.1. Similar to the Marshal-Palmer drop size distribution, the model for the number density of rain cells, as introduced in [99], is assumed to follow an exponential distribution.

$$N(\rho_0, R_M) = N_0(R_M)\ \exp(-\frac{\rho_0}{\bar{\rho}_0(R_M)}) \tag{5.10}$$

Here, $N_0(R_M)$ represents the total number of cells per unit R_M range, and $\bar{\rho}_0$ is the conditional average cell radius. The experimental values are effectively interpolated using a double power-law form.

$$\bar{\rho}_0(R_M) = 1.7\left[\left(\frac{R_M}{6}\right)^{-10} + \left(\frac{R_M}{6}\right)^{-0.26}\right] \qquad R_M > (R_{th} = 5mm/h) \tag{5.11}$$

Equation 5.10 can be linked to the complementary cumulative distribution function (CCDF) of rain density through the following relationship (an example of a typical rain cell is provided in Fig. 5.1).

$$P(R) = \int_R^\infty \int_0^\infty S_0(R, R_M, \rho_0)\, N(\rho_0, R_M)\, d\left(\frac{\rho_0}{\bar{\rho}_0}\right) dR_M \tag{5.12}$$

where $S_0(R, R_M, \rho_0)$ represents the area where the rain rate intensity exceeds R, with the rain rate structure given by Eq. 5.1 for a specific value of $k = 2$:

$$S_0(R, R_M, \rho_0) = \pi\rho^2 = \pi\rho_0^2 \ln^2(R_M/R) \tag{5.13}$$

By performing mathematical operations on Eq. 5.12, as detailed in [99], the function $N_0(R_M)$ is calculated as follows:

$$N_0(R_M) = -\frac{1}{4\,\pi\,\bar{\rho}_0(R_M)}\ \frac{\partial^3 P(R)}{\partial(\ln R)^3}\bigg|_{R=R_M} \tag{5.14}$$

5.2 Implementation of MultiEXCELL on WRF Data

As mentioned, one of the direct outputs from NWP is the rainfall rate. However, due to the relatively low temporal and spatial resolution in NWP, the MultiEXCELL model is employed to address this limitation. This model is capable of recovering the maximum rainfall rate that might be missed due to integration over a time interval (e.g., 5 minutes) in NWPs. In the relationships

5.2-5.9, all the parameters on the left side ($A_{th}, \bar{R}th, \bar{R}max, R_{rms}, R_{dyn}$) are directly calculated from the NWP rain rate.

Typically, the combination of MultiEXCELL and NWPs involves three main steps:

1. Cells Detection
2. Solving cell's characteristics equations
3. New cells execution

Each step and their challenges will be described in following sections

5.2.1 Cells Detection

In the initial step of implementing MultiEXCELL on NWP data, the identification and categorization of individual rain cells within each time frame is crucial. This process consists of two main parts: (a) determining fixed parameters and (b) searching and tracking the rain cells in the domain. MultiEXCELL has predefined parameters that need to be established during the first step, which are primarily discussed in Section 5.2.1.1. The algorithm for searching and tracking individual rain cells is detailed in Section 5.2.1.2.

5.2.1.1 Fix Parameters in Cells Detection

In this step, three crucial parameters for cell detection are defined: the maximum radius (ρ_{th}), the minimum rain threshold (R_{th}), and the minimum of the central rain rate ($R_{M_{min}}$).

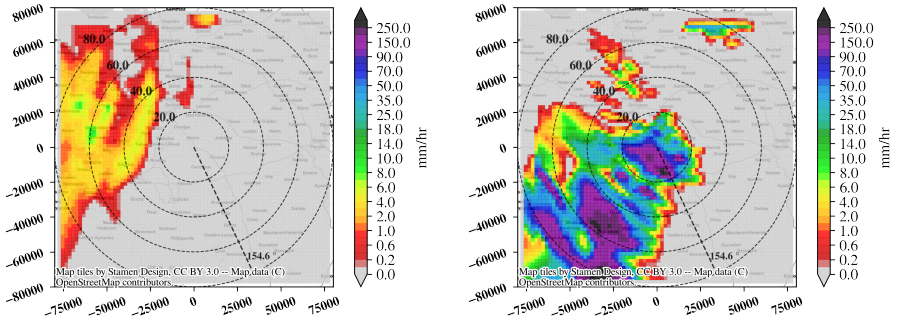
The parameter $R_{M_{min}}$ plays a significant role in determining whether the rain over the domain is predominantly heavy or if there are mainly shallow rain events. This distinction is essential as it is preferable to exclude very small-sized shallow rain events when coexisting with larger, heavier rain events over the domain. A simple procedure for determining this parameter involves:

$$R_{M_{min}} = \begin{cases} 5, & \text{If} \quad R_{rms} \geq 5 \\ 1, & \text{o.c} \end{cases} \tag{5.15}$$

This ensures that the parameter $R_{M_{min}}$ is appropriately chosen based on the expected nature of rain events over the domain. For instance, refer to Figure 5.3 for two different rain events with the identification of $R_{M_{min}}$ according to Equation 5.15. In Figure 5.3a, R_{rms} is 2.6, resulting in $R_{M_{min}}$ of 1 mm/hr, while in Figure 5.3b, R_{rms} is 77.9, leading to $R_{M_{min}}$ of 5 mm/hr.

The other two parameters, ρ_{th} and R_{th}, require careful consideration. According to the main reference [58] which is based on extensive weather radar datasets, typical values of $R_{th} = 1$ mm/hr and $\rho_{th} = 10$ km yield satisfactory results for various types of rain events. The decision about these values necessitates visualizing their effects on the final synthetic cells.

Figure 5.4 clearly demonstrates that large values of $\rho_{th} \geq 10km$ lead to the merging of different rain cells, while very low values of $\rho_{th} \leq 10$ create small rain cells with low precision. On the other hand, Figure 5.4 illustrates that the



(a) 2019-06-05 15:40:00 (b) 2019-07-27 04:00:00

Figure 5.3: (a) and (b) show the original rain rate with the central location at Louvain-la-Neuve. The R_{rms} in (a) is 2.6 and in (b) is 77.9

restriction $R_{th} = 1$ mm/hr ensures the existence of all rain cells in the synthetic model without any removal or addition of original rain events. However, the restriction $R_{th} = 5$ mm/hr may eliminate important shallow rain events. It should be noted that the goal is not to precisely replicate real rain events with MultiEXCELL. Instead, the main objective is to create a model that statistically defines rain attenuation in Earth-space radio wave propagation, approaching reality.

One more parameter that needs to be determined before proceeding is the shape factor k. Lower k makes the rain cell profile sharper near the center but decays more quickly with distance, while higher k produces a more gradual decay and a flatter, more "spread out" cell.

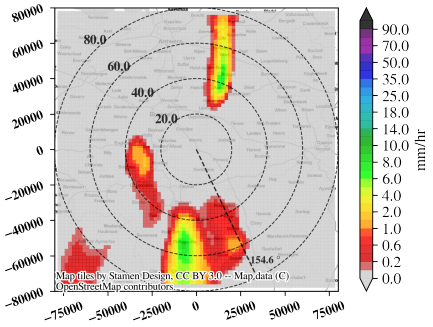
Following [58], the choice of $k = 2$ has been shown to statistically reproduce rain cell shapes that are most consistent with experimental observations from radar and ground-based measurements in temperate climates. In particular, [58] reports that $k = 2$ provides the best fit to the distribution of measured rain cell radii and attenuation gradients, outperforming both lower ($k < 2$) and higher ($k > 2$) values in terms of matching observed spatial rainfall variability.

Therefore, in this work, k is fixed at 2 to ensure compatibility with previous studies and to maintain realistic spatial characteristics of synthetic rain cells.

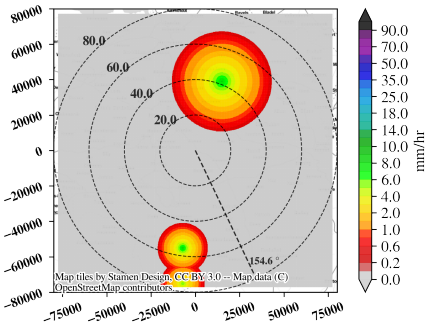
5.2.1.2 Search and Track the Rain Cells

With the predefined parameters in Section 5.2.1.1, the process of identifying individual rain cells within the domain can begin. Various algorithms exist for this task, but the most effective method involves detecting multiple peaks in rain rate. Before starting the search, it is advisable to filter out all rain rate values below $R_{th} = 1$ mm/hr. Figure 5.5 shows the original rain rate distribution before and after removing values below this threshold. This step is crucial for eliminating the influence of very low rain rates, ensuring more accurate solutions for the rain cell equations.

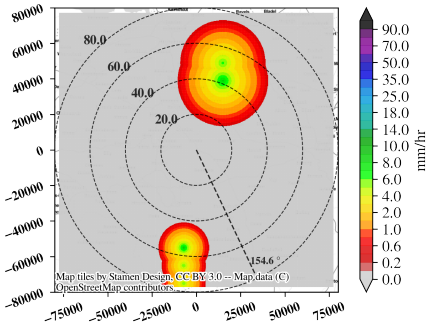
The search and tracking of rain cells are performed over the remaining rain



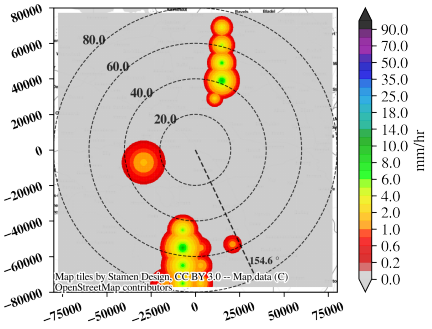
(a) Original rain rate



(b) Synthetic rain cell with $R_{th} = 5\,mm/hr$ and $\rho_{th} = 20\,km$

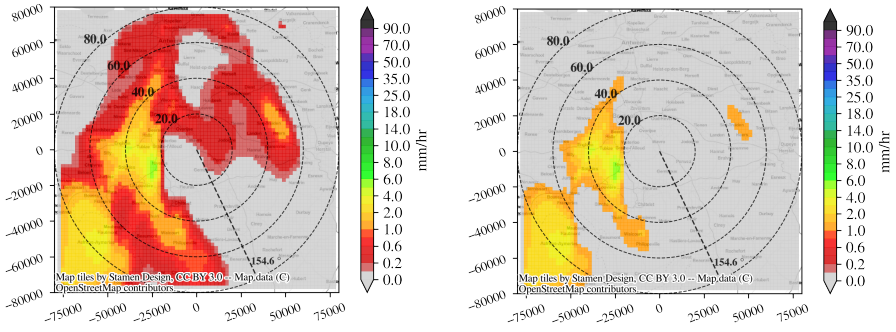


(c) Synthetic rain cell with $R_{th} = 5\,mm/hr$ and $\rho_{th} = 10\,km$



(d) Synthetic rain cell with $R_{th} = 1\,mm/hr$ and $\rho_{th} = 10\,km$

Figure 5.4: (a) Original and (b-d) synthetic rain cells showing the effects of restriction parameters R_{th} and ρ_{th} on the final synthetic rain cells. The central location is at Louvain-la-Neuve and the time is 2019-06-05 03:25:00



(a) Original rain rate

(b) Discarding the rain rate points less than $R_{th} = 1\,mm/hr$

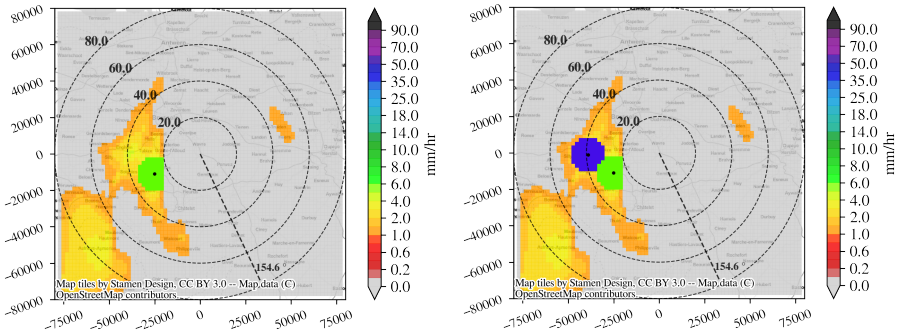
Figure 5.5: original rain rate : before and after discarding low rain rates. The central location is at Louvain-la-Neuve and the time is 2019-06-05 08:40:00

rate points. Finding individual rain cells involves identifying the first maximum rain rate that exceeds the predefined parameter $R_{M_{min}}$ (as defined in Section 5.2.1.1). Pixels of rain rate within a distance less than $\rho_{th} = 10\,km$ from this first maximum are considered part of the first rain cell and are saved for further processing. The first rain cell is marked and saved in green color in Figure 5.6a. Subsequently, the algorithm searches for another maximum rain rate point outside the previously identified cell(s). Similar to the previous step, it collects the rain rate points close to the second maximum, designating them as the second cell (see Figure 5.6b). This process continues until no more rain rate pixels are left in the domain. Rain cells consecutively detected in a single time frame of rain rate issued from NWP, are illustrated in Figure 5.6.

The rain cell detection process being completed, the details of a sample rain cell, that will be utilized in the subsequent processing steps, have been compiled in Table 5.1. Line *29 in Table 5.1, highlighted in cyan, corresponds to the center of the first cell in Figure 5.6a. The last two rows of Table 5.1 present the values of three cell descriptors, defined in equations 5.2, 5.3, and 5.5, offering a description of cell characteristics. A detailed discussion on these descriptors is deferred to Chapter 5.2.2.1. Despite the equi-spaced grid in NWP data, the slight variations in pixel area (A_i in Table 5.1) are attributed to the map projection (see Section 4.2). The last column of Table 5.1 illustrates the distance of each rain rate pixel from the center or the maximum rain rate of the cell.

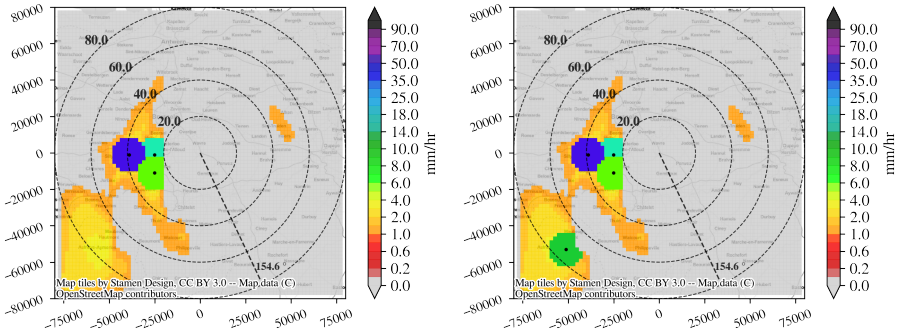
5.2.2 Solving Cell's Characteristics Equations

The characteristics of each rain cell, for different time frames, have been determined in the previous section. Using these data, the cell parameters corresponding to the left sides of equations 5.2, 5.3, 5.5, 5.8, and 5.9 can now be calculated. However, it is not necessary to consider all complementary descriptors in equations 5.5, 5.8, and 5.9 at the same time. Instead, selecting just



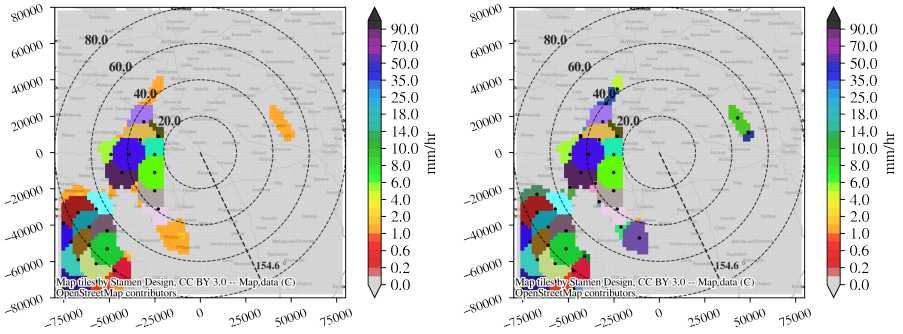
(a) 1^{st} rain cell

(b) 2^{nd} rain cell



(c) 3^{rd} rain cell

(d) 4^{th} rain cell



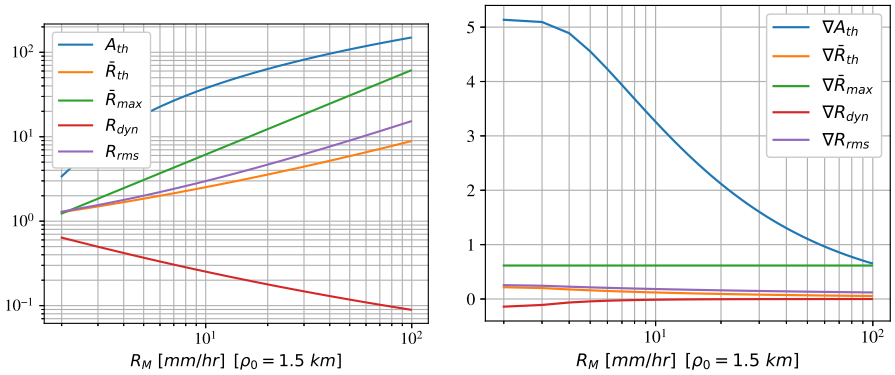
(e) 24^{th} rain cell

(f) 37^{th} rain cell

Figure 5.6: Search and track rain cells by finding the maximum(s) and adapting the rain rate pixels close to the nearest maximum rain rate.

Table 5.1: Details of first rain cell in Figure 5.6a

	Location X[m]	Location Y[m]	Area [km^2]	Rain Rate [mm/hr]	Distance from the center [km]
0	-29095.631118	-19003.270738	4.016508	2.470041	8.954238
1	-27089.170970	-19003.810937	4.015657	3.566504	8.252819
2	-25082.481869	-19004.434957	4.016059	3.976815	8.005795
3	-23075.826346	-19003.443986	4.016260	2.862700	8.252521
4	-21069.148208	-19003.384376	4.015641	1.344464	8.954545
5	-31102.130956	-17001.995809	4.015435	2.121167	8.501459
6	-29095.645824	-17002.033429	4.016058	2.703678	7.221158
7	-27089.201208	-17001.728916	4.016062	3.931924	6.329570
8	-25082.530403	-17001.932285	4.016069	4.633456	6.003292
...					
13	-29095.652054	-15000.791603	4.015640	2.959813	5.667597
14	-27089.227911	-15000.491049	4.016928	4.161149	4.476750
15	-25082.575647	-15000.273763	4.015189	5.167260	4.001634
16	-23075.934961	-15000.987124	4.015423	4.295938	4.477227
17	-21069.297392	-15000.933777	4.015658	2.063386	5.667901
18	-33108.478967	-12999.535141	4.014735	2.138582	8.271519
19	-31102.062118	-12999.923517	4.015389	2.641322	6.343409
20	-29095.649806	-12999.545063	4.015583	3.277533	4.484199
21	-27089.246707	-12999.248464	4.015192	4.301136	2.833548
22	-25082.577728	-12998.186337	4.015198	5.470407	1.999546
23	-23075.996029	-12999.751630	4.014969	4.883735	2.833899
24	-21069.345803	-12999.701550	4.015632	2.439349	4.484485
25	-33108.425023	-10998.274968	4.014745	2.326360	8.025807
26	-31102.066079	-10999.091984	4.015365	2.894704	6.019448
27	-29095.639081	-10998.293615	4.015593	3.566615	4.013021
28	-27089.257593	-10998.000967	4.015167	4.431749	2.006639
*29	-25082.618441	-10998.639886	4.015172	5.592051	0.000000
30	-23076.016543	-10998.511364	4.014087	5.199075	2.006602
...					
48	-27089.211233	-4994.651563	4.015188	4.457695	6.330426
49	-25082.604712	-4994.877300	4.015259	4.866548	6.003763
50	-23076.005724	-4995.183584	4.015984	4.301341	6.329928
51	-21069.376433	-4994.721863	4.015822	2.220157	7.221713
52	-29095.578834	-2993.234451	4.015588	3.433380	8.954907
53	-27089.190484	-2993.382460	4.015261	3.966213	8.252907
54	-25082.574238	-2993.612021	4.014441	4.394635	8.005028
55	-23075.967396	-2994.346179	4.015167	3.778225	8.251992
56	-21069.328233	-2993.887684	4.016287	1.862648	8.954471
eq.5.2-5.3			$A_{th} = \sum A_i = 228.88$	$\bar{R}_{th} = 3.55$	
eq.5.5			$A_p = 4.01$	$\bar{R}_{max} = 5.59$	$\bar{\rho} = 1.13$



(a) Rain cells descriptors

(b) Gradient of rain cells descriptors

Figure 5.7: Rain cell characteristics versus R_M [mm/hr] with fixed value of $\rho_0 = 1.5$ km. (a) shows the solid values of each descriptors and (b) represents the gradient or changes of each descriptors over R_M parameter.

one of these, along with the two primary descriptors 5.2 and 5.3, is sufficient, as discussed in Section 5.2.2.1. Once the appropriate descriptors are chosen and solved for, the results must be carefully examined for accuracy. Additional constraints on these computed variables will be further discussed in this chapter.

5.2.2.1 Suitable Non-Linear Equations in Solver Engine

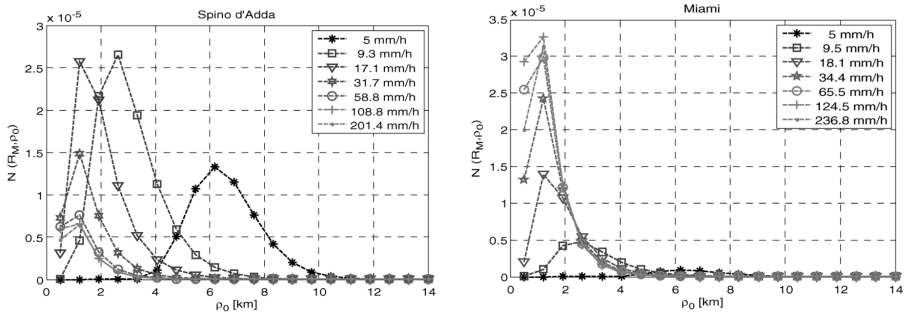
Not all equations from 5.2 to 5.9 are required to determine the unknown parameters R_M and ρ_0, only three are sufficient for the solver engine. As shown in Figure 5.7, the variation of R_{dyn} with respect to R_M is nearly zero, making it ineffective for solving nonlinear equations.

Among the available variables, A_{th} and $\bar{R}_{max}$ show the highest sensitivity to changes in R_M. Additionally, between $\bar{R}_{th}$ and R_{rms}, either one is sufficient for the solver. Based on these observations, the three selected parameters for determining the unknowns are A_{th}, $\bar{R}_{th}$, and $\bar{R}_{max}$.

5.2.2.2 Restriction on Variable ρ_0

There is no guarantee that solving the non-linear equations from 5.2 to 5.9 will yield accurate results. Occasionally, a rain cell may appear at the border of the map projection, leading to erroneous values for R_M and ρ_0. The inaccuracies in the variable ρ_0 tend to be more significant than those in R_M. To further elaborate on the appropriate results for ρ_0, it is beneficial to examine the data presented in [58], illustrated in Figure 5.8.

Figure 5.8 illustrates the probability of rain cell occurrence calculated using Equation 5.10 for two ground stations located in Spino d'Adda, Italy, and Miami, USA. The statistical analysis suggests that, regardless of whether the rain is shallow or heavy, the parameter ρ_0 for rain cells should not exceed 10



(a) Spino d'Adda (45.4° N, 9.5° E) (b) Miami (25.65° N, -80.43° E)

Figure 5.8: Rain cells' probability of occurrence relative to Spino d'Adda and to Miami [58]

km. Consequently, when using the solver engine for equations 5.2 to 5.9, a maximum restriction of 10 km should be applied to the found value of ρ_0.

Figure 5.9a illustrates a rain event centered at Louvain-la-Neuve ground station. The rain event detection algorithm of Section 5.2.1 identifies 30 rain cells, with the 9^{th} cell occurring at the border of the domain. Without the restriction of $\rho_0 \leq 10$ km, the equivalent rain cell becomes excessively wide, as shown in Figure 5.9b. This occurs when only half of the rain cell is available on the map, leading to a large ρ_0 to compensate for this deficiency. Since only rain events close to the ground station are crucial for calculating rain attenuation, we can manually adjust or exclude rain events far from the station or close to the border without affecting the accuracy of the calculation. Two options are available to address this issue.

1. Delete the whole corresponding rain cells with large $\rho_0 > 10\,km$
2. Change the ρ_0 manually for the corresponding rain cells by

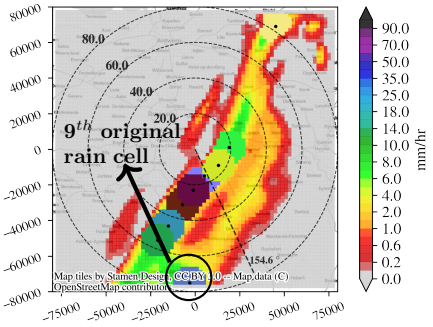
$$\rho_0 = \frac{\rho_{th}}{2} \qquad \text{if } \rho_0 \geq 10\,km \tag{5.16}$$

with $\rho_{th} = 10\,km$

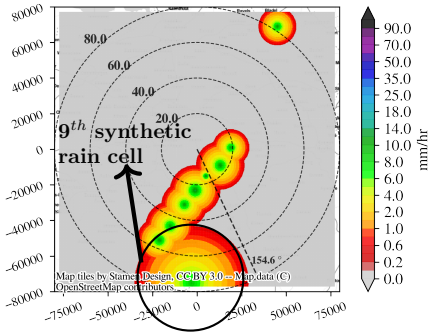
Figures 5.9c and 5.9d present the outcomes of the two aforementioned options. It is important to indicate that these adjustments do not impact rain attenuation calculations, especially when the ground station is situated at the center of the domain. In the subsequent simulations in this dissertation, Option No. 2 has been selected.

5.2.2.3 Center of Rain Cell

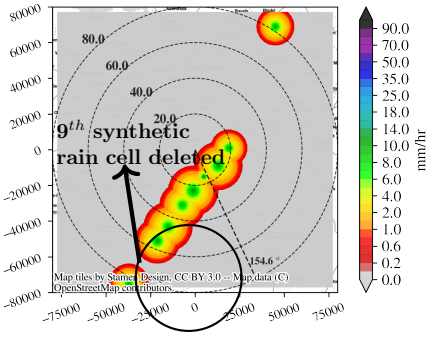
During the rain cell detection process (refer to section 5.2.1.2), it is possible for the identified rain cells to exhibit asymmetry. Such asymmetry often occurs when a rain event is extensive and elongated along a line. In such instances, the center of the rain cell might not align with the position of the maximum



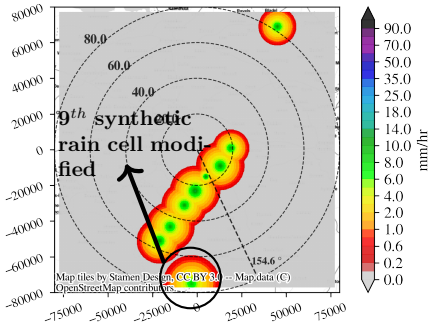
(a) Original rain rate



(b) Synthetic rain cell of 9^{th} rain event without the ρ_0 restriction ($\rho_0 = 12\,km$)



(c) Synthetic rain cell of 9^{th} rain event with deleting the 34^{th} rain cell



(d) Synthetic rain cell of 9^{th} rain event with limitation of $\rho_0 = \rho_{th}/2$

Figure 5.9: Manually modify the $\rho_0 = 12\,km$ parameter for 9^{th} rain event to $\rho_0 = 10/2 = 5\,km$. The Figures (b-d) do not contains all the rain cells and the focus was on 9^{th} rain cell to clearly show the effect of ρ_0. The ground station is at Louvain-la-Neuve at time slot of 2019-06-05 05:05:00.

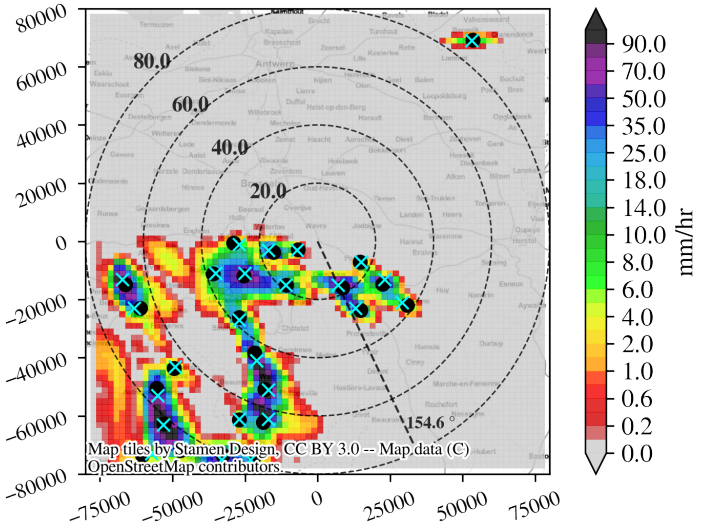


Figure 5.10: Rain cell center: 'x' marks the peak location of rain rates, and '•' are the rain mass's locations. The ground station is at Louvain-la-Neuve at the time slot of 2019-07-27 03:00:00.

rain pixel. In cases of closely spaced rain events, the shape may no longer be entirely homogeneous, and the location of the highest rainfall rate could extend to the cell boundaries. Consequently, two potential choices for defining the rain center are established as follows:

1. The location where the peak of the rain rate occurs. This situation becomes particularly challenging when the rain is highly heterogeneous, featuring multiple peaks, or when the peak location deviates towards the edges of the rain.

2. The center of mass formula can serve as the rain center, with options such as rain rate (R [mm/hr]) or integrated rainwater content M [g/m^2].

$$r_c = \frac{1}{R} \sum R_i \, r_i \tag{5.17}$$

where r_c will be the mass center location, R the summation of rain rate points, R_i denotes the rain rate in each pixel area, and r_i corresponds to the pixel location.

Figure 5.10 illustrates the two types of rain center locations. The dot and cross symbols represent the center of mass and peak locations of rain for individual cells, respectively.

5.2.3 New Rain Cells Execution

In the previous section, all the relevant details of rain cells have been obtained for each time frame. The next step is to combine and process all the cells to-

gether to construct the entire rain event over the domain. This section consists of two steps to finalize the synthetic rain cells. Firstly, the termination value of the rain rate is defined, and then the issue of the intersection area between neighboring cells is addressed.

5.2.3.1 Rain Cells Termination Limit

As discussed in Section 5.2.1.2, low values of rain events have been discarded to prevent processing faults in further steps. However, when reconstructing new rain cells, it is impractical to extend each individual rain cell down to the $0\,mm/hr$ value. Without limitations at the border for termination, each single rain cell would expand over a large area. Figure 5.11a illustrates an example of an original rain event, and the corresponding synthetic rain cells without any termination limit in execution are plotted in Figure 5.11b. This clearly highlights the importance of defining a limitation on rain cell execution; otherwise, faulty rain attenuation results for shallow rain events would occur. Figures 5.11c and 5.11d show the effect of rain rate termination values set at 1 mm/hr and 0.5 mm/hr, respectively. A termination limit of 0.5 mm/hr operates effectively for all types of rain events, yielding final results that closely resemble the original ones. This rain rate termination value of 0.5 mm/hr has been chosen for the subsequent sections of this dissertation.

5.2.3.2 Rain Cells Intersection Area

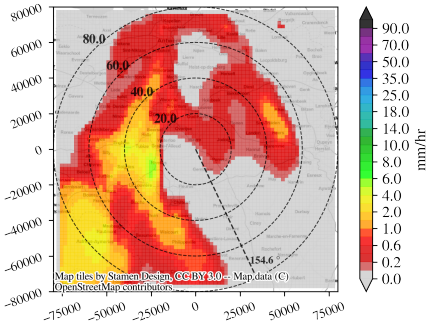
The final step in executing synthetic rain cells addresses the issue of overlapping areas between neighboring cells. Summing up the rain rate in the intersection area is not reasonable, as it would lead to a rupture in the borders. This, in turn, would result in the local $P(R)$ no longer being accurately reproduced, since $N(R_M, \rho_0)$ is calculated based on isolated rain cells. The method proposed in [58] is adopted here as well for processing the intersection area coverage.

The solution involves redistributing all overlapping rain rate values smaller than R_0 around the structure of the aggregated cells (see Figure 5.12a). This ensures that the overall trend of the rain profile still decreases exponentially as one moves away from the center of the structure. However, the decrease is more gradual than in the original rain cells' profile (Figure 5.12b).

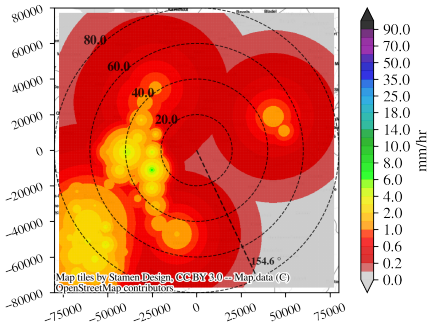
5.3 Conclusion

In this chapter, we addressed a critical limitation in the spatial resolution of rainfall representation for radio wave propagation modeling—particularly at frequencies above 10 GHz. While Numerical Weather Prediction (NWP) models provide valuable atmospheric data, their coarse resolution restricts their ability to capture fine-scale rain cell structures that are essential for accurate attenuation modeling in Low Earth Orbit (LEO) satellite links.

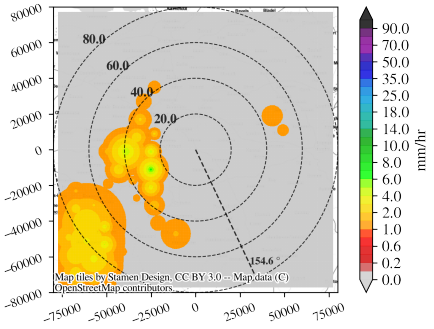
To overcome this constraint, we adopted and extended the MultiEXCELL model, which generates high-resolution synthetic rain fields using statistical



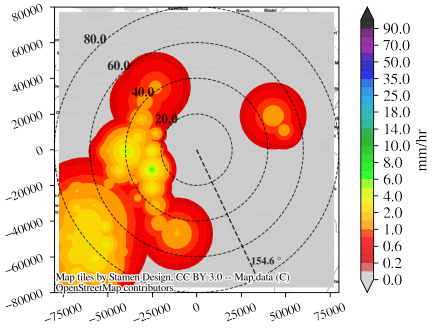
(a) Original rain rate



(b) Rain cells without any termination limit, $R_{th} = 0\,mm/hr$



(c) Rain cells with the termination limit of $R_{th} = 1\,mm/hr$



(d) Rain cells with the termination limit of $R_{th} = 0.5\,mm/hr$

Figure 5.11: Rain rate Termination effect on the final rain cell's execution. The ground station is at Louvain-la-Neuve at time slot of 2019-06-05 08:40:00.

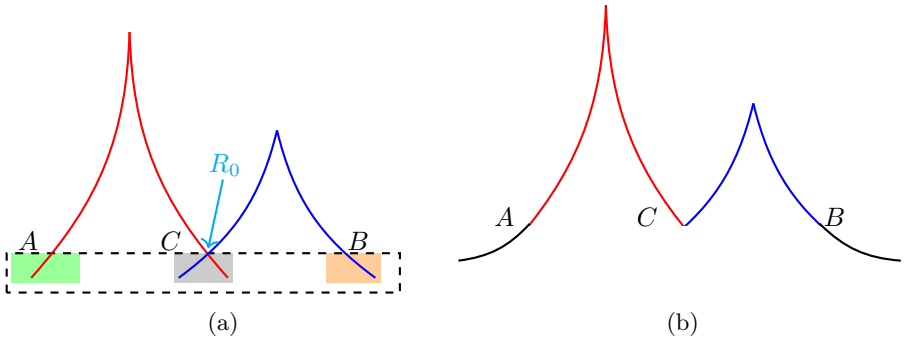


Figure 5.12: Redistribution of the overlapping rain rates around the structure

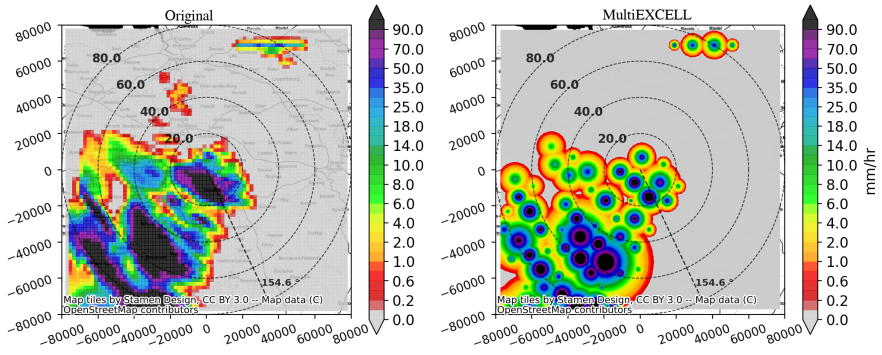


Figure 5.13: The $R_{rms} > 5mm/hr$ in the original domain, then the minimum $(R_M) = 5$ mm/hr

and physically-informed parameters. The foundation of this model lies in the EXCELL analytical rain cell profile, characterized by parameters such as peak rain rate (R_M), equivalent radius (ρ_0), and shape factor (k). These parameters were carefully calibrated against descriptors derived from NWP outputs, enabling consistent and realistic reconstruction of rain cell structures beyond the capability of NWP data alone.

Through a step-by-step method involving rain cell detection, parameter solving, and synthetic execution, we introduce improvements including: adaptive shape factor usage, rain center estimation techniques, practical restrictions on cell radius, and robust handling of cell overlap and termination. Each of these refinements plays a important role in producing a spatially consistent, physically meaningful, and computationally tractable representation of rain fields.

The hybrid approach of combining NWP input with MultiEXCELL modeling paves the way for accurate and scalable simulations of rain-induced attenuation effects in satellite communication studies.

Chapter 6

Improving Rain Cell Temporal Resolution

As the operating frequency of satellite communication systems increases, the propagation impairments caused by atmospheric gases, clouds, and especially rain become more severe [100]. These impairments result in attenuation and scintillation effects that directly threaten link availability. While high static margins could theoretically compensate for such effects, in practice, they are costly and often inefficient—particularly in high-frequency bands where margins would need to be prohibitively large.

To address this challenge, modern systems adopt Fade Mitigation Techniques (FMT), which dynamically adjust link parameters such as power, data rate, and coding based on real-time channel conditions [16]. FMT strategies can be implemented in two principal ways: either at the level of individual terminals (e.g., each Return Channel Satellite Terminal, or RCST, adapting based on local rain attenuation estimates), or centrally, where the Network Control Center (NCC) uses broader atmospheric data—potentially from a weather radar network—to manage resources across the satellite footprint.

Whether for system design or real-time resource allocation, a key requirement for effective FMT is the ability to predict or simulate time-series of attenuation with sufficient temporal resolution. This is especially important in the absence of in-situ measurements at the receiver location. However, the output of Numerical Weather Prediction (NWP) models—commonly used for rain rate and attenuation estimation—is typically limited to temporal resolutions on the order of 5 to 15 minutes due to computational and storage constraints. While a finer resolution (e.g., 1 minute) is feasible for short-term studies, it becomes impractical over long durations. This limitation is particularly relevant for rapidly changing parameters like rain rate, which can exhibit significant variability within a 5-minute timeframe.

In the previous chapter, we addressed spatial resolution limitations by integrating the MultiEXCELL model with NWP outputs. This allowed us to reconstruct high-resolution synthetic rain cells that better represent the small-scale spatial variability critical for accurate attenuation modeling. Building on

this advancement, the current chapter shifts focus to the *temporal domain*.

To improve the temporal resolution of rain event dynamics, we introduce two complementary approaches. The first method, discussed in Section 6.1, considers rain cell displacement as a function of wind speed and direction, leveraging meteorological wind fields to simulate rain motion. The second method, covered in Section 6.2, applies *optical flow* algorithms—borrowed from computer vision—to track and estimate the movement of rain features between consecutive time steps. By interpolating intermediate states based on detected motion, the optical flow method allows us to reconstruct high-resolution temporal sequences of rain fields.

Together, these techniques significantly enhance our ability to simulate fast-varying rain attenuation events, which is essential for evaluating and optimizing FMT performance in high-frequency satellite communication systems, particularly those involving LEO satellites.

6.1 Rain Cell Displacement and Wind Field Complexity

Figure 6.1 illustrates the spatial distribution of simulated precipitation and the wind field at an altitude corresponding to the 700 hPa pressure level, as obtained from the WRF (Weather Research and Forecasting) model. The 700 hPa level, typically located around 3 km above sea level, is a key atmospheric layer where mid-tropospheric dynamics significantly influence convective systems and rainfall patterns.

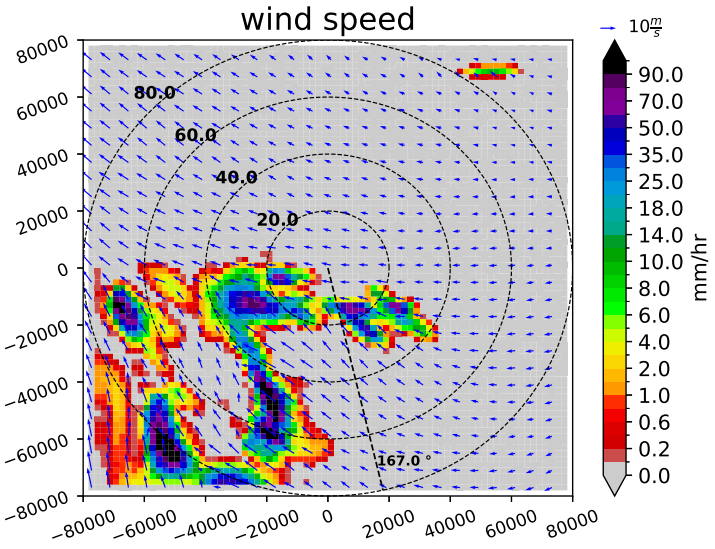
While it may seem intuitive to displace rain cells in the direction of the wind to simulate advection, the process is inherently complex for several reasons:

- **Three-dimensional wind field:** The wind at 700 hPa includes three components — the zonal (u), meridional (v), and vertical (w) velocities. Although the horizontal advection of rain is primarily influenced by the u and v components, the vertical motion (w) significantly impacts the growth, decay, and vertical extent of rain systems.

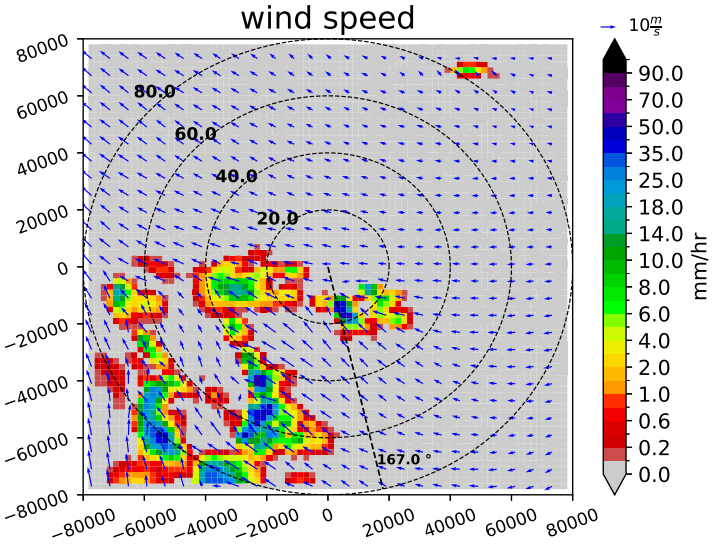
- **Rainfall is not a passive tracer:** Unlike aerosols or pollutants, precipitation is subject to formation and dissipation processes that are closely tied to microphysics, thermodynamics, and vertical motion. Simply shifting rain cells with horizontal wind vectors does not account for processes like evaporation, condensation, or downdrafts.

- **Temporal and spatial variability:** The wind field can vary rapidly in time and space, especially in convective environments. This variability makes it difficult to apply a consistent displacement vector for rain events over extended periods or areas.

- **Shear and deformation effects:** Wind shear and deformation within the 700 hPa layer can distort or stretch rain structures in complex ways. Displacing rain uniformly along the mean wind direction oversimplifies



(a) 2019-07-27 03:00:00.



(b) 2019-07-27 03:05:00.

Figure 6.1: Simulated precipitation intensity and wind vectors at the 700 hPa level using WRF output. Wind field includes horizontal (u, v). The ground station is at Louvain-la-Neuve

these effects and can introduce significant errors in modeled rain distribution.

Therefore, while the idea of displacing precipitation fields according to wind direction seems practical, especially for synthetic time series generation or model simplification, it requires careful consideration of the full 3D wind structure and rain microphysics. In high-resolution simulations like WRF, these interactions are intrinsically modeled, but mimicking them post-simulation through simple advection can lead to inaccurate representations of rain dynamics.

6.2 Optical Flow

Optical flow refers to the pattern of apparent motion observed in a visual scene due to the relative motion between an observer and the scene itself. The concept of optical flow was introduced by American psychologist James J. Gibson in the 1940s, elucidating the visual stimuli experienced by moving animals in their surroundings. The application of optical flow methods for calculating the motion between two image frames captured at different times, denoted as t and $t + dt$, was initially introduced by Horn and Schunck in 1981 [101].

Beyond its origins in image analysis, optical flow has found widespread application in various domains, particularly in robotics research. Its versatility has been leveraged for tasks such as image dominant plane extraction, object detection and tracking, movement detection, robot navigation, and visual odometry [102]. The significance of optical flow extends to the control of micro air vehicles, as recognized by researchers in the field [103].

The versatile applications of optical flow extend to rain motion analysis in radar data, as exemplified by Ayzel in their study [60]. In this particular context, optical flow was utilized for detecting and tracking rain events, highlighting its effectiveness in Numerical Weather Prediction (NWP) and simulation applications related to earth-space satellite communication impairments.

6.2.1 Preliminary Theory

For a 2D dimensional image (brightness image), the intensity $I(x, y, t)$ at location (x, y) and time t will undergo a spatial displacement $(\Delta x, \Delta y)$ after a time interval Δt between two image frames. Most optical flow computation methods assume that the color/intensity of a pixel remains constant under displacement, giving rise to the brightness constancy constraint:

$$I(x, y, t) = I(x + \Delta x, y + \Delta y, t + \Delta t) \tag{6.1}$$

Assuming the displacement is small, the Taylor series can be expanded to obtain:

$$I(x+\Delta x, y+\Delta y, t+\Delta t) = I(x, y, t)+\frac{\partial I}{\partial x}\Delta x+\frac{\partial I}{\partial y}\Delta y+\frac{\partial I}{\partial t}\Delta t+\text{higher-order terms} \tag{6.2}$$

Assuming a linear approximation for the system, the higher-order terms will vanish, resulting in:

$$\frac{\partial I}{\partial x}\Delta x + \frac{\partial I}{\partial y}\Delta y + \frac{\partial I}{\partial t}\Delta t = 0 \tag{6.3}$$

dividing the above equation by Δt:

$$\frac{\partial I}{\partial x}u_x + \frac{\partial I}{\partial y}u_y + \frac{\partial I}{\partial t} = 0 \tag{6.4}$$

where

$$\begin{aligned} u_x &= \frac{\Delta x}{\Delta t} \\ u_y &= \frac{\Delta y}{\Delta t} \end{aligned} \tag{6.5}$$

are two components of the optical flow of the voxel (x, y, t). The $\frac{\partial I}{\partial x}$, $\frac{\partial I}{\partial y}$ and $\frac{\partial I}{\partial t}$ are the derivatives of the image intensity at (x, y, t) in the corresponding components. The equation 6.4 can be rewritten in the form:

$$\nabla I \cdot \mathbf{u} + I_t = 0 \tag{6.6}$$

This equation is known as the aperture problem in optical flow methods, and due to its two unknown parameters (u_x, u_y), it cannot be easily solved. Various methods have been developed to estimate these unknown parameters by introducing additional conditions to the equation.

6.2.2 Methods of Determination

Optical flow refers to a broad class of techniques designed to estimate the apparent motion of objects or patterns between consecutive image frames. A comprehensive quantitative comparison of existing methods can be found in [104, 105]. The most widely adopted optical flow methods include:

- **Lucas–Kanade Method** (and its iterative variant): This method estimates motion within small image patches using an affine model of the flow field. It is well-suited for capturing small and consistent displacements [106].
- **Horn–Schunck Method**: A global method that formulates optical flow as an optimization problem. It minimizes a cost function that combines the brightness constancy assumption with a smoothness constraint, resulting in a dense flow field [101, 106].
- **Buxton–Buxton Method**: This method models edge motion in image sequences and offers a unique perspective on estimating motion along intensity contours [107].

- **Black–Jepson Method**: Focused on coarse motion estimation, this method uses correlation techniques to approximate optical flow across larger image regions [108].
- **Total Variation (TV) Methods**: These techniques extend the Horn–Schunck framework by introducing alternative data fidelity and regularization terms. They are particularly effective in preserving motion discontinuities while maintaining robustness.
- **Phase Correlation Method**: Based on the inverse of the normalized cross-power spectrum, this method is computationally efficient and particularly suitable for translational motion estimation.

Among these approaches, this study focuses on two widely used and well-validated differential methods: the *Lucas–Kanade* and *TV-L1* algorithms. Both rely on evaluating spatial and temporal intensity gradients between consecutive images. These differential methods operate by quantifying the difference in intensity patterns between frames, under the assumption that image brightness remains approximately constant over time.

To compute motion between frames, two images are compared:

- The **template image** T is typically the first frame in a sequence and serves as the fixed reference.
- The **inspection image** I is the second frame, which is assumed to have undergone displacement due to motion in the scene. It is warped or interpolated as $\tilde{I}$ to match the geometry of the template image based on the estimated optical flow vector field.

The goal is to determine the displacement field $\mathbf{u}(\mathbf{k})$ that maps pixels from the template image to their new locations in the inspection image. A good match minimizes the difference in intensity values between $T(\mathbf{k})$ and $\tilde{I}(\mathbf{k}+\mathbf{u}(\mathbf{k}))$ for all pixel positions $\mathbf{k}$.

This similarity is often evaluated using norm-based error metrics:

$$\mathrm{L}_1 \text{ norm} = \sum_{k \in S} \mid T(\mathbf{k}) - \tilde{I}(\mathbf{k} + \mathbf{u}(\mathbf{k})) \mid \tag{6.7}$$

$$\mathrm{L}_2 \text{ norm} = \sum_{k \in S} \Big[T(\mathbf{k}) - \tilde{I}(\mathbf{k} + \mathbf{u}(\mathbf{k})) \Big]^2 \tag{6.8}$$

In these equations:

- $\mathbf{k} = [k, l]^T \in Z^2$ represents the coordinates of a pixel on the image plane.
- $\mathbf{u}(\mathbf{k}) = [u(\mathbf{k}), v(\mathbf{k})]^T$ is the optical flow vector at position $\mathbf{k}$.
- T is the *template image*, and $\tilde{I}$ is the interpolated version of the *inspection image* shifted according to $\mathbf{u}(\mathbf{k})$.
- $S = \{0, ..., K-1\} \times \{0, ..., L-1\}$ defines the set of all pixel positions over the image domain (see Figure 6.2).

These formulations form the basis for accurately estimating and visualizing the motion of rain events between two successive time frames, which is essential for improving the temporal resolution of rain attenuation modeling.

6.2.3 Lucas-Kanade Method

The Lucas–Kanade method is a well-known differential technique for estimating optical flow, particularly under the assumption that image content undergoes only small displacements between two consecutive frames. It is especially effective when the motion is smooth and locally constant.

The core objective of this method is to estimate the optical flow vector field $\mathbf{u}(\mathbf{k})$, which describes how each pixel in the inspection image I must be displaced so that it aligns with the corresponding structure in the template image T. This alignment is evaluated by minimizing the *Displaced Frame Difference (DFD)*, commonly expressed using the L_2 norm.

To perform this alignment, the method relies on a process called **image warping**. Warping is the operation of spatially transforming an image by shifting pixel locations according to a displacement (or flow) field. In the Lucas–Kanade framework, warping maps the inspection image onto the geometry of the template image by applying the estimated flow field $\mathbf{u}(\mathbf{k})$.

Because warping often requires evaluating image intensities at non-integer positions, the pixel values of the inspection image must be interpolated. The Lucas–Kanade method uses an n^{th}-degree separable B-spline interpolation to estimate these values smoothly and accurately [109]:

$$\tilde{I}(\mathbf{x}) = \sum_{\mathbf{k}} a_I(\mathbf{k})\, \beta^n(x-k)\, \beta^n(y-l) \tag{6.9}$$

Here:

- $\mathbf{x} = (x, y)$ is a continuous pixel location,
- $\mathbf{k} = (k, l)$ are integer pixel coordinates in the image grid,
- β^n is the B-spline basis function of degree n,
- $a_I(\mathbf{k})$ are interpolation coefficients, which can be directly equal to $I(\mathbf{k})$ (for bilinear interpolation), or computed using Infinite Impulse Response (IIR) filtering in the case of cubic B-splines [110].

The output of this warping process is the **registered image** $\tilde{I}$. This is the geometrically transformed version of the inspection image, aligned according to the estimated optical flow. The term "registered" refers to the fact that it has been spatially adjusted so that its features correspond as closely as possible to those in the template image.

In summary:

- **Warping** is the spatial transformation of the inspection image based on an estimated flow field.
- The **registered image** is the warped version of the inspection image, now aligned with the template image.

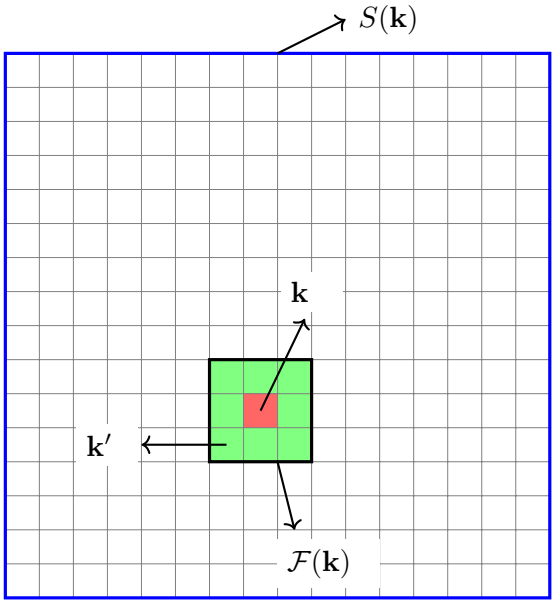


Figure 6.2: Image registration using Lucas-Kanade algorithm

The L_1 norm in Equation 6.7 is computed across the entire image plane, denoted as S. Here, a natural extension of the Lucas-Kanade algorithm can be introduced by integrating the Displaced-Frames-Difference (DFD) criterion. This integrated approach allows for a comprehensive assessment of the optical flow field, enabling an enhanced analysis of image displacement and facilitating the refinement of motion estimation.

$$\mathcal{B}(\mathbf{u}) = \sum_{\mathbf{k}\in S} \mathcal{B}_{\mathbf{u}}(\mathbf{u}(\mathbf{k})) \tag{6.10}$$

with

$$\mathcal{B}_{\mathbf{u}}(\mathbf{u}(\mathbf{k})) = \sum_{\mathbf{k}'\in\mathcal{F}(\mathbf{k})} \Big[T(\mathbf{k}') - \tilde{I}(\mathbf{k}' + \mathbf{u}(\mathbf{k}))\Big]^2 \tag{6.11}$$

In this context, $\mathcal{F}(\mathbf{k})$ represents a window centered on pixel $\mathbf{k}$ (refer to Figure 6.2). The optimization process for each component $\mathbf{u}(\mathbf{k})$ of the optical flow involves the selection of values that minimize the local criterion $\mathcal{B}_{\mathbf{k}}$. This criterion captures the relevant information within the specified window, guiding the optimization procedure to achieve accurate and locally optimized optical flow estimations.

For small values of $\mathbf{u}(\mathbf{k})$, the non-linear term $\tilde{I}(\mathbf{k}' + \mathbf{u}(\mathbf{k}))$ can be linearized using Taylor expansion, resulting in the following equation.

$$\tilde{I}(\mathbf{k}' + \mathbf{u}(\mathbf{k})) = \tilde{I}(\mathbf{k}' + \mathbf{u_0}(\mathbf{k})) + \nabla\tilde{I}(\mathbf{k}' + \mathbf{u_0}(\mathbf{k}))\delta\mathbf{u} \tag{6.12}$$

Here, ∇ denotes the gradient operator, and $\mathbf{u_0}(\mathbf{k})$ can be initialized as 0 for the initial step, subsequently updated in each iteration of the algorithm

based on the values from the preceding step. The specific updating formula, $\mathbf{u_0}(\mathbf{k}) \leftarrow \mathbf{u} = \mathbf{u_0}(\mathbf{k}) + \delta\mathbf{u}$, is detailed in Table 6.1. It is imperative to apply these updates to every pixel $\mathbf{k} \in S$ during each global iteration.

To refine the optical flow estimation, Equation 6.12 can be used with Equations 6.11, resulting in the new local criterion $\mathcal{B}_\mathbf{u}(\mathbf{u}(\mathbf{k}))$. This substitution enhances the accuracy of the optical flow computation, incorporating the iterative adjustments based on local image gradients and pixel displacements.

$$\mathcal{B}_\mathbf{u}(\mathbf{u}(\mathbf{k})) = \sum_{\mathbf{k}' \in \mathcal{F}(\mathbf{k})} \left[T(\mathbf{k}') - \tilde{I}(\mathbf{k}' + \mathbf{u_0}(\mathbf{k})) - \nabla\tilde{I}(\mathbf{k}' + \mathbf{u_0}(\mathbf{k}))\delta\mathbf{u} \right]^2 \tag{6.13}$$

One can have the following relation to find the $\delta\mathbf{u}$ which minimizes the $\mathcal{B}_\mathbf{u}(\mathbf{u}(\mathbf{k}))$:

$$\begin{aligned} 0 &= \frac{\partial \mathcal{B}_\mathbf{u}(\mathbf{u}(\mathbf{k}))}{\partial \delta\mathbf{u}} = \\ &= \sum_{\mathbf{k}' \in \mathcal{F}(\mathbf{k})} -2\nabla\tilde{I}(\mathbf{k}' + \mathbf{u_0}(\mathbf{k})) \left[T(\mathbf{k}') - \tilde{I}(\mathbf{k}' + \mathbf{u_0}(\mathbf{k})) - \nabla\tilde{I}(\mathbf{k}' + \mathbf{u_0}(\mathbf{k}))\delta\mathbf{u} \right] \end{aligned} \tag{6.14}$$

from which

$$\begin{aligned} \delta\mathbf{u} = &\left[\sum_{\mathbf{k}' \in \mathcal{F}(\mathbf{k})} \left(\nabla\tilde{I}(\mathbf{k}' + \mathbf{u_0}(\mathbf{k})) \right)^t \nabla\tilde{I}(\mathbf{k}' + \mathbf{u_0}(\mathbf{k})) \right]^{-1} \times \\ &\left[\sum_{\mathbf{k}' \in \mathcal{F}(\mathbf{k})} \nabla\tilde{I}(\mathbf{k}' + \mathbf{u_0}(\mathbf{k})) \left[T(\mathbf{k}') - \tilde{I}(\mathbf{k}' + \mathbf{u_0}(\mathbf{k})) \right] \right] \end{aligned} \tag{6.15}$$

where t indicates the transpose of the matrix. This formulation corresponds to the direct form of the Lucas-Kanade method, as outlined in [111]. Introducing a regularization parameter, λ (e.g., $\lambda = 10^{-4}$), enhances the scheme's performance across diverse sequences [110]. This modified algorithm, incorporating the regularization parameter, is referred to as the dense Lucas-Kanade method and is presented in Table 6.1.

The primary limitation of the dense Lucas-Kanade algorithm outlined in Table 6.1 lies in its necessity for multiple interpolations and derivations of the inspection image. To illustrate, consider a square window $\mathcal{F}(\mathbf{k})$ of size $F \times F$. For each pixel k, one is required to compute F^2 interpolated values, $\tilde{I}(\mathbf{k}' + \mathbf{u_0}(\mathbf{k}))$, and F^2 gradients, $\nabla\tilde{I}(\mathbf{k}' + \mathbf{u_0}(\mathbf{k}))$.

In response to this computational demand, an iterative solution known as the Modified Iterative Warping Scheme (MIWS) is proposed in [110]. This innovative approach aims to find the optimal values of $\mathbf{u}(\mathbf{k})$ with improved computational efficiency. The MIWS method introduces modifications to the dense Lucas-Kanade algorithm, streamlining the iterative process and reducing the computational load associated with repeated interpolations and derivations.

For those interested in exploring and implementing this optimized approach, an open-source application of the MIWS implementation is available through

Table 6.1: The dense Lucas-Kanade update [110]

1. interpolate $\tilde{I}(\mathbf{k}'+\mathbf{u_0}(\mathbf{k}))$ and compute the gradient, $\nabla\tilde{I}(\mathbf{k}'+\mathbf{u_0}(\mathbf{k}))$ for $\mathbf{k}' \in \mathcal{F}(\mathbf{k})$

2. $\epsilon(\mathbf{k}') = T(\mathbf{k}') - \tilde{I}(\mathbf{k}'+\mathbf{u_0}(\mathbf{k}))\ ,\ \forall\, \mathbf{k}' \in \mathcal{F}(\mathbf{k})$

3. $c(\mathbf{k}) = \sum_{\mathbf{k}'\in\mathcal{F}(\mathbf{k})} \left[\nabla\tilde{I}(\mathbf{k}'+\mathbf{u_0}(\mathbf{k}))\right] \epsilon(\mathbf{k}')$

4. compute pseudo-Hessian matrix $\mathcal{H}(\mathbf{k}) = \sum_{\mathbf{k}'\in\mathcal{F}(\mathbf{k})} \left[\nabla\tilde{I}(\mathbf{k}'+\mathbf{u_0}(\mathbf{k}))\,\nabla\tilde{I}(\mathbf{k}'+\mathbf{u_0}(\mathbf{k}))^t\right]$

5. solve local system : $[\mathcal{H}(\mathbf{k}) + \lambda\mathcal{I}_{2\times2}]\,\delta\mathbf{u} = c(\mathbf{k})$

6. update $\mathbf{u_0}(\mathbf{k}) \leftarrow \mathbf{u_0}(\mathbf{k}) + \delta\mathbf{u}$

[112]. This resource provides accessibility to the enhanced algorithm, facilitating its utilization in diverse applications requiring efficient and accurate optical flow computation.

6.2.4 TV-L1

The TV-L1 method is rooted in the minimization of the $L1$ norm in Equation 6.7, complemented by a regularization term utilizing the total variation (TV) of the flow. This unique approach distinguishes itself by its capacity to account for discontinuities in the flow field, imparting a robustness that surpasses the Lucas-Kanade method in flow field estimation.

In addressing the inherent challenges of solving the system outlined in Equation 6.6, a common strategy involves imposing a smoothness condition, which enforces regularity on the optical flow field $\mathbf{u}$ in a certain context. The seminal work of [101] proposes a functional to be minimized within this scheme, aimed at striking a balance between accurately capturing optical flow information and preserving smoothness in the estimated field.

$$E_{\texttt{Horn_Schunck}}(\mathbf{u}) = \int_{S(\mathbf{k})} \left[\nabla I.\mathbf{u} + \frac{\partial}{\partial t} I\right]^2 + \alpha \left[|\nabla u_1|^2 + |\nabla u_2|^2\right] \tag{6.16}$$

The $|\nabla u_1|^2 + |\nabla u_2|^2$ term confers significant advantages by penalizing high gradients of $\mathbf{u}$ and effectively suppressing discontinuities within the optical flow field.

Consider two sequences of images, $I_1(\mathbf{k})$ and $I_0(\mathbf{k})$, where $\mathbf{k} \in S(\mathbf{k})$, and the objective is to determine the optical flow $\mathbf{u}(\mathbf{k}) = [u_1(\mathbf{k}), u_2(\mathbf{k})]^t$ that minimizes an image-based error function with a regularization norm. Equation 6.6 can be reformulated in a non-linear manner, $I_1(\mathbf{k}+\mathbf{u}(\mathbf{k})) - I_0(\mathbf{k}) = 0$, to accommodate

general image sequences. By applying Taylor expansions to the non-linear term $I_1(\mathbf{k}+\mathbf{u}(\mathbf{k}))$, the ensuing equation provides a foundation for addressing the complex interplay between image-based error minimization and regularization within the optical flow estimation process.

$$\begin{aligned}\rho(\mathbf{u}) &= I_1(\mathbf{k}+\mathbf{u}(\mathbf{k})) - I_0(\mathbf{k}) \\ &= \nabla I_1(\mathbf{k}+\mathbf{u_0}).(\mathbf{u}-\mathbf{u_0}) + I_1(\mathbf{k}+\mathbf{u_0}) - I_0(\mathbf{k}) = 0\end{aligned} \tag{6.17}$$

Here, $\mathbf{u_0}$ represents an approximate estimation of the true optical flow vector $\mathbf{u}$. A novel energy functional, as introduced in [113], is proposed through a modification of the Horn-Schunck energy functional, articulated as follows:

$$E(\mathbf{u}) = \int_{S(\mathbf{k})} |\nabla u_1| + |\nabla u_2| + \lambda\,|\rho(\mathbf{u})| \tag{6.18}$$

This energy functional is structured as the sum of the total variation of $\mathbf{u}$ and an L_1 norm. The parameter λ serves as a free weighting factor that balances the influence between the data fidelity term and the regularization force. This parameter dictates the impact of the regularization term $\rho(\mathbf{u})$ in relation to the data term $\mid \nabla u_1 \mid + \mid \nabla u_2 \mid$. While a value of $\lambda = 20$ has proven effective in yielding favorable results, users have the flexibility to adjust this parameter to suit different scenarios.

Furthermore, the term $\mid \nabla u_1 \mid + \mid \nabla u_2 \mid$ plays a crucial role in smoothing the displacement field $\mathbf{u_k}$ when faced with substantial variations. This component ensures a balanced regularization that promotes smoothness in cases of abrupt changes.

For the efficient minimization of this energy functional, a convex relaxation function is introduced, presenting an effective approach to address the complexities inherent in the optimization process.

$$E_\theta(\mathbf{u},\mathbf{v}) = \int_{S(k)} \mid \nabla u_1 \mid + \mid \nabla u_2 \mid + \frac{1}{2\theta} \mid \mathbf{u}-\mathbf{v} \mid^2 + \lambda \mid \rho(\mathbf{v}) \mid \tag{6.19}$$

In this context, θ stands as a small constant, ensuring that $\mathbf{v_k}$ serves as an intermediate variable, offering a close approximation to $\mathbf{u_k}$. While the newly proposed energy functional may appear distinct from the original energy functional in Equation 6.18, a key observation is that they converge when $\mathbf{u} = \mathbf{v}$. The introduction of the intermediate variable $\mathbf{v}$ into the scheme allows for the segmentation of the system into two sub-systems, facilitating a more structured and manageable approach to the problem.

- $\mathbf{v_k}$ is fixed:

$$\min_{\mathbf{u}} \int_{S(\mathbf{k})} \mid \nabla u_1 \mid + \mid \nabla u_2 \mid + \frac{1}{2\theta} \mid \mathbf{u}-\mathbf{v} \mid^2 \tag{6.20}$$

- $\mathbf{u_k}$ is fixed:

$$\min_{\mathbf{v}} \int_{S(\mathbf{k})} \frac{1}{2\theta} \mid \mathbf{u}-\mathbf{v} \mid^2 + \lambda \mid \rho(\mathbf{v}) \mid \tag{6.21}$$

The resolution of this convex minimization problem involves an iterative algorithm with the sequential updating of $\mathbf{u}$ and $\mathbf{v}$ to minimize the two distinct sub-systems. This iterative process culminates in the merging of $\mathbf{u}$ and $\mathbf{v}$ when they converge to equal values.

The first sub-problem aligns with the total variation denoising model proposed by Rudin–Osher–Fatemi [114], and it is efficiently addressed using Chambolle's duality-based algorithm [115]. The second sub-problem, devoid of dependencies on spatial derivatives of $\mathbf{v}$, is tackled through point-wise thresholding. The detailed algorithm for minimizing each sub-system is thoroughly elucidated in [113], and a comprehensive implementation is readily available in the open-source Python application [112]. This accessible resource facilitates the application and exploration of the proposed convex minimization approach, offering a valuable tool for those engaged in optical flow estimation and related image processing tasks.

6.2.5 Performance Comparison of LK and TV-L1 Algorithms

The performance of optical flow algorithms, particularly Lucas-Kanade (LK) and TV-L1, has been widely studied across various application scenarios [110, 113]. In this section, we aim to conduct a consistent and controlled comparison of these two methods using a set of test cases that simulate typical types of motion.

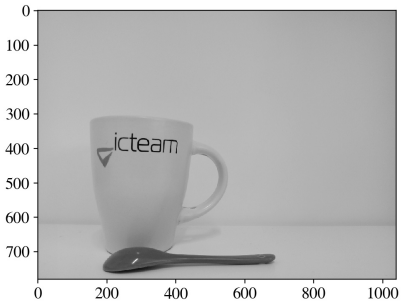
Figure 6.3a shows the reference image (I_0), which contains a cup and a spoon at the initial time step. In Figure 6.3b, the cup has moved horizontally to the right—representing a simple translation. Figure 6.3c introduces a second transformation: the cup moves as before, but the spoon is removed from the frame. Finally, Figure 6.3d presents a more complex transformation, where both the cup and the spoon change positions, including potential rotation or nonlinear motion. These four images, labeled as I_0, I_1, I_2, and I_3, form the basis for our evaluation.

By comparing the transformations from I_0 to each of the subsequent images (I_1, I_2, and I_3), we analyze the ability of each algorithm to detect and represent motion under varying levels of complexity. This side-by-side evaluation provides insights into the strengths and limitations of the LK and TV-L1 methods across simple, moderate, and complex motion scenarios.

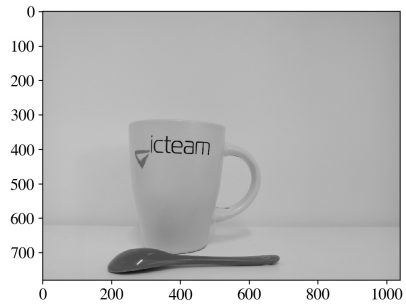
The analysis of the transformation from image frame I_0 to I_1 in Figure 6.3 is illustrated in Figures 6.4a–6.4b, comparing the performance of two optical flow algorithms: Lucas-Kanade (LK) and Total Variation L1 (TV-L1). This case represents a simple scenario involving a horizontal movement of the cup.

Both methods perform well in capturing the flow field associated with this basic motion. As mentioned in Section 6.2.3, the Lucas-Kanade algorithm depends on the size of the local window $\mathcal{F}(\mathbf{k})$ used to estimate motion; in this example, a window size of about 20 pixels is used (Figure 6.4a).

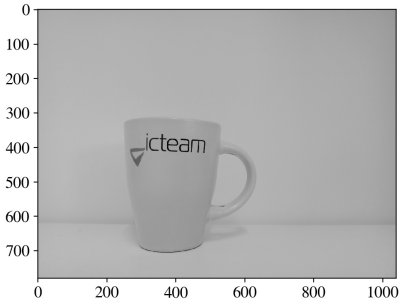
The performance of the TV-L1 method, on the other hand, is influenced by its regularization parameter λ, which controls the trade-off between data fidelity and smoothness. For this comparison, λ is set to 20 (Figure 6.4b).



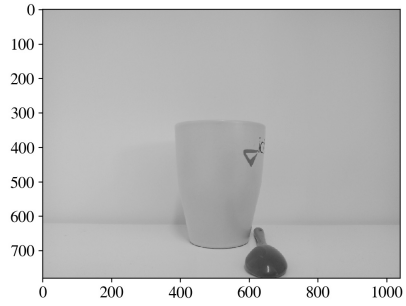
(a) I_0 = The image frame at initial time



(b) I_1 = Cup moved horizontally to the right



(c) I_2 = Cup moved horizontally to the right and the spoon is deleted



(d) I_3 = complex movement of both cup and spoon

Figure 6.3: Propose of three types of transformation for performance investigation of optical flow algorithms. (a) shows the initial image frame, (b) depicts a simple horizontal movement of the cup, (c) contains the movement of the cup and elimination of the spoon, and (d) includes complex movements of the cup and spoon.

The resulting flow fields from both methods are shown in Figures 6.4c and 6.4d. To quantify the alignment between the original image I_1 and the warped version of I_0, we calculate the per-pixel absolute difference $\left|I_1(\mathbf{k}) - \tilde{I}_0(\mathbf{k} + \mathbf{u}(\mathbf{k}))\right|$, visualized in Figures 6.4e and 6.4f.

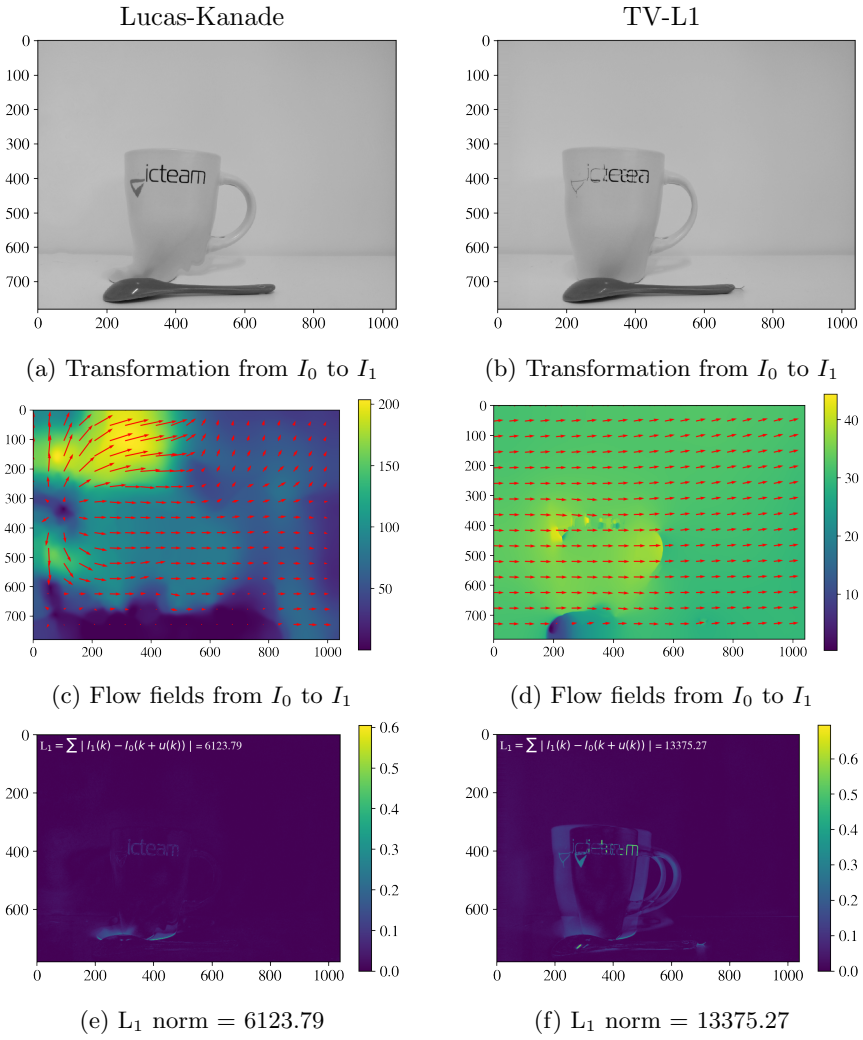
Summing these differences yields the L_1 error: approximately 6123.79 for Lucas-Kanade and 13375.27 for TV-L1. Although the Lucas-Kanade algorithm achieves a lower numerical error, visual inspection reveals more noticeable distortions compared to TV-L1. This highlights a key trade-off: while Lucas-Kanade may minimize pixel-wise differences more effectively, TV-L1 tends to preserve motion structure more faithfully in practice.

The second test case, illustrated in Figure 6.3 as the transformation from I_0 to I_2, involves two simultaneous changes: the cup moves horizontally to the right, and the spoon is removed from the scene. This scenario introduces additional complexity by combining object motion with scene alteration. The performance of the two optical flow algorithms under these conditions is shown in Figures 6.5a to 6.5b. Although the Lucas-Kanade method yields a lower L_1 norm (10302.30) compared to TV-L1 (16937.17), this metric alone does not fully reflect qualitative performance. As evident in Figures 6.5c to 6.5f, TV-L1 performs noticeably better in handling the removal of the spoon, resulting in a smoother transition in the optical flow field. In contrast, TV-L1 shows weaker performance in accurately tracking the cup's movement, while Lucas-Kanade more effectively captures the motion of the cup. This highlights that although Lucas-Kanade excels in preserving fine local motion in simpler transformations, TV-L1 demonstrates superior adaptability to scene changes involving object disappearance.

The third test case examines the transformation from I_0 to I_3 in Figure 6.3, where both the cup and the spoon undergo complex movements, including rotation and translation. This case introduces the most challenging scenario among the three, combining simultaneous and non-linear motion of multiple objects. The performance comparison of the two optical flow algorithms under these conditions is shown in Figures 6.6a to 6.6f.

Despite Lucas-Kanade achieving a lower error metric ($L_1 = 14188.32$) compared to TV-L1 ($L_1 = 20278.62$), visual inspection reveals that Lucas-Kanade struggles to accurately capture the flow fields, resulting in significant distortion, especially in areas of object rotation. In contrast, the TV-L1 algorithm delivers a smoother and more coherent flow field, particularly in handling the rotation and movement of the spoon. However, similar to the previous test case, TV-L1 still falls short in accurately representing the motion of the cup. Overall, this case underscores the robustness of TV-L1 in managing complex scene dynamics, while highlighting the limitations of Lucas-Kanade in highly non-rigid motion scenarios despite its lower numerical error.

After a meticulous examination of the three case studies to assess the performance of Lucas-Kanade and TV-L1, it proves challenging to definitively declare one superior to the other. However, the results obtained from TV-L1 underscore its heightened capability and robust performance, particularly in scenarios involving complex movements. Considering that these methods are intended for application in rain motion detection, where changes are intricate



(a) Transformation from I_0 to I_1

(b) Transformation from I_0 to I_1

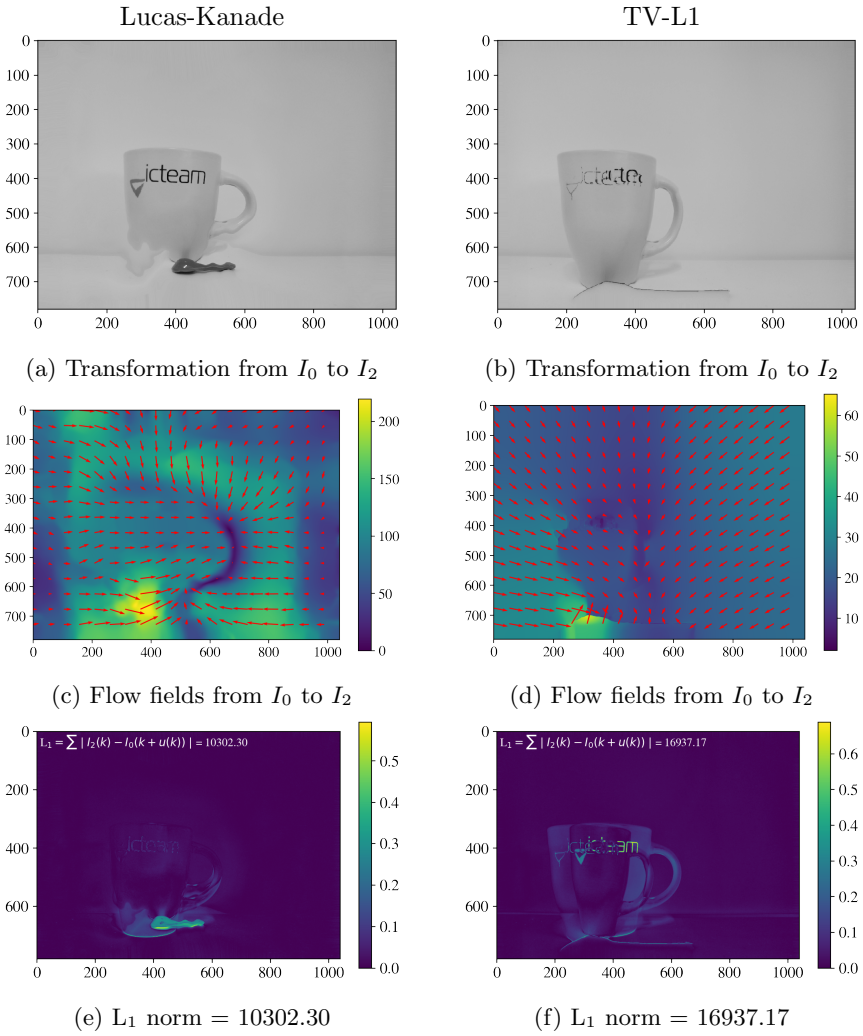
(c) Flow fields from I_0 to I_1

(d) Flow fields from I_0 to I_1

(e) L_1 norm = 6123.79

(f) L_1 norm = 13375.27

Figure 6.4: Performance investigation of the two optical flow algorithms, Lucas-Kanade and TV-L1 for the transformation case from I_0 to I_1 at Figure 6.3. (a,c) the transformation result and optical flow magnitude and vector field by Lucas-Kanade, and (b,d) the transformation result and Optical flow magnitude and vector field by TV-L1. (e-f) shows the error function L_1 norm $= \sum_{\mathbf{k} \in S(\mathbf{k})} \left| I_1(\mathbf{k}) - \tilde{I}_0(\mathbf{k} + \mathbf{u}(\mathbf{k})) \right|$. The window size in LK is about 20 pixels, and the regularization term in TV-L1 is $\lambda = 20$.



(a) Transformation from I_0 to I_2

(b) Transformation from I_0 to I_2

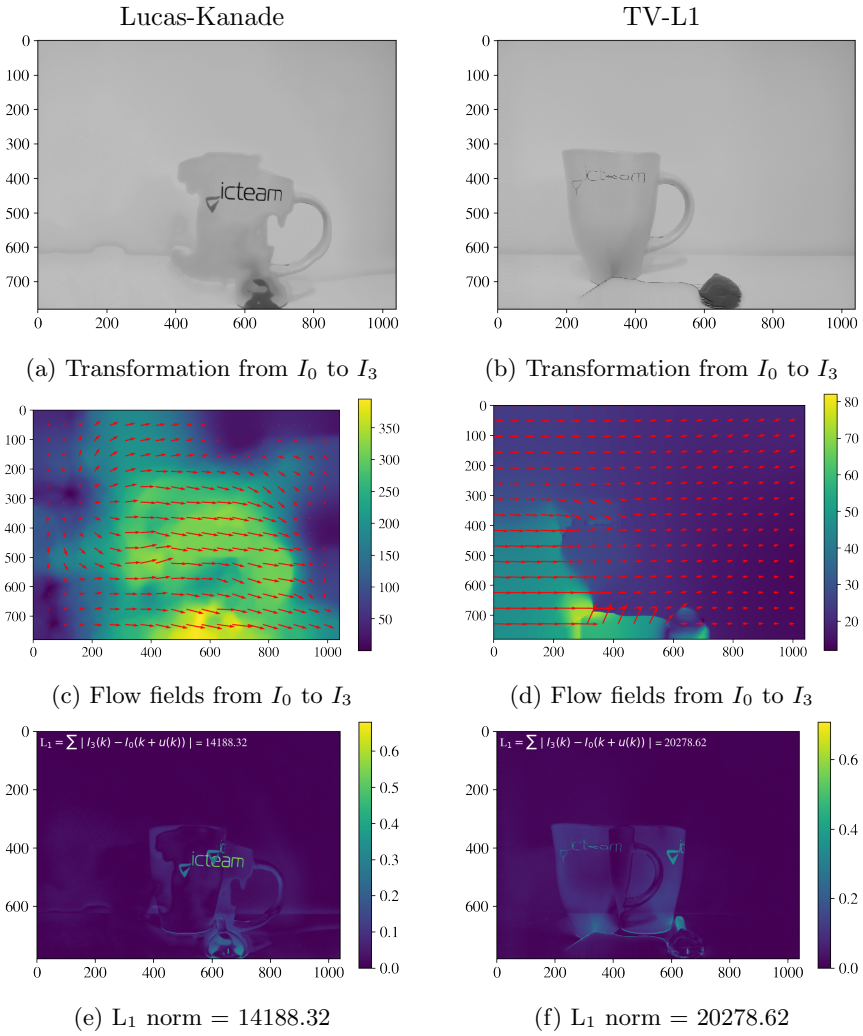
(c) Flow fields from I_0 to I_2

(d) Flow fields from I_0 to I_2

(e) L_1 norm = 10302.30

(f) L_1 norm = 16937.17

Figure 6.5: Performance investigation of the two optical flow algorithms, Lucas-Kanade and TV-L1 for the transformation case from I_0 to I_2 at Figure 6.3. (a,c) the transformation result and optical flow magnitude and vector field by Lucas-Kanade, and (b,d) the transformation result and Optical flow magnitude and vector field by TV-L1. (e-f) shows the error function L_1 norm $= \sum_{\mathbf{k} \in S(\mathbf{k})} \left| I_2(\mathbf{k}) - \tilde{I}_0(\mathbf{k} + \mathbf{u}(\mathbf{k})) \right|$. The window size in LK is about 20 pixels, and the regularization term in TV-L1 is $\lambda = 20$.



(a) Transformation from I_0 to I_3

(b) Transformation from I_0 to I_3

(c) Flow fields from I_0 to I_3

(d) Flow fields from I_0 to I_3

(e) L_1 norm = 14188.32

(f) L_1 norm = 20278.62

Figure 6.6: Performance investigation of the two optical flow algorithms, Lucas-Kanade and TV-L1 for the transformation case from I_0 to I_3 at Figure 6.3. (a,c) the transformation result and optical flow magnitude and vector field by Lucas-Kanade, and (b,d) the transformation result and Optical flow magnitude and vector field by TV-L1. (e-f) shows the error function L_1 norm $= \sum_{\mathbf{k}\in S(\mathbf{k})} \left| I_3(\mathbf{k}) - \tilde{I}_0(\mathbf{k}+\mathbf{u}(\mathbf{k})) \right|$. The window size in LK is about 20 pixels, and the regularization term in TV-L1 is $\lambda = 20$.

and movement evolves over time, TV-L1 emerges as a more suitable algorithm.

It's important to note that the primary drawback of the TV-L1 model is its relatively longer execution time, roughly doubling that of the Lucas-Kanade algorithm. For an image size of 1100×740 pixels, the runtime is approximately 7 seconds on a core i7 processor. Fortunately, this issue is anticipated to be inconsequential in our forthcoming rain motion scheme, given that the image size in our case is only 78×78 pixels. The ultimate decision on which model is more appropriate for rain motion detection will be deferred until Chapter 7, where a comprehensive evaluation, including long-term simulations of the models, will be undertaken.

6.3 Rain Motion

The evaluation of microwave subsystems in Low Earth Orbit (LEO) satellites is crucial to ensure compliance with required benchmarks before the satellite is launched into its designated orbit. Comprehensive testing of the full system under diverse environmental conditions and the influence of various atmospheric factors is paramount for designers.

Achieving a stable link connection, especially during meteorological events such as clouds and rain, necessitates accurate benchmarking of the satellite emitter power. A robust understanding of the impact of weather conditions on radio links enhances the precision of the link budget.

For LEO satellites orbiting at around 800 km altitude, the duration of the link connection is approximately ten minutes during each pass over the receiving station. Guaranteeing a stable connection throughout most of these passes is of utmost importance. To ensure the efficiency of these systems within this limited timeframe, a detailed description of weather effects is crucial, with a particular emphasis on rain, the most significant factor affecting satellite communication impairments.

In the context of Fade Mitigation Techniques, the dynamic nature of the received signal becomes particularly vital within this brief timeframe. Therefore, a meticulous evaluation of the impact of rain is essential, considering both temporal and spatial dimensions around the receiving station.

The creation of a high-resolution spatial distribution of a rain event was discussed in Section 5. This section delves into increasing the time resolution of rain events, leveraging the advantages offered by optical flow algorithms. Optical flow algorithms are designed for image frames, necessitating preprocessing steps before applying them to rain rates data.

This preprocessing procedure is applicable to both the original rain rate and the high-resolution MultiEXCELL rain rate data. However, due to the computationally intensive nature of optical flow algorithms, especially when dealing with the high-resolution output of the MultiEXCELL model, a decision has been made to utilize the original rain rate data from Numerical Weather Prediction (NWP), which is represented as a 78×78 2D dataset.

An inherent challenge arises as, over successive time samples, certain features in the image frame may diminish, leading to the disappearance of some

rain events. This poses a potential hurdle for the registration process, necessitating corrective measures such as considering only a subset of stable rain events to maintain accurate and reliable registration.

The initial step in preparing the 2D rain rate data involves converting them into image value data. Images can be represented in various formats, with describing an image in RGB or grayscale being common for raster image types. RGB images consist of three layers of 2D matrices, where each layer corresponds to the intensity of the primary colors—Red, Green, and Blue. The combination of all three layers creates the full spectrum of colors.

Another widely used raster image format is grayscale or brightness images. Grayscale images comprise only one layer of 2D data, representing the intensity of brightness scaled from 0 to 1. A brightness value of 0 corresponds to black, while a value of 1 represents white. Given that the rain rate data is in a 2D format, grayscale or brightness images are the most suitable in this context.

The subsequent section delves into the process of transforming rain rate data into brightness images.

6.3.1 Rain Rate to Brightness Image

In Section 6.2, we explored methods for image registration to access optical flow fields. To apply these models to 2D rain rate data, it is necessary to scale and normalize the data to a brightness image with intensity ranging from 0 to 1. Consider the image sequence I_0 and I_1 containing rain rate pixels; normalization involves a straightforward mathematical scaling over these two images as described below.

$$c_1 = min(I_0, I_1), \tag{6.22a}$$

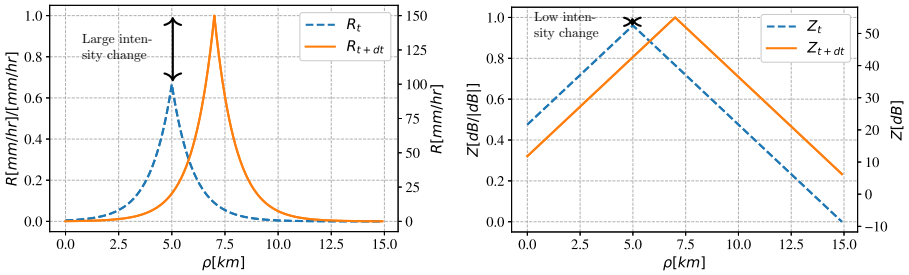
$$c_2 = max(I_0, I_1), \tag{6.22b}$$

$$I_i^{norm} = \frac{I_i - c_1}{c_2 - c_1} \quad , \quad i \in 1, 2 \tag{6.22c}$$

However, a challenge arises with linear normalization. Most of the time, the minimum rain rate is 0, but in the case of heavy rainfall occurring in a small portion of the domain, the difference between the minimum and maximum rain rate can exceed $R > 100, mm/hr$ or even more. Consequently, the disparity between the maximum and minimum values significantly increases, causing very low values of rain rate to disappear during image processing. Additionally, the differences in the peaks of I_0 and I_1 become substantial during heavy rain events. Figure 6.7a illustrates this issue in 1D to clearly define the problem and propose a corresponding solution. The significant differences observed in two consecutive images contradict the brightness constancy constraint outlined in Equation 6.1. In an effort to address this issue, following the suggestions of [116] and [60], the optical flow algorithm utilizes the reflectivity quantity in decibels instead of the raw rain rate.

$$Z = a\, R^b \tag{6.23a}$$

$$Z_{dB} = 10 \log Z \tag{6.23b}$$



(a) Normalized rain rate (b) Normalized reflectivity

Figure 6.7: Comparison of the normalized rain rate versus normalized reflectivity. (a) Normalized rain rate in two time sample which is moved horizontally, and the intensity is increased over time, (b) Normalized reflectivity, which highly cover the change of intensity over time. The blue curve is a cross-section of rain rate distribution at time t and the orange curve is the cross-section of the same rain event after a period of dt time which is displaced horizontally and the intensity of rain rate is increased too.

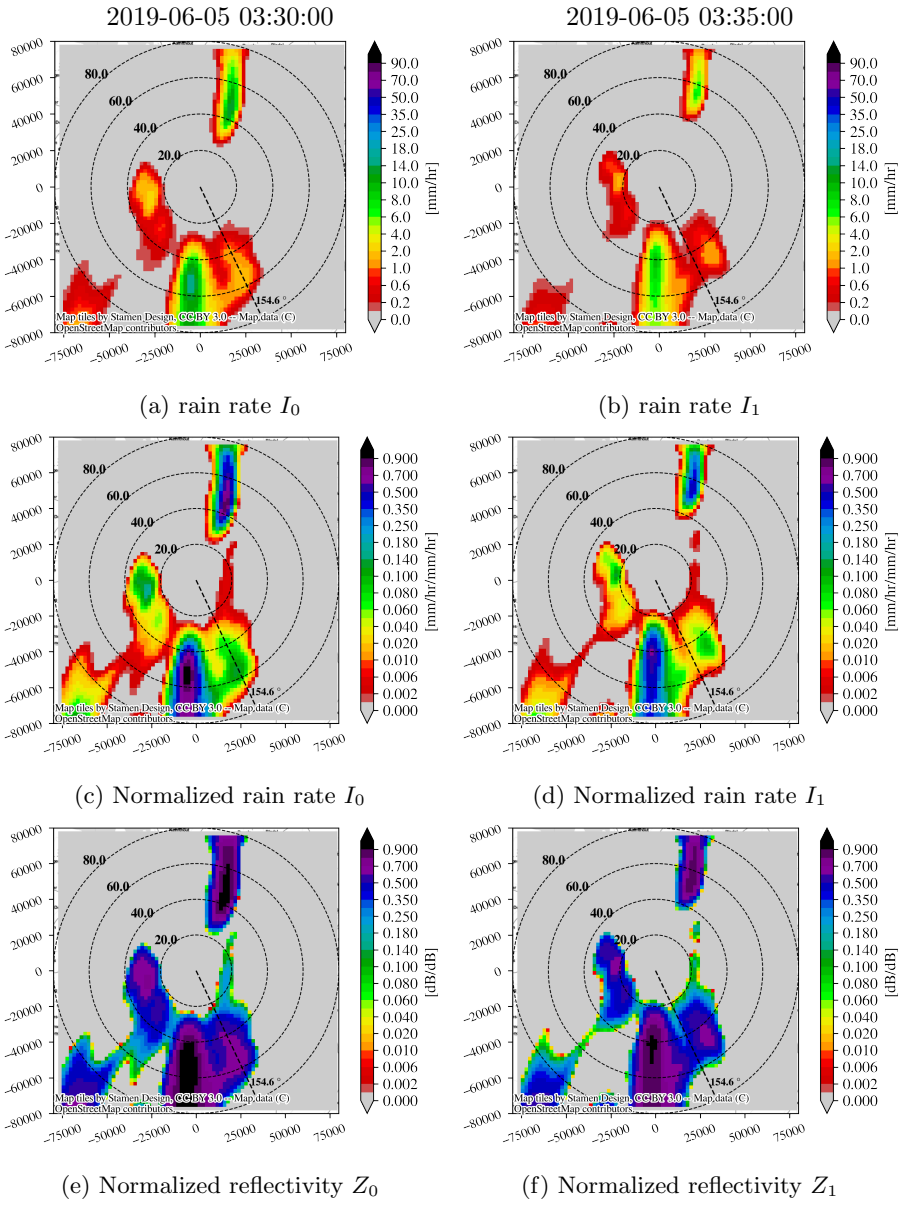
where R represents the rain rate in mm/hr, and the coefficients $a = 256$ and $b = 1.42$ correspond to the power law. The reflectivity Z_{dB} is used in equation 6.22 as input in optical flow models. Opting for the normalized reflectivity is deemed a more effective choice, given that the reflectivity variation is inversely proportional to the rain rate, i.e., $\frac{dZ_{dB}}{dR} \propto R^{-1}$. Thus, the use of normalized reflectivity results in rainfall images being predominantly considered as a constant solid object, as illustrated in Figure 6.7b, which is well-suited for optical flow algorithms.

Figures 6.8a-6.8b showcase two consecutive rain rate datasets, I_0 and I_1, capturing the time evolution of a rain event over a 5-minute interval at 2019-06-05 03:30:00 and 2019-06-05 03:35:00, respectively. The objective is to determine the flow fields of the rain motion during this evolution and interpolate the rain rate within this timeframe to access rain rates at intervals less than 5 minutes. The corresponding normalized rain rate and normalized reflectivity are depicted in Figures 6.8c-6.8f, underscoring once again the importance of employing reflectivity instead of rain rate in the optical flow algorithm.

Figures 6.8e-6.8f distinctly demonstrate that in normalized reflectivity, the shape of the rain event is perceived as more solid and integrated compared to normalized rain rate. Consequently, lower rain rate values and lower intensities are more effectively taken into account, as evidenced in Figures 6.8c-6.8d.

6.3.2 Rain Rate Registration

The preprocessed images, shown in Figures 6.8e and 6.8f, are now ready to be processed using the TV-L1 or Lucas-Kanade optical flow algorithms. The out-



(a) rain rate I_0

(b) rain rate I_1

(c) Normalized rain rate I_0

(d) Normalized rain rate I_1

(e) Normalized reflectivity Z_0

(f) Normalized reflectivity Z_1

Figure 6.8: Transformation of rain rate to normalized reflectivity to be fed in optical flow models. The ground station is at Louvain-la-Neuve on 2019-06-05.

put of these algorithms includes two key elements. First, Figure 6.9a displays the estimated flow fields $\mathbf{u}(\mathbf{k})$, illustrating both the direction and magnitude of the motion between the image frames. Second, Figure 6.9b shows the result of applying this flow field to the original image I_0 to create a new, interpolated version—denoted as $\tilde{I}_0(\mathbf{k}+\mathbf{u}(\mathbf{k}))$. This interpolation process is known as `warping`, and the output image is referred to as the `registered image`, as it aligns geometrically with the target image I_1.

To visually analyze the differences between the registered image $\tilde{I}_0(\mathbf{k}+\mathbf{u}(\mathbf{k}))$ and the target image $I_1(\mathbf{k})$, an RGB visualization technique is employed. An empty RGB image is constructed with three color channels: red, green, and blue. The registered image is assigned to the red channel, while the target image is evenly distributed across the green and blue channels. Since the combination of green and blue produces cyan, this setup allows for intuitive visual interpretation of differences.

In the resulting composite image (e.g., Figure 6.9c), the colors convey the following information:

- **White/gray/black** pixels indicate equal intensity values across all channels, meaning the registered and target images are well-aligned in these regions.
- **Red** pixels highlight areas where the registered image has higher intensity than the target image.
- **Cyan** pixels point to areas where the target image is brighter than the registered one.

This color-based comparison helps quickly identify regions where the optical flow algorithm has estimated motion accurately (gray/white/black zones) versus areas where mismatches occur (red or cyan zones), offering a qualitative assessment of flow estimation performance.

The primary goal of image registration and optical flow field estimation was to bridge the gap between two consecutive rainfall rate images, namely I_0 at $t = 0$ and I_1 at $t = 1$, where here, t denotes the normalized time period. Consider the image sequence

$$I_0, \cdots, I_{i-1}, I_i, I_{i+1} \cdots, I_1 \tag{6.24}$$

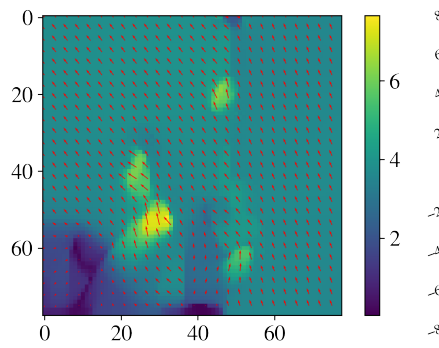
and assuming a linear trajectory between two consecutive images, I_0 and I_1, and utilizing the displacement pattern $\mathbf{u}(\mathbf{k})$, the flow fields for the motion of objects at time t_i can be obtained by.

$$\mathbf{u_i} = t_i \times \mathbf{u}\,, \qquad 0 \le t_i \le 1 \tag{6.25}$$

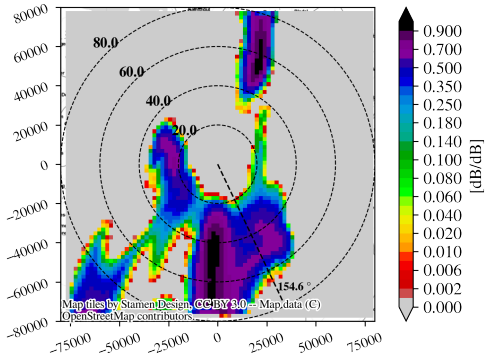
where $\mathbf{u}$ is the optical flow fields, e.g. Figure 6.9a. So each of the I_i is calculated by warping and utilizing the $\mathbf{u_i}$.

$$I_i = \tilde{I}_0(\mathbf{k} + \mathbf{u_i}) \tag{6.26}$$

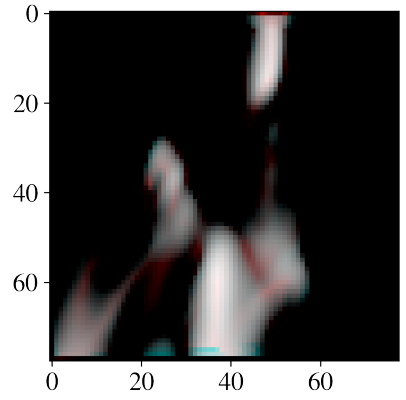
Consider the time evolution of the rain event shown in Figures 6.8a-6.8a as an example. The time period in this sequence is 5 minutes, and through optical



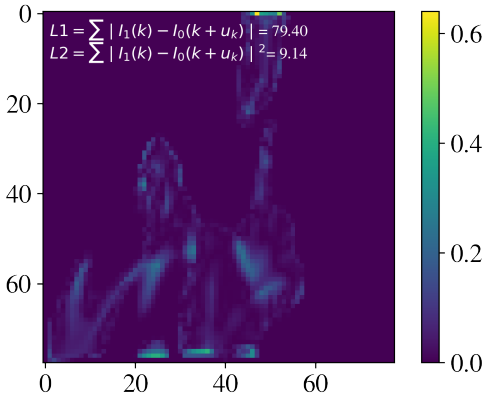
(a) magnitude and direction of flow fields ($\mathbf{u}(\mathbf{k})$) from the rain motion in Figure 6.8e-6.8f



(b) Registered image $\tilde{I}_0(\mathbf{k}+\mathbf{u}(\mathbf{k}))$



(c) Sequence of registered image $\tilde{I}_0(\mathbf{k}+\mathbf{u}(\mathbf{k}))$ and target image $I_1(\mathbf{k})$ as an RGB-image. R:$\tilde{I}_0(\mathbf{k}+\mathbf{u}(\mathbf{k}))$; GB:$I_1(\mathbf{k})$



(d) Pixelwise difference $| I_1(\mathbf{k}) - \tilde{I}_0(\mathbf{k}+\mathbf{u}(\mathbf{k})) |$

Figure 6.9: Normalized reflectivity registration and warping using optical flow algorithms (TV-L1). (a) shows the flow field vector, (b) the registration of $\tilde{I}_0(\mathbf{k}+\mathbf{u}(\mathbf{k}))$ using the flow fields vectors $\mathbf{u}(\mathbf{k})$, (c) representing the registered image $\tilde{I}_0(\mathbf{k}+\mathbf{u}(\mathbf{k}))$ as the red channel and target image $I_1(\mathbf{k})$ as the green and blue channel of an RGB image, (d) the error values L_1 norm between the registered image and target image. The rain event's happened at 2019-06-05 03:30:00 at Louvain-la-Neuve.

flow, it is expected to achieve a 1-minute resolution for the rain rate. The rain motion sequence with a temporal resolution of 1 minute is depicted in Figure 6.10a-6.10f. This rain motion is represented by the normalized reflectivity as a brightness image. By inverting the normalization in equations 6.22-6.23 for each sub-image, the corresponding rain rate values can be determined.

Figure 6.10 illustrates the time evolution of rain events where the intensity remains relatively constant, and the brightness constancy rule is applicable in this scenario. This case represents a simple scenario with smooth motion occurring over a 5-minute period. To assess the capability of optical flow in cases involving complex motions, degradation, or deformation in the rain event, another example should be examined. Figure 6.11 showcases the rain rate registration for the time period from 2019-06-05 06:00:00 to 2019-06-05 06:05:00 with the center at Louvain-la-Neuve. This rain event involves both deformation and changes in intensity within the rain event's shape. While the motion detection of the rain event is well estimated, there is an issue with intensity. A closer look at Figures 6.11e-6.11f reveals a jump in rain intensity from 06:04:00 to 06:05:00. Optical flow algorithms struggle with detecting changes in intensity. This intensity change over the time period is numerically addressed in Section 6.3.3.

6.3.3 Rain Intensity Correction in Optical Flow

As discussed earlier, adhering to the brightness constancy constraint in optical flow is crucial. On the other hand, the rain event undergoes significant changes over short time periods (e.g., 5 minutes). The impact of high variations in rain rate was mitigated by using normalized reflectivity in optical flow algorithms, resulting in acceptable outcomes in motion detection. However, as evident from Figure 6.11, there remains an issue with intensity variations in complex situations.

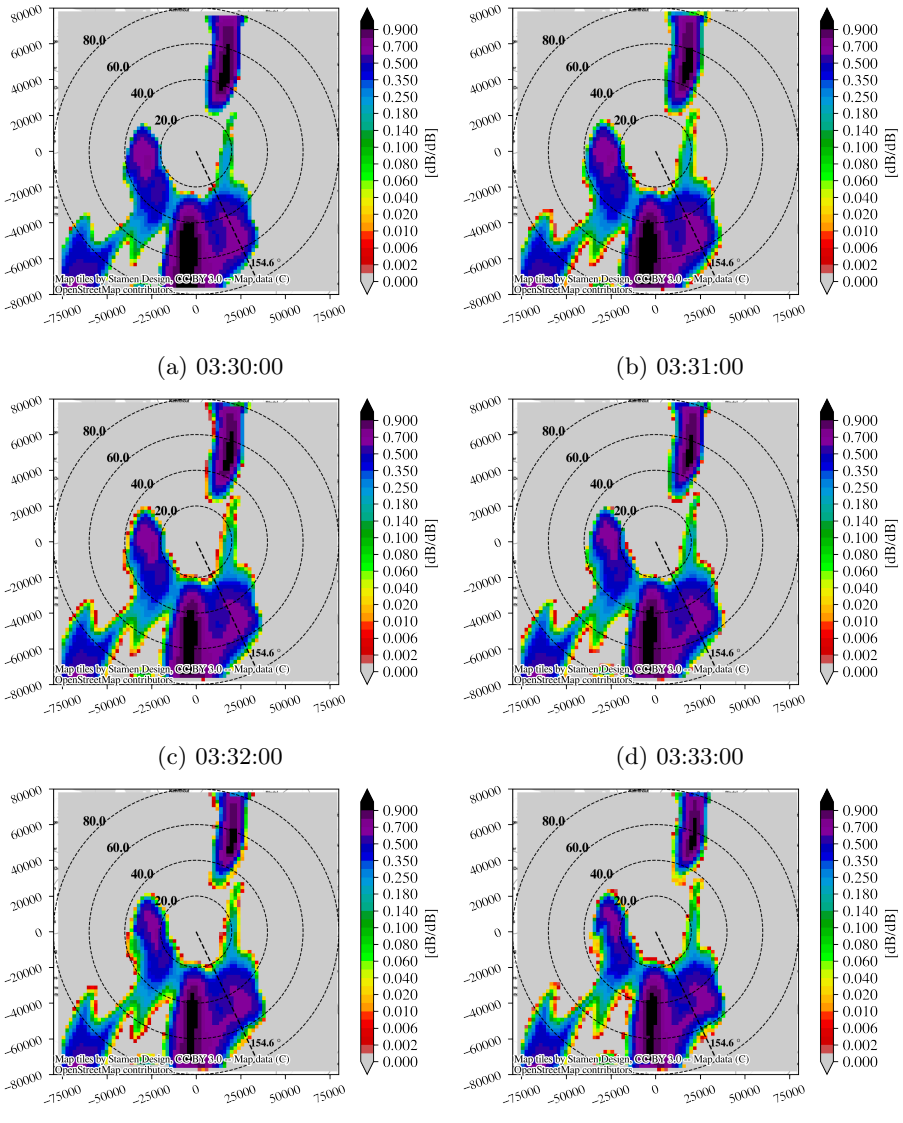
The numerical resolution of intensity discontinuities can be achieved by quantifying the intensity deviation after registration. This deviation can be measured using the equation below:

$$\Delta I = I_1(\mathbf{k}) - \tilde{I}_0(\mathbf{k} + \mathbf{u}(\mathbf{k})) \tag{6.27}$$

This difference can be gradually incorporated into the registered image over time, using:

$$\tilde{I}_0(\mathbf{k} + \mathbf{u_i}) \leftarrow \tilde{I}_0(\mathbf{k} + \mathbf{u_i}) + t_i \times \Delta I \tag{6.28}$$

where $\mathbf{u_i}$ and t_i are defined as in Equation 6.25, and the additional term represents a linear intensity correction applied during the leading time steps. This correction induces a gradual change in image intensity, resulting in a smooth transition. The outcomes presented in Figure 6.11 were re-evaluated with the rain intensity correction procedure, as shown in Figure 6.12. The results clearly demonstrate a smooth intensity transition concurrent with the ongoing rain motion. The detailed analysis of this transition and the impact of rain intensity correction will be explored further in Section 6.4.



(a) 03:30:00

(b) 03:31:00

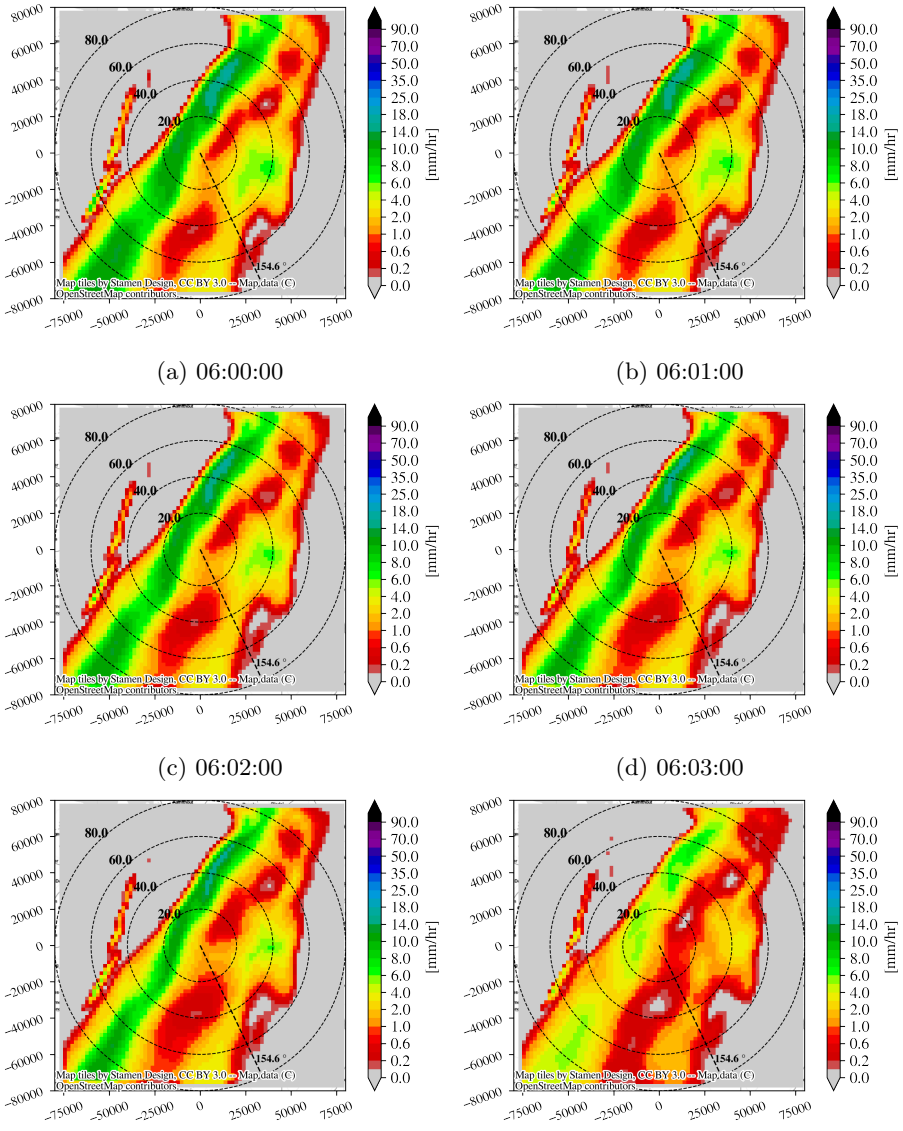
(c) 03:32:00

(d) 03:33:00

(e) 03:34:00

(f) 03:35:00

Figure 6.10: Rain motion using optical flow method in 5-min at the dates 2019-06-05 03:30:00 and 2019-06-05 03:35:00 with temporal resolution of 1-min. The figures are normalized reflectivity which the equivalence rain rate will be known using the inverse procedure at eq. 6.22-6.23



(a) 06:00:00

(b) 06:01:00

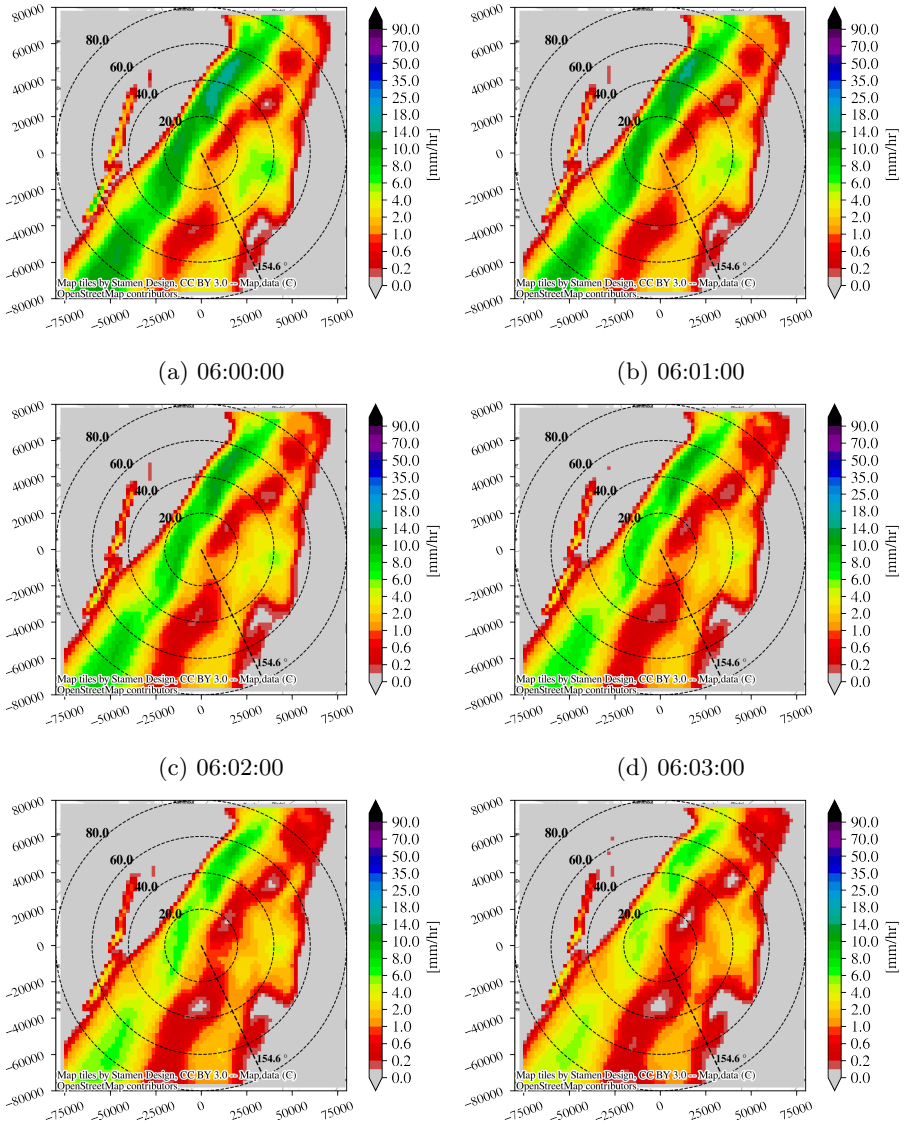
(c) 06:02:00

(d) 06:03:00

(e) 06:04:00

(f) 06:05:00

Figure 6.11: Rain motion using optical flow method in 5-min at the dates 2019-06-05 06:00:00 and 2019-06-05 06:05:00 with temporal resolution of 1-min. The ground station is at Louvain-la-Neuve.



(a) 06:00:00

(b) 06:01:00

(c) 06:02:00

(d) 06:03:00

(e) 06:04:00

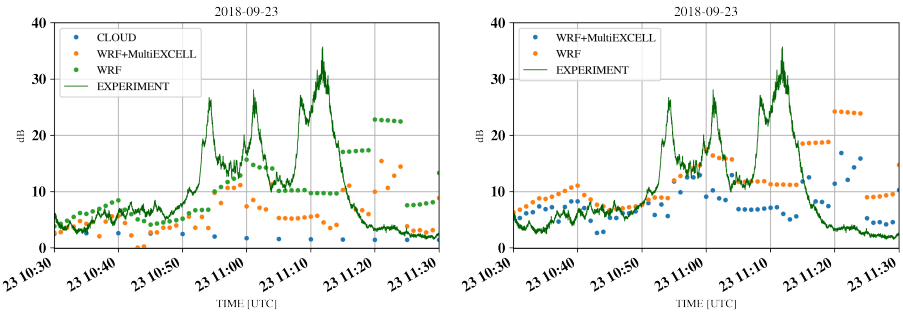
(f) 06:05:00

Figure 6.12: Rain rate intensity correction after registration in optical flow. The event is on the date 2019-06-05 at Louvain-la-Neuve ground station.

6.4 Attenuation Time Series

The rain attenuation and cloud attenuation for a one-day simulation using the proposed model with nowcast rain rates are depicted in Fig. 6.13. Similar to previous cases, nowcast rain rates are employed in both the MultiEXCELL and WRF models to simulate the rain attenuation process. The time series displayed in Fig. 6.13 unmistakably indicates that the dynamic behavior of rain attenuation is more realistic and finely captured in the MultiEXCELL model, particularly with increased time resolution.

To highlight the contributions of both rain and cloud attenuation, it is necessary for the time series of cloud attenuation to match the resolution of the rain attenuation. Given that cloud attenuation is generally smaller and exhibits less variability than rain attenuation, a practical approach involves using linear interpolation to enhance the temporal resolution of cloud attenuation.



(a) Rain and cloud attenuation time series (b) Total attenuation time series

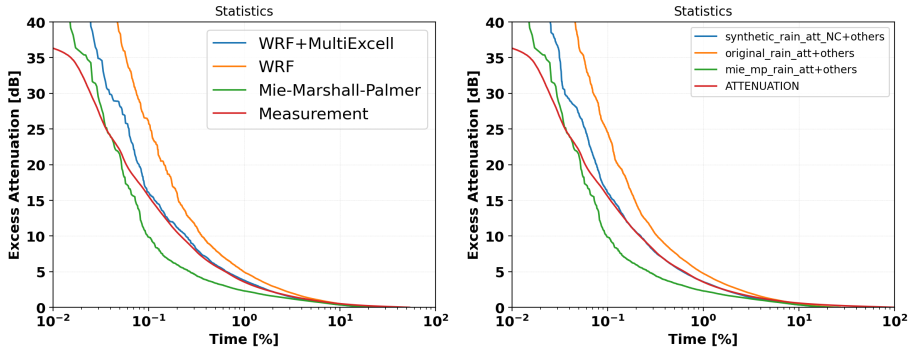
Figure 6.13: (a) The time series attenuation of cloud and rain for two models of MultiEXCELL and original WRF rain rates which, the rain rates have been processed through optical flow algorithm. (b) Contribution of rain and cloud which the temporal resolution of cloud attenuation has been increased by interpolation. The ground station is at Louvain-la-Neuve and the frequency is 39.402 GHz.

Figure 6.13b illustrates the contributions of rain and cloud in the Multi-EXCELL and WRF models, where the rain rates have undergone processing through the optical flow algorithm.

In Figure 6.13, the graph representing WRF exhibits discontinuities every 5 minutes due to variations in rain rate intensity within each 5-minute interval. This issue persists during the optical flow processing. Notably, during the time period from 10:50 to 11:30 in Fig. 6.13, the slope of WRF rain attenuation is smoother every 5 minutes, reflecting a more consistent rain event with mostly constant intensity. This results in a more realistic output from the optical flow algorithm. Conversely, during the time period from 10:40 to 11:30, there is a significant change in the rain event, leading to multiple discontinuities in the heavy rain events.

The long-term statistical results (2018-09-01 to 2019-08-30 at Louvain-la-

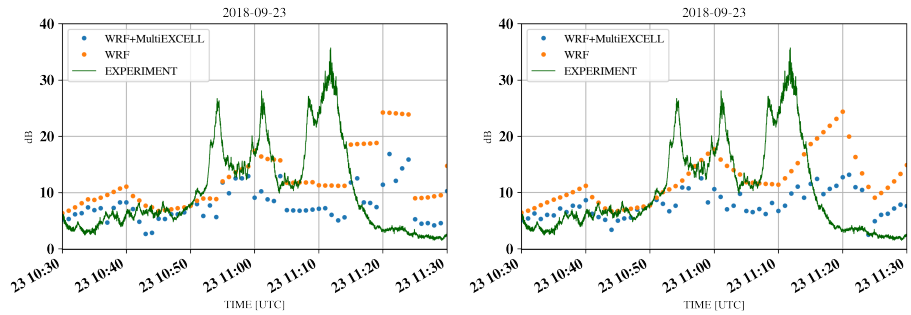
Neuve) of increasing the temporal resolution in rain attenuation time series are presented in Figure 6.14. The figure displays two sets of statistics for time series resolutions of 5 minutes and 1 minute, confirming that increasing the time resolution not only maintains but also enhances the long-term statistical accuracy.



(a) 5-min time series statistics (b) 1-min time series statistics

Figure 6.14: (a) shows the CCDF (2018-09-01 to 2019-08-30 at Louvain-la-Neuve) of the total attenuation time series with 5-min resolution and (b) displays the CCDF of the total attenuation with increased time resolution to 1-min by optical flow model

The Figure 6.13b after rain intensity correction is plotted in Figure 6.15b.



(a) Before rain intensity correction (b) After rain intensity correction

Figure 6.15: The effect of rain intensity correction in registering images at the resulting time series of attenuation. The ground station is at Louvain-la-Neuve and the frequency is 39.402 GHz.

6.5 Conclusion

This chapter introduced a framework to enhance the temporal resolution of rain rate fields derived from Numerical Weather Prediction (NWP) models—an es-

sential step for accurate modeling of rain-induced attenuation in high-frequency satellite communication systems.

Two complementary techniques were proposed to address the coarse temporal granularity of NWP outputs. First, we explored the use of meteorological wind fields to advect rain cells, leveraging the horizontal wind components from WRF simulations at the 700 hPa level. Although conceptually straightforward, this approach was shown to be limited by the inherent complexity of atmospheric motion, including three-dimensional wind structures, non-passive rain processes, and spatial deformation due to shear and convection.

Second, we implemented and evaluated optical flow methods—specifically the Lucas-Kanade and TV-L1 algorithms—to track and interpolate rain motion between two consecutive NWP frames. A detailed theoretical foundation was provided, followed by a quantitative and qualitative performance assessment through synthetic transformation cases. While the Lucas-Kanade method demonstrated efficient estimation for simple and localized motion, the TV-L1 approach exhibited superior robustness in handling complex transformations such as object occlusion and nonlinear motion, making it more suitable for dynamic meteorological environments.

To apply these models to real rain fields, we developed a preprocessing pipeline that converts 2D rain rate data into brightness images using normalized reflectivity. This transformation preserves spatial gradients and intensity continuity, which are essential for optical flow accuracy. Furthermore, we introduced a correction scheme to account for changes in rain intensity over time, improving temporal interpolation in evolving rain systems.

The enhanced temporal resolution was demonstrated on real NWP outputs, achieving 1-minute intervals from original 5-minute frames. These interpolated rain sequences were then used to compute high-resolution attenuation time series. The results showed a more continuous and realistic representation of fast-varying rain attenuation, critical for evaluating the performance of Fade Mitigation Techniques (FMT) in Low Earth Orbit (LEO) satellite systems.

Finally, statistical analysis confirmed that increasing temporal resolution not only improves the fidelity of short-term simulations but also enhances the long-term statistical characterization of attenuation events. These developments lay the groundwork for more responsive and accurate link budget planning in satellite communication networks, especially where real-time adaptation is required.

The final evaluation of the impact of temporal interpolation on attenuation modeling—along with its integration into full-scale system simulations—will be addressed in Chapter 7.

Chapter 7

Model Validation

This chapter presents a comprehensive validation of the rain attenuation modeling framework developed in the previous chapters. The focus is on assessing the performance of models that rely on Numerical Weather Prediction (NWP) data to generate both time series and long-term statistical metrics of propagation attenuation.

We begin in Section 7.1 by discussing the inherent limitations and challenges of using NWP data as a substitute for real measurements. This includes a critical analysis of model initialization, resolution constraints, and the implications for attenuation prediction.

Section 7.4 is dedicated to evaluating the MultiEXCELL-based rain attenuation model. This assessment is performed using two years of geostationary (GEO) satellite link data at a single ground location. The goal is to measure how well the synthetic rain fields generated by MultiEXCELL reproduce observed attenuation events.

In Section 7.4.3, we validate the rain motion model introduced in Chapter 6, which was designed to improve the temporal resolution of rain rate time series. We analyze the impact of this temporal refinement on attenuation prediction, and compare the results with ground-truth observations to assess statistical consistency and accuracy.

Finally, we extend the application of the complete modeling chain—including high-resolution spatial and temporal rain fields—to several Low Earth Orbit (LEO) satellite scenarios (Section 7.4.4). In these cases, we generate attenuation time series and evaluate performance across different link geometries and motion patterns.

Together, these validation efforts aim to provide a solid empirical foundation for the proposed modeling framework and to highlight its practical relevance for the design and optimization of Earth-space communication systems.

7.1 WRF Initialization

The design of the NWP domains will be structured into three distinct domains, namely d01, d02, and d03, each featuring horizontal grid sizes of 18 km, 6

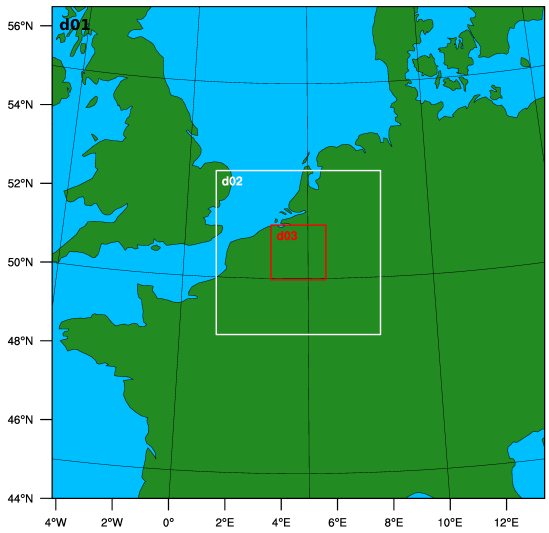


Figure 7.1: WPS domain configuration with three subdomains d01, d02, and d03 centered at Louvain-la-Neuve, Belgium

km, and 2 km, respectively. Figure 7.1 visually depicts these domains in the Lambert Conformal Conic map projection.

In addition to the previously outlined horizontal domains, the specific configuration details for a daily run of WRF are as follows:

- initialization data: ECMWF ERA-5 analysis (0.25°) every 6 h (The data for ERA5 is also available for every 1 hour but the best initialization for WRF software is entering the data every 6 hours).
- vertical coordinates: 50 automatic vertical levels, 50 hPa pressure top.
- lead time : 6 hours (see section 7.1.1)
- run time : 12 hours (see section 7.1.1)
- water microphysics : WRF single-moment 6 (WSM6)
- cloud physics: Tiedtke for (d01,d02) and no cumulus for inner domain (d03).
- surface layer physics: revised MM5 Monin-Obukhov scheme.
- planetary boundary layer physics: Yonsei University (YSU) scheme, called at each time step.
- soil layer physics: unified Noah land-surface model, 4 layers.
- diffusion and damping: second order diffusion on coordinate surfaces, Rayleigh damping with damping coefficient (inverse timescale) 0.2 Hz.

- radiation physics: RRTM schemes for long-wave and Dudhia scheme for short-wave radiations.

In this work, the **WSM6** (WRF Single-Moment 6-class) microphysics scheme was selected for representing rain processes in the WRF simulations. The choice of WSM6 was motivated by its demonstrated ability to provide realistic rain attenuation predictions in mid-latitude climates, as reported in prior studies.

Quibus et al. [44] compared nine different microphysics schemes (four single-moment: WSM6, Lin, Eta, Goddard; and five double-moment: WDM6, Thompson, Milbrandt–Yau, Morrison, NSSL) for rain attenuation prediction using WRF, in conjunction with satellite beacon measurements at 20.2 GHz and 39.4 GHz in Toulouse, France. Their results indicated that the **Lin** and **WSM6** schemes offered the best agreement with experimental data among single-moment schemes, particularly for high-frequency bands, while other schemes (e.g., NSSL) showed discrepancies.

In a later study, Quibus et al. [43] highlighted that the choice of microphysics scheme remains a key factor in the accuracy of rain attenuation estimation. They reported that the **NSSL two-moment** scheme provided the closest match to measured attenuation at high frequencies (39.4 GHz). However, this improvement came at the cost of higher computational demand compared to single-moment schemes like WSM6.

Considering the balance between prediction accuracy, computational cost, and the good performance of WSM6 reported in [44], we adopt WSM6 as a suitable choice for this study. While double-moment schemes such as NSSL may offer marginal improvements in accuracy, WSM6 provides a practical compromise for long-term simulations while maintaining reliable agreement with beacon measurements in comparable climatic conditions.

Other parameters are retained at their default values. Further details on how to select various options are thoroughly explained on the NOAA Earth System Research Laboratory website [117].

7.1.1 Lead Time and Run Time

In weather simulations, Numerical Weather Prediction (NWP) algorithms typically need an initial period to stabilize. During this time, the data produced right after the simulation begins is unreliable. As the simulation progresses, the data becomes more accurate but starts to lose accuracy as it moves further from the starting point. The time it takes for the simulation to stabilize is called the *lead time*. Once the simulation data becomes stable and reliable, it is referred to as the *run time* (see Figure 7.2).

Choosing the right lead and run time is challenging. Several studies discuss the best practices for selecting these parameters [118–120].

Common options for lead time include 6 hours and 12 hours, while the run time can typically be 6 hours, 12 hours, or 24 hours. To evaluate how these choices affect the simulation results, we analyzed a day with heavy rainfall—October 1, 2019—at the Louvain-la-Neuve ground station. Figure 7.3 shows several instances of high attenuation ($\geq$ 10 dB) due to rain during the day at a frequency of 39.402 GHz, with an elevation angle of 30° and an azimuth



Figure 7.2: Lead and Run time configuration in NWP

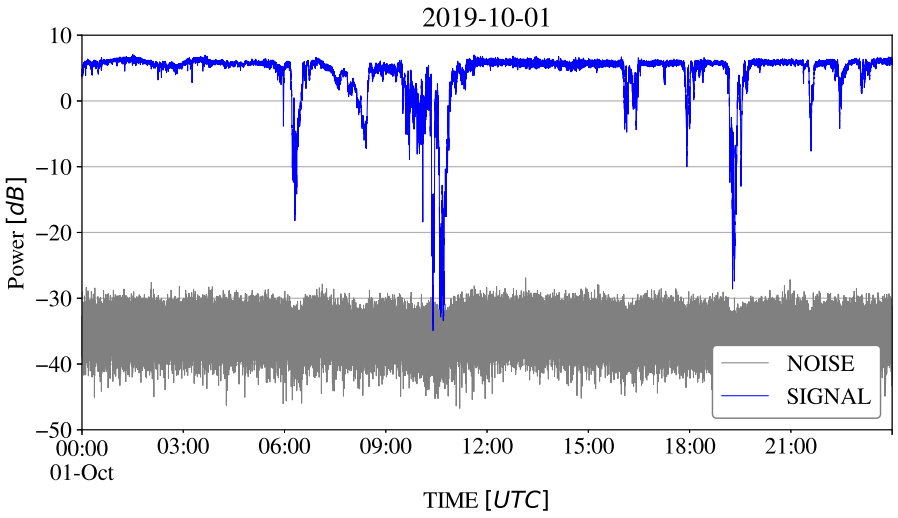


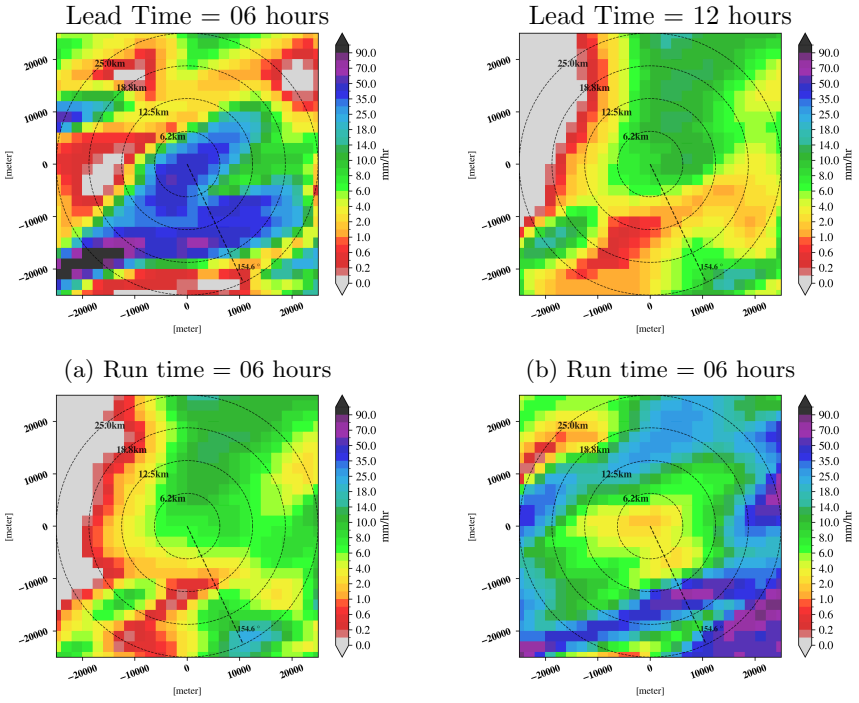
Figure 7.3: Received signal and noise level of Alphasat station at Louvain-la-Neuve at frequency 39.402 GHz.

angle of 154°. Given that the rain height was less than 3 km, we expected the rain event to occur within a 5 km radius from the ground station. This example helps us compare the NWP results with real-world data and investigate how lead and run times affect the estimation of rain rates.

In Numerical Weather Prediction (NWP), the exact timing and location of the output data may not perfectly match real meteorological data. As a result, heavy rainfall events similar to those shown in Figure 7.3 can be expected at different times and locations on the same day. Figure 7.4 shows the NWP rain rate estimation on the morning of October 1, 2019, at Louvain-la-Neuve, for various combinations of lead and run times. By comparing Figures 7.3 and 7.4, it is possible to predict a heavy rainfall event between 10:00 and 11:00 AM. The configuration with 6 hours for both lead and run time (see Figure 7.4a) seems to provide the most accurate match - The same conclusion in [118].

Figures 7.5-7.6 shows the final rain attenuation time series, which offers a clearer view of how lead and run time affect the accuracy of rain attenuation estimation. By comparing the subfigures 7.5 and 7.6 with the experimental data, we can draw the following conclusions:

- In all cases, the simulation estimates some rain events that were not observed in the experimental data. However, these simulated events may have occurred near the ground station, where the NWP slightly misjudged



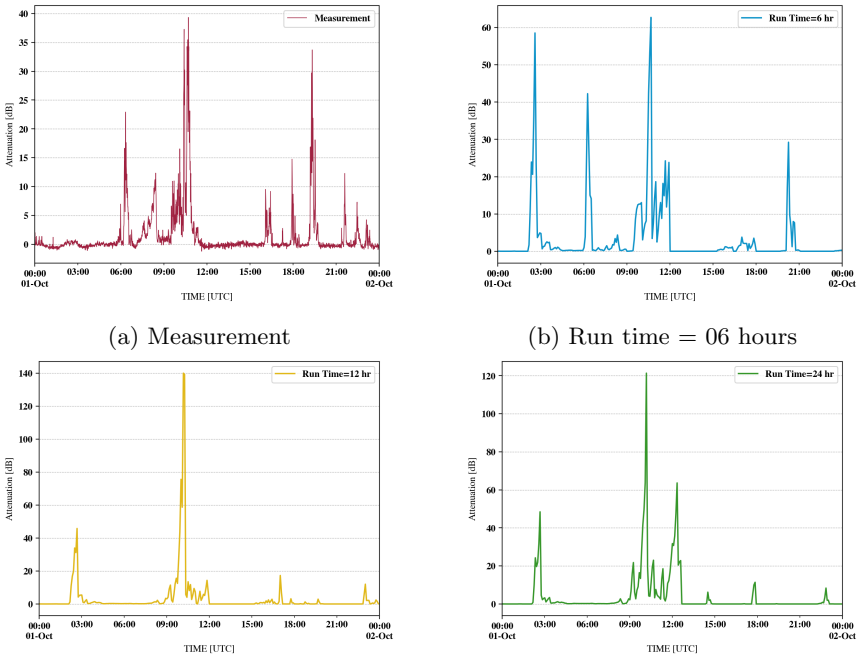
(a) Run time = 06 hours

(b) Run time = 06 hours

(c) Run time = 12 hours

(d) Run time = 12 hours

Figure 7.4: Studying the effect of lead time and run time in rain rate simulation of NWP. Lead time for the left and right columns are 06 and 12 hours. The fix time of the event is 2019-10-01 10:40:00 centered at Louvain-la-Neuve.



(a) Measurement

(b) Run time = 06 hours

(c) Run time = 12 hours

(d) Run time = 24 hours

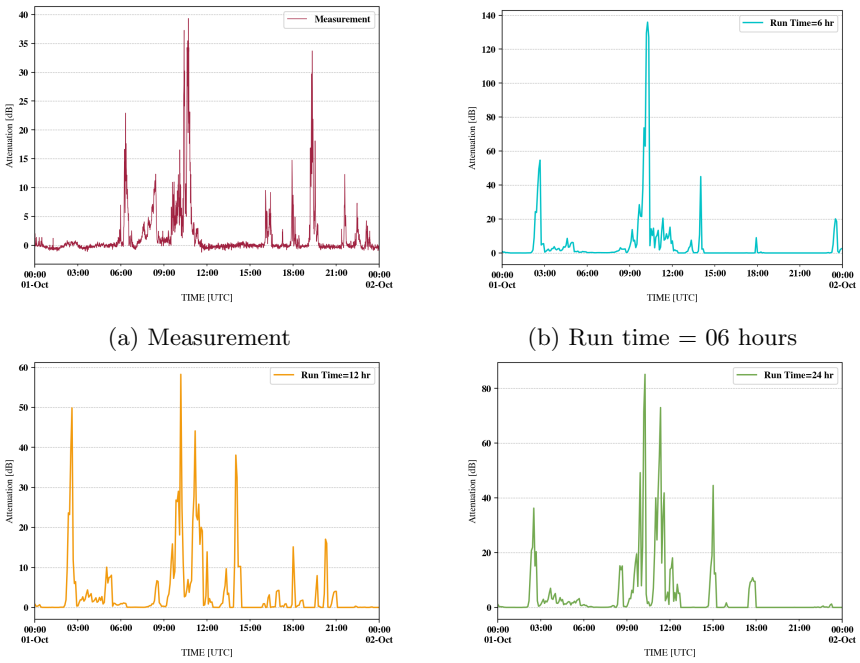
Figure 7.5: Studying the effect of **lead time 6 hours** and different run time of NWP in rain attenuation time series. The experiment data is of Alphasat station at 2019-10-01, centered in Louvain-la-Neuve.

their location, leading to their detection in the simulation.

- The continuity of the time series is more stable for the configuration with a 24-hour run time compared to the others. However, the accuracy of the rain attenuation estimate is lower for this configuration.

- The best scenario is observed with the combination of a 6-hour lead time and a 6-hour run time (shown by the blue curve in Figure 7.5b).

The optimal choice is the setup with 6 hours for both lead and run time, as this provides the best balance of accuracy and simulation efficiency. This setup requires running the NWP simulation twice, which results in a longer simulation time. To optimize both accuracy and computation time, the final choice is a combination of 6 hours for lead time and 12 hours for run time, as represented by the orange curve in Figure 7.5c.



(a) Measurement

(b) Run time = 06 hours

(c) Run time = 12 hours

(d) Run time = 24 hours

Figure 7.6: Studying the effect of **lead time 12 hours** and different run time of NWP in rain attenuation time series. The experiment data is of Alphasat station at 2019-10-01, centered in Louvain-la-Neuve.

7.2 Estimation of Excess Attenuation from Alphasat Measurements

The estimation of excess (rain + cloud) attenuation from the Alphasat ground station at Louvain-la-Neuve (Table 7.1) was carried out through a semi-manual yet systematic approach, combining visual inspection, signal flagging, and post-processing using the PDPS (Propagation Data Processing Software) tool.

Table 7.1: Ground station parameters at Louvain-la-Neuve

Parameter	**Value**
Location (City)	Louvain-la-Neuve, Belgium
Latitude	50.67° N
Longitude	4.61° E
Altitude	160 m above sea level
Elevation angle	$\approx 30°$
Azimuth angle	$\approx 154°$
Carrier Frequency #1	19.701 GHz
Polarization (Tilt, τ)	0° (Horizontal)
Carrier Frequency #2	39.402 GHz
Polarization (Tilt, τ)	45° (Slant)

Manual Identification of Weather Events: The process began with a manual inspection of the raw received signal power time series. Based on the observed signal fluctuations, potential rain and cloud attenuation events were identified and flagged. This step relied on visual pattern recognition to distinguish between clear sky periods and periods affected by atmospheric disturbances (see Figure 7.7).

Signal Classification and Flagging: Each segment of the time series was labeled either as a clear-sky interval or as affected by rain or cloud attenuation. Non-flagged intervals were assumed to represent clear-sky conditions and served as the reference baseline for further analysis.

Calculation of the Reference Level: To estimate the clear-sky reference level, a low-pass filter was designed and applied to the signal during clear-sky periods. This filtering process removed short-term fluctuations and isolated the slowly varying baseline signal that represents the undisturbed propagation condition. The resulting filtered signal was considered as the reference level (see Figure 7.8).

Attenuation Computation: Rain and cloud attenuation values were then calculated by measuring the difference between the raw received signal and the estimated clear-sky reference level. This differential approach allows a direct estimation of the total excess attenuation due to weather phenomena (see Figure 7.9).

Post-Processing in PDPS: Finally, the PDPS tool was used to compute and organize the attenuation data using the flags provided during manual classification. The tool systematically applied the reference level and performed the subtraction to yield attenuation time series for rain and cloud events.

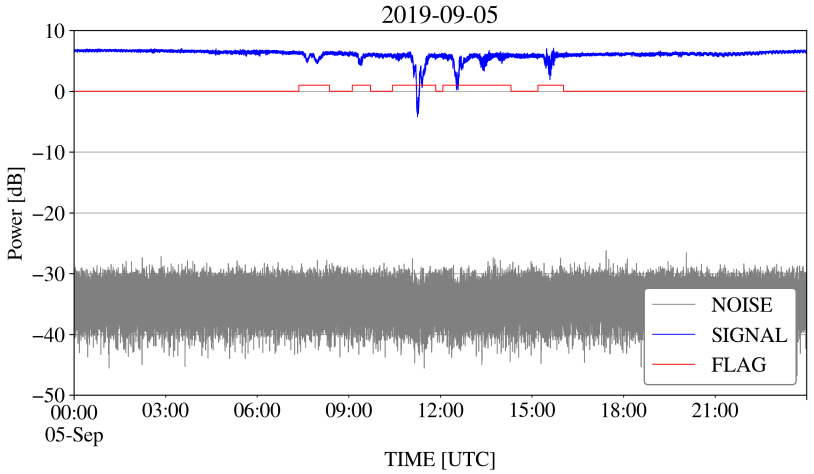


Figure 7.7: Raw received signal power at 39.402 GHz from the Alphasat ground station. Rain and cloud events are manually flagged based on visible drops in signal level.

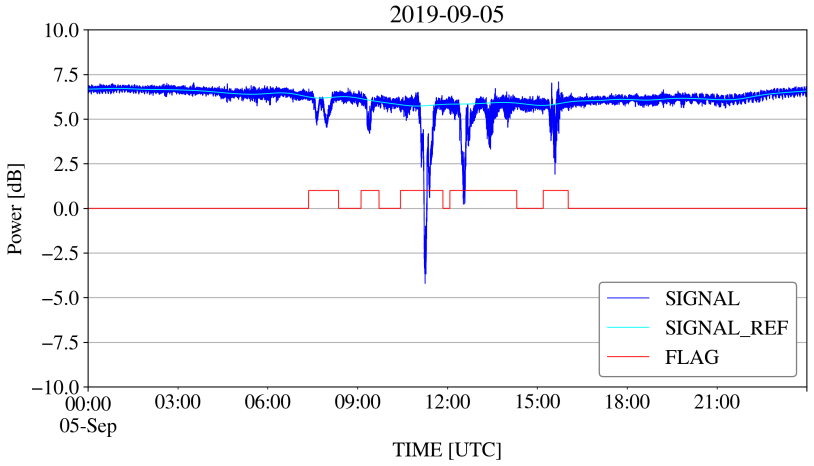


Figure 7.8: Low-pass filtered reference signal (blue) overlaid on the raw signal (gray). Clear-sky intervals were used to estimate the stable baseline level.

This methodology allowed for reliable estimation of atmospheric attenuation based on empirical signal observations and supports the validation of numerical predictions discussed in the following sections.

It is important to clarify the type of attenuation retrieved from the Alphasat beacon measurements. The raw beacon signal inherently contains all propagation impairments, including gaseous absorption, cloud attenuation, and rain attenuation. However, in our preprocessing procedure, the reference level is obtained by applying a low-pass filter to periods flagged as clear-sky. This

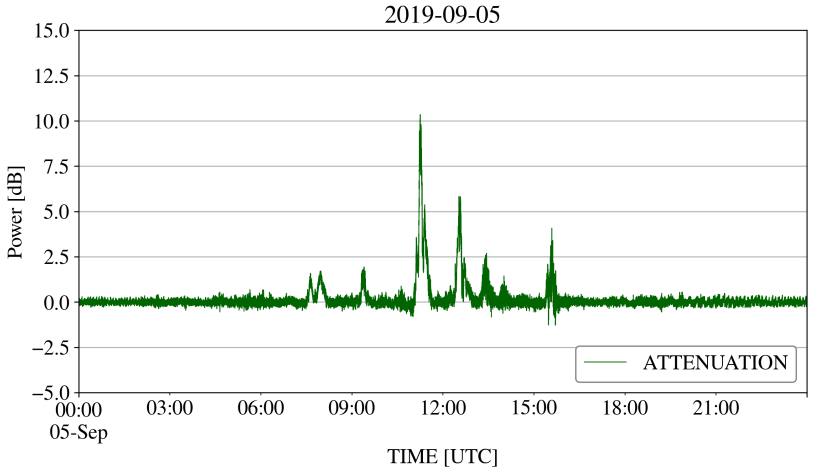


Figure 7.9: Computed rain and cloud attenuation as the difference between the raw signal and reference level. This attenuation time series represents the atmospheric impact on the downlink.

means that the slowly varying gaseous absorption is included in the reference baseline and thus effectively removed from the time series.

As a consequence, the attenuation derived from our measurements corresponds to excess attenuation, i.e., the combined effect of clouds and rain, rather than the total attenuation including gases. This distinction is crucial for comparison with simulations:

- When validating against **rain+cloud simulations**, the comparison is direct and consistent.
- When validating against **total attenuation simulations** (rain + cloud + gases), the gaseous component must be either removed from the simulation or added back to the measurements to ensure consistency.

This limitation is inherent to the beacon measurement correction process where gaseous attenuation could not be retrieved independently from beacon data without additional radiometric instruments. For this reason, the comparisons at section 7.4.3.4 in this chapter focus primarily on the excess attenuation (cloud + rain), which is the measurable component at our station.

7.3 Summary of Attenuation Time Series Generation and Resolution Considerations

This section provides a structured overview of the methodology used to generate attenuation time series for gaseous, cloud, and rain components. The complete processing workflow is summarized, from the extraction of atmospheric parameters in WRF outputs to their conversion into attenuation using

ITU-R formulations, Mie scattering, or statistical downscaling methods (e.g., MultiEXCELL, optical flow).

Particular emphasis is placed on the spatial and temporal resolutions adopted in this study (100 m and 1 minute, respectively), together with a discussion of their practical justification and associated trade-offs. The restrictions inherent to each model, along with their known limitations in different climatic regimes and precipitation regimes, are also addressed. These considerations form the basis for evaluating the reliability and applicability of the generated time series in propagation impairment studies.

7.3.1 Overview of Attenuation Time Series Generation

In this study, attenuation time series for gaseous, cloud, and rain components were generated using multiple processing paths derived from Weather Research and Forecasting (WRF) model outputs. The methods differ in how the raw meteorological fields are transformed into attenuation values, as illustrated in Figure 7.10.

- **Rain attenuation paths:**
  - *WRF Rain Rate Path (RR[WRF]):* Ground-level rain rate from WRF (2 km spatial, 5-min temporal resolution) was enhanced in time using Optical Flow to 1-min resolution. The resulting fields were directly converted to **specific attenuation** using ITU-R P.838 coefficients [56], and then integrated along the path to produce the rain attenuation time series.
  - *MultiEXCELL-enhanced Rain Rate Path (RR[MultiEXCELL]):* The Optical Flow–enhanced WRF rain rate fields were spatially refined using MultiEXCELL to $\leq$100 m resolution. The enhanced fields were then converted to **specific attenuation** (ITU-R P.838 [56]) and integrated to obtain high-resolution rain attenuation time series.
  - *WRF Rainwater Content Path (Mie-based):* Rainwater mixing ratio from WRF was converted to specific attenuation using Mie scattering theory with Marshall–Palmer drop size distribution. This produced rain attenuation at 2 km and 5-min resolution, which was later interpolated to 1-min resolution for combination with other components.
- **Cloud attenuation path:** Cloud liquid water content from WRF (2 km, 5-min) was processed using ITU-R P.840 [55] formulations to produce cloud-specific attenuation and then integrated to form the cloud attenuation time series. These were interpolated from 5-min to 1-min resolution for combination with rain and gas components.
- **Gaseous attenuation path:** WRF pressure, temperature, and humidity fields (2 km, 5-min) were processed using ITU-R P.676 [54] absorption models for oxygen and water vapour. The resulting gaseous attenuation time series were interpolated to 1-min resolution for total attenuation analysis.

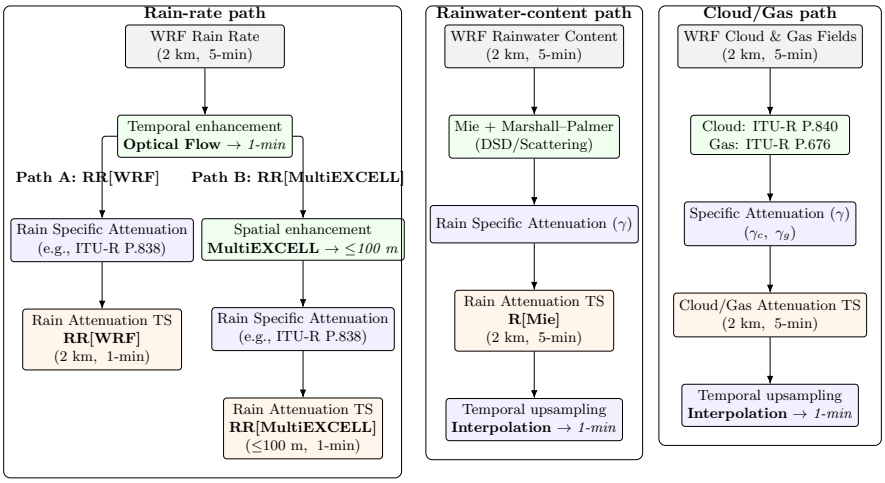


Figure 7.10: Processing chains for rain rate, rainwater content, and cloud/gas.

7.3.2 Resolution Choices and Limitations

The baseline resolution adopted in this work is 100 m in space and 1 minute in time. This choice reflects a balance between the smallest scales that can be meaningfully reconstructed from the available WRF outputs, the capabilities of the enhancement methods, and computational practicality.

It is important to stress that the effective resolution of the simulations is constrained not only by the WRF model configuration but also by the resolution of both the boundary/initial conditions and the static geography data. In this study:

- The boundary and initial conditions were taken from ERA5 reanalysis, with 0.25° (∼25 km) horizontal resolution, updated every 6 hours (`interval_seconds = 21600`).
- Three nested WRF domains were employed: d01 = 18 km, d02 = 6 km, and d03 = 2 km horizontal resolution.
- WRF output frequency was set through `history_interval = '60, 60, 5'`, i.e., 60 min for d01/d02 and 5 min for d03.
- The static geography fields (terrain height, land-use/land-cover, albedo, green fraction, etc.) provided by WPS are typically available at resolutions between ∼1 km (GTOPO30, MODIS) and ∼90 m (SRTM)[1], depending on dataset availability [64, 65]. This means that small-scale orography and land-cover detail cannot exceed the intrinsic resolution of the underlying geog data, even if the WRF grid spacing is finer (see Figures 7.11 and 2.1).

[1] Arc-second spacings are angular: 1° latitude ≈ 111 km everywhere, so 30″ ≈ 0.9 km (N–S). For longitude, the distance scales with $\cos\varphi$; at mid-latitudes ($\varphi \sim 50°$), 30″ corresponds to ∼0.6 km (E–W).

As a consequence, although post-processing methods (Optical Flow, MultiEXCELL) allow refinements down to 100 m and 1 minute, the dynamical information at scales smaller than the forcing data (ERA5: 25 km, 6 h) and the static geog datasets (typically ∼1 km) is generated internally by WRF physics. Therefore, very fine resolutions (e.g., 10 m, 1 s) should not be interpreted as physically validated atmospheric structures but only as synthetic realizations.

Higher resolutions, such as **10 m** spatial and **1 s** temporal, are theoretically achievable with the processing chain used here, but only under specific constraints:

- **Optical Flow:** Temporal refinement can be pushed below 1 minute, potentially down to 1–5 s, provided advection patterns remain coherent. At sub-second scales, however, variability is dominated by turbulence and noise rather than meaningful atmospheric dynamics.
- **Using MultiEXCELL:** Spatial downscaling can, in principle, reach resolutions finer than 100 m, even approaching 10 m, but the realism of such fields becomes increasingly uncertain at very small scales. Rain cell structure and turbulence below 50–100 m are largely stochastic, and any generated patterns at these scales should be treated as synthetic realizations rather than deterministic predictions.
- **Practical recommendation:** Resolutions beyond 100 m in space or 1 minute in time should be considered for sensitivity testing or Monte Carlo analyses [2]rather than as physically validated products.

In summary, while Optical Flow and MultiEXCELL enable significant refinement of WRF outputs, their validity is bounded by the resolution of ERA5 forcing (25 km, 6 h) and WRF's internal nesting (down to 2 km, 5 min). The **100 m / 1 min baseline adopted in this work** therefore represents the finest resolution that can be physically justified given the model chain (see Figure 7.11).

7.3.3 Verification and Validation Strategy

Given that WRF-based time series cannot reproduce exact in-situ measurements at specific instants, validation was focused on cumulative statistics such as Complementary Cumulative Distribution Functions (CCDFs). This approach is supported by previous works (e.g., [41, 43, 45, 47]) showing that long-term statistics can be reliably reproduced even if instantaneous values differ. Verification steps included:

- Comparison of simulated and measured CCDFs for each attenuation type.
- Cross-validation with ITU-R reference models for typical and extreme percentiles.

[2]The Monte Carlo method is a statistical simulation approach that generates a large number of realizations of a system by introducing random variations in certain parameters or inputs. The resulting outputs are then analyzed to assess the distribution, variability, and uncertainty of the predictions.

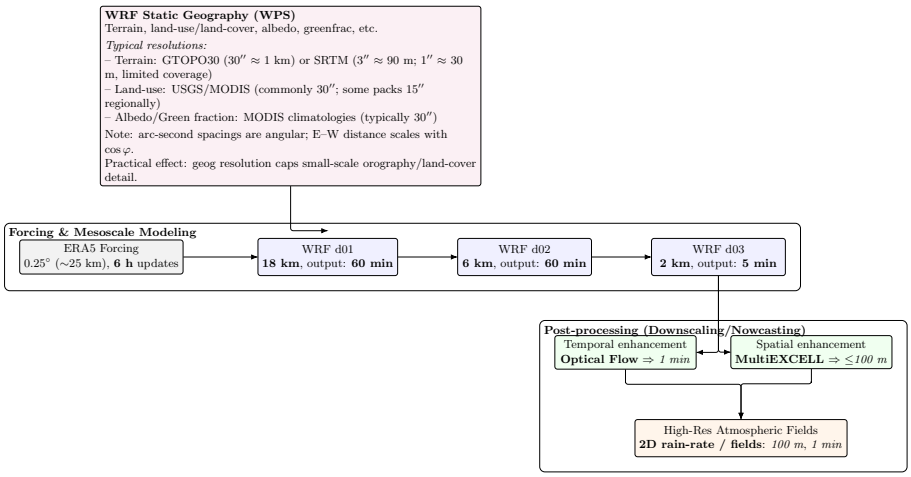


Figure 7.11: Resolution cascade from ERA5 forcing and static geog data to nested WRF domains and post-processing (Optical Flow for temporal refinement; MultiEXCELL for spatial downscaling) yielding *1-min / 100-m* products.

- Sensitivity tests on lead time and run time, confirming stability of statistical outputs for the chosen forecast configuration.

7.3.4 Limitations of MultiEXCELL

While MultiEXCELL provides a powerful framework for statistically downscaling rainfall fields and generating high-resolution synthetic rain structures, it also presents several intrinsic limitations that must be acknowledged:

1. **Climatic applicability:** MultiEXCELL was originally developed and validated for mid-latitude convective and stratiform rain structures. Its parameterizations may not fully capture the physics of:
   - **High latitudes**, where snowfall, mixed-phase precipitation, and large-scale synoptic systems dominate.
   - **Tropical climates**, where convective systems are extremely intense and localized, often with dynamics outside the scope of the model assumptions.
2. **Statistical parameterization constraints:** The model relies on empirical descriptors of rain cells (e.g., peak rain rate, equivalent radius, inter-cell spacing) derived mainly from mid-latitude radar observations. Applying the same parameterization universally may lead to unrealistic rain fields when the underlying drop-size distribution (DSD) or convective organization differs strongly from the reference datasets.
3. **Precipitation-type sensitivity:** MultiEXCELL does not reproduce well:

- **Very shallow, widespread stratiform rain** (<1 mm/h), which is smooth in space and time but relevant for weak attenuation.
- Events dominated by **non-liquid precipitation** (snow, ice, mixed-phase), since the model is inherently designed around liquid rain cells.

In summary, while MultiEXCELL is valuable for generating realistic high-resolution rain fields in temperate mid-latitudes, its use outside those regimes should be undertaken with caution, and potentially re-parameterized with region-specific observational data.

7.3.5 Lead Time and Run Time Considerations

The lead time/run time configuration was chosen to balance forecast spin-up effects and temporal coverage. While qualitative inspection of time series can show mismatches, statistical comparisons over many events confirm the adequacy of the chosen parameters. Longer lead times tend to reduce small-scale temporal accuracy but preserve statistical validity [118, 119].

7.3.6 Model Limitations and Physical Assumptions

Several limitations of the current modelling framework must be stressed:

- **Light rain bias:** WRF tends to misrepresent low-intensity rain, which can disproportionately affect low-elevation links where long slant paths amplify attenuation.
- **Vertical rain rate profile:** Rain rate is assumed constant with height; bright band effects from melting snow are neglected, potentially leading to underestimation near the freezing level.
- **Microphysical simplifications:** The chosen microphysics scheme (WSM6) does not explicitly resolve drop size distributions, limiting fine-scale accuracy in rain attenuation estimates.

In summary, the simulated time series should be interpreted as statistical surrogates, not exact replicas of site measurements. The approach is valid for long-term performance evaluation and model inter-comparison, but not for reproducing individual events at sub-minute resolution.

7.4 Results

This section begins by showcasing representative examples generated from the WRF and MultiEXCELL models, along with a description of the post-processing steps applied to the data. The examples include attenuation time series for both GEO and LEO satellite links, as well as azimuth–elevation maps that illustrate the individual contributions of rain, cloud, and gaseous attenuation. Key NWP parameters used in the simulations are also provided for context.

Following the qualitative overview, a quantitative evaluation is conducted. This includes a comparison of statistical distributions using error metrics for the GEO satellite attenuation components at an elevation angle of 30°. The comparison draws on multiple sources: experimental measurements, ITU-R model predictions, direct WRF simulation outputs, MultiEXCELL model results, and the enhanced outputs obtained through the optical flow technique.

7.4.1 Propagation Azimuth-Elevation Maps

One important step before computing attenuation time series is generating azimuth–elevation (AE) specific attenuation maps, as described in Section 4.4.1. Figure 7.12 shows examples of such maps for different atmospheric components—namely, gaseous, cloud, and rain attenuation—at a representative time: 2018-09-23 10:55:00 UTC, centered over Louvain-la-Neuve.

The gaseous attenuation map (Figure 7.12a) displays the expected azimuthal symmetry, with only a slight variation (about 0.4 dB) observed at 5° elevation. These values closely follow the standard cosecant scaling law: for example, attenuation is around 0.48 dB at the zenith and approximately 0.958 dB at 30° elevation—very close to the theoretical 0.96 dB. Small deviations from perfect symmetry or scaling (see Figure 7.13a) are minor, but at very low elevation angles, the signal path may fall slightly below the tropopause, introducing some irregularities. While the WRF domain (d03) covers elevations down to 5°, the post-processing in this study was limited to a smaller 160 km × 160 km subdomain centered on Louvain-la-Neuve. Additionally, since refraction is not accurately modeled, the statistical analyses in the following sections are restricted to elevation angles of 10° and above.

From this analysis, it is evident that 3D NWP data is not strictly necessary to model gaseous attenuation accurately—simpler 1D vertical profiles would often suffice. Nonetheless, gaseous attenuation serves as a useful reference baseline for assessing the overall performance of the NWP-based modeling strategy, thanks to its predictable and well-understood behavior.

Figure 7.12b presents the cloud attenuation map. In this case, attenuation is derived from the modeled cloud liquid water content using the method described in Section 3.4. Unlike the gaseous case, the cloud attenuation shows clear azimuthal asymmetry, with higher concentrations of cloud water—and thus higher attenuation—appearing in the southwestern part of the map.

At 30° elevation, the cloud attenuation ranges from 1.8 dB to 2.1 dB, with the theoretical value from the scaling law being 1.99 dB (see Figure 7.13b). At lower elevations, such as 5°, the attenuation increases significantly, ranging from 9.2 dB to 16.3 dB, compared to the expected 11.43 dB.

Although the scaling law provides a reasonable average estimate, it fails to capture the spatial heterogeneity of cloud distribution. This highlights the importance of using full 3D NWP data, which offers a more accurate, location-specific view of cloud-induced attenuation—especially useful for short-term or localized assessments.

Figures 7.12c–7.12e display rain attenuation maps produced using different modeling approaches, as introduced in Sections 3.6.1 and 3.6.4. These methods include estimates based on volumetric rainwater content, WRF-derived

ground-level rain rate (RR[WRF]), and the MultiEXCELL-enhanced rain rate (RR[MultiEXCELL]).

Although all three methods yield similar attenuation patterns, RR[WRF] generally predicts higher values. In the zenith direction, the estimated rain attenuations are approximately 2.0 dB, 6 dB, and 5 dB, respectively (Figures 7.12c–7.12e). These values indicate the presence of heavy rainfall, exceeding roughly 10 mm/h across the domain. Notably, rain attenuation dominates over gaseous and cloud attenuation in magnitude. A clear azimuthal dependence is also observed, with stronger attenuation concentrated toward the northwest.

For the method described in Section 3.6.1, azimuthal variability is minimal at 30° elevation, with attenuation ranging from 2.0 to 2.1 dB (compared to the expected 2.0 dB from the scaling law). At a lower elevation angle of 5°, however, the spread becomes much more significant—from 12 dB up to 27 dB—despite the scaling law predicting only 12 dB.

In contrast, the approach based on Section 3.6.4 produces slightly larger variations, particularly at higher elevation angles. For instance, at 30° elevation, the attenuation spans from 8.0 dB to 12 dB (vs. 10 dB expected), and at 5°, it ranges widely from 20 dB to 58 dB (while the scaling law suggests only 10 dB).

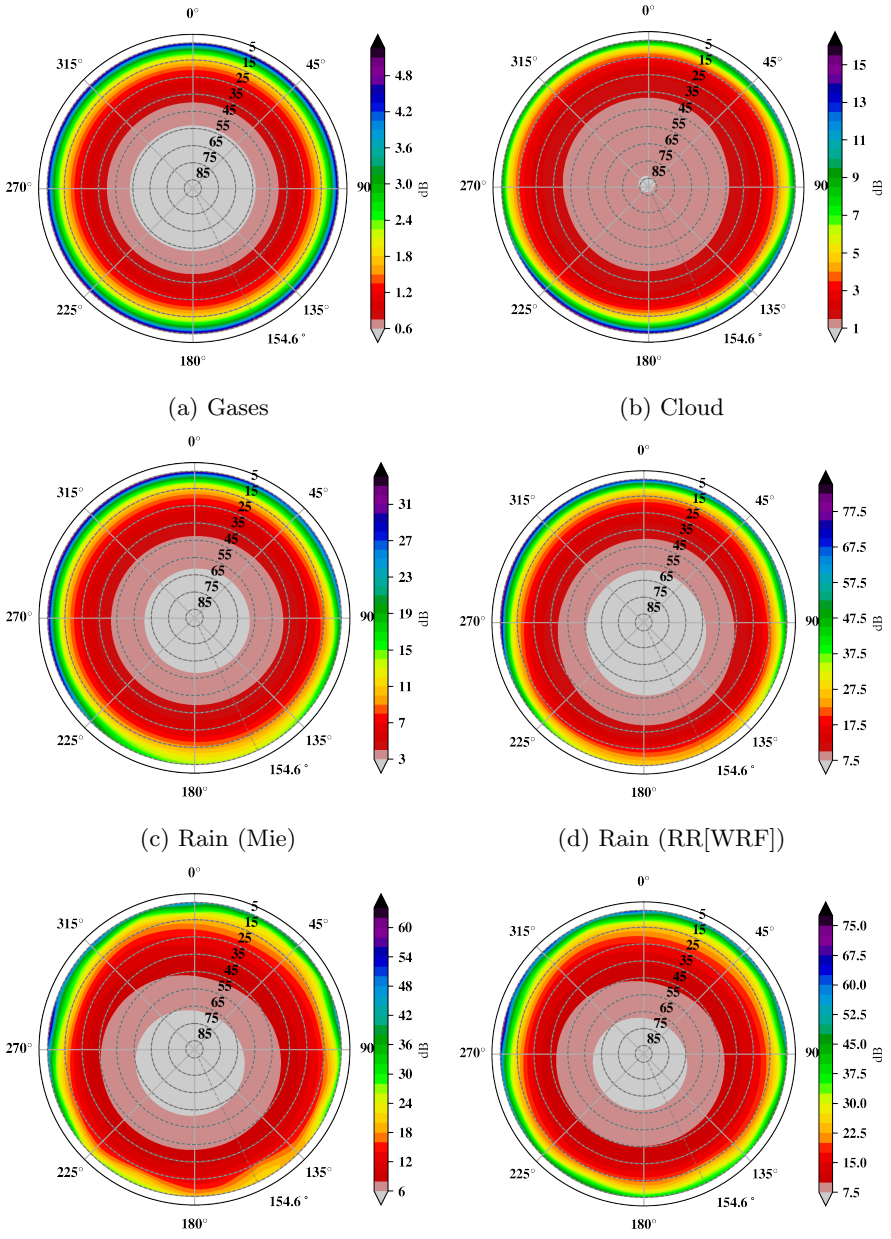
Overall, while the attenuation values deviate from scaling law predictions —especially at low elevations —the general trends of azimuthal dependence and elevation-based scaling are still reasonably preserved, particularly at moderate to high elevation angles.

In summary, having access to 3D atmospheric information is essential for producing accurate, instantaneous estimates of rain attenuation. However, at higher elevation angles, the rain attenuation appears to follow the expected azimuthal symmetry and scaling laws more closely than cloud attenuation. This suggests that commonly used modeling strategies—which rely solely on ground-based rain rate measurements at the station—are reasonable approximations in many cases. That said, localized convective rain cells can introduce significant azimuthal variations and lead to noticeable deviations from the scaling law.

	θ=5°	θ=30°	θ=90°
Min Cloud Att. [dB]	9.25611	1.800515	0.99678
Max Cloud Att. [dB]	16.317324	2.12034	0.99678
Cosecant law [dB]	11.436764	1.993559	0.99678

Table 7.2: Cloud attenuation vs it's cosecant law for three elevation angles. The data is for Louvain-la-Neuve on the 2018-09-23 at 10:55:00 UTC at 39.402 GHz.

Overall, the added value of 3D atmospheric data varies depending on the attenuation component. For gaseous attenuation, the benefits are minimal, and the simple cosecant law provides a reliable baseline for validation and benchmarking. In contrast, both cloud and rain attenuation exhibit stronger spatial variability, highlighting the advantages of leveraging full 3D NWP data for more accurate and realistic modeling.



(a) Gases

(b) Cloud

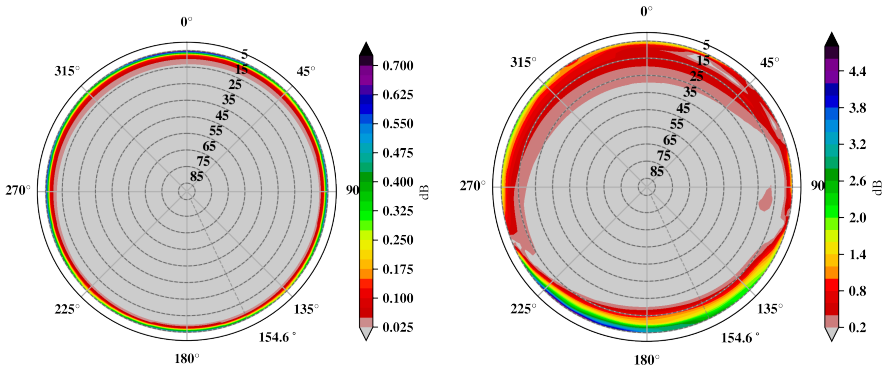
(c) Rain (Mie)

(d) Rain (RR[WRF])

(e) Rain (RR[MultiEXCELL])

(f) Total (Gases+Cloud+RR[MultiEXCELL])

Figure 7.12: Example of WRF-derived attenuation maps at 39.402 GHz for Louvain-la-Neuve on the 2018-09-23 at 10:55:00 UTC



(a) $|A_{gas} - \frac{A_{gas}[\theta=90°]}{\sin\theta}|$ (b) $|A_{cloud} - \frac{A_{cloud}[\theta=90°]}{\sin\theta}|$

Figure 7.13: Difference of the (a)gaseous and (b)cloud attenuation vs their cosecant law at 39.402 GHz for Louvain-la-Neuve on the 2018-09-23 at 10:55:00 UTC

	θ=5°	θ=30°	θ=90°
Min Gas Att. [dB]	4.773612	0.957245	0.480042
Max Gas Att. [dB]	5.258176	0.961502	0.480042
Cosecant law [dB]	5.507864	0.960084	0.480042

Table 7.3: Gaseous attenuation vs it's cosecant law for three elevation angles. The data is for Louvain-la-Neuve on the 2018-09-23 at 10:55:00 UTC at 39.402 GHz.

7.4.2 Time Series of Attenuation

Figures 7.14a and 7.14b present both measured and simulated rain attenuation time series at 39.402 GHz for a GEO satellite link observed from Louvain-la-Neuve on September 23, 2018. The link geometry is fixed with an elevation angle of 30° and an azimuth of 154.6°. Each time point is derived from azimuth-elevation attenuation maps generated every 5 minutes. In Figure 7.14b, the time resolution of the rain rate datasets (RR[WRF] and RR[MultiEXCELL]) has been enhanced to 1 minute using the optical flow technique. For consistency, the other attenuation components (gaseous and cloud) are interpolated linearly to match this higher resolution. The curves are presented in a stepwise fashion, showing first gaseous attenuation, then the addition of cloud attenuation, and finally the total attenuation (excluding scintillation effects).

From the measurement data, a light rain event is evident during the early morning hours, peaking at 02:20 UTC. The simulated results using the three modeling approaches—volumetric attenuation (Section 3.6.1), rain rate from WRF (Section 3.6.4), and MultiEXCELL (Chapters 6–5)—generally align with this observed event and exhibit a good degree of correlation. Among them, the rain attenuation derived from RR[MultiEXCELL] shows the closest agreement with the measurements, outperforming both the Mie scattering approach and

the direct WRF-based rain rate.

Cloud attenuation, also visible during the morning period, appears to correlate with rain, as the two phenomena are often coupled. In fact, distinguishing between light rain and cloud attenuation can be challenging when they overlap. Meanwhile, gaseous attenuation remains relatively stable throughout the day, with only minor variations of about 0.2 dB—starting at roughly 0.8 dB and dropping to about 0.6 dB by midday. These slow changes suggest that a 5-minute resolution is sufficient for modeling gaseous attenuation. However, for clouds and rain, higher temporal resolution is more valuable, especially when capturing peak events and rapid variability.

Figure 7.15 presents the simulated attenuation time series at 39.402 GHz for several LEO satellite links—specifically, Starlink-1256, Starlink-1260, Starlink-1263, and Starlink-1265—observed from Louvain-la-Neuve on September 23, 2018, using WRF outputs. The corresponding satellite elevation angles over time are shown in Figure 7.15b, illustrating their visibility during the day.

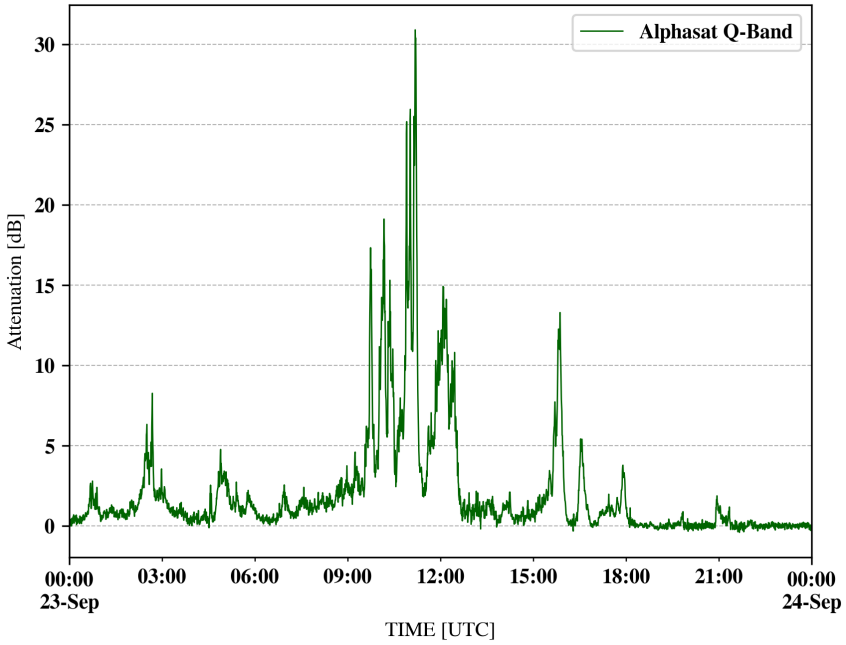
A minimum elevation angle of 5° is used to define when a satellite is considered "visible" from the ground station. With this threshold, each peak in the attenuation curves can be directly matched with a specific satellite pass across the sky. On this particular day, all passes occur during or shortly after a midday rain event, meaning that most of the attenuation observed is attributable to rain.

Each pass starts with the satellite at 5° elevation, corresponding to attenuation values between roughly 2 dB and 30 dB—and even exceeding 30 dB in some cases. This aligns well with expectations, given that the gaseous attenuation at 30° elevation (as observed in the GEO case) ranged between 0.6 dB and 0.8 dB. As the satellites ascend, the attenuation generally decreases, though the minimum attenuation reached during each pass varies depending on the satellite's maximum elevation.

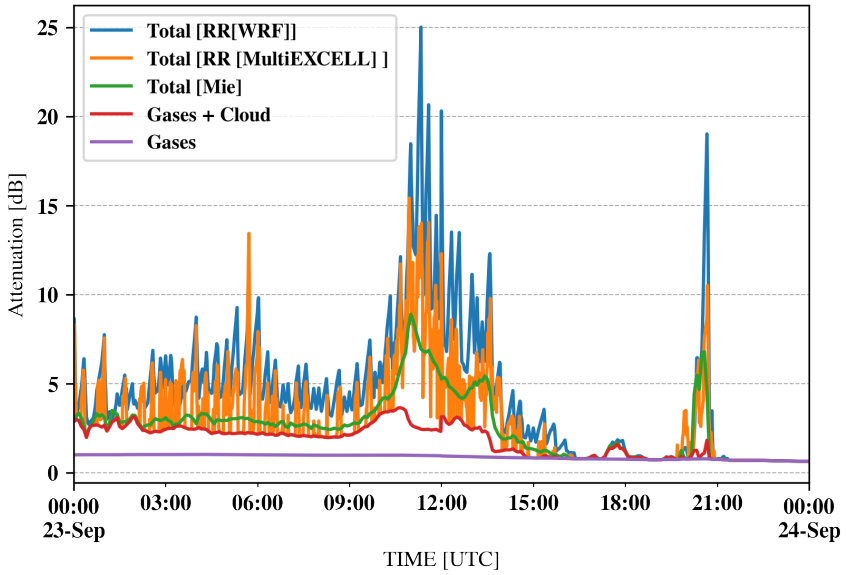
On this day, each satellite completes about six passes between 06:00 and 18:00 UTC. Since these satellites follow sun-synchronous orbits, the timing and number of daily passes are nearly identical from one day to the next, with a repeat cycle of about one month.

Interestingly, the passes of the four Starlink satellites do not overlap in time, a pattern that holds for other days as well. This means there are no periods where multiple satellites are simultaneously visible, eliminating the possibility for satellite diversity during a single rain event.

Another notable point is that, despite the presence of extended light rain and cloud cover in the morning, none of the satellite passes appear to be significantly affected by cloud or rain attenuation during that time. This highlights a potential limitation of relying solely on GEO-based statistics: if a GEO model reports attenuation for this day, it may overestimate the impact by including weather effects that were not actually experienced during the LEO satellite passes.

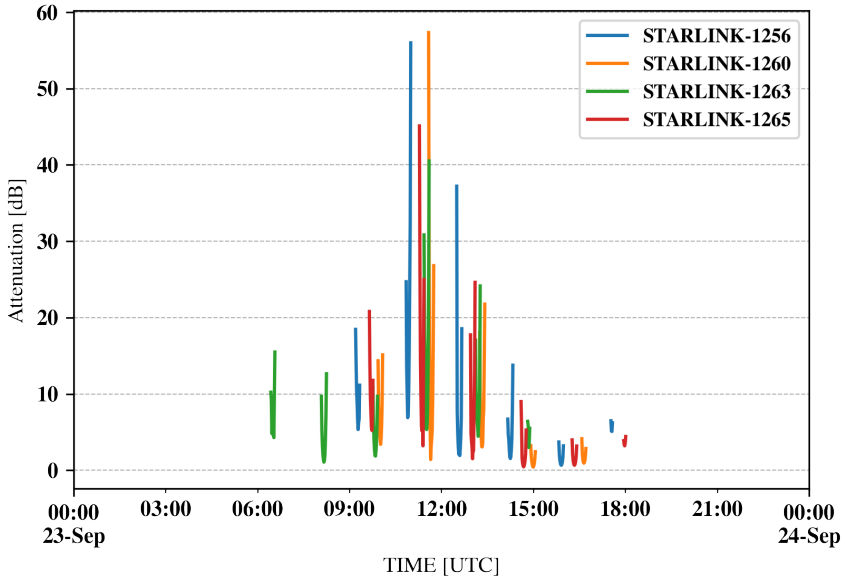


(a) Measurement

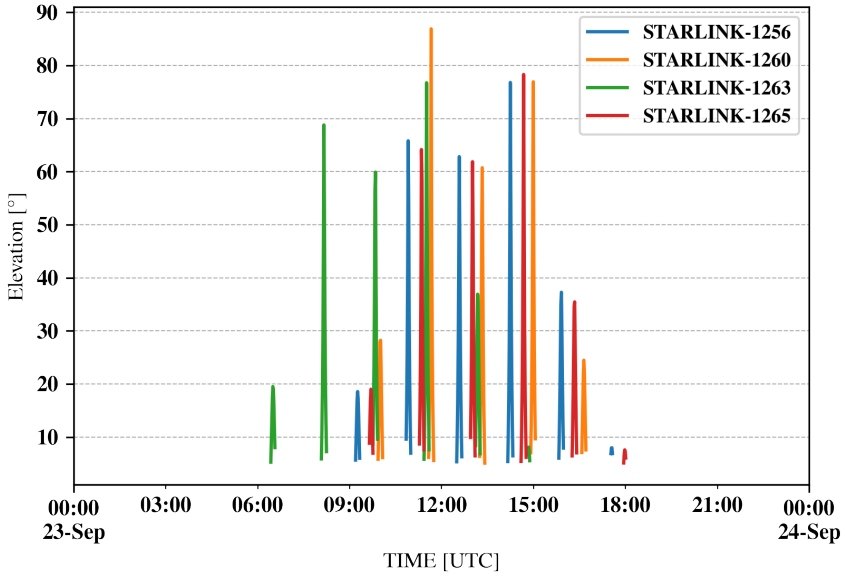


(b) Simulation

Figure 7.14: Example of WRF-derived attenuation time series at 39.402 GHz for Louvain-la-Neuve, at 30° in elevation and 154.6° in azimuth, on the 2018-09-23

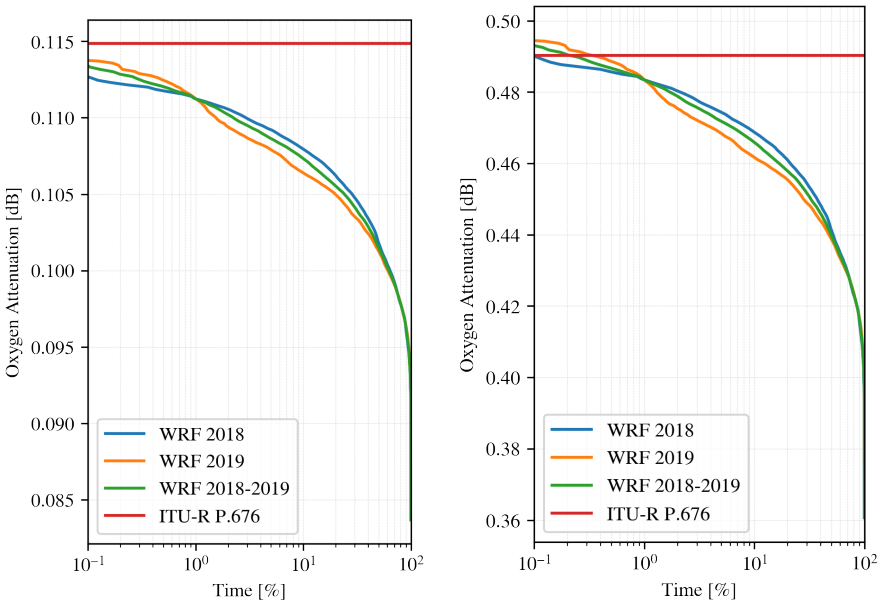


(a) Total ttenuation [rain+cloud+gaseous]



(b) Elevation

Figure 7.15: Example of WRF-derived attenuation time series at 39.402 GHz for Louvain-la-Neuve, for a couple of Starlink satellites on the 2018-09-23



(a) Frequency 19.701 GHz (b) Frequency 39.402 GHz

Figure 7.16: Oxygen attenuation CCDFs with WRF and ITU-R P.676 [54], at 19.701 and 39.402 GHz and 30° in elevation, for Louvain-la-Neuve in 2018-2019

7.4.3 Attenuation Probability for GEO Satellite Components

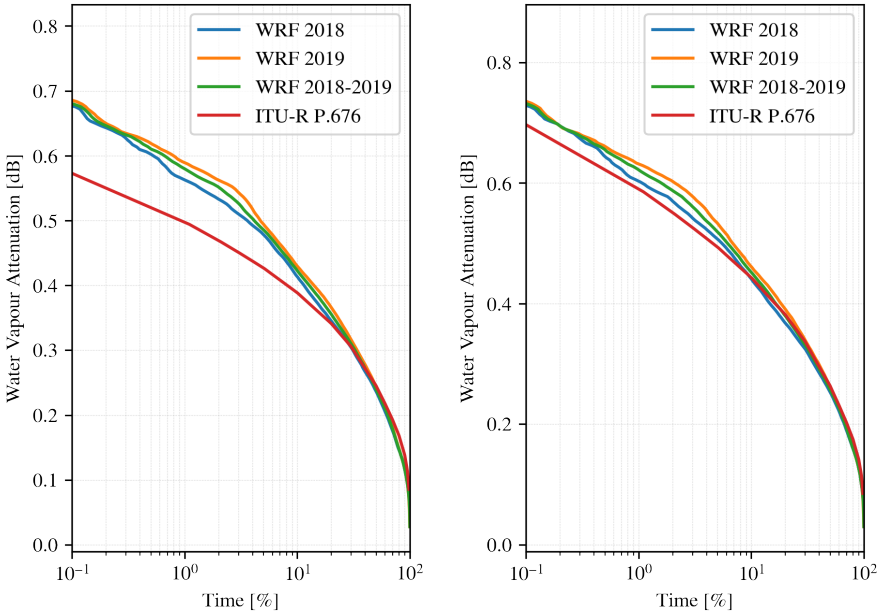
This section presents the attenuation statistics for different atmospheric components at two frequencies of interest (19.701 GHz and 39.402 GHz), as observed at the Louvain-la-Neuve ground station. Each type of weather-related attenuation—gaseous, cloud, and rain—is evaluated in terms of its statistical impact on a GEO satellite link.

7.4.3.1 Gaseous attenuation for GEO Satellite

We begin by validating gaseous attenuation estimates from NWP-based models (WRF) against the ITU-R P.676-11 recommendation [54]. The gaseous attenuation is split into its two main contributors—oxygen and water vapor—and evaluated separately before analyzing their combined effect.

Figure 7.16 displays the complementary cumulative distribution functions (CCDFs) of oxygen attenuation at an elevation angle of 30° for the two frequencies of interest: 19.701 GHz and 39.402 GHz. Overall, the agreement between WRF simulations and ITU-R values is strong, with low root mean square (r.m.s.) errors over the two-year period—around 10% for both frequencies, as detailed in Table 7.4.

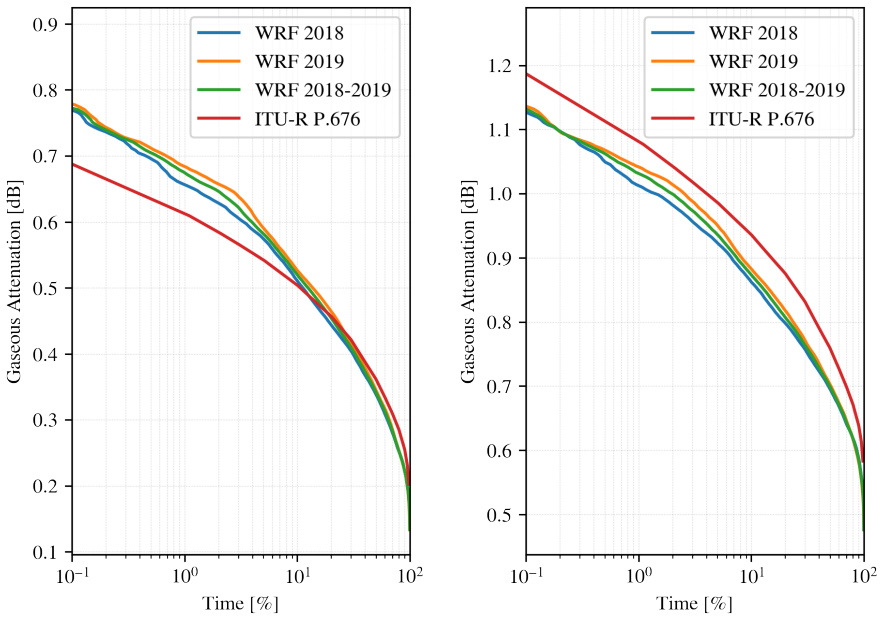
At 19.701 GHz (left panel of Figure 7.16), the WRF and ITU-R curves stay within a narrow band of 0.085 to 0.115 dB over the full probability range



(a) Frequency 19.701 GHz

(b) Frequency 39.402 GHz

Figure 7.17: Water vapour attenuation CCDFs with WRF and ITU-R P.676 [54], at 19.701 and 39.402 GHz and 30° in elevation, for Louvain-la-Neuve in 2018-2019



(a) Frequency 19.701 GHz

(b) Frequency 39.402 GHz

Figure 7.18: Gaseous (Oxygen+Water Vapour) attenuation CCDFs with WRF and ITU-R P.676 [54], at 19.701 and 39.402 GHz and 30° in elevation, for Louvain-la-Neuve in 2018-2019

	19.7 GHz			39.402 GHz		
	WRF 2018	WRF 2019	WRF 2018-19	WRF 2018	WRF 2019	WRF 2018-19
μ[%]	7.7	7.6	7.6	6.1	6.5	6.3
σ[%]	7.1	7.0	7.0	7.4	6.7	7.1
ρ[%]	10	10	10	9.7	9.4	9.5

Table 7.4: Error analysis of Figure 7.16 for oxygen attenuation. μ, σ, and ρ are mean, standard deviation and r.m.s of relative error. ITU-R P. 676 is considered as the reference value in error analysis. Data for comparison of prediction methods are tabulated at fixed probability levels, 0.1%, 1%, 10%, and 100% of the year.

	19.7 GHz			39.402 GHz		
	WRF 2018	WRF 2019	WRF 2018-19	WRF 2018	WRF 2019	WRF 2018-19
μ[%]	12.5	19.46	15.95	2.98	10.46	6.46
σ[%]	4.19	6.68	4.36	1.82	8.65	4.3
ρ[%]	13.18	20.57	16.54	3.49	13.57	7.76

Table 7.5: Error analysis of Figure 7.17 for water vapour attenuation. μ, σ, and ρ are mean, standard deviation and r.m.s of relative error. ITU-R P. 676 is considered as the reference value in error analysis. Data for comparison of prediction methods are tabulated at fixed probability levels, 0.1%, 1%, 10%, and 100% of the year.

	19.7 GHz			39.402 GHz		
	WRF 2018	WRF 2019	WRF 2018-19	WRF 2018	WRF 2019	WRF 2018-19
μ[%]	7.5	11.54	9.66	6.72	6.03	6.24
σ[%]	3.97	4.54	3.95	1.1	2.6	1.75
ρ[%]	8.48	12.4	10.44	6.81	6.57	6.48

Table 7.6: Error analysis of Figure 7.18 for gaseous attenuation. μ, σ, and ρ are mean, standard deviation and r.m.s of relative error. ITU-R P. 676 is considered as the reference value in error analysis. Data for comparison of prediction methods are tabulated at fixed probability levels, 0.1%, 1%, 10%, and 100% of the year.

from 0.1% to 100%. WRF consistently predicts slightly lower attenuation than ITU-R, and interannual variability remains minimal—below 0.002 dB at the 0.1% exceedance level.

At 39.402 GHz (right panel of Figure 7.16), the agreement is even closer: WRF deviates from ITU-R by no more than 0.001 dB at low exceedance probabilities, with WRF again slightly underestimating attenuation. The mean relative error between the WRF and ITU-R models is 7.6% for 19.701 GHz and 6.3% for 39.402 GHz, as reported in Table 7.4.

It's important to note that the ITU-R model provides a fixed value for gaseous attenuation, whereas WRF captures slight temporal variability. While this variability is negligible at 19.701 GHz, it becomes more relevant at higher frequencies where oxygen absorption plays a more significant role.

From an engineering perspective, the ITU-R estimate serves as a conservative upper bound for oxygen attenuation. This is particularly acceptable at 19.701 GHz, where the absolute attenuation values are very low—typically around 0.1 dB—and thus have a minimal impact on the overall link budget. However, the WRF-based NWP results demonstrate that using real atmospheric profiles allows for a more detailed and dynamic estimation of attenuation. This is especially valuable at higher frequencies, such as 39.402 GHz, where gaseous absorption becomes more significant. By capturing temporal and seasonal variations, NWP-driven models can help optimize fade margins and improve the precision of link budget design, particularly for systems operating under tight performance constraints or in frequency bands susceptible to atmospheric effects.

Regarding water vapour attenuation, the associated error metrics are summarized in Table 7.5. The root mean square errors (ρ) are approximately 16.54% at 19.701 GHz and 7.76% at 39.402 GHz. These values indicate slightly higher discrepancies compared to oxygen attenuation and show a more noticeable dependence on frequency.

The corresponding complementary cumulative distribution functions (CCDFs) at 30° elevation are shown in Figure 7.17. At 19.701 GHz (Figure 7.17a), the WRF-based estimates consistently exceed those from the ITU-R model across both individual years. Similarly, Figure 7.17b shows the CCDFs at 39.402 GHz, where the differences between WRF and ITU-R are negligible near the 100% exceedance level but grow to around 0.1 dB at 19.701 GHz and 0.05 dB at 39.402 GHz for lower probabilities. The corresponding mean errors over the two-year period are 15.95% and 6.46% for two frequencies, respectively, as listed in Table 7.5.

These findings suggest that while ITU-R estimates offer a simplified reference, the WRF model captures more dynamic atmospheric behavior— particularly for water vapour—which may lead to improved accuracy in attenuation modeling for satellite link budgets.

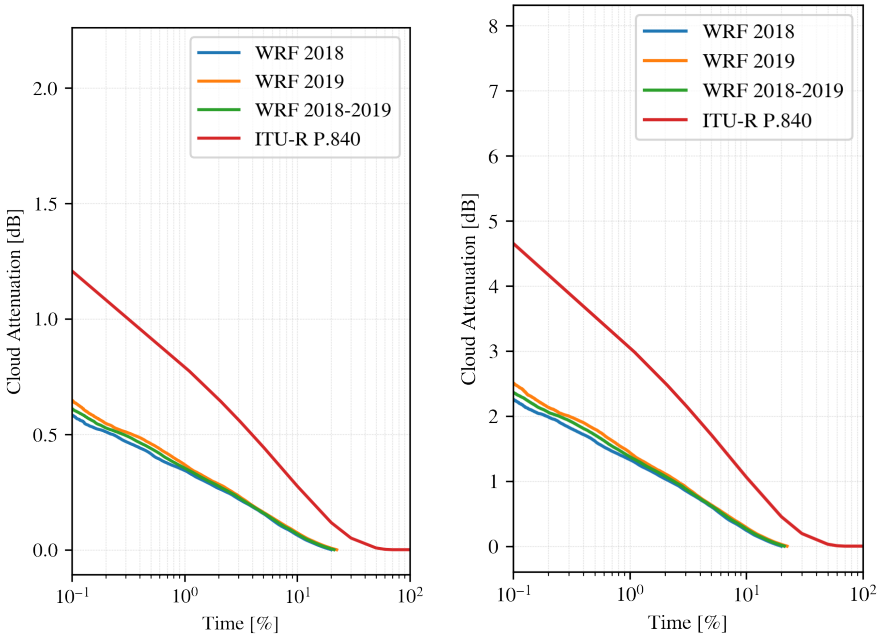
When combining the effects of oxygen and water vapour to compute total gaseous attenuation, the error metrics—summarized in Table 7.6—reveal that water vapour contributes more significantly to the overall error. The root mean square (r.m.s) errors are approximately 10.44% at 19.701 GHz and 6.48% at 39.402 GHz over the two-year evaluation period. These values are slightly lower than the individual errors observed for water vapour and oxygen attenuation, suggesting that the combined attenuation benefits from some degree of error compensation.

Similarly, the mean errors (ME) for the total gaseous attenuation are around 9.66% at 19.701 GHz and 6.24% at 39.402 GHz. These values are also slightly improved compared to those for water vapour alone. This improvement is expected, as WRF tends to overestimate water vapour attenuation and underestimate oxygen attenuation when compared to the ITU-R P.676 model,

leading to a partial balancing of the errors.

7.4.3.2 Cloud attenuation for GEO Satellite

As discussed in Section 3.4, cloud attenuation is far more localized in both time and space than gaseous attenuation. While it may not always dominate, cloud attenuation can contribute significantly—sometimes even approaching rain levels—depending on the location, season, and meteorological conditions. At the frequencies of interest in this study, cloud attenuation is an essential component of the non-rainy attenuation and must be estimated independently, as it cannot be accurately derived from beacon measurements alone. The methodology recommended by ITU-R [55] is used for this purpose.



(a) Frequency 19.701 GHz (b) Frequency 39.402 GHz

Figure 7.19: Cloud attenuation CCDFs with WRF and ITU-R P.840 [55], at 19.701 and 39.402 GHz and 30° in elevation, for Louvain-la-Neuve in 2018-2019

Table 7.7 summarizes the error metrics for cloud attenuation computed by WRF versus ITU-R P.840 for the years 2018–2019. For both models, attenuation is estimated using the cloud liquid water content derived from the models' internal parametrizations. The RMS errors are approximately 61.04% at 19.701 GHz and 60.74% at 39.402 GHz—substantially higher than the errors found for gaseous attenuation. Similarly, the mean errors are high, at 60.04% and 59.72% for the two frequencies, respectively. These metrics highlight a consistent underestimation by WRF when compared to ITU-R, suggesting that WRF may either underestimate the amount of cloud liquid water or detect it

	19.7 GHz			39.402 GHz		
	WRF 2018	WRF 2019	WRF 2018-19	WRF 2018	WRF 2019	WRF 2018-19
μ[%]	61.89	57.74	60.04	61.68	57.3	59.72
σ[%]	11.07	11.39	11.04	11.08	11.39	11.04
ρ[%]	62.87	58.85	61.04	62.67	58.42	60.74

Table 7.7: Error analysis of Figure 7.19 for cloud attenuation. μ, σ, and ρ are mean, standard deviation and r.m.s of relative error. ITU-R P. 840 is considered as the reference value in error analysis. Data for comparison of prediction methods are tabulated at fixed probability levels, 0.1%, 1% and 10% of the year.

less frequently. As expected, the discrepancy becomes more pronounced at higher frequencies.

Figures 7.19a and 7.19b further illustrate these discrepancies using CCDFs of cloud attenuation at 19.701 GHz and 39.402 GHz, respectively.

- **At 19.701 GHz (Figure 7.19a)**, ITU-R predicts cloud attenuation of approximately 1.25 dB for 0.1% of the time, and attenuation drops to 0 dB beyond the 60% exceedance level. In contrast, WRF estimates are significantly lower, with only 0.6 dB at 0.1% exceedance and a shift to 0 dB already by 20% of the time. This suggests that WRF underrepresents prolonged or thick cloud coverage.

- **At 39.402 GHz (Figure 7.19b)**, the pattern remains similar but with greater absolute differences. ITU-R shows a maximum attenuation of 4.5 dB at 0.1% of the time, again reducing to 0 dB above 60%. WRF estimates are about 2.5 dB at 0.1%, and 0 dB by 20%. These deviations reflect the stronger sensitivity of this higher frequency to cloud liquid water and indicate a more substantial underestimation by WRF.

These comparisons demonstrate a consistent negative bias in the WRF-derived cloud attenuation when compared to ITU-R values. While the ITU-R model may act as a conservative upper bound, especially useful for link margin design, the use of WRF data offers a more dynamic but potentially less conservative estimation. This emphasizes the need to assess and possibly recalibrate the cloud microphysics schemes in WRF for propagation studies at high frequencies.

7.4.3.3 Rain attenuation for GEO Satellite

Rain attenuation is the most significant contributor to signal degradation in satellite communication links. It often represents the primary factor necessitating adaptive coding schemes or link margin adjustments to ensure reliable performance. While predicting rain attenuation as a time series using Numerical Weather Prediction (NWP) models remains a challenge—primarily due to their limited ability to accurately forecast rainfall at specific locations and

times—there is still potential for NWP-based simulations to approximate long-term statistics. Specifically, the cumulative distribution functions (CCDFs) of simulated rain attenuation can reasonably reflect the trends observed in long-term beacon measurements or those modeled by ITU-R recommendations.

In this thesis, three distinct approaches are employed to model rain attenuation:

- **Volumetric Rain Content + Mie Scattering (Section 3.6.1)**: This approach uses the 3D distribution of rainwater content from WRF simulations combined with Mie scattering theory to estimate rain attenuation. It provides a physically detailed model but is limited to WRF.
- **Surface Rain Rate [RR (WRF)] (Section 3.6.4)**: This method estimates rain attenuation using the ground-level rain rate directly extracted from the WRF output, following conventional models such as those defined in ITU-R P.618.
- **Synthetic Rain Fields with MultiEXCELL + Optical Flow [RR (MultiEXCELL)] (Section 7.4)**: This model enhances the temporal resolution of WRF-derived rain rate data using the MultiEXCELL statistical generator and optical flow techniques, improving the realism of high-resolution rain attenuation time series.

These complementary methods allow for both instantaneous and long-term evaluation of rain attenuation, supporting a comprehensive validation framework.

To better assess the long-term performance of each rain attenuation model, Figure 7.20 presents the complementary cumulative distribution functions (CCDFs) over the years 2018 and 2019—individually and combined—at two frequencies: 19.701 GHz and 39.402 GHz. These results demonstrate that the combination of MultiEXCELL and optical flow performs well in estimating rain attenuation for time percentages above 0.1%. Below this threshold, however, the interannual variability in attenuation becomes substantial.

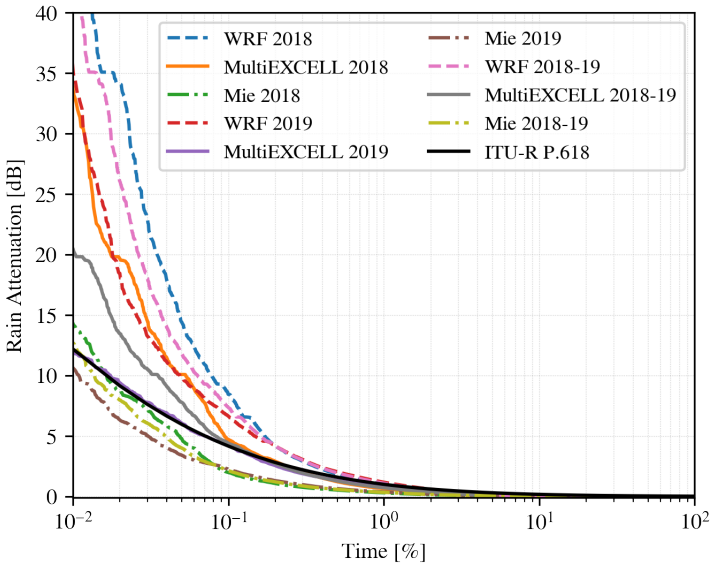
To quantify model accuracy, the error evaluation method described in Section 4.5.2 is employed. This approach includes a regulation factor to temper the impact of very large attenuation errors (typically ≥ 10 dB). The error statistics corresponding to Figure 7.20 are summarized in Table 7.8.

For clarity, the CCDF probability range is divided into two parts:

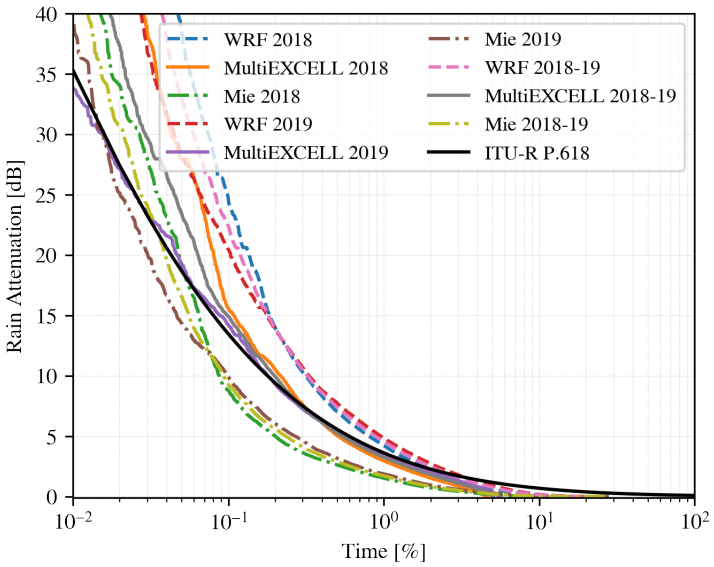
- **Part 1:** [0.1%, 0.2%, 0.3%, 0.5%, 1%]
- **Part 2:** [0.01%, 0.02%, 0.03%, 0.05%, 0.1%]

For **Part 1**, the root mean square (r.m.s) errors over two years (2018–2019), relative to ITU-R P.618 [3], are:

- **At 19.701 GHz:** RR[WRF] = 28.13%, RR[MultiEXCELL] = 12.82%, Mie = 66.11%
- **At 39.402 GHz:** RR[WRF] = 34.86%, RR[MultiEXCELL] = 7.04%, Mie = 53.61%



(a) Frequency 19.701 GHz



(b) Frequency 39.402 GHz

Figure 7.20: Rain attenuation CCDFs with WRF and ITU-R P.618 [3], at 19.701 and 39.402 GHz and 30° in elevation, for Louvain-la-Neuve in 2018-2019

Table 7.8: Error analysis of Figure 7.20 for rain attenuation. μ, σ, and ρ are mean, standard deviation and r.m.s of relative error. ITU-R P. 618 is considered as the reference value in error analysis. Data for comparison of prediction methods are tabulated at fixed probability levels : Part 1 =[0.1, 0.2, 0.3, 0.5, 1]% and Part 2=[0.01, 0.02, 0.03, 0.05, 0.1]%

Frequency 19.701 GHz							
		Part 1			Part 2		
		μ[%]	σ[%]	ρ[%]	μ[%]	σ[%]	ρ[%]
2018	WRF	24.33	20.21	31.62	106.83	35.98	112.73
	MultiEXCELL	13.35	9.03	16.12	59.22	30.39	66.57
	Mie	73.89	6.11	74.14	21.4	21.17	30.1
2019	WRF	24.33	10.13	26.36	62.39	24.23	66.93
	MultiEXCELL	9.83	5.11	11.08	1.91	0.72	2.04
	Mie	59.26	3.94	59.39	38.24	13.73	40.63
2018-19	WRF	24.06	14.56	28.13	85.82	30.75	91.16
	MultiEXCELL	10.81	6.9	12.82	29.86	15.63	33.7
	Mie	65.93	4.88	66.11	26.36	18.35	32.12
Frequency 39.402 GHz							
		Part 1			Part 2		
		μ[%]	σ[%]	ρ[%]	μ[%]	σ[%]	ρ[%]
2018	WRF	32.55	16.59	36.53	92.13	25.81	95.67
	MultiEXCELL	10.44	5.21	11.67	49.75	22.11	54.44
	Mie	62.28	10.07	63.09	24.7	14.1	28.44
2019	WRF	33.35	6.39	33.95	53.47	15.74	55.74
	MultiEXCELL	3.13	1.45	3.45	2.93	1.72	3.4
	Mie	44.79	7.98	45.49	18.16	8.65	20.12
2018-19	WRF	33.06	11.08	34.86	73.76	20.6	76.58
	MultiEXCELL	6.24	3.25	7.04	25.47	9.54	27.2
	Mie	52.95	8.43	53.61	18.37	12.43	22.18

It is evident that in this range, the RR[WRF] model tends to overestimate attenuation, while the Mie model systematically underestimates it. RR[MultiEXCELL] consistently yields the best agreement.

For **Part 2**, which focuses on rarer, more intense rain events:

- **At 19.701 GHz:** RR[WRF] = 91.16%, RR[MultiEXCELL] = 33.7%, Mie = 32.12%
- **At 39.402 GHz:** RR[WRF] = 76.58%, RR[MultiEXCELL] = 27.2%, Mie = 22.18%

These results confirm that the RR[MultiEXCELL] approach performs more reliably across all time percentages, especially in critical regions of the CCDF. It is important to note that the ITU-R P.618 model is only validated for exceedance probabilities below 5%, and thus the tail of the distribution above this threshold is not strictly meaningful for validation purposes. Interestingly, the r.m.s. errors tend to decrease at higher frequencies, suggesting improved agreement during strong rain events—those that most influence the overall link margin.

Figure 7.20 highlights a significant difference in rain attenuation between the years 2018 and 2019 for time percentages below 0.1%. This discrepancy is primarily due to several intense rain events that occurred in 2019. Notable heavy rain cases were recorded on the following dates:

- September 2018: 06
- November 2018: 29
- May 2019: 2, and 19
- June 2019: 5 and 15
- July 2019: 27
- August 2019: 9, 17, and 18

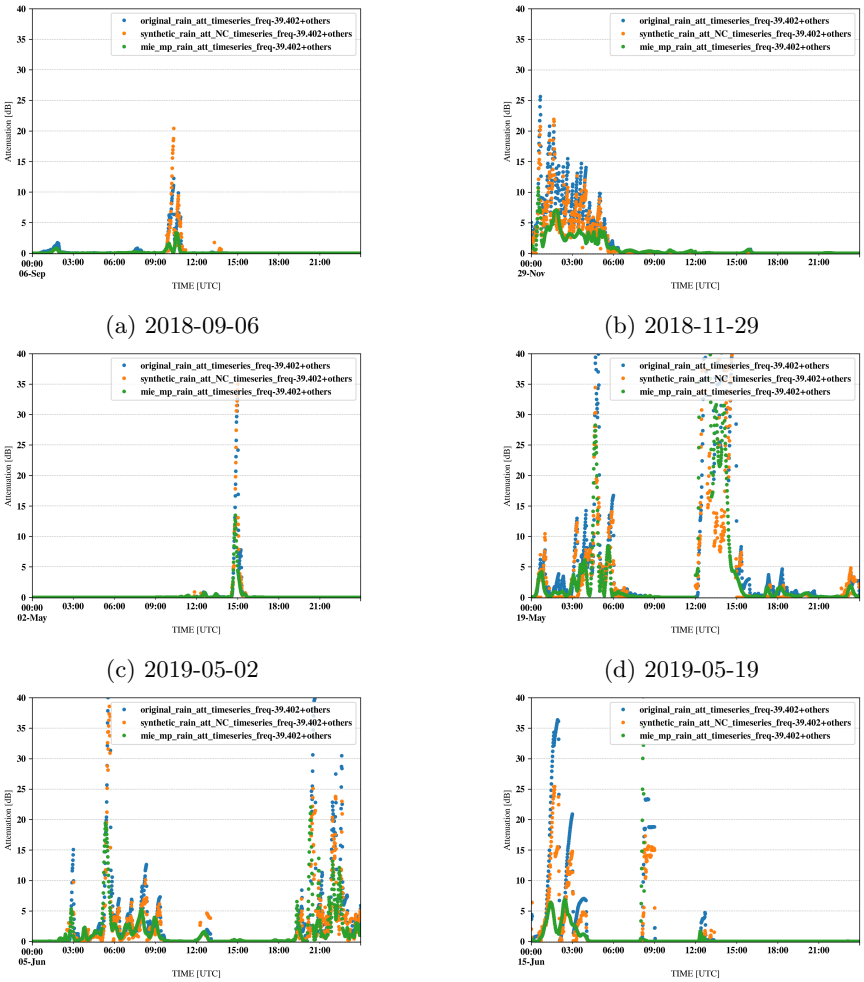
The corresponding rain and cloud attenuation time series at 39.402 GHz for these days are shown in Figures 7.21–7.22.

7.4.3.4 Excess Attenuation for GEO Satellite vs Measurememnt

Figures 7.23 and 7.24 present the complementary cumulative distribution functions (CCDFs) for the excess (rain+cloud) atmospheric attenuation at the two study frequencies: 19.701 GHz and 39.402 GHz. These figures follow the same structure as previous results.

Figure 7.23 focuses on the yearly statistics for 19.701 GHz. For clarity, the legend refers to the years as “2018” and “2019,” which correspond to the periods from September 2018 to August 2019, and from September 2019 to August 2020, respectively. The combined two-year CCDF for 19.701 GHz is shown in Figure 7.23b.

To ensure a meaningful comparison with measurement data, the total attenuation shown here includes only the sum of cloud and rain attenuation



(a) 2018-09-06

(b) 2018-11-29

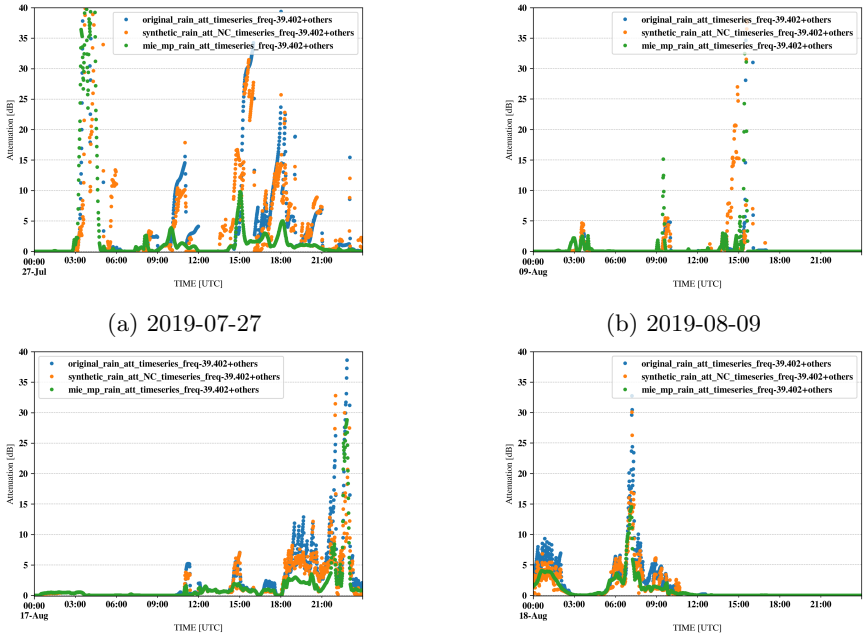
(c) 2019-05-02

(d) 2019-05-19

(e) 2019-06-05

(f) 2019-06-15

Figure 7.21: Rain and cloud attenuation time series at 39.402 GHz and 30° in elevation, for Louvain-la-Neuve ground station.



(a) 2019-07-27

(b) 2019-08-09

(c) 2019-08-17

(d) 2019-08-18

Figure 7.22: Rain and cloud attenuation time series at 39.402 GHz and 30° in elevation, for Louvain-la-Neuve ground station.

components, excluding gaseous and scintillation contributions. Five datasets are compared:

- **WRF-based model**
- **MultiEXCELL + Optical Flow**
- **Mie scattering-based model**
- **ITU-R Recommendations** [3, 55]
- **Experimental data (EXP)** from the Alphasat beacon measurements at Louvain-la-Neuve (30° elevation, 154° azimuth)

The corresponding CCDFs for 39.402 GHz are shown in Figure 7.24, following the same structure.

A first glance at both figures reveals that the MultiEXCELL-based model provides the best overall match to the experimental data when compared with the other simulation methods. It demonstrates consistent performance across both frequencies and time periods, making it a strong candidate for reliable long-term rain attenuation prediction.

To conclude the GEO satellite validation of excess attenuation using NWP-based models, we examine the corresponding error metrics and statistics. Table 7.9 summarizes the performance of the different models, comparing simulated results with experimental measurements. The error evaluation follows the methodology previously described in Section 4.5.2, using the mean (μ), standard deviation (σ), and root mean square error (ρ) as performance indicators.

Given the varying behavior of the CCDFs across the probability scale, the time percentages are divided into two intervals:

- **Part 1:** [0.1%, 0.2%, 0.3%, 0.5%, 1%] – representing moderately rare events
- **Part 2:** [0.01%, 0.02%, 0.03%, 0.05%, 0.1%] – representing very rare, extreme attenuation events

At 19.701 GHz, in Part 1, the overall two-year root mean square errors (ρ) are approximately:

- **WRF:** 26.72%
- **MultiEXCELL:** 15.34%
- **Mie:** 57.17%
- **ITU-R:** 14.87%

These results clearly demonstrate that the MultiEXCELL model provides the best performance among the simulation methods in this moderate attenuation range.

In Part 2 (rare events), the precision of MultiEXCELL declines slightly, with an overall ρ of 32.62%, which remains far better than WRF's 90.42%. However, in this region, Mie and MultiEXCELL perform comparably, particularly in the

two-year average, with Mie performing slightly better in capturing extreme cases.

At 39.402 GHz, MultiEXCELL shows even stronger performance. In Part 1, its ρ is around 7.6% over the two years, significantly lower than the 37% error seen with both WRF and Mie. Remarkably, MultiEXCELL even outperforms ITU-R in this frequency band and range.

In Part 2 at 39.402 GHz, the same trend is observed as at 19.701 GHz: MultiEXCELL's accuracy drops while Mie's accuracy improves. The overall ρ values for this range are:

- **WRF:** 71.89%
- **MultiEXCELL:** 22.27%
- **Mie:** 19.1.11%
- **ITU-R:** 8.5%

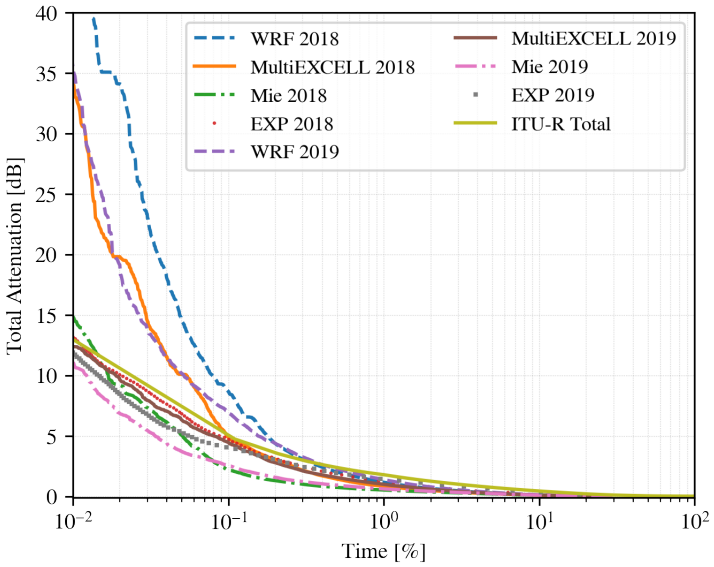
In summary, MultiEXCELL delivers the most consistent and accurate results for most of the attenuation range, particularly in the operationally significant range above 0.1% of time. For extremely rare events, both MultiEXCELL and Mie offer complementary strengths.

7.4.4 Excess Attenuation Probability for LEO Satellite

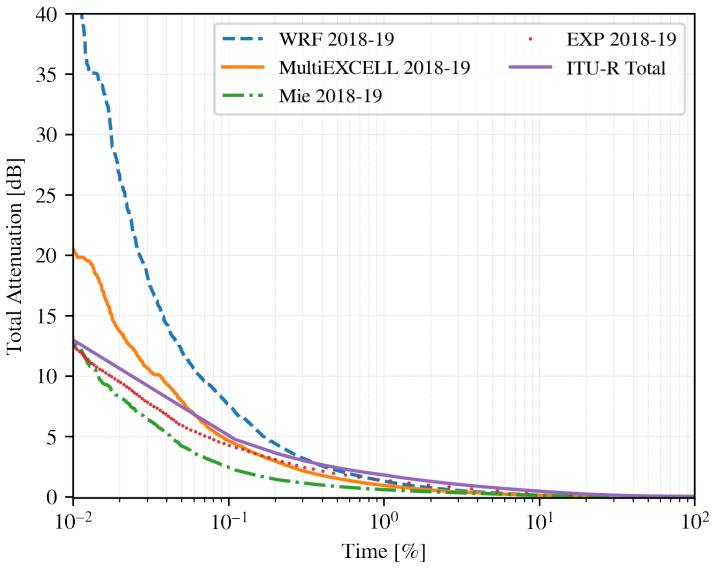
Now that the validation for the GEO attenuation has been conducted at 30° in elevation, it is possible to consider what happens in the case of LEO satellites. As was discussed previously, the CCDF of a LEO satellite can be derived from LEO time series generated or from a set of GEO CCDFs at multiple elevation angles according to the details described in section 4.4.2.

Concerning the time series approach, it is desirable to have a temporal resolution corresponding both to dynamic atmospheric conditions and shorter than the duration of the satellites passes. So, the optical flow approach in chapter 6 has given us the beneficence of high resolution (= 1 min) of time series of attenuation for rainy events suitable for LEO satellites. Concerning the GEO CCDFs approach, it is necessary to establish the histogram of the elevation at which the LEO satellite is visible. There are lots of LEO satellites to be chosen in our simulation part, and finally since there are hundreds of Starlink satellites available to check their statistical links, it's decided to simulate our models based on the links of a couple of Starlink satellites. The Figure 7.25b shows the elevation histogram for a couple of Starlink satellites for two years period September 2018 - August 2020. The Figure 7.25b clearly shows that the satellites are more visible in lower elevation angles than higher elevations. It is worthwhile to also investigate the histogram for the azimuth, which is shown in Figure 7.25d. There is a clear preference for the 75/285° azimuth, i.e. towards the East/West, with about twice the probability to see the satellite from that direction than from the 0/180° azimuth, i.e. from the North/South.

The resulting LEO total attenuation CCDFs, for which 100% of the time represent a year at Figures 7.26 and 7.28 or two years data at Figures 7.27, and

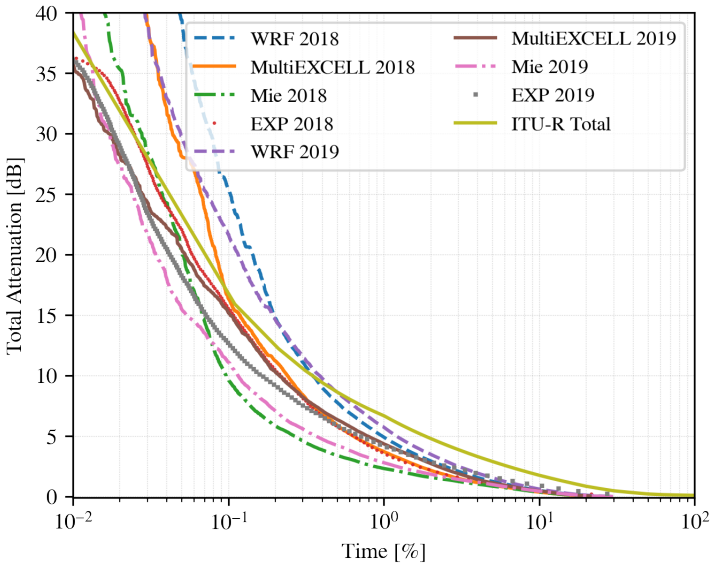


(a) Statistics for each year at 2018, 2019 at 19.7 GHz

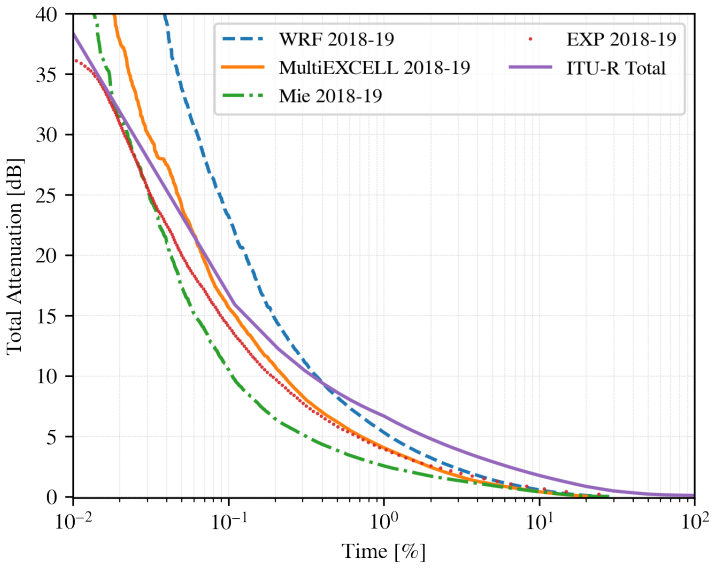


(b) Statistics over two years 2018-2019 at 19.7 GHz

Figure 7.23: Excess attenuation (rain + cloud) CCDFs with WRF, MultiEXCELL rain rate, Mie and ITU-R P.618 [3] and Experimental, at 19.701 GHz and 30° in elevation, for Louvain-la-Neuve in 2018, 2019



(a) Statistics for each year at 2018, 2019 at 39.402 GHz

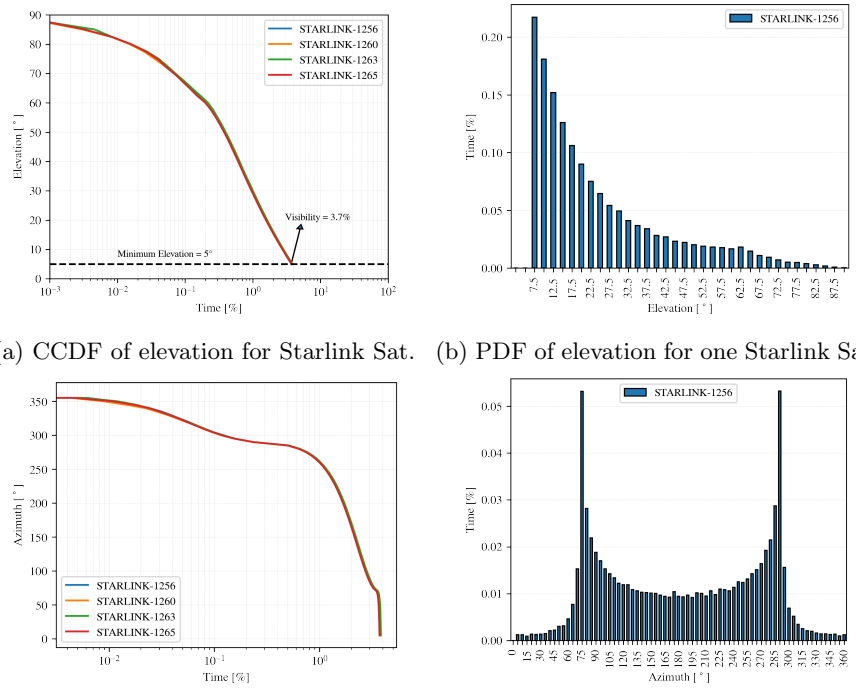


(b) Statistics over two years 2018-2019 at 39.402 GHz

Figure 7.24: Excess attenuation (rain+cloud) CCDFs with WRF, MultiEXCELL rain rate, Mie, ITU-R P.618 [3] and Experimental, at 39.402 GHz and 30° in elevation, for Louvain-la-Neuve in 2018, 2019

Table 7.9: Error analysis of Figure 7.23 and 7.24 for total attenuation. μ, σ, and ρ are mean, standard deviation and r.m.s of relative error. EXP curve (Experimental curve) is considered as the reference value in error analysis. Data for comparison of prediction methods are tabulated at fixed probability levels : Part 1 =[0.1, 0.2, 0.3, 0.5, 1]% and Part 2=[0.01, 0.02, 0.03, 0.05, 0.1]%

Frequency 19.701 GHz							
		Part 1			Part 2		
		μ[%]	σ[%]	ρ[%]	μ[%]	σ[%]	ρ[%]
2018	WRF	21.01	17.47	27.33	98.7	36.31	105.17
	MultiEXCELL	12.12	9.22	15.22	50.33	30.81	59.01
	Mie	65.07	4.93	65.25	26.43	20.84	33.66
	ITU-R	14.1	6.75	15.63	2.33	1.18	2.62
2019	WRF	21.67	14.62	26.14	71.53	21.99	74.83
	MultiEXCELL	13.49	6.26	14.87	11.25	4.32	12.06
	Mie	50.46	6.41	50.87	23.23	10.48	25.48
	ITU-R	14.93	1.22	14.97	16.67	4.44	17.25
2018-19	WRF	21.66	15.64	26.72	85.56	29.25	90.42
	MultiEXCELL	13.16	7.89	15.34	29.6	13.7	32.62
	Mie	56.97	4.84	57.17	22.98	14.86	27.36
	ITU-R	14.7	2.27	14.87	7.91	3.9	8.82
Frequency 39.402 GHz							
		Part 1			Part 2		
		μ[%]	σ[%]	ρ[%]	μ[%]	σ[%]	ρ[%]
2018	WRF	33.01	8.41	34.07	80.03	29.08	85.14
	MultiEXCELL	4.01	1.74	4.37	38.02	24.81	45.4
	Mie	48.72	7.9	49.36	21.34	18.04	27.95
	ITU-R	27.06	15.46	31.16	4.75	1.96	5.14
2019	WRF	40.23	9.42	41.32	57.53	12.02	58.77
	MultiEXCELL	9.64	5.09	10.9	7.15	6.75	9.83
	Mie	26.17	7.16	27.13	11.42	3.81	12.04
	ITU-R	32.52	4.22	32.8	13.35	7.99	15.56
2018-19	WRF	36.69	8.57	37.68	68.93	20.39	71.89
	MultiEXCELL	6.95	3.06	7.6	20.47	8.78	22.27
	Mie	36.68	4.05	36.9	14.63	12.3	19.11
	ITU-R	29.75	9.48	31.23	6.83	5.06	8.5



(a) CCDF of elevation for Starlink Sat. (b) PDF of elevation for one Starlink Sat.

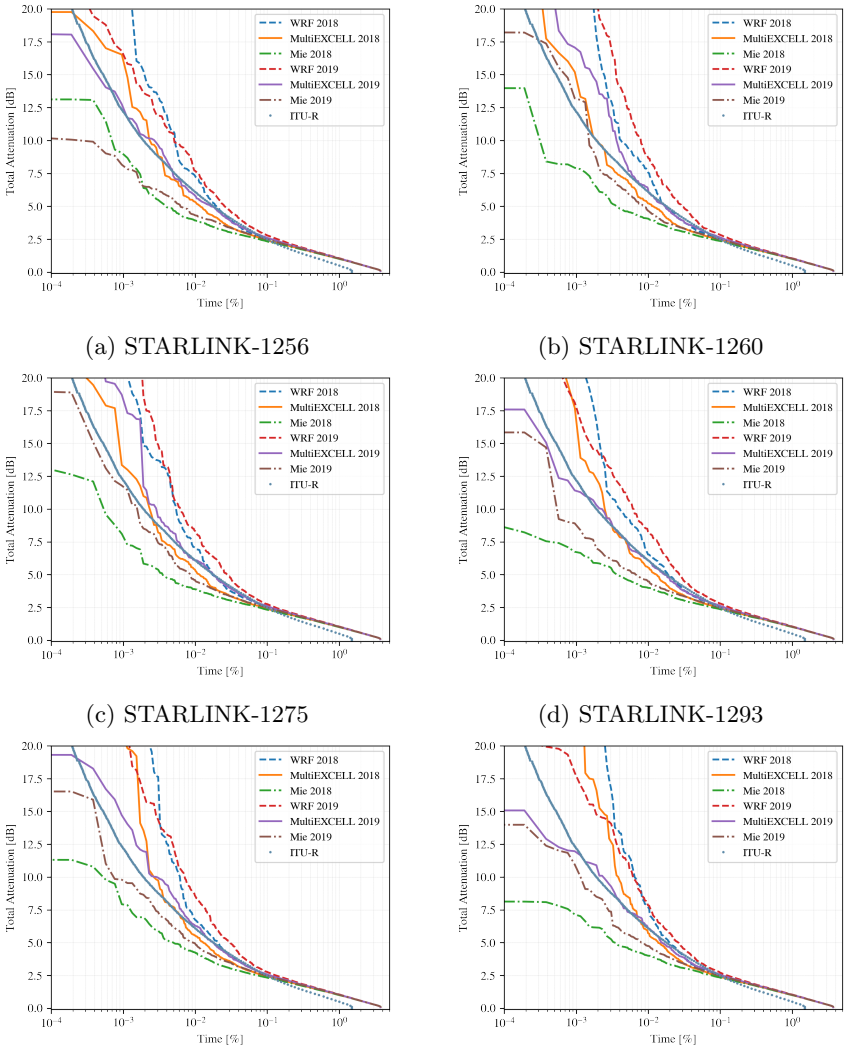
(c) CCDF of azimuth for Starlink Sat. (d) PDF of azimuth for one Starlink Sat.

Figure 7.25: Statistics of Elevation and Azimuth for Starlink satellites at Louvain-la-Neuve in 2018-2019

7.29. The visibility criterion of the LEO satellites is chosen the Elevations above 5° as initiated at Figure 7.25a. The total attenuation CCDFs are obtained for WRF, considering its native cloud content, using either the rain attenuation obtained from Mie scattering or from the rain rate WRF and MultiEXCELL, and the gaseous attenuation. The statistics corresponding either to the time series of the Starlink satellites, or corresponding to weighted conditional combinations of GEO CCDFs. For the conditional method, the ITU-R reference CCDFs are considered with the probability of visibility at Figure 7.25b.

Unsurprisingly, some of the features observed on the 30° CCDFs are also present for the LEO attenuation. The WRF total attenuation using Mie scattering is below the one using the NWP/MultiEXCELL rain rate. There is a gap in the higher part of the probabilities between the WRF CCDFs and the ITU-R one, due to the interpolation and conditional probability calculation of equation 4.24 at Section 4.4.2.

The Figure 7.26-7.29 depicts the LEO statistics for 19.701 and 39.402 GHz for yearly and two year in combination. This is clearly visible that ITU-R statistics is always static while the results of NWP is variable in each satellite. These results clearly prove the importance of having a dynamic models that works fine for LEO satellites.



(a) STARLINK-1256

(b) STARLINK-1260

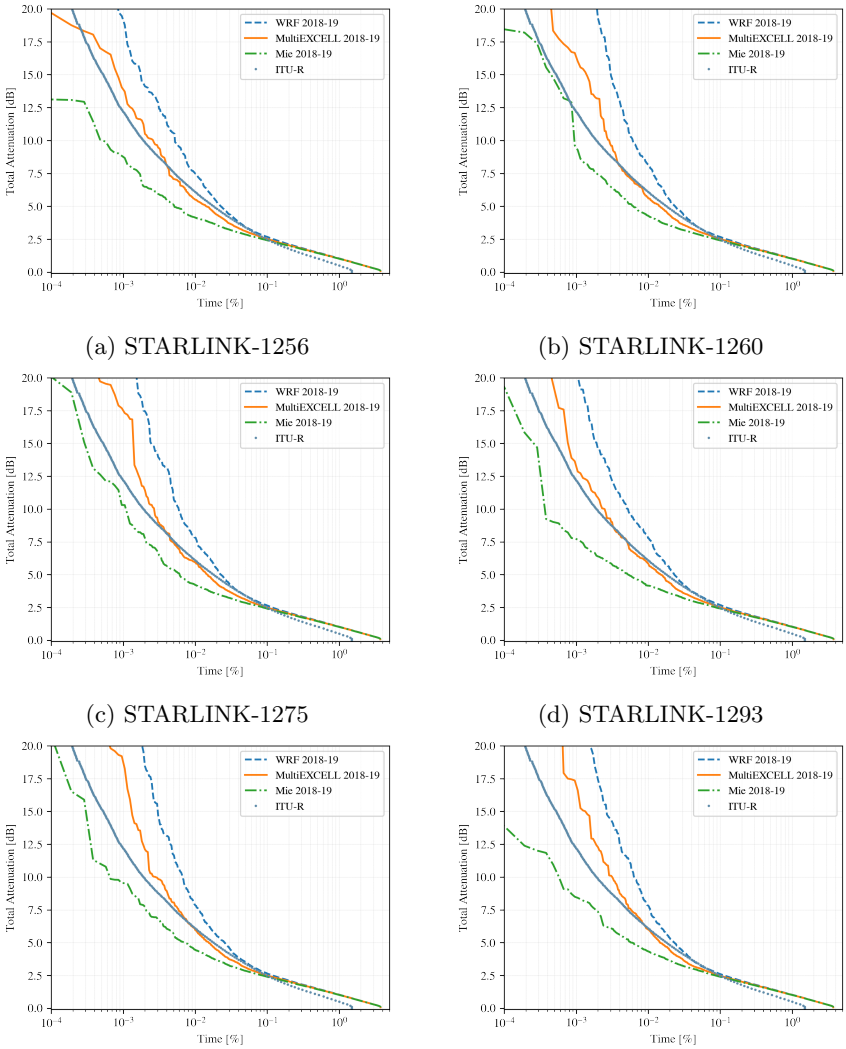
(c) STARLINK-1275

(d) STARLINK-1293

(e) STARLINK-1316

(f) STARLINK-1282

Figure 7.26: Total attenuation (rain+cloud+gaseous) CCDFs with WRF, MultiEXCELL, Mie rain attenuation style and the ITU-R conditional probability attenuation [3], at 19.701 GHz for Starlink Satellites, for Louvain-la-Neuve in 2018, and 2019 separately



(a) STARLINK-1256

(b) STARLINK-1260

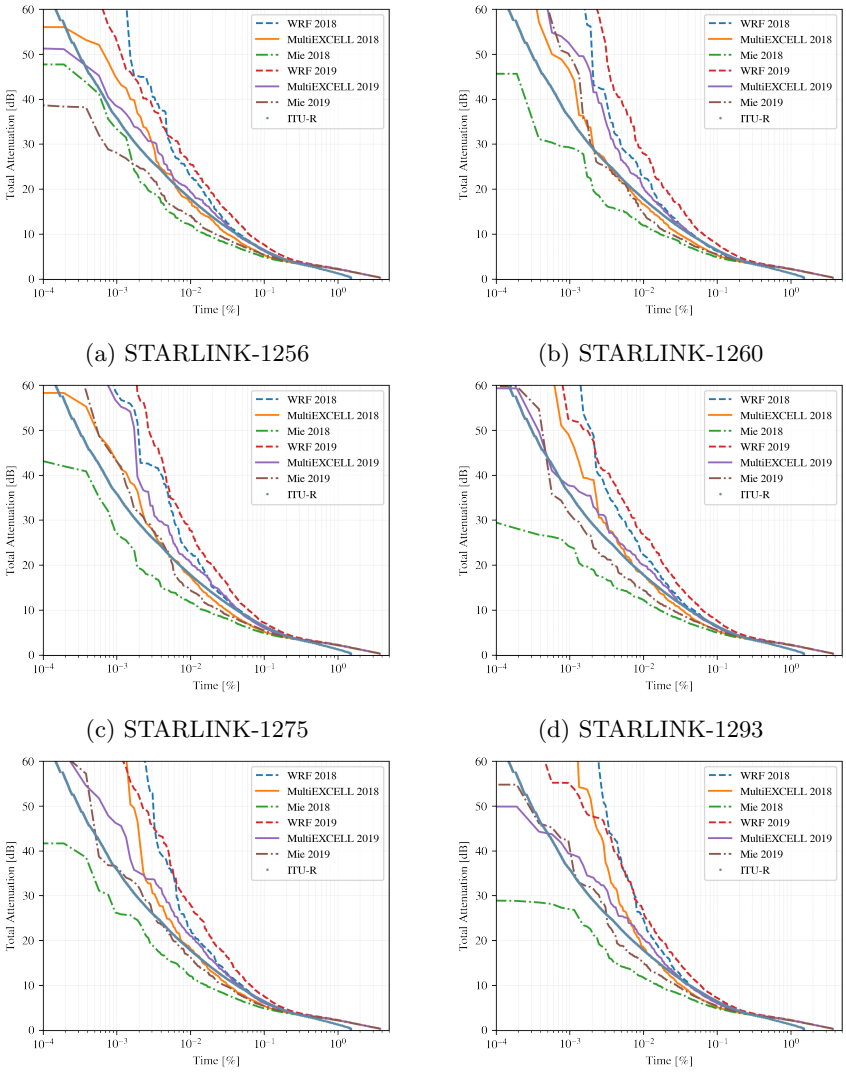
(c) STARLINK-1275

(d) STARLINK-1293

(e) STARLINK-1316

(f) STARLINK-1282

Figure 7.27: Total attenuation (rain+cloud+gaseous) CCDFs with WRF, MultiEXCELL, Mie rain attenuation style and the ITU-R conditional probability attenuation [3], at 19.701 GHz for Starlink Satellites, for Louvain-la-Neuve in 2018-2019 combination.



(a) STARLINK-1256

(b) STARLINK-1260

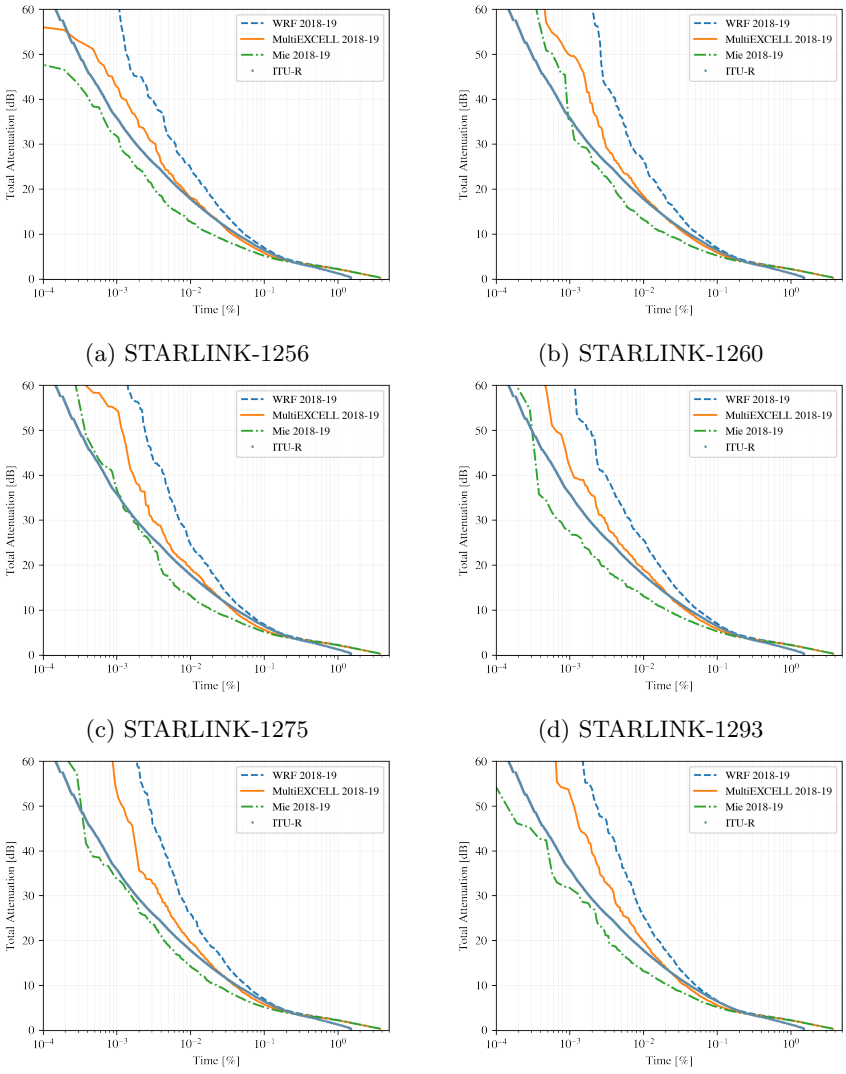
(c) STARLINK-1275

(d) STARLINK-1293

(e) STARLINK-1316

(f) STARLINK-1282

Figure 7.28: Total attenuation (rain+cloud+gaseous) CCDFs with WRF, MultiEXCELL, Mie rain attenuation style and the ITU-R conditional probability attenuation [3], at 39.402 GHz for Starlink Satellites, for Louvain-la-Neuve in 2018, and 2019 separately



(a) STARLINK-1256

(b) STARLINK-1260

(c) STARLINK-1275

(d) STARLINK-1293

(e) STARLINK-1316

(f) STARLINK-1282

Figure 7.29: Total attenuation (rain+cloud+gaseous) CCDFs with WRF, MultiEXCELL, Mie rain attenuation style and the ITU-R conditional probability attenuation [3], at 39.402 GHz for Starlink Satellites, for Louvain-la-Neuve in 2018-2019 combination.

7.5 Conclusion

This chapter provided a detailed validation of the rain attenuation modeling framework developed in earlier chapters, focusing on assessing the performance of models that rely on Numerical Weather Prediction (NWP) data to generate time series and long-term statistical metrics of propagation attenuation. The validation process involved several key steps:

- **Initial Model Limitations:** The chapter began by addressing the inherent challenges associated with using NWP data in rain attenuation models, including issues related to model initialization, resolution constraints, and the accuracy of attenuation predictions derived from such data.
- **Evaluation of MultiEXCELL-Based Model:** The MultiEXCELL-based rain attenuation model was thoroughly evaluated using two years of geostationary (GEO) satellite link data. The model's ability to reproduce observed attenuation events was critically analyzed, with promising results indicating that MultiEXCELL provides a reliable framework for estimating rain attenuation in satellite communication systems.
- **Temporal Refinement of Rain Motion:** The chapter also used the rain motion model designed to improve the temporal resolution of rain rate time series. This model was validated by comparing its output to ground-truth observations, showing that temporal refinement significantly enhances the accuracy of attenuation predictions.
- **LEO Satellite Application:** A key extension of the modeling framework involved applying the validated model to Low Earth Orbit (LEO) satellites. Simulated attenuation time series were generated for several LEO link geometries, and the performance of the model was assessed across varying link motions and atmospheric conditions. This highlighted the practical relevance of the model for Earth-space communication systems.
- **Empirical Validation:** The chapter culminated in the empirical validation of the proposed modeling framework against experimental data from the Alphasat satellite beacon measurements at Louvain-la-Neuve. The results demonstrated a strong correlation between simulated and measured rain and cloud attenuation, particularly when using the MultiEXCELL-enhanced models. Statistical analyses, including complementary cumulative distribution functions (CCDFs), further confirmed the reliability of the simulation results for both GEO and LEO satellite scenarios.
- **Final Remarks:** In conclusion, the validation efforts presented in this chapter offer a robust foundation for the rain attenuation modeling framework, demonstrating its practical applicability for the design and optimization of Earth-space communication systems. The integration of high-resolution NWP data and advanced post-processing techniques, such as

the MultiEXCELL model, provides a reliable tool for predicting and mitigating atmospheric impairments in satellite links. These findings underscore the importance of dynamic, 3D atmospheric models for accurate real-time attenuation predictions, especially for LEO satellites, where link geometries and atmospheric conditions are more variable.

Chapter 8

Conclusion and Future Work

This thesis has presented a comprehensive framework for modeling and validating the propagation impairments encountered in high-frequency satellite communication links, with a particular focus on the Q-band and Ka-band. By integrating Numerical Weather Prediction (NWP) data with synthetic modeling techniques and beacon measurements, the work provides a pathway for realistic, data-driven attenuation estimation over both short- and long-term timescales.

- **Chapter 1** outlined the motivation and scope of the study, emphasizing the growing relevance of high-frequency satellite systems (especially in LEO) and the critical need for accurate modeling of atmospheric propagation effects, particularly in the context of rain, cloud, and gaseous attenuation.

- **Chapter 2** introduced the NWP framework used in the study. The chapter detailed the domain configuration, resolution, and physical processes represented in the WRF model. It highlighted the balance between spatial detail and computational cost when simulating rain events and extracting hydrometeorological variables for propagation modeling.

- **Chapter 3** reviewed the electromagnetic theory underpinning radio wave attenuation through the atmosphere. The chapter dissected the contributions of oxygen, water vapor, clouds, and rain, providing both theoretical formulations and frequency-dependent behavior. It also discussed permittivity models and their implications for modeling at millimeter-wave frequencies.

- **Chapter 4** focused on the transformation of raw NWP outputs into propagation-relevant fields. The chapter included vertical interpolation to constant height grids, conversion of hydrometeors to attenuation-relevant quantities, and a discussion of spatial and temporal resolution implica-

tions. These steps formed the basis for accurate map-based and time-series attenuation modeling.

- **Chapter 5** introduced the MultiEXCELL model as a means to generate high-resolution rain fields from coarse NWP rain rates. The chapter presented the cell-fitting methodology, explained parameter tuning, and discussed how this synthetic model improves spatial realism in rain attenuation maps. The approach was especially effective for capturing localized convective structures not fully resolved in the native WRF fields.

- **Chapter 6** addressed the temporal limitations of NWP by developing a displacement tracking mechanism based on optical flow. This allowed the simulation of high-resolution rain field evolution, supporting 1-minute attenuation time-series generation for both GEO and LEO links. The temporal interpolation of rain events proved critical for accurately modeling short-duration, high-intensity fade events.

- **Chapter 7** presented the validation of the proposed framework. GEO attenuation models were evaluated using two years of beacon measurements from Alphasat at Louvain-la-Neuve. The cloud and rain attenuation were isolated from the signal via a manual flagging method and low-pass filtered reference level. Rain attenuation models based on WRF volumetric rain (Mie), surface rain rate (RR[WRF]), and the synthetic model (RR[MultiEXCELL]) were compared against ITU-R recommendations and measurements. The MultiEXCELL model consistently showed the best agreement, particularly for attenuation values occurring above 0.1% of the time. Total attenuation was also compared, and again the RR[MultiEXCELL] model provided the most accurate CCDF match, especially at 39.402 GHz.

Future Work

While the results validate the proposed methodology, several areas remain open for further development:

- **Refinement of microphysical models**: Enhance the accuracy of attenuation estimation by calibrating cloud and rain parameterizations with high-resolution measurements from additional beacon stations across different climates.

- **Model generalization**: Extend the validation to other sites and satellite links (e.g., V band) to test the scalability and robustness of the MultiEXCELL and WRF-based framework.

- **Inclusion of additional impairments**: Incorporate effects such as scintillation, depolarization, and wet antenna attenuation to provide a full link budget impairment model.

- **Real-time applications**: Investigate real-time implementation of the framework using nowcasting and AI-assisted post-processing of operational NWP forecasts, enabling adaptive satellite link management.
- **GEO/LEO hybrid studies**: Expand the use of this model to dual satellite systems, integrating cloud-rain spatial dynamics and link diversity analysis in environments with mixed visibility windows.

In summary, this thesis demonstrates the feasibility of using NWP-driven models, enhanced with spatial and temporal correction techniques, to estimate propagation impairments with high accuracy. The methods developed contribute to improved link design, planning, and adaptive control for future high-frequency satellite communication systems.

Appendix I

Published Papers

- M. Razavian, L. Quibus, D. Vanhoenakcer-Janvier, "USING NUMERICAL WEATHER PREDICTIONS TO COMPARE THE LEO ATTENUATION STATISTICS COMPUTED FROM FIXED-ELEVATION STATISTICS AND FROM LEO TIME SERIES", *25th Ka and broadband communications conference*, sorrento, italy, 2019.

- M. Razavian, L. Quibus, D. Vanhoenakcer-Janvier, "Roadmap to model LEO links attenuation by integrating Numerical Weather Predictions, ST-MultiEXCELL, and traffic radar data", 28^{th} *URSI Benelux Forum*, Brussels, Belgium, 2019.

- M. Razavian, C. Oestges, D. Vanhoenakcer-Janvier, "Combined use of MultiEXCELL and Numerical Weather Prediction to improve the prediction of rain attenuation at Q band", 15^{th} *EuCAP*, Düsseldorf, Germany, 2021.

- M. Razavian, C. Oestges, and D. Vanhoenacker-Janvier, "Synthetic Rain Models and Optical Flow Algorithms for Improving the Resolution of Rain Attenuation Time Series Simulated From Numerical Weather Prediction," Radio Science, vol. 58, p. e2022RS007553, Jan. 2023.

Appendix II

Basic Formulas of Statistical Theory

Expected Value

$$E(X) = \sum xP(X = x) \quad Discrete\,random\,variable \tag{8.1}$$

$$E(X) = \int xf_X(x)dx \quad Continuous\,random\,variable \tag{8.2}$$

assume a and b are constants:

$$E(a) = a \tag{8.3}$$

$$E(aX + bY) = aE(X) + bE(Y) \tag{8.4}$$

if two variables X and Y are independent, the expected value of their product is given by:

$$E(XY) = E(X)E(Y) \tag{8.5}$$

The population mean of a finite population of size N with values x_i is given by

$$E(X) = \mu = \frac{1}{N}\sum_{i=1}^{N} x_i \tag{8.6}$$

Variance

$$Var(X) = \sigma_X^2 = E[(X - E(X))^2] = E(X^2) - E(X)^2 \tag{8.7}$$

assume a and b are constants:

$$Var(a) = 0 \tag{8.8}$$

$$Var(aX) = a^2 Var(X) \tag{8.9}$$

$$Var(aX \pm bY) = a^2 Var(X) + b^2 Var(Y) \pm ab\,Cov(X, Y) \tag{8.10}$$

if two variables X and Y are independent, the variance of their product is given by:

$$Var(XY) = E(X^2)E(Y^2) - E(X)^2\,E(Y)^2 \tag{8.11}$$

The population variance of a finite population of size N with values x_i and population mean of μ is given by

$$Var(X) = \sigma_X^2 = \frac{1}{N}\sum_{i=1}^{N}(x_i - \mu)^2 \tag{8.12}$$

$$= \left(\frac{1}{N}\sum_{i=1}^{N} x_i^2\right) - \mu^2 \tag{8.13}$$

Calculation of Autoregressive Model Parameters

$$X(t) = a_0 + a_1 X(t-1) + Z(t) \tag{8.14}$$

expected value operator is applied on both sides:

$$E(X(t)) = E[a_0 + a_1 X(t-1) + Z(t)] \tag{8.15}$$

$$= a_0 + a_1 E[X(t-1)] + E[Z(t)] \tag{8.16}$$

since it's assumed the time series $X(t)$ is stationary, then mean value will remain constant during time shifts, $E[X(t)] = E[X(t-1)]$ and $Z(t)$ is assumed a white noise with zero mean ($E[Z(t)] = 0$) and a constant variance, σ^2, the above equation will be written as:

$$E(X(t)) = \mu = \frac{a_0}{1 - a_1} \tag{8.17}$$

By applying the $Var(.)$ operator on both sides of Eg. 8.14 and using the properties in Eq. 8.8-8.10, the variance of $X(t)$ will be:

$$Var(X(t)) = a_1^2 Var(X(t-1)) + Var(Z(t)) + 2a_1 Cov(X(t-1), Z(t)) \tag{8.18}$$

since it's assumed that the noise $Z(t)$ is independent of $X(t)$, then the last term of above equation will be zero and the variance of a stationary time series will be constants during the time shifts ($Var(X(t)) = Var(X(t-1))$), then by re-arranging the equation:

$$Var(X(t)) = \sigma_X^2 = \frac{\sigma^2}{1 - a_1^2} \tag{8.19}$$

which σ^2 is the variance of noise $Z(t)$. Substituting Eq. 8.17 into Eq. 8.14 and re-arranging the equation, we will have:

$$X(t) - \mu = a_1\,(X(t-1) - \mu) + Z(t) \tag{8.20}$$

let $\tilde{X}(t) = X(t) - \mu$, then Eq. 8.20 can be written as:

$$\tilde{X}(t) = a_1 \tilde{X}(t-1) + Z(t) \tag{8.21}$$

The autocovariance between observations separated by τ periods is then:

$$\begin{aligned}\gamma_\tau &= Cov(X(t), X(t-\tau)) = E[(X(t)-\mu)(X(t-\tau)-\mu)] \\ &= E[\tilde{X}(t)\tilde{X}(t-\tau)] \\ &= E[(a_1\tilde{X}(t-1) + Z(t))\,\tilde{X}(t-\tau)] \\ &= a_1 E[\tilde{X}(t-1)\tilde{X}(t-\tau)] \;+\; E[\tilde{X}(t-\tau)Z(t)]\end{aligned}$$

The noise is uncorrelated with the past values of the time series, then $E[\tilde{X}(t-\tau)Z(t)] = 0$ and the equation will change to:

$$\gamma_\tau = a_1\gamma_{\tau-1} \tag{8.22}$$

With start value $\gamma_0 = \sigma_X^2 = \frac{\sigma^2}{1-a_1^2}$. The Eq. 8.22 is a recursive formula, the general sample of this recursive formula will be:

$$\gamma_\tau = \frac{\sigma^2}{1-a_1^2}a_1^\tau \tag{8.23}$$

The autocorrelation function will be :

$$\rho_\tau = \frac{\gamma_\tau}{\sigma_X^2} = a_1^\tau \tag{8.24}$$

Appendix III

WRF Output Variables

VARIABLE NAME	UNIT	COMMENT
RAINC	mm	convective accumulated precipitation
RAINNC	mm	Microphysics accumulated precipitation
RAINSH	mm	shallow accumulated precipitation
PH	m^2/s^2	perturbation geopotential
PHB	m^2/s^2	base-state geopotential
HGT	m	Terrain Height
P	pa	perturbation pressure
PB	pa	base state pressure
PSFC	pa	surface pressure
T	K	perturbation potential temperature theta-t0
U	m/s	x-wind component
V	m/s	y-wind component
W	m/s	z-wind component
QCLOUD	kg/kg	Cloud water mixing ratio
QRAIN	kg/kg	Rain water mixing ratio
QVAPOR	kg/kg	Water vapor mixing ratio
QSNOW	kg/kg	Snow mixing ratio
QICE	kg/kg	Ice mixing ratio
QGRAUP	kg/kg	Graupel mixing ratio
COSALPHA		Local cosine of map rotation
SINALPHA		Local sine of map rotation

Appendix IV

Difference Between Adaptive Modulation and Coding (AMC) and Advanced Coding and Modulation (ACM)

In the context of wireless and satellite communications, the terms *Adaptive Modulation and Coding (AMC)* and *Advanced Coding and Modulation (ACM)* are sometimes used interchangeably, but they refer to distinct concepts with different scopes and implementations.

Adaptive Modulation and Coding (AMC)

AMC is a real-time link adaptation technique that dynamically adjusts the modulation scheme and coding rate according to the instantaneous channel conditions, such as signal-to-noise ratio (SNR), fading, or atmospheric attenuation. The goal is to maximize spectral efficiency while maintaining a reliable communication link.

This adaptation typically occurs on a per-frame or per-packet basis and relies on feedback from the receiver to the transmitter. For example, under adverse weather conditions (e.g., heavy rain), the system might switch to a lower-order modulation such as QPSK with a strong forward error correction code. Conversely, under clear-sky conditions, the system may use higher-order modulation such as 16-QAM or 32-APSK with weaker coding to increase throughput.

AMC is widely used in terrestrial systems such as LTE, 5G, and WiMAX, and is also employed in satellite communications, particularly for return links or spot beam optimizations.

Advanced Coding and Modulation (ACM)

ACM, on the other hand, is a broader concept commonly used in satellite communication standards such as DVB-S2 and DVB-S2X. It refers to a family of techniques that includes AMC but also encompasses additional mechanisms for system-wide adaptation.

ACM typically includes:

- Real-time link adaptation based on receiver feedback (i.e., AMC)

- Use of high-performance channel coding schemes (e.g., LDPC with BCH)
- Beam-specific adaptation for high-throughput satellites (HTS)
- Weather-aware adjustments based on rain fade predictions
- Application-layer or QoS-aware transmission policies

Unlike AMC, which is often confined to simple feedback-driven adaptation, ACM can involve centralized control at the gateway and system-level resource optimization across multiple users and beams.

Comparison Summary

Feature	**AMC**	**ACM**
Full Name	Adaptive Modulation and Coding	Advanced Coding and Modulation
Scope	Per-link adaptation	System-wide strategy
Adaptation Trigger	Channel feedback (e.g., SNR)	Channel, weather, application demand
Granularity	Frame or packet level	Per user or per beam
Use Case	LTE, 5G, WLAN, VSAT	DVB-S2, DVB-S2X, HTS
Includes	Modulation and coding switch	AMC + coding + scheduling

Comparison between AMC and ACM techniques

To summarize, AMC is a subset of the broader ACM framework. While AMC focuses on reactive, per-link adaptation, ACM encompasses a more advanced and strategic use of modulation and coding schemes, particularly in satellite systems, where it integrates multiple adaptation layers for improved efficiency, reliability, and throughput.

Bibliography

[1] ITU-R Recommendation V.431, "Nomenclature of the frequency and wavelength bands used in telecommunications," 2015.

[2] D. M. Pozar, *Microwave Engineering*. Wiley, 4th ed., 2012.

[3] ITU-R Recommendation P.618-13, "Propagation data and prediction methods required for the design of Earth-space telecommunication systems," tech. rep., International Telecommunication Union, 2017.

[4] L. Ippolito, "Propagation Effects Handbook for Satellite System Design—Section 2 Prediction," *ACS Stanford Telecommun., Tech. Rep*, p. 129, 1999.

[5] E. Vilar, P. Lo, J. Haddon, and T. Moulsley, "Measurement and modelling of amplitude and phase scintillations in an earth–space path," *Journal of the Institution of Electronic and Radio Engineers*, vol. 55, no. 3, pp. 87–96, 1985.

[6] J. R. Crepp, S. O. Letchev, S. J. Potier, J. H. Follansbee, and N. T. Tusay, "Measuring phase errors in the presence of scintillation," *Optics Express*, vol. 28, no. 25, pp. 37721–37733, 2020.

[7] M. Hayman, S. Spuler, and B. Morley, "Polarization lidar observations of backscatter phase matrices from oriented ice crystals and rain," *Optics Express*, vol. 22, no. 14, pp. 16976–16990, 2014.

[8] C. Moroder, U. Siart, C. Chwala, and H. Kunstmann, "Modeling of wet antenna attenuation for precipitation estimation from microwave links," *IEEE Geoscience and Remote Sensing Letters*, vol. 17, no. 3, pp. 386–390, 2020.

[9] A. Jamalipour, *Low Earth Orbital Satellites for Personal Communication Networks*. 1997.

[10] N. P. Nagendra and T. Segert, "Challenges for NewSpace Commercial Earth Observation Small Satellites," *New Space*, 2017.

[11] M. N. Sweeting, "Modern Small Satellites-Changing the Economics of Space," *Proceedings of the IEEE*, 2018.

[12] B. Sklar, *Digital Communications: Fundamentals and Applications*. Prentice Hall, 2001.

[13] S. Karapantazis and F.-N. Pavlidou, "Broadband communications via high-altitude platforms: A survey," *IEEE Communications Surveys & Tutorials*, vol. 7, no. 1, pp. 2–31, 2005.

[14] G. Gallinaro, A. Vernucci, and C. Moreau, "Protocols and signalling for fade mitigation techniques (fmt) in dvb-rcs multi-beam systems: Final report," June 2005.

[15] A. Kelmendi, A. Švigelj, T. Javornik, and A. Hrovat, "Propagation-impairments modelling and fade-mitigation techniques for earth-satellite links," *SpringerBriefs in Applied Sciences and Technology*, pp. 5–30, 2023.

[16] L. Castanet, A. Bolea-Alamañac, and M. Bousquet, "Interference and fade mitigation techniques for Ka and Q/V band satellite communication systems," in *Proc. 2nd International Workshop of COST Action*, vol. 280, 2003.

[17] Digital Video Broadcasting (DVB), "DVB Specifications," technical report, European Broadcasting Union (EBU), Mar. 2025. Accessed: 2025-04-17.

[18] A. Pietrabissa and A. Fiaschetti, "Dynamic uplink frame optimization with acm in dvb-rcs2 satellite networks," in *2012 IEEE First AESS European Conference on Satellite Telecommunications (ESTEL)*, pp. 1–7, 2012.

[19] T. O. El Shabrawy and S. H. A. Wahed, "Adaptive modulation and coding for broadcast dvb-h systems," in *2009 IEEE 20th International Symposium on Personal, Indoor and Mobile Radio Communications*, pp. 1292–1296, 2009.

[20] L. Vignaroli, V. Mignone, M. Rossini, A. Bertella, M. Tabone, A. Vaccaro, and G. Boccolini, "Dvb-s2 acm and acm/qos integration for triple-play bi-directional satellite services in the unic project," in *2008 10th International Workshop on Signal Processing for Space Communications*, pp. 1–7, 2008.

[21] L. Z. Hui and G. Q. Yang, "Uplink user power control for low-orbit satellite communication systems," in *2018 IEEE 4th International Conference on Computer and Communications (ICCC)*, pp. 634–639, 2018.

[22] A. D. Panagopoulos, T. D. Kritikos, and J. D. Kanellopoulos, "Adaptive uplink power control in adjacent DVB-RCS networks: Interference statistical distribution," in *2007 IEEE 18th International Symposium on Personal, Indoor and Mobile Radio Communications*, pp. 1–4, 2007.

[23] E. Lagunas, S. K. Sharma, S. Maleki, S. Chatzinotas, and B. Ottersten, "Power control for satellite uplink and terrestrial fixed-service coexistence in ka-band," in *2015 IEEE 82nd Vehicular Technology Conference (VTC2015-Fall)*, pp. 1–5, 2015.

[24] P. O. Riza, K. Tanjung, G. Hendrantoro, and A. Mauludiyanto, "Implementation site diversity method on ka-band satellite to reduce the impact of rain attenuation in the tropics area," in *International Conference on ICT for Smart Society*, pp. 1–6, 2013.

[25] S. N. Livieratos and J. D. Kanellopoulos, "Prediction of the degradation of the carrier-to-noise plus interference ratio concerning a site diversity system suffering from differential rain attenuation," *Radio Science*, vol. 37, no. 5, pp. 1–13, 2002.

[26] C. Capsoni, M. D'Amico, and R. Nebuloni, "Time and site diversity gain: A close relationship," in *2009 International Workshop on Satellite and Space Communications*, pp. 166–170, 2009.

[27] R. J. Acosta, E. Matricciani, and C. Riva, "Slant path attenuation and microscale site diversity gain measured and predicted in guam with the synthetic storm technique at 20.7 GHz," in *2013 7th European Conference on Antennas and Propagation (EuCAP)*, pp. 61–64, 2013.

[28] N. Lyras, C. I. Kourogiorgas, A. Panagopoulos, and S. Ventouras, "Rain attenuation statistics at ka and q band in athens using sst and short scale dynamic diversity gain evaluation," in *2016 Loughborough Antennas & Propagation Conference (LAPC)*, pp. 1–5, 2016.

[29] M. M. Alam, I. M. Rafiqul, K. Badron, D. A. Farah, A. K. Lwas, and H. Dao, "Time diversity gain analysis for earth to satellite link based on measured rain rate," in *2018 7th International Conference on Computer and Communication Engineering (ICCCE)*, pp. 109–113, 2018.

[30] I. M. Rafiqul, M. L. Altajjar, M. S. Habib, K. Abdullah, M. M. Rashid, and K. L. Bashar, "Frequency diversity improvement factor for rain fade mitigation in malaysia," in *2015 IEEE International WIE Conference on Electrical and Computer Engineering (WIECON-ECE)*, pp. 159–163, 2015.

[31] A. Z. Papafragkakis, C. I. Kourogiorgas, and A. D. Panagopoulos, "Triple frequency diversity and frequency scaling experimental campaign in attica, greece: Preliminary results," in *2020 XXXIIIrd General Assembly and Scientific Symposium of the International Union of Radio Science*, pp. 1–4, 2020.

[32] W. Chujo, T. Manabe, S.-i. Yamamoto, and K. Suzuki, "Dual frequency use technique for 40-ghz satellite communication during rainfall attenuation," in *2015 International Symposium on Antennas and Propagation (ISAP)*, pp. 1–3, 2015.

[33] P. Fan, X. Cui, and M. Lu, "Space and frequency diversity characterization of mobile gnss receivers in multipath fading channels," *Tsinghua Science and Technology*, vol. 25, no. 2, pp. 294–301, 2020.

[34] T. Teramoto, S. Chihara, W. Chujo, T. Manabe, S. Yamamoto, and A. Tsuzuku, "Ka- and ku-band satellite availability and frequency diversity characteristics during rain using state transition matrix," in *2010 Asia-Pacific Microwave Conference*, pp. 2107–2110, 2010.

[35] E. Johnson, "ARQ protocol features for HF radio links," in *MILCOM 2002. Proceedings*, vol. 1, pp. 125–130 vol.1, 2002.

[36] G. Maral and M. Bousquet, *Satellite Communications Systems: Systems, Techniques and Technology.* John Wiley & Sons, 5 ed., 2009.

[37] H. Hemmati, *Near-Earth Laser Communications.* CRC Press, 2020.

[38] O. Kodheli, E. Lagunas, N. Maturo, *et al.*, "Satellite communications in the new space era: A survey and future challenges," *IEEE Communications Surveys & Tutorials*, vol. 23, no. 1, pp. 70–109, 2021.

[39] A. Guidotti, A. Vanelli-Coralli, and S. Cioni, "Architectures and key technical challenges for 5g systems incorporating satellites," *International Journal of Satellite Communications and Networking*, vol. 35, no. 4, pp. 253–272, 2017.

[40] R. J. Watson and D. D. Hodges, "A real-time shf propagation forecasting system using numerical weather predictions and radar measurements," in *2005 IEEE Antennas and Propagation Society International Symposium*, vol. 4, pp. 47–50, IEEE, 2005.

[41] N. Jeannin, M. Outeiral, L. Castanet, C. Pereira, D. Vanhoenacker-Janvier, C. Riva, C. Capsoni, L. Luini, M. Cossu, and A. Martellucci, "Atmospheric channel simulator for the simulation of propagation impairments for Ka band data downlink," in *8th European Conference on Antennas and Propagation, EuCAP 2014*, (The Hague, Netherlands), pp. 3357–3361, 2014.

[42] M. Biscarini, R. Nebuloni, L. Dossi, S. D. Fabio, P. Scaccia, T. Cherubini, C. Riva, and L. Luini, "A model-chain to generate q-/v-band attenuation time series from short-term numerical weather predictions at continental scale," *IEEE Transactions on Antennas and Propagation*, vol. 72, pp. 8696–8708, 2024.

[43] L. Quibus, V. Le Mire, J. Queyrel, X. Boulanger, L. Castanet, and L. Féral, "Estimating annual temperate rain attenuation distributions at 20/40 ghz with a high-resolution numerical weather prediction model," *IEEE Antennas and Wireless Propagation Letters*, vol. 22, no. 3, pp. 601–605, 2022.

[44] L. Quibus, V. Le Mire, J. Queyrel, L. Castanet, and L. Féral, "Rain attenuation estimation with the numerical weather prediction model wrf: Impact of rain drop size distribution for a temperate climate," in *2021 15th European Conference on Antennas and Propagation (EuCAP)*, pp. 1–5, IEEE, 2021.

[45] A. Marziani, F. Consalvi, G. Fusco, C. Riva, L. Luini, A. Parodi, L. Pulvirenti, M. Lagasio, M. Biscarini, N. Pierdicca, *et al.*, "Microwave tropospheric scintillation and excess attenuation prediction for satellite to earth links using 3d high-resolution meteorological forecast models: Data validation and case study," in *2019 PhotonIcs & Electromagnetics Research Symposium-Spring (PIERS-Spring)*, pp. 3405–3411, IEEE, 2019.

[46] R. Nebuloni, M. Biscarini, L. Dossi, S. Di Fabio, P. Scaccia, P. Antonelli, L. Bernardini, C. Riva, and L. Luini, "Exploiting numerical weather prediction data for radiopropagation modeling of satcom links," in *2024 18th European Conference on Antennas and Propagation (EuCAP)*, pp. 1–5, IEEE, 2024.

[47] M. Outeiral García, N. Jeannin, L. Féral, and L. Castanet, "Use of WRF model to characterize propagation effects in the troposphere," in *7th European Conference on Antennas and Propagation (EuCAP)*, (Gothenburg, Sweden), IEEE, 2013.

[48] K. H. Grythe, L. E. Bråten, S. S. Rønning, and T. Tjelta, "Predicting near-time satellite signal attenuation at ka-band using tropospheric weather.," in *EuCAP 2018–The 12th European Conference on Antennas and Propagation, London, 9-13 April 2018*, 2018.

[49] C. Kourogiorgas, A. Z. Papafragkakis, A. D. Panagopoulos, and S. Ventouras, "Long-term and short-term atmospheric impairments forecasting for high throughput satellite communication systems," in *12th European conference on antennas and propagation (EuCAP 2018)*, p. 260, IET, 2018.

[50] T. Tjelta, J. E. Håkegård, M. Rytir, and K. Grythe, "Short-term forecast of the signal propagation conditions, based on numerical weather prediction, radar, and satcom ground terminal data," in *2023 17th European Conference on Antennas and Propagation (EuCAP)*, pp. 1–5, IEEE, 2023.

[51] V. Le Mire, X. Boulanger, L. Castanet, B. Benammar, and L. Féral, "Potentialities of the numerical weather prediction model wrf to produce attenuation statistics in tropical regions," in *2020 14th European Conference on Antennas and Propagation (EuCAP)*, pp. 1–4, IEEE, 2020.

[52] T. Wardah, S. S. N. Huda, R. Suzana, A. Hamzah, and W. Maisarah, "Wrf model input for improved radar rainfall estimates using kalman filter," in *2014 International Symposium on Technology Management and Emerging Technologies*, pp. 322–327, IEEE, 2014.

[53] E. W. Alsaker and M. Rytir, "Variability of gaseous attenuation at very low elevation angle slant paths; measurements and modelling," in *2020 14th European Conference on Antennas and Propagation (EuCAP)*, pp. 1–5, IEEE, 2020.

[54] ITU-R Recommendation P.676-11, "Attenuation by atmospheric gases," tech. rep., International Telecommunication Union, 2016.

[55] ITU-R Recommendation P.840-7, "Attenuation due to clouds and fog," tech. rep., International Telecommunication Union, 2017.

[56] ITU-R Recommendation P.838-3, "Specific attenuation model for rain for use in prediction methods," tech. rep., 2005.

[57] ITU-R Recommendation P.1853-2, "Time series synthesis of tropospheric impairments," tech. rep., ITU, 2019.

[58] L. Luini and C. Capsoni, "MultiEXCELL: A new rain field model for propagation applications," *IEEE Transactions on Antennas and Propagation*, vol. 59, pp. 4286–4300, nov 2011.

[59] B. D. Lucas and T. Kanade, "An iterative image registration technique with an application to stereo vision," in *Proceedings DARPA Image Understanding Workshop*, pp. 121–130, 1981.

[60] G. Ayzel, M. Heistermann, and T. Winterrath, "Optical flow models as an open benchmark for radar-based precipitation nowcasting (rainymotion v0.1)," *Geosci. Model Dev*, vol. 12, pp. 1387–1402, 2019.

[61] NCAR, "National center for atmospheric research." https://ncar.ucar.edu/.

[62] NCEP, "National centers for environmental prediction." https://www.weather.gov/ncep/.

[63] W. C. Skamarock, J. B. Klemp, J. Dudhia, D. O. Gill, Z. Liu, J. Berner, W. Wang, J. G. Powers, M. G. Duda, D. M. Barker, and X.-Y. Huang, "A Description of the Advanced Research WRF Model Version 4.3," tech. rep., NCAR/UCAR, Boulder, Colorado, 2021.

[64] W. C. Skamarock, J. B. Klemp, J. Dudhia, D. O. Gill, D. M. Barker, M. G. Duda, X.-Z. Huang, W. Wang, and J. G. Powers, *WRF Model Users Page: WRF Version 4.3 User's Guide*. NCAR, 2021. https://www2.mmm.ucar.edu/wrf/users/docs/user_guide_v4/v4.3/contents.html.

[65] NCAR/UCAR, "WPS geographical static data downloads page." https://www2.mmm.ucar.edu/wrf/users/download/get_sources_wps_geog.html.

[66] ITU-R Recommendation P.453-14, "The radio refractive index: its formula and refractivity data P Series Radiowave propagation," 2019.

[67] V. Mattioli, P. Basili, S. Bonafoni, P. Ciotti, and E. R. Westwater, "Analysis and improvements of cloud models for propagation studies," *Radio Science*, vol. 44, no. 2, pp. 1–13, 2009.

[68] H. J. Liebe, "MPM-An atmospheric millimeter-wave propagation model," *International Journal of Infrared and Millimeter Waves*, vol. 10, pp. 631–650, jun 1989.

[69] P. S. Ray, "Broadband Complex Refractive Indices of Ice and Water," *Applied Optics*, vol. 11, p. 1836, aug 1972.

[70] H. J. Liebe, G. A. Hufford, and T. Manabe, "A model for the complex permittivity of water at frequencies below 1 THz," *International Journal of Infrared and Millimeter Waves 1991 12:7*, vol. 12, pp. 659–675, jul 1991.

[71] H. J. Liebe and T. Manabe, "Millimeter-Wave Attenuation and Delay Rates Due to Fog/Cloud Conditions," *IEEE Transactions on Antennas and Propagation*, vol. 37, no. 12, pp. 1617–1623, 1989.

[72] N. Jeannin, M. Outeiral, L. Castanet, Carlo, Capsoni, L. Luini, C. Riva, D. Vanhoenacker-Janvier, and C. Pereira, "Channel Modeling for Design of Earth Observation Ka-band Data Downlink Systems: TN 4 Simulator Description and Test Document," tech. rep., ESTEC 4000105326/12/NL/LVH, ESA, Sept. 2014.

[73] H. C. van de Hulst, *Light Scattering by Small Particles (Dover Books on Physics)*. Dover Publications, 2 ed., 1981.

[74] T. Manabe, T. Ihara, and Y. Furuhama, "Inference of raindrop size distribution from attenuation and rain rate measurements," *IEEE transactions on antennas and propagation*, vol. 32, no. 5, pp. 474–478, 1984.

[75] J. S. Marshall, W. M. K. Palmer, J. S. Marshall, and W. M. K. Palmer, "The Distribution of Raindrops With Size," aug 1948.

[76] R. Gunn and G. D. Kinzer, "The terminal velocity of fall for water droplets in stagnant air," *Journal of Atmospheric Sciences*, vol. 6, pp. 243–248, aug 1949.

[77] ITU-R Recommendation P.839-4, "Rain height model for prediction methods," tech. rep., 2013.

[78] R. Burtch, "A Comparison of Methods used in Rectangular to Geodetic Coordinate Transformations," *ACSM Annual Conference and Technology Exhibition*, pp. 1–25, 2006.

[79] W. E. Featherstone and S. J. Claessens, "Closed-form transformation between geodetic and ellipsoidal coordinates," *Studia Geophysica et Geodaetica*, vol. 52, pp. 1–18, jan 2008.

[80] R.-J. You, "Transformation of Cartesian to Geodetic Coordinates without Iterations," *Journal of Surveying Engineering*, vol. 126, pp. 1–7, feb 2000.

[81] D. A. Vallado, P. Crawford, R. Hujsak, and T. S. Kelso, *Revisiting Spacetrack Report #3*. AIAA/AAS Astrodynamics Specialist Conference, 2006.

[82] J. P. Snyder, "Map projections - a working manual," tech. rep., Washington, D.C., 1987.

[83] Matplotlib, "Matplotlib basemap toolkit." https://matplotlib.org/basemap/.

[84] P. T. Inc., "Collaborative data science." https://plotly.com/python/map-configuration/.

[85] K. Jordahl, J. V. den Bossche, M. Fleischmann, J. Wasserman, J. McBride, J. Gerard, J. Tratner, M. Perry, A. G. Badaracco, C. Farmer, G. A. Hjelle, A. D. Snow, M. Cochran, S. Gillies, L. Culbertson, M. Bartos, N. Eubank, maxalbert, A. Bilogur, S. Rey, C. Ren, D. Arribas-Bel, L. Wasser, L. J. Wolf, M. Journois, J. Wilson, A. Greenhall, C. Holdgraf, Filipe, and F. Leblanc, "geopandas/geopandas: v0.8.1," July 2020.

[86] Contextily, "Context geo tiles in python." https://contextily.readthedocs.io/en/latest/#.

[87] CelesTrak, "Satellites Orbit Data." www.CelesTrak.com.

[88] B. Rhodes, "sgp4 2.20." https://pypi.org/project/sgp4/.

[89] B. Rhodes, Rhodes, and Brandon, "Skyfield: High precision research-grade positions for planets and Earth satellites generator," *ascl*, p. ascl:1907.024, 2019.

[90] International Telecommunication Union Radio communication (ITU- R), "SG 3 Databanks - Formatted Tables." https://www.itu.int/en/ITU-R/study-groups/rsg3/Pages/dtbank-form-tables.aspx, June 2019.

[91] Recommendation ITU-R P.1623-1, "Prediction method of fade dynamics on Earth-space paths," tech. rep., 2003.

[92] M. M. Van de Kamp, "Statistical analysis of rain fade slope," *IEEE Transactions on Antennas and Propagation*, vol. 51, pp. 1750–1759, aug 2003.

[93] J. Feil, L. J. Ippolito, H. Helmken, C. E. Mayer, S. Horan, and R. E. Henning, "Fade slope analysis for Alaska, Florida, and New Mexico ACTS propagation data at 20 and 27.5 GHz," *Proceedings of the IEEE*, vol. 85, no. 6, pp. 926–935, 1997.

[94] J. S. Simonoff, *Smoothing methods in statistics*. Springer Science & Business Media, 2012.

[95] A. Kelmendi, A. Hrovat, A. Svigelj, and M. Mohorcic, "Fade Slope Analysis of Alphasat Satellite Measurements at Ka and Q Bands," *15th European Conference on Antennas and Propagation, EuCAP 2021*, mar 2021.

[96] I.-R. S. Groups, "Test variables for the selection of prediction methods," tech. rep., 2016.

[97] C. Capsoni, L. Luini, A. Paraboni, C. Riva, and A. Martellucci, "A new prediction model of rain attenuation that separately accounts for stratiform and convective rain," *IEEE Transactions on Antennas and Propagation*, vol. 57, no. 1, pp. 196–204, 2009.

[98] G. H. Bryant, I. Adimula, C. Riva, and G. Brussaard, "Rain attenuation statistics from rain cell diameters and heights," *International Journal of Satellite Communications*, vol. 19, pp. 263–283, may 2001.

[99] C. Capsoni, F. Fedi, C. Magistroni, A. Paraboni, and A. Pawlina, "Data and theory for a new model of the horizontal structure of rain cells for propagation applications," *Radio Science*, vol. 22, no. 3, pp. 395–404, 1987.

[100] E. Salonen, S. Karhu, P. Jokela, W. Zhang, S. Uppala, H. Aulamo, S. Sarkkula, and J. P. V. Poiares Baptista, "Modelling and calculation of atmospheric attenuation for low-fade-margin satellite communications," *ESA Journal*, vol. 16, no. 3, pp. 299–317, 1992.

[101] B. K. Horn and B. G. Schunck, "Determining optical flow," *Artificial Intelligence*, vol. 17, pp. 185–203, aug 1981.

[102] K. R. T. Aires, A. M. Santana, and A. A. D. Medeiros, "Optical Flow Using Color Information. ACM New York, NY, USA," 2008.

[103] G. L. Barrows, J. S. Chahl, and M. V. Srinivasan, "Biologically inspired visual sensing and flight control," *The Aeronautical Journal*, vol. 107, no. 1069, pp. 159–168, 2003.

[104] J. L. Barron, D. J. Fleet, and S. S. Beauchemin, "Performance of Optical Flow T echniques," *IJCV*, pp. 43–77, 1994.

[105] S. Baker, D. Scharstein, J. P. Lewis, S. Roth, M. J. Black, and R. Szeliski, "A database and evaluation methodology for optical flow," *International journal of computer vision*, vol. 92, no. 1, pp. 1–31, 2011.

[106] G. Zhang and H. Chanson, "Application of local optical flow methods to high-velocity free-surface flows: Validation and application to stepped chutes," *Experimental Thermal and Fluid Science*, vol. 90, pp. 186–199, 2018.

[107] G. W. Humphreys and V. Bruce, *Visual cognition: Computational, experimental, and neuropsychological perspectives*. Psychology Press, 2021.

[108] S. S. Beauchemin and J. L. Barron, "The computation of optical flow," *ACM computing surveys (CSUR)*, vol. 27, no. 3, pp. 433–466, 1995.

[109] M. Unser, "Splines: A perfect fit for signal and image processing," *IEEE Signal processing magazine*, vol. 16, no. 6, pp. 22–38, 1999.

[110] G. L. Besnerais and F. Champagnat, "Dense optical flow by iterative local window registration," *Proceedings - International Conference on Image Processing, ICIP*, vol. 1, pp. 134–137, 2005.

[111] S. Baker and I. Matthews, "Lucas-kanade 20 years on: A unifying framework," *International journal of computer vision*, vol. 56, no. 3, pp. 221–255, 2004.

[112] S. van der Walt, J. L. Schönberger, J. Nunez-Iglesias, F. Boulogne, J. D. Warner, N. Yager, E. Gouillart, T. Yu, and the scikit-image contributors, "scikit-image: image processing in Python," *PeerJ*, vol. 2, p. e453, 6 2014.

[113] J. Sánchez Pérez, E. Meinhardt-Llopis, and G. Facciolo, "TV-L1 Optical Flow Estimation," *Image Processing On Line on*, vol. 3, pp. 137–150, 2013.

[114] L. I. Rudin, S. Osher, and E. Fatemi, "Nonlinear total variation based noise removal algorithms," *Physica D: nonlinear phenomena*, vol. 60, no. 1-4, pp. 259–268, 1992.

[115] A. Chambolle, "An algorithm for total variation regularization and denoising," *J. Math. Imaging Vision*, vol. 20, pp. 89–97, 2004.

[116] M. Heistermann, S. Jacobi, and T. Pfaff, "An open source library for processing weather radar data (wradlib)," *Hydrology and Earth System Sciences*, vol. 17, no. 2, pp. 863–871, 2013.

[117] NOAA, "Earth System Research Laboratory." https://esrl.noaa.gov/gsd/wrfportal/namelist_input_options.html.

[118] J.-B. Jee and S. Kim, "Sensitivity Study on High-Resolution WRF Precipitation Forecast for a Heavy Rainfall Event," *MDPI*, p. 17, 2017.

[119] J. Jang and S. Hong, "Quantitative forecast experiment of a heavy rainfall event over korea in a global model: horizontal resolution versus lead time issues," *Meteorology and Atmospheric Physics*, vol. 124, pp. 113–127, 2014.

[120] S. Dravitzki and J. McGregor, "Predictability of heavy precipitation in the waikato river basin of new zealand," *Monthly Weather Review*, vol. 139, no. 7, pp. 2184–2197, 2011.